Smart Magnetic Dispersions – From Switchable Release to Well-Defined Hybrid Nanofibers

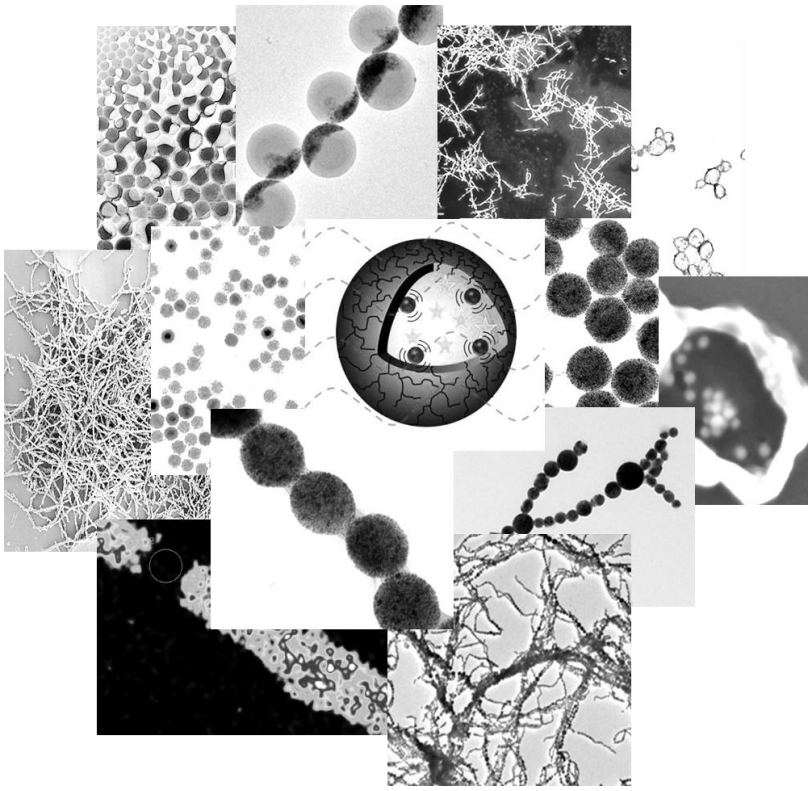

Markus Bannwarth

Dissertation

Max-Planck-Institut für Polymerforschung

Max Planck Institute for Polymer Research

Smart Magnetic Dispersions – From Switchable Release to Well-Defined Hybrid Nanofibers

Dissertation

Zur Erlangung des Grades

„Doktor der Naturwissenschaften“

im Promotionsfach Chemie

dem Fachbereich Chemie, Pharmazie und Geowissenschaften

der Johannes Gutenberg-Universität Mainz.

Markus Bannwarth

Geboren in Basel (CH)

Mainz 2013

Dekan:

1. Gutachter:

2. Gutachter:

Tag der mündlichen Prüfung:

Table of Contents

1 Introduction

When Richard Feynman announced that there was still "*plenty of room at the bottom*" more than 50 years ago, he set a direction for a new era - the age of nanoscience.[1] Ever since his speech, many scientists have been attracted to work in the field of nanoscience like gold diggers rushing after their precious treasure. In the meantime, many of the raised expectations from Feynman's speech could be fulfilled. Nowadays, a large abundance of research groups have based their research on the field of nanoscience. However, many problems still have to be solved and new opportunities arise. In recent years two important trends have evolved in the field of nanoscience: On the one hand, the use of nanoparticles and nanocapsules for biomedical applications has emerged as an important field of research in academia and industry.[2-3] On the other hand, the self-assembly of colloidal building blocks has drawn attention in materials science.[4-5] In both cases, going into the nanometer size range is beneficial and multifunctionality is mandatory. A high control over size, implementation of hybrid structures, and surface functionality is often a necessity. Heterophase polymerization (especially miniemulsions and their relatives) is a suitable tool to fulfill the desired requirements. The heterophase platform provides facile access to multifunctional nanoparticles which can then be used for either biomedical application or for self-assembly (Figure 1). In the case of biomedical applications, various opportunities arise ranging from diagnostics and imaging (such as magnetic resonance imaging - MRI) to responsive nanosystems for controlled drug release for therapeutic use. For self-assembled nanostructures, the high degree of order provides the possibility to pattern surfaces or to improve optical, electric, or magnetic properties.

Within the presented work, the synthetic heterophase platform is used for two main purposes: i) In order to explore and establish novel nanocapsules and nanoparticles which can be stimulated on an individual nanocapsule base; ii) To tailor the cooperative behavior of an ensemble of nanoparticles upon application of an external magnetic field and to self-assemble the nanocolloids in a controlled fashion.

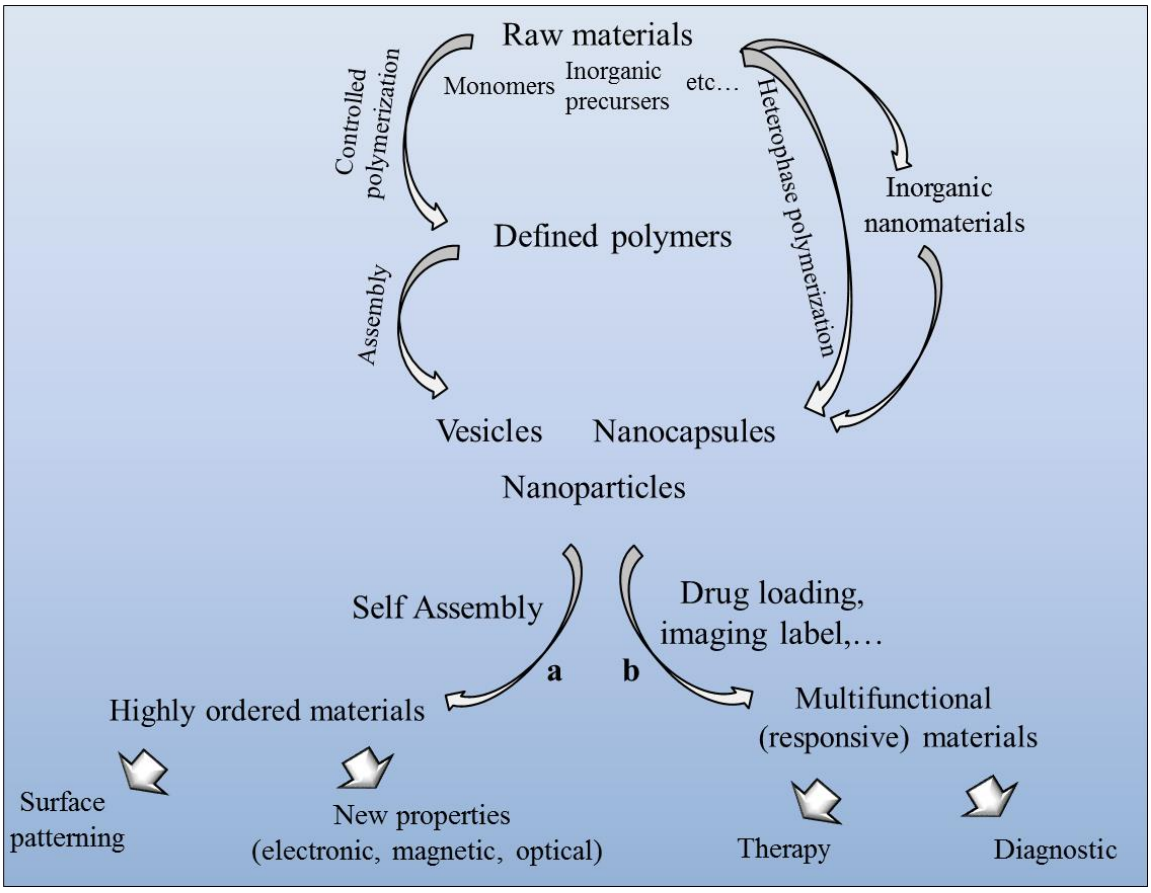

Figure 1. *From raw materials to functional nanomaterials for self-assembly (a) or biomedical applications (b). A prominent route includes the synthesis of multifunctional nanomaterials using heterophase polymerization (especially miniemulsions) and a further step (e.g. self-assembly or drug loading) for their final uses.*

Encapsulation and Triggered Release

The entrapment and controlled release of functional compounds is of fundamental interest. Active compounds such as catalysts, drugs, self-healing materials or adhesives are deactivated by encapsulation. Upon application of a stimulus (change in mechanical force, temperature, pH, salt concentration, application of light, etc.) the protective shell is deformed or decomposed and the active compound is released followed by a desired reaction of the active compound. In contrast to the aforementioned release triggers, a magnetic field is (almost) inert and interacts only with the deliberately integrated magnetic moiety. A release can be achieved without influencing the environment. As a consequence, the stimulus is not harming the environment (*e.g.* healthy tissue around a tumor) and the stimulus is not retarded (*e.g.* light gets absorbed). Such a specific stimulus is highly desirable in many cases. Exemplary, drugs can be released in remote-controlled fashion at a desired time.

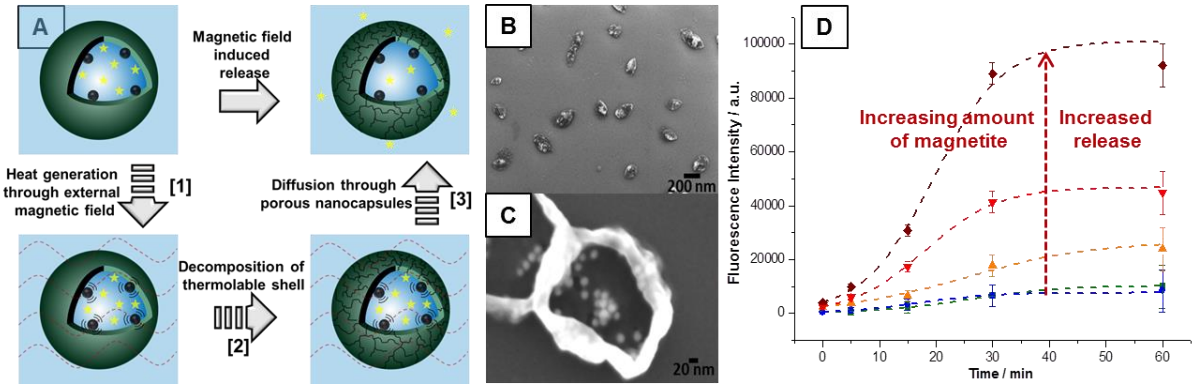

Figure 2. *Release of functional compounds upon application of an alternating magnetic field. A: Schematic illustration of the release. [1] Heat is generated in an external magnetic field. [2] The thermolabile shell decomposes. [3] Active substances diffuse out. B+C: Nanocapsules loaded with magnetic nanoparticles. D: Release of a fluorescent compound.*

In order to achieve a magnetic field induced release from nanocapsules, we combined the encapsulation of magnetic nanoparticles into polymer nanocapsules and the use of a thermolabile compound as shell material (Figure 2). The magnetic nanoparticles act as generators for heat, which is absorbed by the decomposition of the thermolabile compound. The shell degrades and active substances can be released.

From Spherical Nanocolloids to Fibers and Colloidal Polymers with Higher Architecture

Besides making a single nanoparticle or nanocapsules responsive towards an external stimulus, it is of fundamental interest to influence the response of an ensemble of particles in a cooperative fashion. By tailoring the attraction/repulsion forces of nanoparticles, arrangements of higher order are possible. Through the assembly of zero-dimensional (0D) spherical colloids, ordered structures in 1D, 2D or 3D can be realized. For many applications it is mandatory not only to arrange spheres, but to permanently maintain the arrangement. A very simplified example can be given by the film formation process. Polymer spheres arrange in 2D-fashion on a "templating surface" and are sintered to form a stable coating.

In the presented work, it was possible to show a combination of a magnetic self-assembly and a sintering of neighboring particles upon an increase in temperature above the glass transition temperature (T_g). Various stable linear structures with tunable periodicity can be obtained following the approach (Figure 3C) to obtain magnetic polymer nanofibers. Inserting nanoparticles with a higher complexity results in more elaborate linear arrangements (Janus nanoparticles give zigzag arrangements).

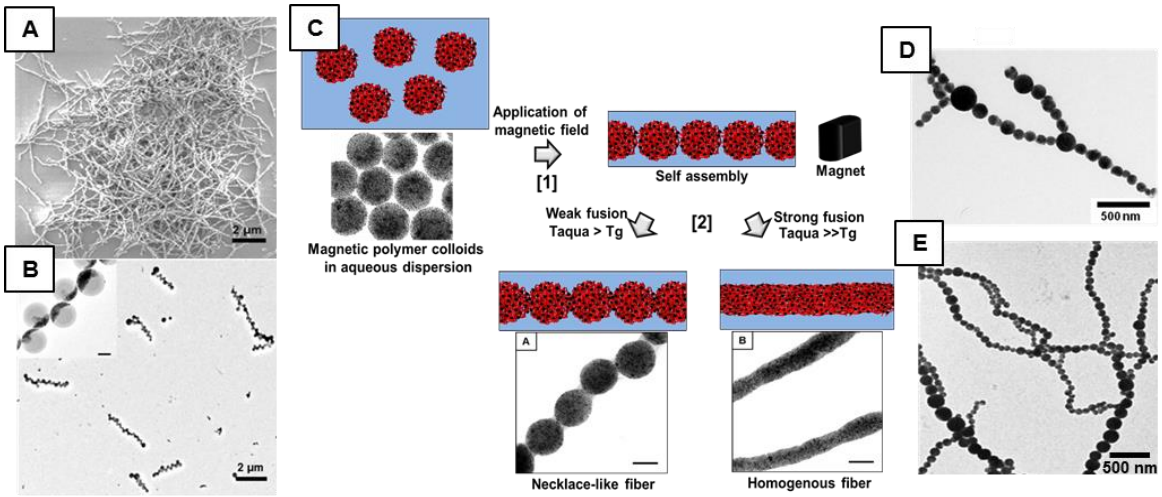

Figure 3. *Defined sintering of magnetically self-assembled nanoparticles. A: Scanning electron microscopy (SEM) image of linear necklace-like nanochains. B: Janus nanoparticles sintered in zigzag-fashion. C: Schematic illustration of the sintering process. D: Introduction of junction points through variation of large to small particles. E: Self-assembly of large and small particles.*

Only a thermal regulator, a pump and a static magnet are used to achieve fiber formation. The fibers are sintered within a timeframe of milliseconds-seconds. The beauty of the invented process lies in its frugality, although it is offering multiple possibilities. Besides linear structures, the aqueous flow setup also allows to produce novel arrangements with higher complexity in analogy to polymer architectures: As for polymers with more than two functionalities, junction points can be introduced. The introduction of junction points is achieved by the insertion of nanoparticles with different sizes (Figure 3D). For copolymerization, two common cases are block copolymers and statistical copolymers. The type of copolymers that results from a comonomer mixture is depending on the reactivity ratio of the two monomers. For the colloidal polymers, both cases, block-like or statistical arrangements of differently sized nanoparticles can be achieved only by varying the flow velocity and particle concentration (Figure 3).

The described method holds great potential to imitate known polymer architectures (*e.g.* linear-, branched-, and block copolymers) using colloidal building blocks. Thus, novel possibilities in colloidal materials science become possible.

Furthermore, the linear assembly and linkage of magnetic nanocolloids can be made reversible when linking the particles with a redoxresponsive complex. For this purpose, hydroxamic acid decorated iron oxide/polymer hybrid nanoparticles were especially designed. Application of a magnetic field assembles the nanocolloids in linear fashion and addition of iron(III) salts cross-links the particles. The reversibility of the linear assembly is demonstrated by the addition of vitamin C, which causes reduction of the iron(III) and destabilization of the linking complex.

In summary, the achieved results open doors in two main areas, making use of magnetic moieties. In the field of drug delivery a multifunctional carrier system for drugs could be demonstrated. A combined use of the system for a remote-controlled release of substances upon application of an external magnetic field and the possibility to trace the nanocapsules *via* MRI becomes possible. Moreover, magnetically labeled polymer nanoparticles can be used to make fibers with distinct arrangements. The fibers could become interesting for catalytic applications, especially for high performance lithium storage or catalysis of oxygen reduction reaction.

2 Theoretical Background

2.1 Magnetism[6]

In principle, every material responds to changes in magnetic fields. The response is a diamagnetic response (Figure 4). For the diamagnetic materials, interactions with magnetic fields are commonly very weak and based on the induction of circular electron movement and therewith small magnetic moment upon a change in the surrounding magnetic field.[7] The application of an external magnetic field yields in repelling forces for diamagnets and in attractive forces for all other forms of magnetism. However, besides the omnipresent diamagnetic property, additional magnetic interactions are possible arising from either unpaired electrons creating a permanent magnetic moment or electronic bands in metals. The unpaired electrons provide an intrinsic magnetic moment in each atom which strongly responds to external magnetic fields. Among the materials with unpaired electrons, different stages can be distinguished. Depending on the thermal conditions, the magnetic spins can be either disordered and act in an independent fashion (paramagnetism) or can be ordered and act in a cooperative way. For ordered spins, many possibilities exist including ferromagnetism, antiferromagnetism and ferrimagnetism.

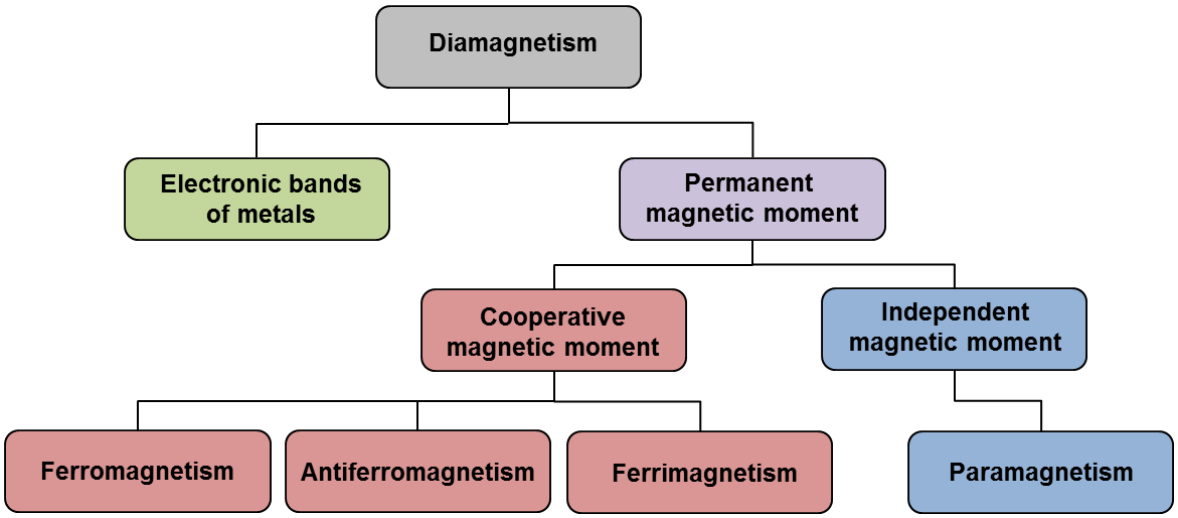

Figure 4. *Different types of magnetism.*[8] *All materials comprise diamagnetic properties. In some cases, an additional type of magnetism is possible depending on the existence of electronic bands or permanent magnetic moments. Depending on the cooperative behavior of permanent moments, different types can be distinguished.*

2.1.1 Diamagnetism

All elements consist of a nucleus and a surrounding shell of electrons. When all electrons are paired, the material is diamagnetic. Owing to the coupling of electrical fields with magnetic fields as given by the Maxwell rules,[9] however interactions between the electron motion and a change in the magnetic field are possible. As a response, a magnetic field which is oppositely vectored to the external field is induced. The induced field is in general very weak. Very strong magnetic fields are required to observe a macroscopic effect. Thus, magnetic fields usually do not affect diamagnetic materials and the materials are usually inert to external magnetic fields. Nevertheless, as a prominent example for a visible consequence of magnetic fields on diamagnetic materials, dizziness can occur when a very strong magnetic field is applied during magnetic resonance imaging (MRI) on patients.

2.1.2 Paramagnetism

Whenever there are unpaired spins in a material, the spins couple with each other. As an antagonist to the coupling force which aims at a higher order of the spins, the thermal motion of the spins creates disorder. In the case of paramagnetism, the thermally induced and entropically favored disorder is stronger. Thus, the spins are completely disordered and no net magnetization can be detected. Under application of an external magnetic field however, the spins align slightly in the direction of the external field. A cooperative behavior of the spins still is not observed. Cooling down a paramagnet below a certain temperature, the Curie temperature, the thermal disorder becomes weaker and the spins form cooperative domains. At the Curie temperature, a transition of magnetically ordered states such as ferromagnetism to paramagnetism is observed. Above the Curie temperature, the magnetization M of paramagnets with an external field H can be described as follows:

$$M = \frac{C}{T} H$$

C is the material specific constant. With increasing temperature, the magnetization scales in reciprocal linearity with the temperature T.

2.1.3 Magnetism with Magnetic Order

Different types of magnetism with magnetic order are known such as ferromagnetism, ferrimagnetism, and antiferromagnetism. Additionally, in superparamagnetism a certain magnetic order can be found, however it is a special case and within the following chapter, only ferro-, ferri- and antiferromagnetism will be described. The next chapter will describe the phenomenon of superparamagnetism and in chapter 2.4 the synthesis, stabilization and applications of superparamagnetic nanoparticles will be discussed in detail.

Whenever magnetic spins couple with each other strongly, a magnetic order can be achieved up to a certain temperature. The order is only given locally in the presence of Weiss domains for which all spins are coupled. Several possibilities for such a coupling exist. All spins can be aligned parallel (ferromagnetism) or the spins can be aligned alternatingly in 180° fashion. In the latter case, the two oppositely oriented spins can carry the same magnetic moment (antiferromagnetism) or a different moment (ferrimagnetism). In the case of ferro- and ferrimagnetism, each Weiss domain generates a magnetic field. However, due to a statistical orientation of the Weiss domains, no effective magnetic field is observed when no external magnetic field is present. For antiferromagnetism, the Weiss domains generate no magnetic field since the oppositely oriented spins erase each other. The interaction of ferromagnetic materials and with an external magnetic field is depicted in Figure 5. When an external field is applied and removed, a retentivity remains in the ferromagnetic material.

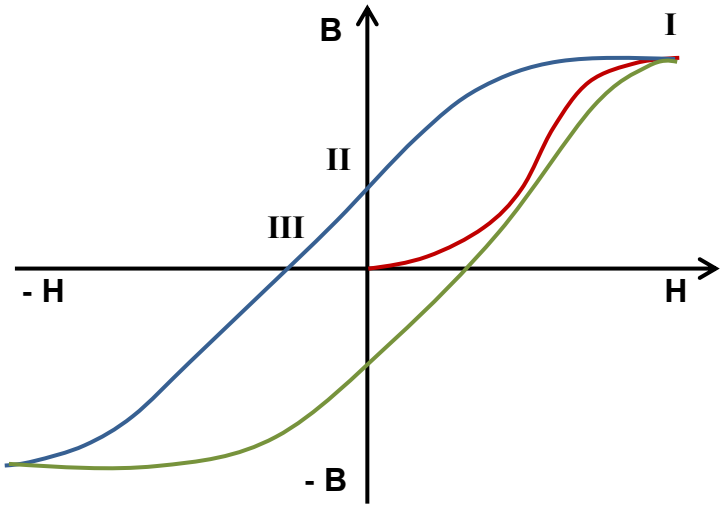

Figure 5. *Hysteresis loop for ferromagnetic materials depicting the flux density B with the external magnetic force H. The red curve shows the first application of the external field and reaches the saturation magnetization at I. Decreasing the magnetic force (blue line) to zero leaves a retentivity (II). The external field that is needed to be applied in the*

opposite direction to demagnetize the material is the so called coercivity field (III).The same behavior is observed in both directions (see green line).

2.1.4 Superparamagnetism

When a strong magnetic field is generated from a substance only upon application of an external magnetic field without retentivity (see Figure 5), the phenomena is called superparamagnetism. Superparamangetic behavior is observed, whenever the small nanoparticles consisting of a ferri- or ferromagnetic material are in the size range of Weiss domains. The single nanoparticle is highly magnetic owing to an alignment of all single spins. However, due to a fast change in the magnetic moment of the nanoparticle, the so called Néel relaxation, no effective magnetic field results. The thermal energy is already high enough to imply a fast change of the direction of the magnetic moment, so that no measureable magnetic moment in certain direction can result. However, when superparamagnetic nanoparticles are aligned in an external magnetic field, a strong and directed magnetization is induced. All magnetic moments of the nanoparticles align at already small external fields and create a strong magnetic moment. A detailed overview over the synthesis of superparamagnetic nanoparticles, their stabilization in dispersion and their multiple applications is given in chapter 2.4.

2.2 Nanocolloid Synthesis in Dispersion

For the synthesis of nanocolloids, different cases have to be distinguished. Mainly three categories exist: The synthesis of mostly/purely inorganic, organic and hybrid nanoparticles which consist of an organic and an inorganic moiety. In all cases, two major pathways are used to prepare the nanocolloids. On the one hand, a bottom up fabrication starting from a seed which grows with the addition of single building blocks is possible. On the other hand, a top down approach which generates small nanocolloids from larger structures can be used. Often the small colloids are firstly produced from liquids to form droplets and then polymerized to obtain solid nanoparticles.

2.2.1 Inorganic Nanocolloids

A commonly used procedure for the synthesis of inorganic nanoparticles is the bottom up approach.[10] Even if top down grinding can yield small inorganic nanoparticles

(sometimes in the nano-regime), the control over the obtained product is very low and a defined shape and size as well as a good dispersibility is not given. As a result the properties of the colloids such as magnetism can be influenced and weakened by grinding.[11] Additionally, for many applications the colloids have to be dispersed after grinding which is not easily accomplished. The bottom up fabrication of superparamagnetic nanoparticles in different solvents is described and discussed in chapter 2.4 and will only be briefly mentioned here. Usually, the process includes two steps, the nucleation stage and the growth step. For the formation of nanocolloids from single building blocks, the thermodynamic energy with respect to the size of the growing crystal can be described as shown in Figure 6. The surface energy (ΔG_{surf}) of the nanoparticle nuclei and their energy gain in volume (ΔG_{vol}) combined account for the total energy (ΔG_{tot}) which is positive for small sizes and negative for larger sizes. Once the energetic nucleation barrier (ΔG^*) is overcome, growth of the crystals is thermodynamically favored.[12] Because the assembly of only few ions is energetically unfavored, nucleation has to be induced. Therefore different possibilities exist: An increase in temperature and thus, in thermal energy increases the energetic level of the single building blocks and promotes the formation of a nucleus. An increase in the energetic level can also be achieved by an increase of the pH value for the formation of metal oxide nanoparticles. Additionally, by adding catalytic agents, the energy barrier can be lowered and the formation of nuclei is possible. Such a catalytic effect is often seen in the case of heteronucleation, where impurities induce nucleation and growth.[13]

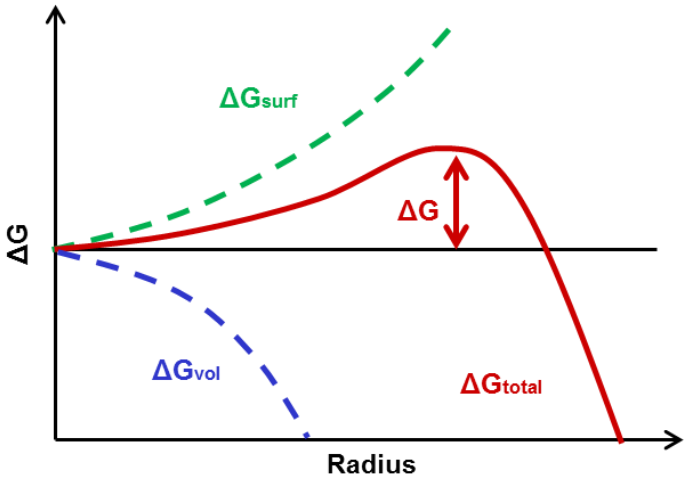

Figure 6. *Thermodynamics energy of nanoparticle formation with increase in radius.[14] The nucleation barrier has to be overcome in order to get thermodynamically stable nanoparticles.*

Even if the theory behind the crystal formation and growth has been investigated for many years, new insights in the understanding of the formation of the very early stages are still to be unraveled.[15]

2.2.2 Organic Nanocolloids

For the preparation of purely organic nanoparticles, the bottom up and the top down method are widely applied. The large abundance of different polymers and copolymers provides many possibilities to obtain different organic nanoparticles. Most commonly, the polymer particle is fabricated from monomers which are polymerized. The fabrication process can be done in different ways: i) A nanoreactor type of process: The monomer is liquid and immiscible with the continuous phase. An initiator is dissolved in the bulk monomer and by energy input into the system (*e.g.* sonication), small nanodroplets of the monomer dissolving the initiator are formed in the continuous phase. A temperature increase or photo-irradiation activates the initiator and polymerizes the monomer to give a polymer nanoparticle as in the case of *e.g.* miniemulsion polymerization.[16-17] ii) A seeded process: Surfactant micelles act as seeds for the polymerization of liquid monomers. Therefore, large droplets of the liquid monomer are formed in a very weakly miscible continuous phase. Small parts of the monomer are present in the continuous phase where the initiator is located and starts the polymerization. The activated monomers/oligomers diffuse into the micelles and with additional diffusion of monomer, the polymerization proceeds and the nanoparticle grows as in the case of *e.g.* emulsion polymerization.[18]

2.2.3 Hybrid Nanocolloids

Even if for the (bottom up) synthesis of inorganic nanoparticles a stabilizer is needed in a dispersion which consists typically of organic building blocks, the actual particle is composed completely of inorganic materials and the organic surfactant is typically loosely attached to the surface in equilibrium with the continuous phase. However, for the synthesis of organic-inorganic hybrid nanoparticles, the actual particle consists of a permanently linked organic and inorganic moiety. In order to fabricate such a particle, pre-synthesized inorganic nanoparticles or inorganic complexes are often introduced in a heterophase polymerization process such as the miniemulsion technique.[19] Therefore, the inorganic moiety shall be homogeneously dispersed in the monomer in order to be well distributed within the resulting hybrid nanoparticle after droplet formation and polymerization. Other possibilities include the formation of

inorganic particles in a pre-synthesized organic nanogel[20] or onto surface functionalized organic nanoparticles,[21] or a grafting of organic compounds onto inorganic nanoparticles (or the other way around).[22]

2.3 Stabilization of Colloids

The stabilization of colloids is directly linked to their size: With decreasing size of the colloids in dispersion, the surface to volume ratio increases. Due to increasing van der Waals interactions with an increased surface area, the particles tend to aggregate and have to be stabilized. The repulsive stabilization force shall be high enough to compensate the van der Waals attraction and to create an energy barrier which is high enough. The barrier has to be many times higher (~10) than the thermal energy and its fluctuations to ensure a stability of the colloids in dispersion.

For the stabilization of colloids two main mechanisms are known and applied: i) The stabilization with charged surfactants based on electrostatic repulsion of the colloids with equal charge. ii) Non-ionic stabilizers from oligomers or polymers, mainly block copolymers, which prevent aggregation based on entropic effects. Both mechanisms of stabilization will be discussed in the following chapters in more detail. The electrostatic stabilization comprises a couple of advantages over the steric stabilization. The stabilization is usually more efficient in oil-in-water emulsions and therefore the dispersion more stable. Thus, smaller particle sizes can be stabilized. Additionally, the size distribution is typically narrower than in the case of steric stabilization. Furthermore, the water resistance after film formation (a common application of dispersions as described in chapter 2.4.4) is higher. The drawback of the electrostatic stabilization is the low stability against electrolytes. An increase in ionic charge often leads to destabilization and aggregation of the colloid dispersion. Additionally, foaming can occur which is unwanted in many applications. Furthermore, electrostatic stabilizers can only be used in polar medium, whereas steric stabilization is in principle possible in every continuous phase.[23]

2.3.1 Electrostatic Stabilization

Electrostatic stabilization is achieved with charged surfactants or stabilizers. In the model case, the surfactants consist of a hydrophilic, charged head group and an aliphatic tail. The stabilization scales exponentially with the dielectric constant of the solvent which makes the stabilization only effective in polar solvents, especially aqueous

dispersions.[24] The electrostatic stabilization is based on the coulomb repulsion of two equally charged surfaces. An illustration of the total energy of attraction, repulsion, and their sum is shown in Figure 7.[25] The overall energy barrier (I) has to be high enough to prevent aggregation which irreversibly occurs due to a high attraction force at very low distances. At higher distances an energetic minimum is possible (II) which can lead to a reversible aggregation of the colloids in dispersion.

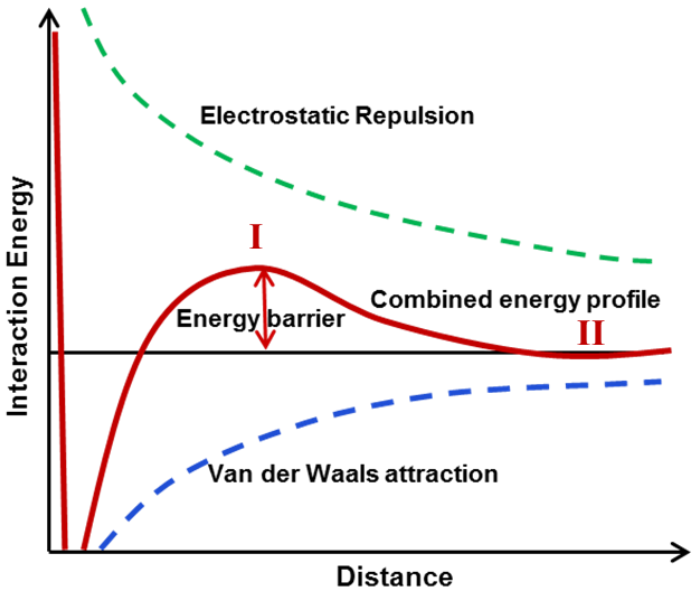

Figure 7. *Illustration of the interparticle interactions consisting of electrostatic repulsion and van der Waals attraction. The overall energy profile accounts for the colloid stability. The energy barrier has to be high enough to prevent aggregation which occurs once the barrier is passed. At small distances a strong attraction leads to an irreversible aggregation. Interestingly, a potential minimum of the combined energy profile at larger distances can lead to reversible aggregation of the colloids upon energy application.*[26]

2.3.2 Steric Stabilization[27]

The steric stabilization of colloid dispersions is achieved with polymer stabilizers. In the common case, the polymers are composed of a block which has a high affinity towards the disperse phase and makes the polymer attach onto the colloid surface. The other block ensures the dissolution of the polymer in the continuous phase and plays the major role in the stabilization mechanism of the polymer. When all colloids are homogeneously dispersed in the continuous phase, the polymer stabilizer attached to the colloids has maximum entropy. Colloids interacting with each other cause reduction in

freedom of the polymer block soluble in the continuous phase. Its entropy is reduced which is energetically unfavored. The steric repulsive forces have to be larger than the attractive van der Waals interactions to prevent colloid aggregation in dispersion. Commonly used steric stabilizers consist of an aliphatic tail and a hydrophilic poly(ethylene glycol) (PEG) block. In such a case, a temperature dependent stabilization is observed. Above the lower critical solution temperature the PEG-chains are insoluble in water and the colloids precipitate. Only below the lower critical solution temperature (LCST) point the polymer stabilizer is useful to prevent the colloids from aggregation.

2.4 Superparamagnetic Nanoparticles[28]

The most commonly used superparamagnetic nanoparticles are iron oxide based. Typically, a spinel crystal structure (M_3O_4) with oxygen ions forming a cubic close packing is the basis for the superparamagnetic nanoparticles. Iron ions then fill the octahedral and tetrahedral sites. However, iron oxides in combination with other, divalent anions in the composition MFe_2O_4 are also possible (M = Co^{2+}, Cu^{2+}, Mg^{2+}, Ni^{2+}, Zn^{2+} and others). The size of the nanoparticles typically ranges from 4-25 nm. Their mass magnetization is dependent on the composition and the crystal structure can reach up to 110 $emu \cdot g^{-1}$.[28] However, more exotic crystals such as $Fe_{40}Co_{60}$ can reach up to 215 $emu \cdot g^{-1}$ as shown by Seo et al.[29] The next chapters will concentrate on the synthesis of the nanostructured crystals, the importance of a suitable surface stabilizer especially in aqueous medium, and their applications in material science and biomedicine.

2.4.1 Synthesis and Surface Modification[30]

Two basic principles for the formation of iron oxide based superparamagnetic nanoparticles are widely used. i) A thermal decomposition of organometallic compounds. Upon heating, decomposition of the organometallic compound leads to the formation of nanoparticles and the decomposed ligand as small gas molecules as a side product. ii) When the pH of an iron containing aqueous solution is increased, the concentration of hydroxide ions also increases and interactions with iron in combination with a second deprotonating step leads to the formation of iron oxide nanoparticles. Having a look at the energy scheme in Figure 6, it can be observed, that the increase in thermal energy promotes the system to overcome the energy barrier and form nuclei. An increase in pH leads to the formation of higher reactive hydroxyl and oxygen anions with a higher chemical potential which enables nuclei formation.

Depending on the conditions for the nanoparticle synthesis, the polydispersity can vary strongly. Nanoparticle formation under basic conditions from aqueous solutions usually gives a broad size distribution.[31] Almost monodisperse crystals can be obtained by the thermal decomposition route of metal oxides.[32] A typical procedure to improve the size distribution is to use small crystals as seeds for the further growth by addition of precursors.[33]

Besides the composition, crystal structure, size and polydispersity of the nanoparticles which account for their magnetic properties, the surface stabilization is of particular importance in dispersions. An very common stabilizer is oleic acid, which enables to disperse the nanoparticles very well in organic solvents.[34] However, in a majority of cases, the superparamagnetic nanoparticles have to be made operational in biological medium and thus in aqueous dispersion or even better, in blood serum. During the last decade, the synthesis of superparamagnetic iron oxide nanoparticles (SPIONs) which are dispersible in water has been a research area of great interest. Various possibilities have been shown including coating with biopolymers[35] or lipids.[36] Additionally, PEG-based surfactants are commonly used such as PEG-catechol[37] and PEG-phosphine oxide.[38] Additionally, the surfactant can also play a major role in controlling the nucleation and growth as well as the obtained crystal structure.[39]

Nevertheless, the before mentioned stabilization procedures suffer from drawbacks since for most of them the concentration of SPIONs has to be almost minute to prevent aggregation. In many cases, additionally, the amount of stabilizer has to be far higher than the amount of core nanoparticle. As alternative stabilizers, a group of electrostatic stabilizers derived from quaternary amines comes into play. Especially tetramethylammoniumhydroxide (TMAOH) is an excellent stabilizer for inorganic nanoparticles in aqueous dispersions and allows for a dispersion of the nanoparticles up to very high concentrations.[40] However, there is a price that has to be paid for the exquisite performance. In the case of quarternary amines, they are not suitable for biomedical applications owing to a couple of factors: Besides their incapability to stabilize nanoparticles in blood serum due to a collapse in electrostatic stabilization caused by the ionic strength of the blood serum, the quaternary amines can be harmful to the body.[41] Therefore a combination of the quaternary amines with other, biocompatible stabilizers is favorable. At first, the hydrophobic nanoparticle are transferred into an aqueous dispersion *e.g.* with the help of TMAOH and the surfactant is then exchanged with a steric stabilizer such as a carboxylated polyvinyl alcohol. Nevertheless, there is still room for improvement when it comes to the stabilization of SPIONs in aqueous medium and especially blood serum.

2.4.2 Applications[42]

Most of the everyday objects around us are diamagnetic. Thus, the introduction of a magnetic label into materials opens up the unique property to address only the magnetic moiety, leaving every other diamagnetic part of the composite material non-influenced.[43] Additionally, our body responds only very weakly to magnetic field and magnetic labeling is possible here as well. In order to achieve a response in a magnetically labeled material, two major possibilities are to be considered: i) The interaction between the magnetic label and an external magnetic field induces an attractive force which can lead to a separation of magnetic dispersions or a change in shape. Whenever the shape is coupled with properties,[44] the properties can be changed upon application of a magnetic field. In most cases, the shape is recovered when the external magnetic field is removed. ii) The application of an alternating magnetic field and thus the switching of the magnetic dipole of the introduced (superpara)magnetic moiety leads to energy dissipation and an increase in temperature. The increase in temperature can either lead to irreversible destruction or be reversible when switching the external magnetic field off and hence, letting the material cool down and relax into its original state.

Table 1 lists different options for the use of magnetic materials. The magnetic moiety is mainly used for either magnetic attraction forces, as heat source or for magnetic imaging. In combination with different materials (often polymers), different applications and uses become possible.

Table 1. *Summary of the use of magnetic (hybrid) materials. The table shows the relationship between the function of the magnetic moiety and the composite material to achieve a certain use or application.*

Use/application	Hybrid composition	Magnetic moiety as		
		magnetic attraction force	contrast agent	source of heat
Magnetic triggered release	Polymer capsules[45-46]	-	-	Yes
	Liposomes[47]	-	-	Yes
	Silica[48]	-	-	(Yes) - to increase diffusion
Nanorotors	Silica[49]	(Yes) – movement along with magnet	-	-
Shape change materials and deformation	Shape memory polymer[50]	-	-	Yes
	Flexible	Yes	-	-

		polymers/ferrogels[51]			
Surfactant stability		Thermoresponsive polymers[52]	-	-	Yes
Optical switch[53]		-	(Yes) – attractive forces between single particles	-	-
Magnetic drug targeting		Various types[54]	Yes	-	-
Removable catalyst		Without composite material[55] Catalytic nanoparticles[56] Graphenes[57]	Yes	-	-
Water purification		Ligands etc. capturing heavy metal ions[58]	Yes	-	-
Hyperthermia treatment		Various types[59]	-	-	Yes
Separation of cells and biomolecules		Cells[60] Specific biomolecules (DNA, Proteins,…)[61]	Yes	-	-
MRI and MPI[62]	Examples:				
	Tracking[63]	*e.g.* Cells	-	Yes	-
	Activity visualization[64]	Various types	-	Yes	-
	Sensors in biology and medicine[65]	Various types	-	Yes	-

A more detailed description of the possible application listed in Table 1 for (superpara)magnetic materials will be given in the upcoming chapters 2.4.2.1 and 2.4.2.2.

2.4.2.1 Materials with a Magnetic Switch

Whatever the intention for implementation of a magnetic moiety is, a polymer matrix is required in almost all the cases.[66] Mostly, polymers are used as structuring matrix. In some cases, additional properties of polymers *e.g.* thermoresponsive behavior come into play. In the following chapters, the interplay of superparamagnetic

nanoparticles together with a polymer matrix in a well-defined nano- or micromaterial is described in more details.

2.4.2.1.1 Encapsulation of Active Compounds and Magnetically Triggered Release

According to the model of Ringsdorf, drugs can be made water soluble/dispersible by conjugating the drug to a polymer.[67] Additionally the polymer provides a selective targeting function. The Ringsdorf model has expanded and its principle is applied to a large variety of delivery systems. Various methods have been demonstrated in the last decades to trap and, upon an external trigger, release active compounds. A broad variety of active substances such as drugs[68] and catalysts[69] could be encapsulated in various containers including vesicles,[70] capsules,[71] dendrimers,[72] nanoparticles[73] and hydrogels[74] and many others. Changes in temperature,[75] pH[76] or irradiation with light[77] among others have been used to achieve a triggered release of active substances.[78] Additionally, it could be demonstrated, that a microwave assisted[79] or electric[80] and magnetic field[81] induced release is suitable as well. Of all the different types to achieve a triggered release, the magnetic field is particularly interesting because it only interacts with the (superpara)magnetic label. Such a label is needed especially for drug delivery since the human body is nearly inert to magnetic fields. In all other stimulated options of release, two major drawbacks have to be considered: Either the stimulus is harming the environment (*e.g.* healthy tissue around a tumor) or the stimulus is retarded (*e.g.* light gets absorbed) and cannot induce a release. Another important advantage of implementing a magnetic stimulus for a triggered release for biomedical applications is the additional use of the superparamagnetic substances as imaging agents or for a magnetic field guided targeting.[82] However, the highly beneficial way of a triggered release is a very challenging one. Only very few examples of a magnetic field induced release are reported in the literature and describe mostly the encapsulation of the active compound in vesicles or capsules, a rather complicated synthetic procedure. In almost all of the cases, a core-shell morphology is described where the core is either liquid or consists of solid, magnetic nanoparticles. The shell is usually the important part which has to react in some way upon changes in the environment.[83-84] Both, hydrophilic and hydrophobic compounds have already been encapsulated and could be released upon application of an external stimulus.[46] Several mechanisms of release are possible: i) The excitation of loose magnetic nanoparticles within a capsule leads to a faster diffusion of encapsulated substances.[48, 85] ii) The magnetic nanoparticles are integrated into lipid vesicles and, upon application of an alternating magnetic field, increase the permeability in the soft shell.[47, 86] iii) A magnetic core is functionalized with thermoresponsive

polymers. The polymer shell is loaded with drugs and releases them once the solid core is being excited and generates heat.[87-88] iv) Thermoresponsive polymers are integrated into the shell. When exciting the magnetic nanoparticles, the temperature is increased. The shell responds to the change in temperature and encapsulated active compounds can diffuse out through newly created pores. v) In a similar approach, a thermolabile compound is inserted in the shell. Upon application of an alternating magnetic field and thus a temperature increase, the shell decomposes irreversibly and a release is achieved. The last case was achieved for the first time as described in chapter 4.1.1. Additionally, we show that it is possible to use the introduced magnetic nanoparticles into a nanocapsule delivery system for a combination of magnetic resonance imaging and magnetic triggered release. Important for the application as drug delivery vehicles, the biocompatibility of the nanocapsules could be shown.

2.4.2.1.2 Deformation, Rotation and Shape Change[89]

The integration of superparamagnetic particles into a diamagnetic matrix enables to address only the particles when applying an external magnetic field. Thus, magnetic forces are suitable for a mechanical deformation. Depending on the matrix properties, the deformation can be reversible or irreversible. Not only can magnetically labeled composite materials be deformed by a magnetic field. Additionally, they can be rotated in the case of a rotating magnetic field. The rotating composite material can be used as a nanorotor.[90] Linear nanochains containing a superparamagnetic moiety within a micrometer emulsion droplet can take over the function of a stirbar within the droplet.[49] In addition to the use of superparamagnetic nanoparticles to induce mechanical forces, they can be used as heat generators under application of an alternating magnetic field. A hybrid material composed of the magnetic nanoparticles as heat source and a thermoresponsive polymer give way to trigger the deformation or shape change in a material by magnetic field application and thus, heat generation. Especially of interest are shape memory polymers, which can change their shape depending on the temperature.[91] A combination of an elastic polymer based on entropic forces and a stiff composite part which is dominating the shape below a certain temperature provides for such a shape changing material. Upon temperature increase, the stiff part becomes more flexible and the shape of the composite material can be changed in a desired way. By decreasing the temperature, the shape can be frozen again. Then, upon temperature increase, the original shape, which is energetically preferred, is recovered. The recovery is driven by the elastic part of the composite material. An introduction of a magnetic trigger has proven to change the macroscopic shape of such composite polymer objects back into the preferred state by applying a magnetic trigger as heat source.[50] Magnetically switchable materials

build from biodegradable polymers have promising perspectives especially as implant materials.[92]

2.4.2.1.3 Magnetically Influencing Surfactant

The use of superparamagnetic nanoparticles as heat source in an alternating magnetic field opens up the possibility to tailor the stability of colloids in dispersion owing to a temperature dependent stabilization with thermoresponsive polymers as surfactants. To give an example, commonly used and commercially available block copolymer stabilizers often consist of a hydrophilic PEG-block. Upon a temperature increase, their ability to sterically stabilize colloids is not maintained and precipiatation of the colloids occurs. The reason herefore is the LCST of PEG. Above the LCST, the solubility of PEG dramatically drops. Depending on the molecular weight and copolymer amount, the LCST of PEG can vary from 9-82 °C.[93] The temperature dependency originates mainly from entropic effects which are linearly increasing with temperature.[94] The entropy of liquid solvent molecules is often higher when no polymer is dissolved. Thus, when the temperature is increased and the entropic effect becomes more influential, the polymer precipitates when reaching a certain temperature, at which the enthalpic energy gain is as big as the entropic energy loss for a dissolved state, the so called LCS temperature. Gelbricht et al. have shown that when superparamagnetic particles are stabilized with thermoresponsive polymers, application of an alternating magnetic field can lead to controlled precipitation of the colloids from solution.[52] Additionally, the group of Schmidt has shown, that also ionic stabilizers which interact with ferromagnetic iron ions can be influenced under application of an external magnetic field causing attraction and deformation of the droplet.[95]

2.4.2.2 Superparamagnetic Dispersions

2.4.2.2.1 Magnetically Induced Reversible Assembly and Disassembly

The assembly of nanoparticles upon application of an external field and their disassembly when removing the field becomes interesting when the assembly/disassembly process is coupled with a certain property. One of the properties is the optical response. The use of magnetic nanoparticle dispersions that possess switchable optical properties has been shown in a couple of examples. For switching the optical properties, the properties of a superparamagnetic dispersion have to be coupled with a

distinct size of the nanocolloids. When the size of the colloids is in the range of the optical wavelength or below with a very narrow size distribution, interaction with light can take place. When light with multiple wavelengths is irradiated in direction of the one dimensionally assembled nanoparticle chains, only some of the wavelengths are reflected by the periodic lattice of particles. The dispersion appears colored. The Bragg reflection accounts for the reflection of only distinct wavelengths. Depending on the size of the nanoparticles the reflected wavelengths and thus color, can be tuned.[53, 96]

2.4.2.2.2 Magnetic Targeting

Very harmful drugs are applied in order to prevent cancer cells from proliferating. To ensure that the drugs are not being taken up by healthy cells, they have to be efficiently encapsulated and addressed only to cancer cells. Several opportunities have already been demonstrated to achieve such a targeted drug delivery. On the one hand, a passive targeting becomes possible by making use of the enhanced permeability and retention (EPR) effect.[97-98] The EPR effect is based on the fast growth of tumors and the therewith along going formation of defect containing endothelium which enables penetration of nanoparticles with a certain size (~20-200 kDa) through the endothelium. Nanoparticles in the blood stream can then enter the cancer tissue directly and thus, nanoparticle drug transporters can be targeted simply because of their size.[99] Another possibility for a selective targeting is the surface labeling of the drug vehicle to allow specific interactions with cancer cells. For the active targeting approach, different labels are possible such as antibodies[100] and others.[101]

Additionally to the passive and active types of targeting, a magnetic field assisted accumulation of magnetically labeled nanoparticles can be achieved.[102] When a superparamagnetic moiety is introduced into the drug delivery system, local application of a magnetic field causes attraction and enrichment of the nanoparticles in the area of desire.

It has to be mentioned, that the surface of the nanoparticular delivery systems in all of the mentioned cases has to be made inert towards interactions with healthy tissue. A "stealth effect" has to be achieved which then guarantees for a long circulation of the nanoparticles in the blood stream, allowing enough time for the selective targeting. The most commonly used approach is to PEGylate the surface.[103] Additionally, other options are also possible such as the use of hydroxyethylstarch.[104-105]

2.4.2.2.3 Removable Catalysts and Water Purification

Whenever a magnetic label is introduced into a composite material, the label can be addressed specifically. In some cases, catalysts are labeled with (superpara)magnetic particles.[57, 106] After performing the catalytic reaction the catalyst can be magnetically separated from the product containing solution/dispersion. Educts and products can be exchanged and when redispersing the catalyst, the reaction can take place again.

In other cases, the magnetically labeled particles are added to a water solution in order to purify it from heavy metal ions,[58] hydrophobic impurities[107] or from bacteria.[108] The metal ion or bacterium is captured on the surface of the particle and can easily be removed magnetically to obtain a purified water solution.

2.4.2.2.4 Separation of Cells and Biomolecules

To investigate complex signaling and trafficking pathways of biomolecules and cells, efficient labeling and separation techniques are a necessity. The labels, which often assist the separation process or enable the detection, can be of many kinds. Most abundantly, fluorescent labels are used which offer the opportunity to simultaneously label, separate and detect. The introduction of florescent labels with different emission wavelength can be used and up to ~30 labels can be detected simultaneously using multiplex immune-bead assays.[109] Other possibilities for the labeling include the introduction of lanthanide isotopes which can further increase the number of labels that can be detected simultaneously.[110] After labeling the compound it is possible to separate it from all other species by the well-known and ubiquitously found technique of fluorescence activated cell sorting (FACS).[111] Here, the device can distinguish between labeled and non-labeled species and separate accordingly. In analogy to FACS, a magnetic cell separation system (MACS) could be demonstrated in the early 90s and is by now established and commercially available.[60] It makes use of the introduction of superparamagnetic nanoparticles as labels into a diamagnetic environment and guarantees for a fast and efficient separation of magnetically labeled compounds. Making use of the MACS system, many different cells could efficiently be labeled and detected as shown for cancer cells,[112] HIV-1 infected cells[113] and others.

2.4.2.2.5 Hyperthermia

Cells are very sensitive towards changes in temperature. Already an increase of a few degrees Celsius can be lethal for the cell. The sensitivity of cells towards a change in temperature can be of use in the case of cancer therapy. Combining the ability to target

superparamagnetic nanoparticles selectively to cancer cells and the use of the particles as local heat generators in an alternating magnetic field (see chapter 4.1.1.5), they can be used for hyperthermia treatment.[114] By definition, cells are heated up to temperatures between 41 and 46 °C for a hyperthermia treatment.[115] Hyperthermia is often applied in combination with radiotherapy in a so called thermo-radiotherapy. Here, heating the cells to a critical, but not lethal temperature makes them more sensitive towards the radiotherapy.

2.4.2.2.6 Magnetic Resonance Imaging (MRI) or Magnetic Particle Imaging (MPI)

The ability of superparamagnetic nanoparticles to only possess a magnetic moment upon application of an external field makes them suitable for many applications, especially in biomedicine. The particles are "inert" as long as no external field is present. When the external magnetic field is applied, the particles are stimulated and can be used for magnetic resonance imaging (MRI), magnetic targeting, hyperthermia treatment or magnetic field induced release.[116-118] For MRI, the change in magnetic field in the surrounding of superparamagnetic nanoparticles is used. The detected signals arise from protons of water molecules which feel a different magnetic field in the presence of superparamagnetic nanoparticles. The presence of the superparamagnetic particles leads to a decrease in the relaxation time of excited protons. Thus, when pulsing several times in a row, the fast relaxing protons have already gone back to ground state and can give a stronger signal. Using a gradient field, a three dimensional image can be obtained.

An additional opportunity to use superparamagnetic particles for imaging is the so called magnetic particle imaging (MPI).[62] MPI is a method that has just recently been applied. It is based on detecting the superparamagnetic particles themselves instead of the surrounding water molecules as for MRI. An oscillating magnetic field is used to induce a rapid change in the magnetization of the superparamagnetic nanoparticles. The change in magnetization is then used for detection. MPI is a promising method for future use, owing to a high sensitivity and a good resolution in time.[119] A gradient magnetic field is applied to obtain a resolution in space as in the case of MRI.

2.4.3 One Dimensional Superparamagnetic Polymer Materials[120]

The synthesis of defined polymer materials with magnetic entity has been attracting great attention in recent years. A major focus was drawn by spherical hybrid nanoparticles which can be synthesized making use of different approaches including the

miniemulsion,[121-122] a combination of emulsion and miniemulsion,[123-124] or the synthesis of gels[125] among others. For the more elaborate synthesis of one dimensional magnetic polymer hybrid nanomaterials however, less examples have been described. In principle, three different techniques are used to access the hybrids: i) The 1D materials are developed in a templating matrix. Several working steps have to commonly be achieved, jet, the abundance of accessible 1D nanohybrids is high. The matrix carrying hollow tubular structures can be made from inorganic materials like aluminum which makes it easy to dissolve the matrix in basic aqueous solution from the formed 1D hybrids.[126] Other possibilities for the matrix creation include the assembly of block copolymer templates with linear gaps,[127] cylindrical polymer brushes[128] or the use of biological templates such as magnetotactic bacteria.[129] ii) The electrospinning technique.[130] The method is facile and larger quantities can be produced .[131] In theory, magnetic nanoparticles can be spun with any polymer processable *via* electrospinning. However, before spinning, the magnetic particles have to be homogenously dispersed in the polymer or together with the polymer in the solvent. The dispersion process limits the amount of magnetic moiety which in most cases cannot be introduced in high amounts.[132] iii) The self-assembly and locking of (superpara)magnetic nanoparticles is an additional possibility for the fabrication of 1D nanohybrids. Here either the assembled nanoparticles can consist of polymer and magnetic particles[133] or only consist of magnetic particles which are linked by a polymer moiety.[134] Different types of linkages have been demonstrated including physical interactions,[135] encapsulation,[136] electrolyte complexes,[137-138] and covalent binding.[139] Additionally, a variety of different polymers could be introduced with various properties ranging from biocompatibility to conductivity. However, the control over the 1D structure and the precision of length, homogeneity of thickness and/or corrugation are limited.

The properties which are possessed by 1D magnetic polymer hybrid nanomaterials are composed of the magnetic and the polymer property as well as the one dimensional geometry. Exemplary, optically responsive, fluorescent PPV/Fe_3O_4 hybrid fibers could be produced by Xin et al.[140] Furthermore, 1D hybrid materials composed of DNA and a magnetic moiety were used by Kinsella et al. to change the conductivity upon application of an external magnetic field.[141] In the case of biocompatible magnetic polymer hybrid materials, it could be shown that for the 1D structure a higher relaxivity was achieved for MRI.[136] Another example shown by Greiner et al. demonstrated the use of 1D hybrids to interconnect hippocampal neurons.[142]

2.4.4 Polymer Particle Sintering – From 2-Dimensional Film Formation to 1-Dimensional Magnetic Fibers

Polymer coatings are widely used to improve the surface properties of materials. A large abundance of polymers are not water soluble and dissolve only in organic solvents.[143] Two major possibilities have been established for film formation of such polymers. i) A solution of polymers dissolved in the corresponding organic solvent is used for the coating. The organic solvent is evaporated and the polymer chains remain as thin film. ii) Polymer nanoparticle dispersions in aqueous medium provides for the polymer coating. Taking environmental considerations into account, the waterborne coatings are favored to method I and have been in developed and improved over the last decades.[144] In order to understand the process of film formation for the waterborne polymer dispersions, one has to have a more detailed look on the film forming polymer chains: Owing to the unique property of polymers to undergo a transition from rigid to ductile at the glass transition temperature (T_g), they can be made accessible for film formation above the T_g. In detail, when reaching the T_g, the thermal energy is high enough to allow bond rotation and certain chain flexibility. Above the T_g, the polymers can be deformed in the presence of forces. In the case of film formation, the reduction of the surface tension between the polymer particles and its surrounding is responsible for the deformation. In a cross-linked polymer network, the deformation goes along with a decrease in entropy and thus, is thermodynamically unfavored. As soon as the external stress is released, the deformation reversibly goes into its original state. When the polymer chains are not cross-linked above T_g, the single chains are able to diffuse randomly within the polymer matrix. Deformation of the polymer matrix occurs upon application of external forces and is irreversible. Non cross-linked polymer chains with a low T_g are essential for polymer film formation. Additionally, the duration of film formation is dependent on the diffusion of the chains which is related to their molecular weight (M_w). For the dependency of the polymer chain diffusion on M_w, two cases can be distinguished:[145] i) When M_w is lower than the entanglement molecular weight M_e, a linear dependence of the viscosity with the molecular weight is described. ii) When the critical molecular weight M_c is about 2-4 times higher than M_e, the viscosity is highly dependent on M_w as follows:

$$\eta_0 \propto M_w^{3.4-3.6} \; for \; M_w > M_c$$

When all requirements for film formation are fulfilled by the polymer particles, the two steps will occur once the particles dispersion is dropped onto a substrate and the aqueous phase evaporated (Figure 8 left side). At first deformation of the round shaped

particles into hexagonal structures takes place. Secondly, polymer chain diffusion forms a homogenous film.

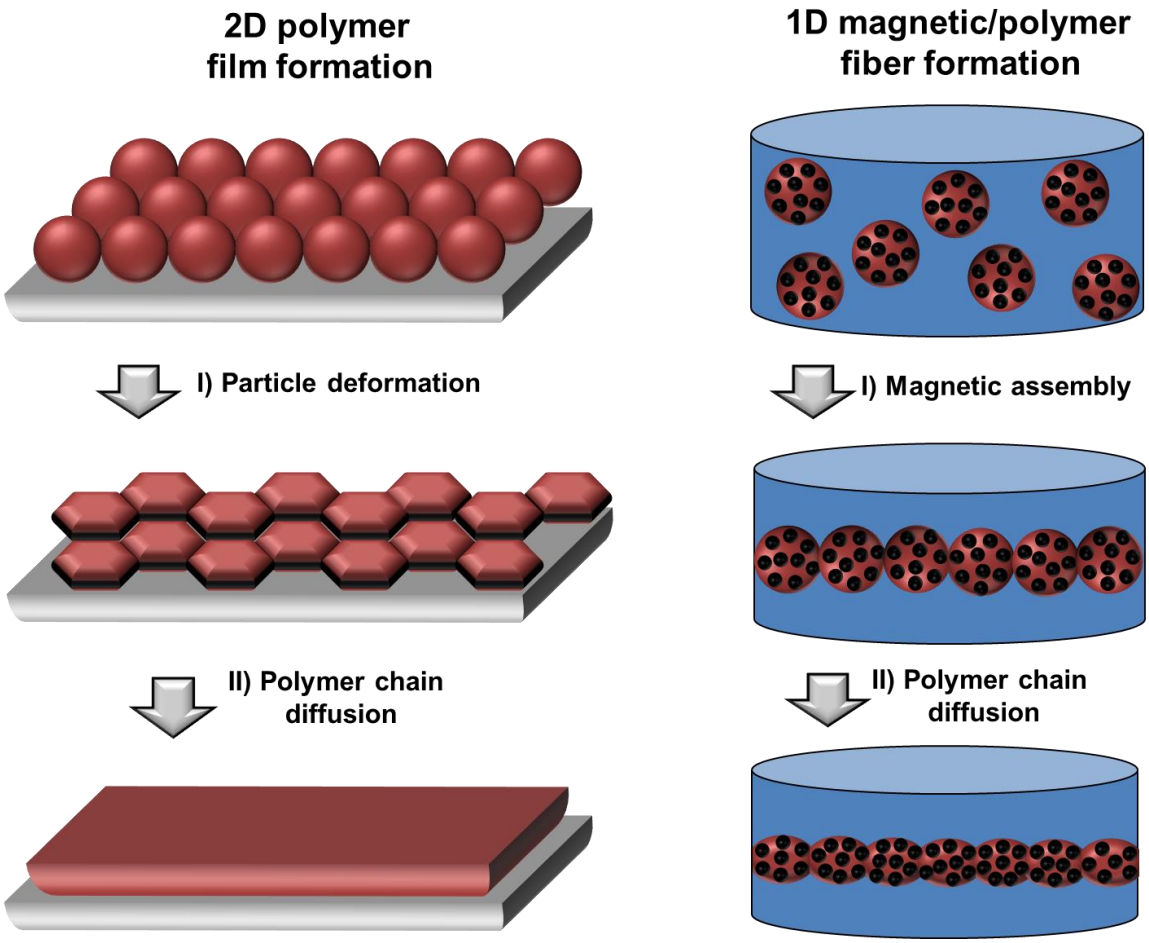

Figure 8. *Left side: Film formation of polymer colloids on a templating substrate as a two-step process. I) Deformation of the colloids increases the contact area between the particles. II) Polymer chain diffusion above the glass transition temperature of the polymer leads to the formation of a homogeneous film. Right side: Linear fiber formation of magnetic/polymer nanoparticles without a template through magnetic alignment and polymer chain diffusion.*

While the 2 dimensional film formation process of polymer colloids has been intensively studied during the last century,[146] recent trends are pointing into other directions as well. Since more elaborate nano- and microparticular arrangements by different patterning and assembly techniques have become accessible,[147-149] a prominent method to maintain the arrangements is to sinter the polymer colloids together (Figure 8 right side). Nevertheless, a sintering of colloids to form elaborate architectures has been shown only for very few systems and arrangements. Since 2012 colloids carrying an electric dipole have been aligned in 1 dimensional fashion in a plate condensator setup

and thermally sintered together as shown by Vukuturi et al.[150-151] The obtained beaded linear structures can be tuned in their flexibility properties by controlling the degree of stiffness between two neighboring particles by the sintering conditions. Going into the nanoscale, the use of superparamagnetically labeled polymer nanocolloids as building blocks for the formation of nanofibers by application of an external magnetic field and sintering of the particles could be demonstrated (see chapter 0).[133] Not only could the degree of fusion be tailored by variation of fusion time and temperature to obtain smooth fibers, additionally, the introduction of 0 dimensional colloids with higher complexity resulted in 1D fibers with more elaborate structure. Insertion of Janus nanoparticles into the fiber fabrication process gave zigzag arrangements with a tunable degree of corrugation. A similar control over corrugation can be achieved by applying an alternating and a static magnetic field at the same time.[152] However, the process described by Ruditskiy et al. not allows for a permanent linkage of the particles and only few stages of corrugation can be adjusted.

2.5 Well-defined Colloids for Self Assembly[153]

Having a deeper insight into the internal structure of molecules, one will find them to be highly defined. The number of the single building blocks, the atoms, is commonly precisely defined and the bonding angles are very accurate. The high precision of the single atoms accounts for all types of molecules, from very small structures such as CO_2 or ethylene to large ones as in the case of DNA, proteins and others. The high precision originates from defined energy states and energy differences between states resulting from quantum mechanics considerations and accounting *e.g.* for the number of binding partners, the bond distances and angles. When making use of colloids as building blocks, in most of the cases the forces however play a minor role and other interactive forces have to be considered and can be used to architect defined structures. Nevertheless, the high precision that was discussed for molecules can typically not be reached. In order to understand why, not only the defined energy states of atomic interactions which yield in the high precision of molecular structures have to be taken into account, additionally a deeper look into the interactive forces of the colloidal building blocks with respect to their physical properties has to be made.[154] The forces can be of various kind and include van der Waals,[155] molecular,[156] electrostatic,[157] entropic,[158] ligand binding[159] and magnetic interactions.[133, 160]

For each of the different types of interactions the forces are dependent on various parameters and have to be calculated with an independent formula. Some of the formulas are listed in Table 2 for spherical particles.[154] In the case of van der Waals interactions

the potential between two particles can be approximated as the size of the particles divided by the distance of the two. For other types of interactions such as electrostatic or magnetic, not only the size of the colloids and their distance matters. Here, the origin of the force is the electric charge or the magnetic moment of the particles which is the interaction driving force. Additionally, the direction of the magnetic moment or the screening length of the charged particle has to be taken into account.

Table 2. *Relationship between the type of interaction and the interaction potential with respect to the distance and other properties of two colloids. The equations are valid under consideration of a given range.*[154]

Interaction	Formula	Range
Any type	$U(r) \approx \frac{2\pi a_1 a_2}{(a_1 + a_2)} \int_h^\infty U_{FP}(z) dz$	$r \ll \frac{a_1 a_2}{a_1 + a_2}$
Van der Waals	$U_{vdW} \approx \frac{-Aa}{24r}$	$r \ll a$
Electrostatic	$U_{es} = \frac{Q_1^\infty Q_2^\infty}{4\pi\varepsilon_0\varepsilon(1+\kappa a_1)(1+\kappa a_2)} \frac{e^{[-\kappa(r-a_1-a_2)]}}{r}$	$r \gg \kappa^{-1}$
Magnetic	$U_{dd} = \frac{m_1 \cdot m_2 - 3(m_1 \cdot \dot{r})(m_2 \cdot \dot{r})}{4\pi\mu_0 r^3}$	$all\ r$

With
Colloid radius a_i of particle i
Distance of the colloids r
Hamaker coefficient $A \approx 5 \cdot 10^{-20}$ J (or 13 kT at room temperature)
Effective "renormalized" charge Q_i
Screening length κ^{-1}
Dielectric constant ε
Magnetic moment m_i of particle i
Unit vector $\dot{r}$
Magnetic permeability μ_0

Not only directed forces can be used to assemble and lock colloids in a defined way. An additional option is the use of interfaces, which are often preferred by colloids in comparison to bulk medium. Owing to the defined structure of the interfaces in space they guide the colloids as templating matrix and force a structured self-assembly. In most cases, both of the two phases have to account for certain mobility and are therefore a liquid or gas phase (liquid-liquid, or gas-liquid). Often found and of large impact is the assembly of solid particles at the liquid-liquid interface to stabilize small droplets of one phase in another, immiscible phase.[161] Besides the "3D-assembly" of colloids, 2D arrangements have been demonstrated on a gas-liquid interface. Deposition of the

assembled colloids at the interface onto a substrate can be used to pattern surfaces. Not only can a simple closest packing of colloids be achieved. Additionally, two different sized colloids can be assembled at the 2D interface in high degrees of order.[162]

As in the case of atoms, for ordered colloidal self-assembly, the complexity of the possible arrangement scales with how elaborate the inserted single colloidal building blocks are. As a facile example, the use of polymer/magnetic nanocolloids with homogeneously distributed magnetic moiety in a magnetic alignment process leads to the formation of linear structures. When however implementing Janus nanoparticles into the alignment process, zigzag arrangements with tunable corrugation depending on the ratio of polymer to magnetic building block are obtained.[133] Furthermore, highly elaborate linear (and other) structures are possible when inserting magnetic particles with even higher complexity.[163-164] An additional example has been given by Granick's group who demonstrated the formation of supraparticular structures from defined colloidal building blocks by the addition of salt and selective destabilization of particle domains.[165] In the case of colloidal molecules, the single colloidal building blocks have to be highly defined in order to achieve a selective buildup of 3D structures.[166-167] Here, the valency of the colloid has to be as high as the connected colloids. Thus, a precise synthesis of the single building blocks has to be achieved beforehand. Suitable therefore are methods of controlled seeding of monomer onto surface functionalized silica nanoparticles.[168] The combination of precise control over surface functionalization and heterophase seeding allows the formation of different valency up to high percentages. Further seeding can cover the pre-formed colloids partially. Surface functionalization of the parts sticking out allows for a defined reactivity of the non-spherical colloids in space.[166]

3 Characterization Methods

3.1 Transmission Electron Microscopy (TEM)

The transmission electron microscopy is an imaging method to visualize the shape and internal structure of objects. The use of electrons as beam source enables a high resolution (down to several Ångström[169-170]) due to the short wavelength of the electrons and their small uncertainty. The electron beam is focused through a cascade of Wehnelt cylinders and transmitted through a thin sample layer. Interaction between the negatively charged electrons and the charged compounds of the sample atoms (nucleus and electrons) causes scattering of the electrons which cannot be accessed by the detector, which is placed behind the sample. Owing to the nature of the interaction force, which is proportional to the square of the atomic number, higher elements scatter stronger and therefore give lower signal intensity. Two dimensional resolution is achieved by utilization of a charge coupled device (CCD) camera with many independently working sensors.[171]

For the presented work, TEM plays a crucial role in visualization of the synthesized nanoparticles, capsules and fibers. Owing to the fact, that electron scattering is highly dependent on the number of charges in an atom, the scattering of the employed inorganic compounds (mainly iron containing nanoparticles) is significantly higher than of the organic polymer matrix. The high dependency of the scattering intensity on the atomic number allows imaging the distribution of inorganic compounds inside the polymer matrix very well.

3.2 Scanning Electron Microscopy (SEM)

In accordance to TEM, scanning electron microscopy makes use of the interaction between electrons and the atoms in order to visualize probes. Instead of the transmitted electron beam, the scattered electrons are detected. From the detected electrons information about the surface of the sample can be collected and an image created. The dependency of the amount of scattered electrons with the atomic number is the same as for TEM. A large variety of different samples can be investigated under SEM including biological probes. Sputtering the surface with gold is a common method to increase the

contrast of the surface.[172] Alike for TEM imaging, a resolution in the sub-nanometer regime can be achieved.[173] Combining transmission and scanning electron microscopy, an even higher resolution is possible.[174]

SEM imaging is a good tool for the presented work to have the possibility to visualize the surface of nanoparticles and fibers and to have an imaging view inside of magnetite loaded nanocapsules.

3.3 Dynamic Light Scattering (DLS)

The hydrodynamic size and size distribution of nanoparticle dispersions and polymer solutions can be analyzed by dynamic light scattering.[175] Coherent light is emitted from a laser and passed through the sample. Parts of the photons are scattered in all directions due to a difference in diffractive index between solution and dispersed colloid or dissolved polymer (Figure 9). The scattered photons interfere with each other to give either a wave with larger intensity (constructive interference) or a weaker intensity (destructive interference).

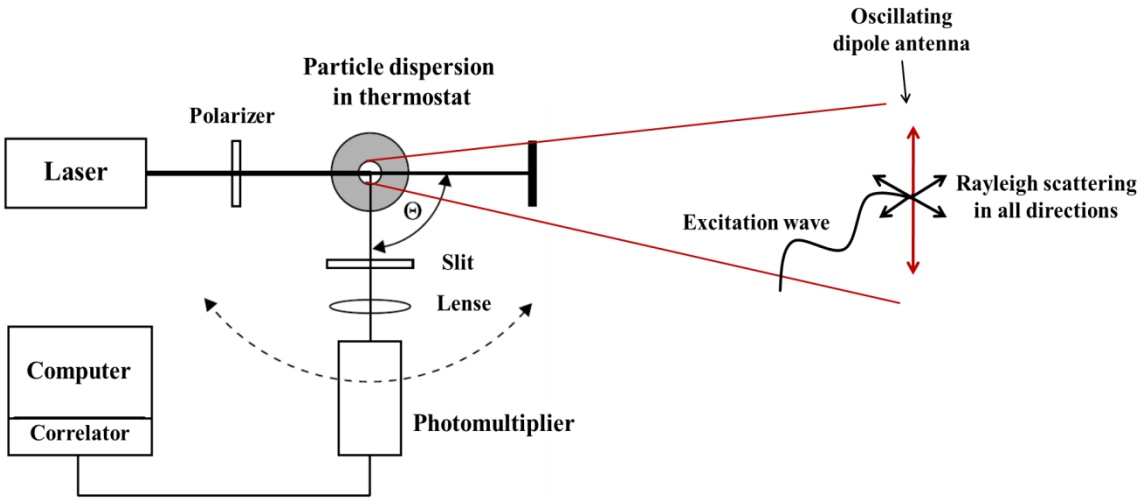

Figure 9. *Design of a dynamic light scattering device (left side). Excitation of the dispersed particles resulting in a dipole antenna sending out Rayleigh scattering in all directions (right side).*

Constructive and destructive interference are dependent on the distance of the scattering centers. Due to Brownian motion of all colloids in solution, the interference changes over time. When colloids move fast in solution, the interference pattern changes rapidly, for slow colloids it changes slower. How quick the colloids move is determined

by the self-diffusion coefficient (D_s) which stands in direct relation to the hydrodynamic radius of the colloids:

$$D_s = \frac{k_B T}{6\pi\eta r}$$

The signal intensity of scattered light is detected over time and the gained values used to generate an intensity autocorrelation function. For very short time intervals, the intensity values are dependent to each other, the longer the time intervals, and the more independent the intensity values are. The slope of decrease of the autocorrelation function is then used to calculate D_s. Sizes which are suitable for analysis range from the lower nanometer to the low micrometer scale. A restriction when measuring very small particles is mainly the very low scattering intensity (which is proportional to the square of the molecular weight). A limitation when measuring very large particles is mainly the slow movement and therefore long measurement time to generate enough data for a statistical analysis.

DLS is a very suitable method to determine the hydrodynamic size of the synthesized nanoparticles and nanocapsules. The size of the colloids ranges from 100-500 nm and is ideal for DLS analysis. Advantages are the large number of colloids measured in a short time.

3.4 Size Exclusion Chromatography (SEC)

The size exclusion or gel permeation chromatography is an often used analytical method to determine the molecular weight and polydispersity index (PDI) of polymers. The polymer sample is measured together with an internal standard, typically two different molecular weight standards with very narrow size distribution, for calibration. To ensure a similar equilibrium behavior of internal standard and sample between the immobilized and the mobile phase, similar, or in the best case the same polymer is chosen as internal standard. As immobilized phase, cross linked polymer beads are used with a continuous pore size distribution. The pores of the immobilized phase offer dissolved polymer chains the possibility to enter and exit, whenever the polymer chain is smaller than the pore. In consequence, small polymer chains spent more time in the pores and it takes longer to elute them through the immobilized phase (Figure 10).

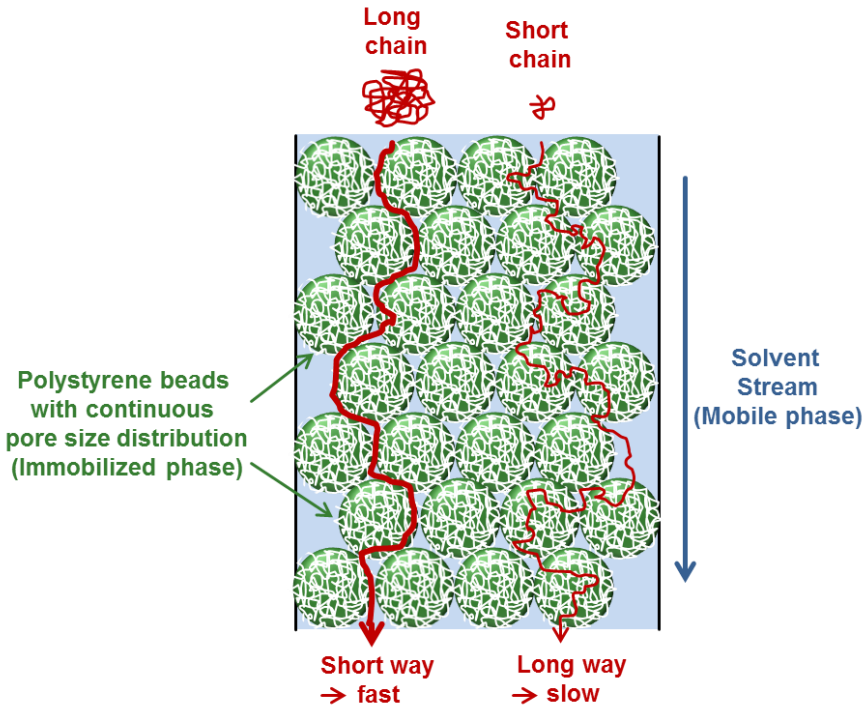

Figure 10. *Schematic illustration of the operation principle of a GPC column.*

Size exclusion chromatography is a suitable method for the determination of the molecular weights of the synthesized nanoparticles presented in the thesis. The determination of the molecular weight and the PDI is fundamental to explain the fiber fusion processes in the chapters 0 and 4.7.

3.5 Zeta Potential Measurement

The zeta potential measurement is used to reveal the surface charges of colloids. Most commonly, colloids dispersed in aqueous medium are stabilized through electrostatic repulsion (chapter 2.3.1). Therefore, each colloid has to carry negative or positive surface charges to achieve repulsive forces. Thus, performing a zeta potential measurement on a colloid dispersion can indicate its stability in aqueous medium. A zeta potential value <-40 mV or >40 mV indicate a good colloidal stability. For values from -10 to 10 mV the dispersion is not stable and coagulation occurs rapidly. Dispersions with values in between are often stable only for a short time. The zeta potential is not the absolute value to derive the colloidal stability of a dispersion. Additional factors like the salt concentration have to be taken into account.

For determining the zeta potential, a uniform electric field is applied on the particles dispersion. Electrostatic interactions between the charged colloids and the external field lead to a directed motion of the colloids along the field, the so called electrophoresis.

From the motion of the colloids in solution, which is monitored by a laser, the zeta potential can be calculated using the Smoluchowski equation.[176-177]

3.6 Thermogravimetric Analysis (TGA)

For samples composed of inorganic and organic compounds, the thermogravimetric analysis is a feasible method to determine the percentage of inorganic moiety. Basic elements of TGA include a balance, heater and heat control. The sample is heated steadily under detection of the weight of the sample. At temperatures around 250-400 °C, decomposition of the organic part of the sample leads to a weight loss. The inorganic components remain in their amorphous or crystal state and do not evaporate. Commonly, the atmosphere is chosen to be inert (nitrogen) to prevent oxidation or other reactions of gas (air) with the sample.

3.7 Vibrating Sample Magnetometer (VSM)[178]

The VSM device provides information about the magnetic properties of a substance. It gives facile access to hysteresis curves from magnetic compounds. Therefore, a uniform magnetic field is applied on the sample to align each magnetic dipole of the sample along with the external field. Pickup coils are placed next to the sample. The sample is set into vibration and moves in and out of the coils. Depending on the magnetic field strength of the sample, the magnetic flux through the coil changes more or less with the vibration of the magnetic sample. The change in magnetic flux induces a voltage in the coil which is proportional to the magnetic moment of the sample. Performing the measurement for various different uniform magnetic fields, a hysteresis curve can be obtained. The hysteresis curve provides important information about the magnetic properties of the sample such as superparamagnetism or magnetization.

Making use of VSM measurements is essential for the characterization of the different magnetic nanoparticles and composite particles and capsules. It gives rise to the superparamagnetic behavior of the magnetite and manganese ferrite nanoparticles. Additionally, the saturation magnetization can be determined from the measurements and was an eminent value to make predictions about the interactions of magnetic nanoparticles[133] (see chapters 0, 4.7 and 4.8) and to calculate their relaxivity (see chapter 4.3.1).

3.8 Ultraviolet-Visible (UV-Vis) and Fluorescence Spectroscopy

The UV-Vis or absorption spectroscopy and the fluorescence spectroscopy are optical methods to quantify the interaction between light with a defined wavelength and matter. Commonly, the sample is measured in a dissolved state. Irradiation of the optically active sample leads to excitation of electrons into higher energetic levels, the so called absorption. The absorption wavelength λ is reciprocal proportional to the energy difference between the levels ΔE with the speed of light c and the Planck constant h as constant of proportionality as follows:

$$\Delta E = \frac{h \cdot c}{\lambda}$$

The absorbance of light is detected by the decrease in transmittance in a linear setup. The electrons in excited states are able to go back into their ground state by irradiating light among other processes. The irradiated, fluorescent light is usually not as energetic as the absorbed energy and can therefore be separately detected, which is usually done at a certain angle (*e.g.* 90°).

3.9 Nuclear Magnetic Resonance (NMR)[179] and Magnetic Resonance Imaging (MRI)[180]

The NMR spectroscopy is commonly used for the structure determination of molecules. Requirement for the measurement is the existence of a magnetic moment, which is the case for isotopes with an uneven number of protons and/or of neutrons. Typical isotopes which can be detected are ^{1}H, ^{13}C, ^{15}N, ^{19}F and ^{31}P. Application of an external magnetic field on the isotopes leads to the so called Zeeman effect, leading to a split-up of the energetic levels of the nucleus spin which is proportional to the applied field. The different energetic levels are populated following the Boltzmann distribution. Owing to the fact, that the energy difference between the levels is marginally small, the different levels are occupied almost with the same probability. When exciting the sample, only little spins are accessible to be transferred into a higher energy level. Therefore, the energetic levels have to be split-up as high as possible by application of a very strong magnetic field. Besides the Boltzmann distribution, also the natural occurrence of the isotopes, the sample amount and the measurement time account for the signal intensity.

Structure determination becomes possible due to the interaction of electrons with the applied field. According to Lenz's law, a change in the magnetic field induces the electrons to from ring current which generates a magnetic field opposite to the applied

one. Depending on the electron density, the external field is suppressed stronger or weaker. As a result, in dependence on the electron density, a change in chemical shift can be detected. Additional information can be obtained by coupling of spins. NMR spectroscopy can not only be used for the structure determination of small molecules and synthetic polymers, but also for biomolecules and their interactions.[181]

For MRI or nuclear magnetic resonance imaging (NMRI), the interaction of NMR active protons from water molecules with an external magnetic field is detected. It is mainly used to obtain information about internal structures of the body. For MRI, the chemical shift or the coupling of protons are not important. Major importance plays the relaxation time of the excited spins back into the Boltzmann distribution, the so called T_1 relaxation time. The relaxation is highly dependent on environment, especially on the presence of magnetic species. Interaction between excited spins and locally present magnetic moieties leads to a fast relaxation of the spins. When exciting several times in a row, the contrast is therefore enhanced for fast relaxation times. Additionally, when exciting the spins with a 90° pulse and a series of fast further orthogonal pulses of 180°, a relaxation time T_2 can be obtained. In order to obtain space-resolved resolution, a magnetic field gradient is applied and several scans are performed.

3.10 Fourier Transform Infrared Spectroscopy (FTIR)

FTIR spectroscopy is based on the absorption of electromagnetic radiation in the infrared regime (0.8-500 µm), causing vibrational excitation of molecules. The energy difference between the vibrational bands is characteristic for a specific type of binding *e.g.* C=O stretching. The energy difference between the states E_ϑ of excitation is dependent on the reduced mass μ and the force constant k:

$$E_\vartheta \sim \sqrt{\frac{k}{\mu}}$$

For the presented results FTIR-spectroscopy provides a useful tool for the detection of synthesized compound where functional groups are either introduced or reacted away.

4 Results and Discussion

4.1 Encapsulation and Stimuli-Responsive Release from Polymer Nanocapsules

Within the following chapter the encapsulation of active substances into responsive polymer nanocapsules is described. Different possibilities to introduce the stimulus responsive moiety are comprised. Firstly, the encapsulation of a magnetic stimulus and a release upon application of an external magnetic field is demonstrated. Several strategies to obtain iron oxide labeled capsules are described with the main focus on the surface functionalization of the iron oxides and their stabilization in aqueous environment. The different aqueous dispersible iron oxides were implemented into nanocapsules and investigated with respect to their release behavior when applying an alternating external magnetic field. With one of the ligation strategies for the iron oxides and their encapsulation into capsules, the release could successfully be triggered by an external field and thus, to a desired time. Furthermore, it is shown that their use as contrast agents for MRI is possible and their biocompatibility is proven. Moreover, an opportunity to introduce an IR-light responsive stimulus into the capsules is suggested. Therefore, gold nanoparticles are synthesized and encapsulated.

4.1.1 Magnetic Tracing and Releasing from Nanocapsules for Combined Imaging and Therapy

In the present chapter, the synthesis of a novel nanocapsule carrier system, predestined for tracing of drug delivery shuttles by magnetic resonance imaging (MRI) and triggered release in remote-controlled fashion of encapsulated compounds upon application of an external magnetic field, is described. In order to achieve a magnetic tracing and releasing from nanocapsules, polymer capsules containing a high amount of superparamagnetic $MnFe_2O_4$ nanoparticles and a thermodegradable shell were fabricated *via* a miniemulsion route. The process allows the facile encapsulation of hydrophilic compounds, as demonstrated for a model dye. Release of the encapsulated dye was achieved upon application of an external alternating magnetic field. Encapsulation of $MnFe_2O_4$ nanoparticles additionally provides the possibility to image the nanocapsules by magnetic resonance imaging, owing to high r_2 relaxivity values of 96-120 $Hz \cdot mmol^{-1}$. In toxicity experiments, the nanocapsules show no cell toxicity up to fairly high

concentrations (600 µg·mL^{-1}). Due to their dual-functionality, the nanocapsules possess a high potential as nanocarriers with combined magnetic imaging and release capability.

4.1.1.1 Background and the Release Strategy

In biomedicine and materials sciences, the encapsulation and controlled release of functional compounds is of fundamental interest. The activity of drugs, but also of monomers and catalysts for self-healing materials can be ensured *via* encapsulation by a protective shell[182-185]. Moreover, upon application of an external stimulus, the active compound is released and can react at a destination and time of desire. In biomedicine, the encapsulation and triggered release of drugs is essential for an efficient local treatment of diseases. The drug is delivered to its target and operates only when reaching the affected tissue. Especially for cancer therapy, the targeted delivery plays a major role due to the harmful drugs that have to be applied for therapy. For targeted delivery, a variety of drug delivery systems have already been developed such as dendrimers[186-187], capsules[188-189], gels[190] among others. Surface labeling with targeting moieties enables the controlled delivery of the transport vehicles to the destiny of desire[116, 191]. Implementation of delivery vehicles with functional polymers or inorganic nanoparticles with stimuli responsive behavior can provide a responsive release towards switches in the environment, *e.g.* temperature, pH or UV radiation[117, 192]. Further modification with magnetic nanoparticles enables the combined use as transport vehicles for drugs and magnetic resonance imaging (MRI) as tool for tracing of the vehicle[63]. A release can be achieved without influencing the environment. As a consequence, the stimulus is harmless for the environment (*e.g.* tumor surrounding tissue) and the stimulus is not retarded (*e.g.* light gets absorbed). The magnetic labeling additionally provides a possible magnetic targeting, making use of magnetic attraction forces[48, 116, 118, 193-194]. Moreover, the magnetic nanoparticles can be used as heat generators under application of an external alternating magnetic field. Since only a slight increase in temperature can cause cell death, magnetic nanoparticles are predestined for use in hyperthermia treatment[195-196]. Going one step further, the generated heat from the magnetic nanoparticles can induce a release of substances[46, 197-198] in a remote-controlled fashion. The drug can be released at a desired time and, in the case of a selective targeting, place of destiny. However, a magnetic field induced release could only be shown for a very few carrier systems. Nanocapsules with the combination of a magnetic field induced "payload" release and a high r_2 relaxivity value for efficient MR-imaging could not be shown yet to the best of our knowledge.

Here, the development of a nanocarrier system with several functionalities to enable a combined tracing and therapy is described. Efficient entrapment of drugs, labeling with magnetic nanoparticles and thermolabile moieties as part of the shell were combined in one capsule. Due to the challenging requirements, a successful release of substances upon application of a magnetic field is hardly known and novel methods have to be developed to enable such a release from multifunctional delivery systems. For the synthesis of the nanocapsules, we chose the miniemulsion approach. To obtain nanocapsules, a polyaddition reaction at the interface of soft templating miniemulsion droplets is carried out. A large abundance of different monomers can be used as building blocks for the polymer nanocapsules and thus, the composition of the shell can be adapted for its desired application. Well-defined nanocapsules in a size range of 150 - 300 nm can be obtained following such an approach. The nanocapsules show beneficial properties for drug delivery applications due to an efficient encapsulation of hydrophilic substances and the possibility to modify the surface in order to achieve a selective targeting[104]. Choosing a thermally decomposing shell, the encapsulated substances can be released upon temperature increase to achieve a stimulated release[199]. When encapsulating a magnetic stimulus responsive and a thermolabile compound into the nanocapsules and applying an external alternating magnetic field, a magnetic field induced release can be achieved as Figure 11 illustrates: 1) Application of an alternating external magnetic field leads to excitation of the magnetic nanoparticles and dissipation creates thermal energy. 2) The local increase in temperature then enhances the decomposition of the thermolabile azo-diol inside of the shell to create pores. 3) Encapsulated substances are released as they diffuse through the porous nanocapsule shell.

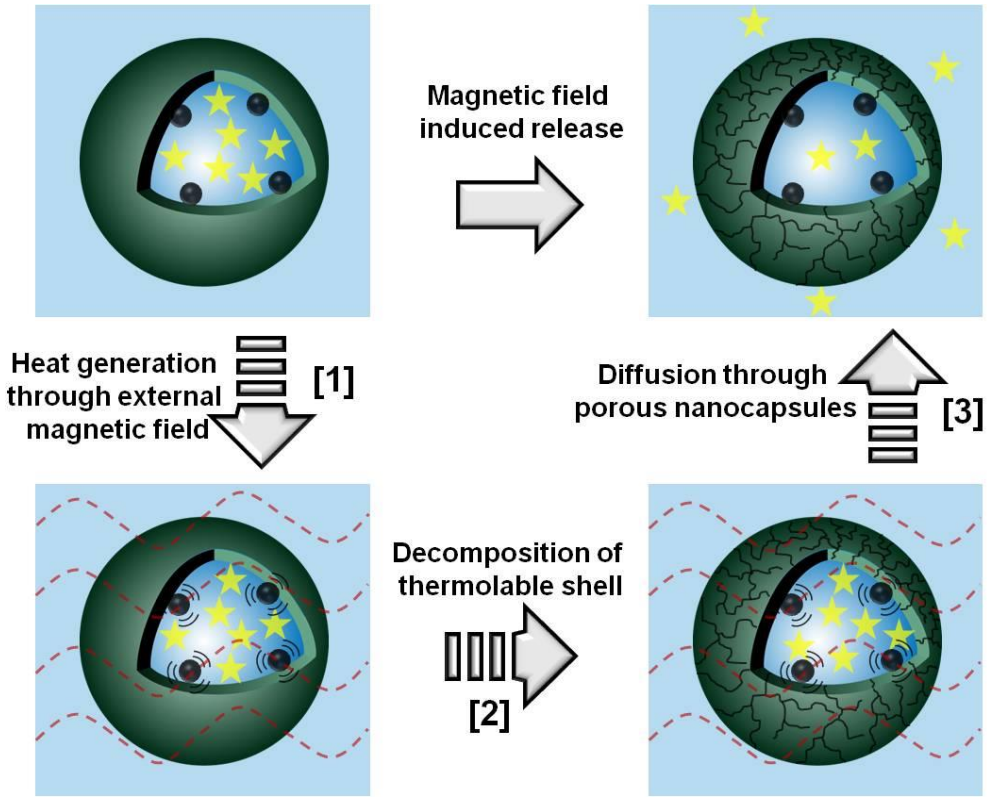

Figure 11. *Schematic illustration of magnetic field induced release from nanocapsules. 1) Application of an alternating external magnetic field stimulated the magnetic nanoparticles, leading to generation of heat. 2) The generated heat induces the decomposition of the thermolabile shell. 3) Encapsulated substances can diffuse through the porous shell and thus be released.*

Therefore, the magnetic nanoparticles were synthesized by thermal decomposition of precursor complexes in an organic phase. A transfer of the particles into aqueous solution was achieved through ligand exchange process. Once transferred into aqueous medium, an inverse miniemulsion was generated containing the magnetic particles in the dispersed phase and the particles were encapsulated in polymer nanocapsules by a polyaddition reaction at the interface of the miniemulsion droplets. The concentration of the magnetic nanoparticles could be varied up to high contents. As thermolabile compound, an azo-diol initiator was implemented in the shell[199]. *Via* NMR-spectroscopy, its reaction into the shell of the nanocapsule could be followed. A model hydrophilic dye was efficiently encapsulated and released upon application of an external alternating magnetic field. The synthesized nanocapsules labeled with $MnFe_2O_4$ nanoparticles possess a high relaxivity value as demonstrated with agarose phantoms and thus, are suitable contrast agents for MRI. To evaluate potential applications of the nanocapsules as drug delivery systems with remote-controlled release properties and high r_2 relaxivity values for potential MRI, cell toxicity experiments were conducted and revealed their biocompatibility.

The strategy presented will be segmented in the following chapters into its single parts: i) Synthesis of the magnetic stimulus and its encapsulation. ii) Introduction of a thermally decomposing shell. A combination of magnetic label and thermoresponsive shell (iii) in order to achieve a magnetic field stimulated release from the capsules (iv). Finally, use of the hybrid nanocapsules as contrast agents for MR imaging is confirmed by their high relaxivity values (v) and their biocompatibility proven by low cell toxicity (vi).

4.1.1.2 The Magnetic Stimulus

Oleate and oleylamine capped $MnFe_2O_4$ nanoparticles were employed as magnetic moiety of the nanocapsules. Besides their superparamagnetic properties and their relatively high saturation magnetization, the nanoparticles are commonly used as negative contrast agents for MRI due to their high relaxivity values.[200-202]

The synthesis of the oleate and oleylamine capped $MnFe_2O_4$ nanoparticles was achieved by thermal decomposition of manganese and iron acetylacetonates in organic medium (see chapter 5.1.1.1.1 for experimental details). The obtained hydrophobic oleate and oleylamine capped nanoparticles display an average diameter of 16.1 ± 2.7 nm as determined from transmission electron microscopy (TEM) micrographs (Figure 12).

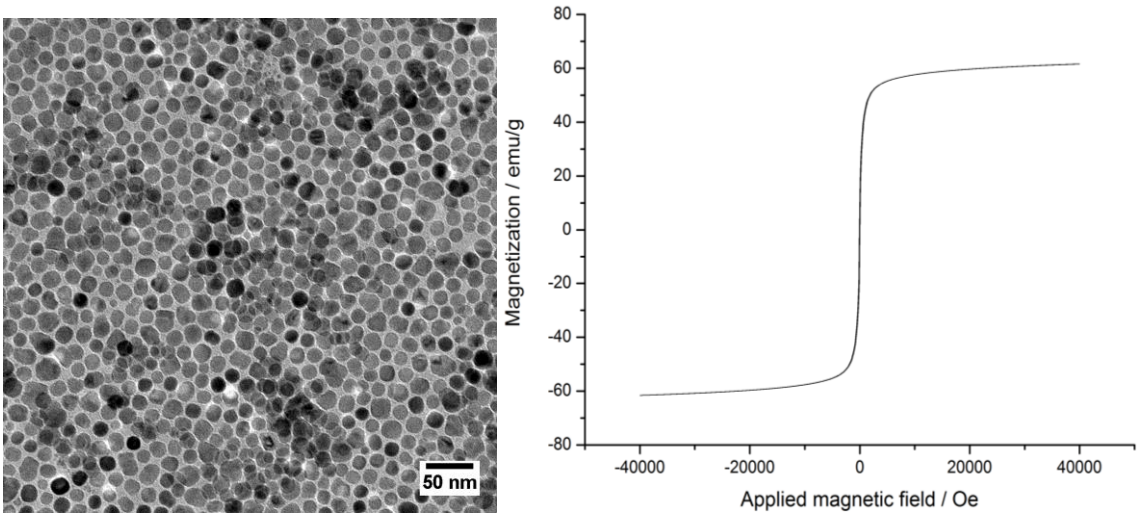

Figure 12. *Left: TEM image of oleate and oleylamine capped $MnFe_2O_4$ nanoparticles drop-casted from a THF dispersion. Right: Hysteresis curve of $MnFe_2O_4$ nanoparticles.*

The employed nanoparticles exhibit a saturation magnetization value of 62 emu·g^{-1} which is close to the saturation magnetization of bulk $MnFe_2O_4$.[203] The hysteresis loop shows no retentivity, demonstrating a superparamagnetic behavior of the nanoparticles.

Transfer of the nanoparticles into aqueous medium was accomplished through ligand exchange of oleylamine and oleate with tetramethylammoniumhydroxide (TMAOH). The electrostatic stabilization with TMAOH provides a good dispersability of the magnetic nanoparticles in pure water up to high concentrations. However, when the ionic strength is too high, ionic repulsion forces between the particles are not strong enough to prevent particle aggregation. Such ion-sensitivity can be decreased through addition of an additional stabilizer, carboxymethylated poly(vinyl alcohol) (CMPVA), to the particles dispersion, as demonstrated by Liong *et al.*[41] CMPVA works as a steric stabilizer for nanoparticles dispersions. Hence, the stability of the dispersion is not affected by the ionic strength. As a result, the $MnFe_2O_4$ nanoparticles become more stable in salt containing aqueous dispersions. Without CMPVA we observed precipitation of the manganese ferrite nanoparticles when the thermolabile monomer, 2,2'-azobis[2-[1-(2-hydroxyethyl)-2-imidazolin-2-yl]propane]dihydrochloride (VA-060), was added. Additionally, VA-060 has to be purified thoroughly by recrystallization to prevent precipitation of the nanoparticles due to impurities.

4.1.1.3 Thermolabile Nanocapsules

The synthesis of polymer nanocapsules can be achieved through a polyaddition reaction of various functional monomers at the interface of miniemulsion droplets.[16, 204] One prominent example is to make use of the reaction of hydrophobic diisocyanates and hydrophilic amine- or hydroxyl-functionalized monomers at the droplets interface to generate polyurea or polyurethane nanocapsules as illustrated in Figure 13.[205] In a first step, an inverse miniemulsion is formed by sonication (I). Addition of a comonomer to the continuous phase initiates the polyaddition reaction of diol and diisocyanate at the interface (II + III). In a side reaction the isocyanate groups react with water and under decomposition of CO_2, form highly reactive amines. The amines then react with isocyanates to form urea.[206] Thus, the polymers of the resulting capsule contain a mixture of urethane and urea groups. IV) In a last step, the nanocapsules are redispersed in aqueous SDS containing solution.

For the preparation of the nanocapsules, we chose to use the water soluble monomer 1,6-hexanediol (HD) and the oil soluble monomer 2,4-toluenediisocyanate (TDI). When using the bifunctional monomers, linear polymers are produced as building blocks of the nanocapsule. However, when encapsulating a dye, leakage cannot efficiently be avoided by the non-cross-linked nanocapsule shell. Thus, we introduced the multifunctional surfmer (a combination of surfactant and monomer) polyglycerol polyriccinolate (PGPR 90) to obtain a cross-linked shell. Through introduction of the cross-linker, leakage can be prevented efficiently. After several days, only little leakage

of encapsulated dye (< 5%) was observed. Additionally, we introduced the thermolabile monomer VA-060. The azo-group of VA-060 decomposes upon increase. Hence, the shell of the nanocapsules can be decomposed when increasing the temperature and encapsulated substances can be released.

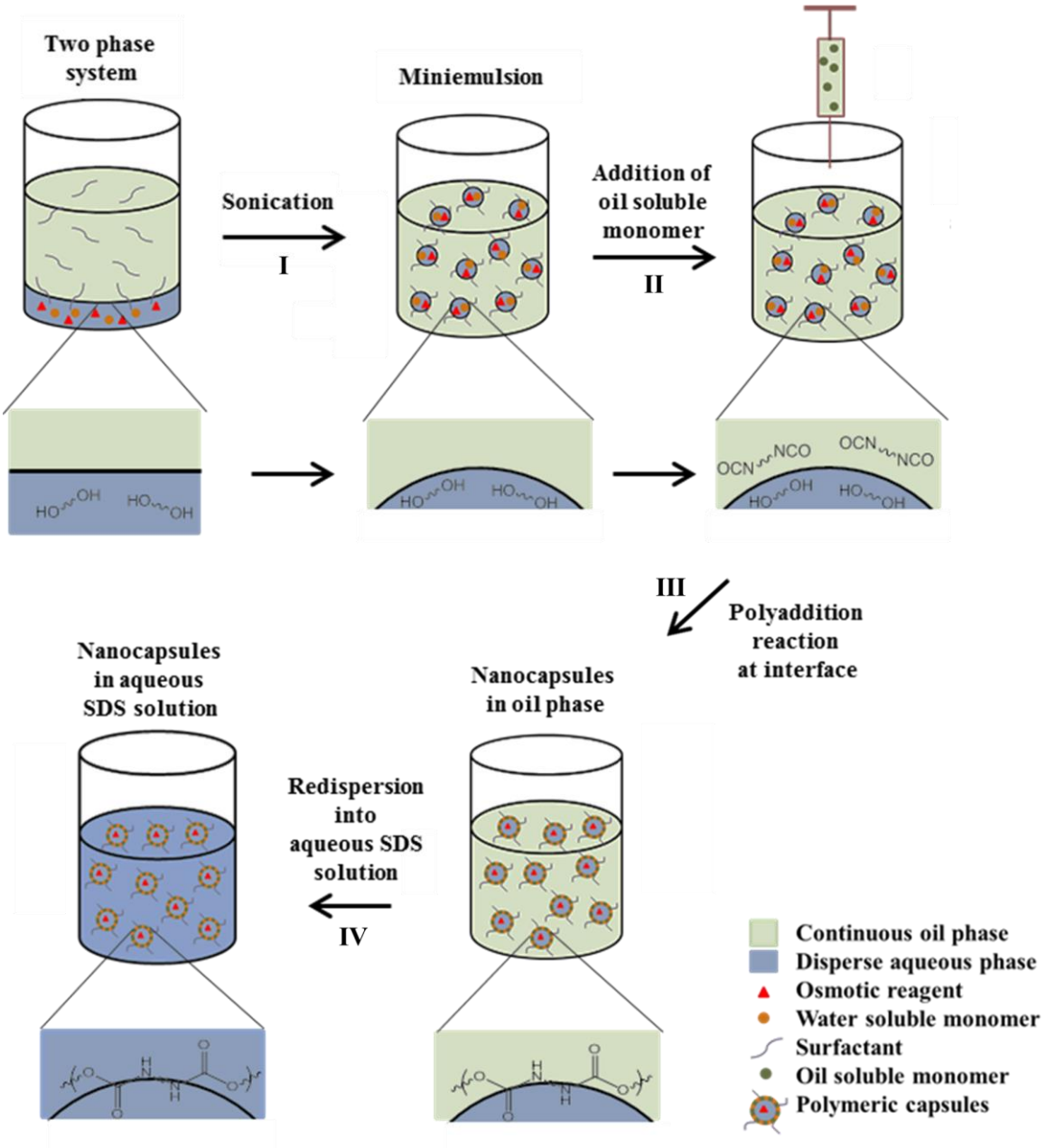

Figure 13. *Schematic illustration of the synthesis of polyurethane/urea nanocapsules. Sonication forms an inverse miniemulsion (I). Addition of an oil soluble diisocyanate monomer (II) leads to a polyaddition reaction at the droplets interface (III). Redispersion into SDS containing aqueous solution yields water in water nanocapsules (IV).*

The reaction of the hydroxyl-groups from VA-060 with the isocyanate was monitored *via* proton nuclear magnetic resonance (^{1}H-NMR) spectroscopy in order to proof the integration of VA-060 into the shell of the nanocapsules (Figure 14). Therefore, a molar ratio of 50:50 of VA-060 and HD were employed in a typical nanocapsule synthesis (as described in the experimental section). The proton signal of the hydroxyl-group of HD appears at 4.4 ppm, the signal of VA-060 at 5.4 ppm. When the hydroxyl-group reacts with an isocyanate group to form a urethane unit, the proton signal disappears, which enables to monitor the reaction of the monomers with TDI and therefore the integration into the nanocapsule shell. Tetrabromethane (TBE) was used as an internal standard to follow the reaction quantitatively. Figure 14 shows the relevant section of the NMR spectrum before and after nanocapsule formation. After capsule formation, ~35% of hydroxyl groups of VA-060 and ~30% of the groups of HD are unreacted. The remaining groups can be assigned to hydroxyl end groups of the polyurethane or unreacted monomers. Hence, the majority of both monomers has reacted and is part of the capsules shell. Thus, the shell contains many thermally decomposing groups.

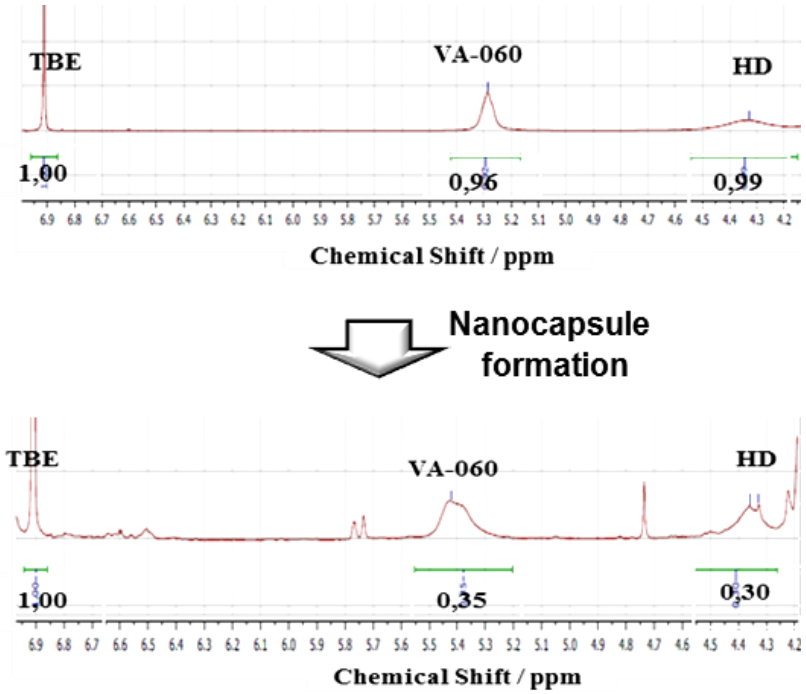

Figure 14. *Study of the reaction between two hydroxyl-monomers (VA-060 and HD) and diisocyanates. Upper part: NMR spectrum before nanocapsule formation. Lower part: NMR spectrum after nanocapsules formation. The decrease in NMR-signal intensity can be assigned to the reaction of the hydroxyl with an isocyanate group.*[207]

4.1.1.4 Magnetic Nanocapsules with Thermolabile Shell

In order to achieve a magnetic labeling of the polymer nanocapsules, CMPVA coated superparamagnetic $MnFe_2O_4$ nanoparticles (as described in chapter 4.1.1.2) dispersed in aqueous medium were employed as dispersed phase of the inverse miniemulsion (for experimental details see chapters 5.1.1.1.2 and 5.1.1.1.3). Interfacial polyaddition encapsulates all components dispersed in the aqueous phase and therewith the magnetic nanoparticles as well. Owing to the CMPVA functionalization of the manganese ferrite, the many surface hydroxyl groups can react at the interface as well and the magnetic particles get integrated into the shell. The superparamagnetic behavior of the $MnFe_2O_4$ nanoparticles guarantees, that a magnetic field is only generated from the particles as a response towards an external magnetic field. Due to their high magnetization value, they are suitable as an efficient heat source under application of an alternating external magnetic field. Due to the possibility to load the nanocapsules with a high amount of magnetic nanoparticles (35 wt%), the local temperature increase inside of the capsule can be tuned to high values enabling a fast decomposition of the thermolabile shell. Figure 15 depicts SEM micrographs of manganese ferrite loaded polymer nanocapsules with a high loading of magnetic nanoparticles (35 wt%). The size of the nanocapsules was measured to be 166 ± 41 nm from 100 SEM capsules. As clearly visible from the micrographs, the magnetic nanoparticles can be found in each capsule and are distributed well within the capsule. No magnetic nanoparticles can be observed outside of the capsules.

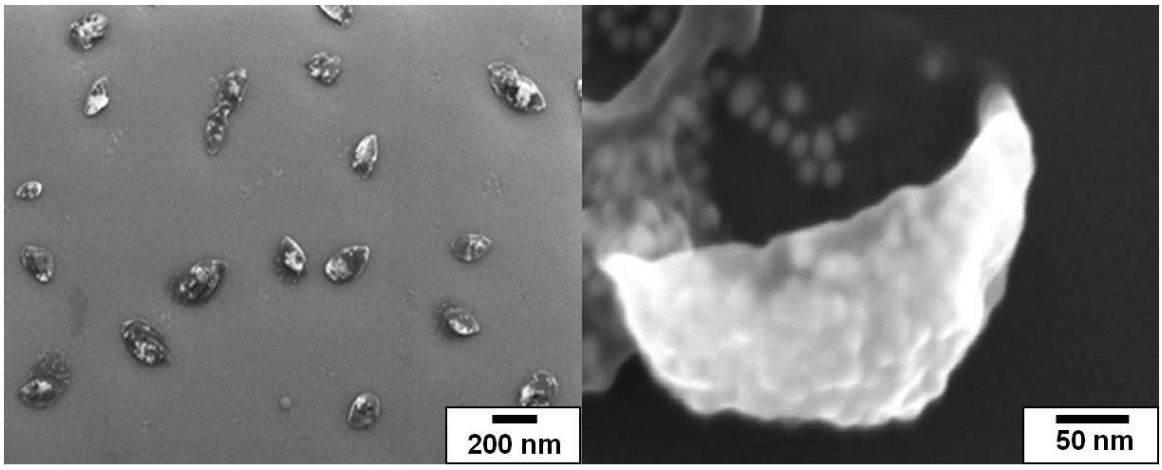

Figure 15. *Scanning electron micrographs of polymer nanocapsules highly loaded with magnetic nanoparticles.*

4.1.1.5 Magnetic Field Induced Release Studies

In order to study the release properties of the nanocapsules upon application of an external magnetic field, a variety of different nanocapsules was synthesized (Table 3). To study the release in dependency of the presence of a thermolabile group as part of the shell, nanocapsules consisting of a shell of only VA-060 as diol compound and nanocapsules with a shell consisting only of HD as reference sample were produced.

Table 3. *Nanocapsule samples with different amounts of $MnFe_2O_4$ nanoparticles with and without thermolabile shell (using VA-060).*

Sample	Thermolabile compound	Amount of $MnFe_2O_4$ [wt%]
HD-Med	No	21.1
HD-High	No	33.6
VA-060-Low	Yes	12.6
VA-060-Med	Yes	19.2
VA-060-High	Yes	35.0

To investigate release properties upon application of the external alternating magnetic field with respect to the content of $MnFe_2O_4$ nanoparticles, different amounts of the magnetic particles (Low, Med and High) were introduced into the nanocapsules. The $MnFe_2O_4$ content was determined via thermogravimetric analysis (TGA) as displayed in Figure 16.

All of the nanocapsules were loaded with the hydrophilic fluorescent dye sulforhodamine 101 as model component. The encapsulation efficiency of the dye for all synthesized nanocapsules was found to be > 95%. Non-encapsulated dye was separated by magnetic precipitation of the nanocapsules and decanting of the supernatant solution containing traces of dye. Leakage of encapsulated dye could be observed only very little (Figure 17) and after several days less than 5% of dye had been leaking out.

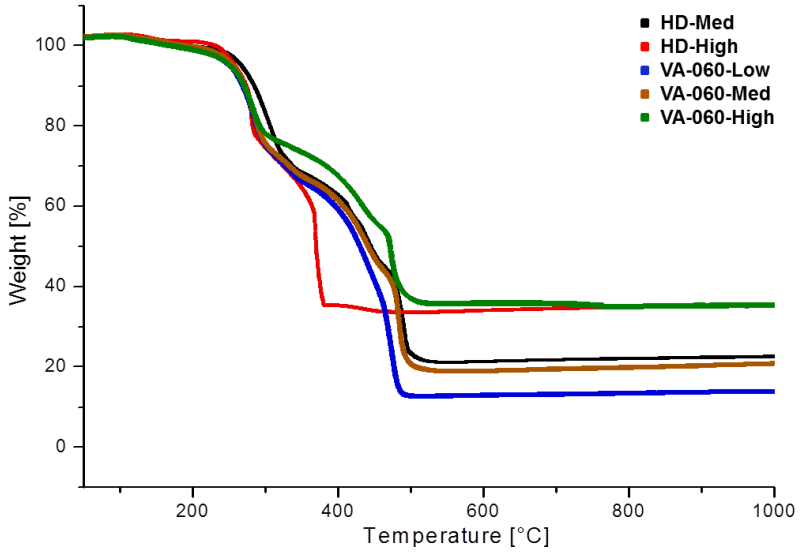

Figure 16. *TGA curves of nanocapsules containing different percentages of $MnFe_2O_4$ nanoparticles.*

The release experiments of the different nanocapsules were carried out as described in the experimental section (chapter 5.1.1.4). The concentration of nanocapsules was chosen to be low (≤ 0.1 wt%) in order to prevent a strong heating of the entire nanoparticles dispersion through a high content of magnetic nanoparticles. The temperature of the five different dispersions displayed similar values after 1 h application of the external alternating magnetic field. The detected temperature difference from nanocapsule dispersions containing low manganese ferrite content and those containing the highest amount was found ~5 °C. The small temperature difference provides a magnetic field induced release based on the effect of the magnetic nanoparticles inside of the nanocapsules and not the cooperative effect of all magnetic nanoparticles on all nanocapsules. Hence, a release is possible independently from the concentration of nanocapsules. The corresponding release curves are displayed in Figure 17. The release of dye from nanocapsules which do not have a thermolabile group in the shell (HD-Med and HD-High) is minute over the investigated timeframe of 60 min. Implementation of a thermolabile group and the amount of magnetic nanoparticles have no effect on the release and the encapsulation of fluorescent dye inside the capsules is efficient. When the thermolabile group VA-060 is introduced (VA-060-Low, VA-060-Med and VA-060-High), the release of fluorescent dye highly increases upon application of an alternating magnetic field. It can be concluded that for an efficient release, introduction of the thermolabile group into the nanocapsules is necessary. For the release intensities of the thermolabile group containing nanocapsules, the amount of encapsulated magnetic compound plays a crucial role. The higher the encapsulated amount of $MnFe_2O_4$ nanoparticles, the larger the released amount of fluorescent dye.

For the release behavior all of the capsules with a thermodegradable shell display a similar trend: After the first 5 min the release is slow. When 15 min are reached, the release increases rapidly. After 30 min the release curve plateaus and in the following 30 min, only little further release can be observed. The slow release in the beginning can be attributed to two factors: i) Heat generation of the magnetic nanoparticles takes some time, leading to a delay in decomposition of the thermolabile compound. ii) Decomposition of the thermolabile compound occurs over time. Thus, sufficiently large pores in the nanocapsules are not immediately generated after switching on the external magnetic field. Once efficient heat is generated, VA-060 decomposes and pores in the shell are created. The dye can leak out fast. Application of the magnetic field for longer than 30 minutes shows no significant further release. Those nanocapsules which are loaded with sufficient magnetic nanoparticles to generate a large amount of heat, have released their payload.

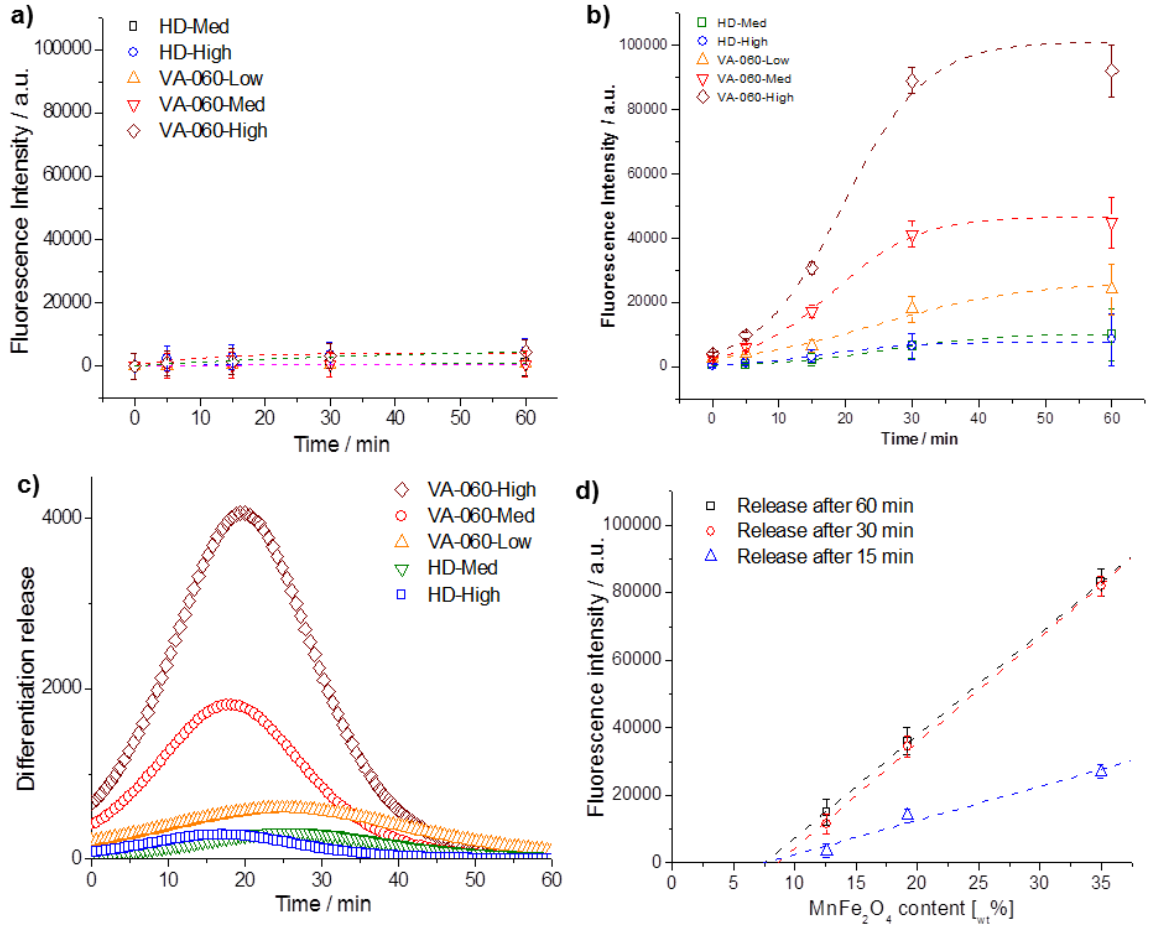

Figure 17. *Fluorescent spectroscopy of the release of a fluorescent dye from nanocapsules at room temperature without application of an external alternating magnetic field (a). Release of fluorescent dye from $MnFe_2O_4$ containing, thermolabile nanocapsules through application of an alternating external magnetic field (b) and its release kinetics displayed as differentiation of the curves (c). Release of fluorescent dye*

from magnetic, thermolabile nanocapsules as a function of $MnFe_2O_4$ content for different release time periods (15, 30 and 60 min) including linear fits as assigned to the single data points (d).

The release kinetic was additionally displayed as a function of the differentiated release curve against time (Figure 17). From the differentiated curve, it becomes obvious, that for all $MnFe_2O_4$ concentrations, the maximum amount of released dye per time lies between 20-25 min.

In order to understand the role of $MnFe_2O_4$ nanoparticles not only as a heat source for the entire aqueous dispersion, but also as a local heat generator, the magnetic field induced release curves were investigated in more detail. Several observations can be made: i) A higher amount of magnetic nanoparticles leads to a larger overall amount of released dye. ii) The magnetic field induced release reaches its maximum after approximately 30 min. The release behavior stands in contrast to the release from an externally heated aqueous thermolabile nanocapsules dispersion (see Figure 18), which increases almost steadily over the timeframe (after a short induction period) and releases less dye compared to VA-060-High and VA-060-Med (for 50 and 75 °C). Additionally, in contrast to the release curves of nanocapsules dispersions heated through magnetic excitation, it does not rapidly release and plateau after approximately 30 min (Figure 18). iii) A linear fit of the released dye against the amount of $MnFe_2O_4$ nanoparticles (Figure 17) results in a similar intersection point with the x-axis (at around 8 wt%). All the observations indicate that not the average amount of magnetic nanoparticles in dispersion is the crucial value for the release, but the amount of encapsulated $MnFe_2O_4$ in a single nanocapsule. A certain amount is needed in one capsule to induce an efficient heating and release (observation iii). If such an amount is present, after a short initialization time, the release is fast (observation i) and highly efficient (observation ii).

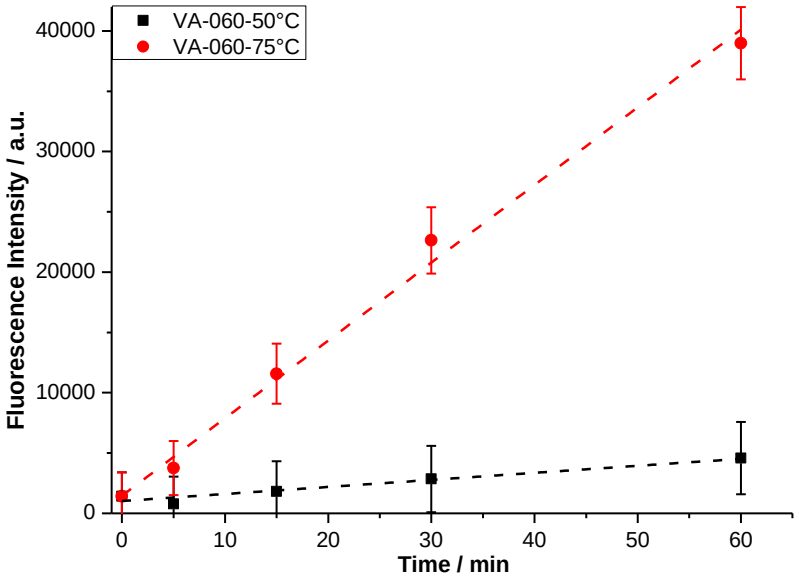

Figure 18. *Release curve of fluorescent dye from thermolabile nanocapsules under the influence of different temperatures (50 and 75 °C) as monitored via fluorescence spectroscopy.*

4.1.1.6 Relaxivity Measurements for MRI

In order to use the nanocapsules simultaneously for magnetic field induced release and magnetic tracing, efficient labeling has to be achieved. It is beneficial to our system, that the integration of $MnFe_2O_4$ nanoparticles not only provides heat generators for the external magnetic field induced release of encapsulated substances, but additionally as MRI imaging agents with a high r_2 relaxation rate. A high r_2 relaxation rate leads to a rapidly decreasing spin echo amplitude, which in turn leads to a diminishing MRI signal. Hence, such contrast agents are referred to as negative contrast agent. Exemplary, the agents are often used for gastrointestinal MRI.[208]

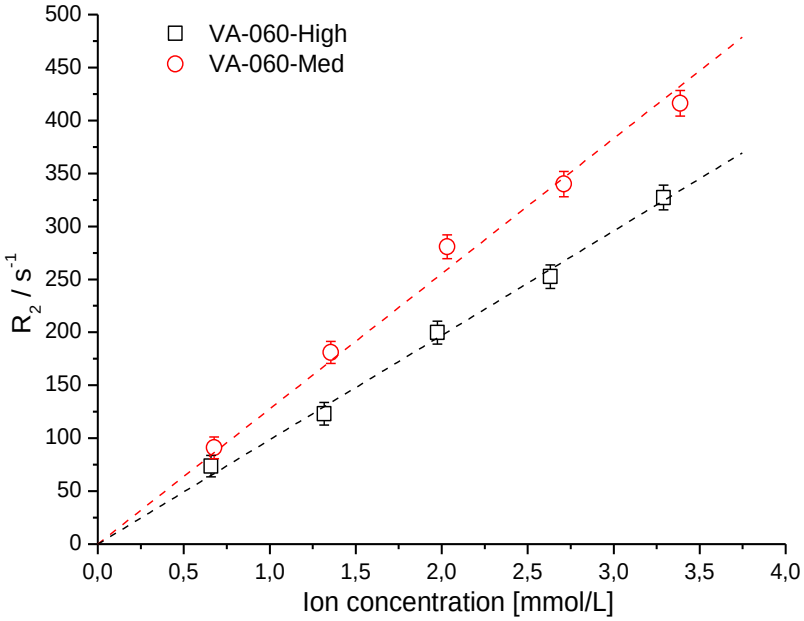

Figure 19. *r_2 relaxivity rates of VA-060-High and VA-060-Med against $MnFe_2O_4$ concentration. Five different concentrations were measured. Fitting the values gave the corresponding relaxivities.*

For determination of the r_2 values, the nanocapsules which show an efficient release upon application of an external alternating magnetic field (VA-060-High and VA-060-Med) were embedded in an agarose phantom and measured as described in the experimental section. The obtained r_2 values for the different concentrations are displayed in Figure 19. High r_2 relaxivity rates of 96.4 ± 8.8 Hz for VA-060-High and 120.4 ± 11.0 Hz for VA-060-Med related to 1 mmol of metal ion (iron or manganese) were determined. Longitudinal relaxivity rates r_1 were determined to be below 1 Hz·mmol^{-1} of metal ion for all cases. The reason for the low rates is probably due to a restricted water exchange between the interior of the nanocapsules and the bulk water thus decreasing the inner sphere relaxation rate.[209] Compared to literature values for negative contrast agents, the relaxivity rates measured for the capsules are high which makes the $MnFe_2O_4$ loaded nanocapsules very well suited as contrast agents for MR imaging applications.[210]

4.1.1.7 Cell Toxicity Assay

To demonstrate the potential use of the nanocapsules for biomedical applications, the $MnFe_2O_4$ loaded nanocapsules were added to a cell culture medium and their toxicity effect was determined on HeLa cells. Therefore, the thermoresponsive nanocapsules with the higher $MnFe_2O_4$ loading (VA-060-High and VA-060-Med) were incubated over 24 h.

After the incubation time, the cell viability was determined via a MTS assay to evaluate the toxic effect of the nanocapsules on the cells (Figure 20).

The results show, that for nanocapsule concentrations up to 600 µg·mL^{-1}, only little toxic effect could be observed. Thus, lower nanocapsule concentrations are suited for their use in biological systems.

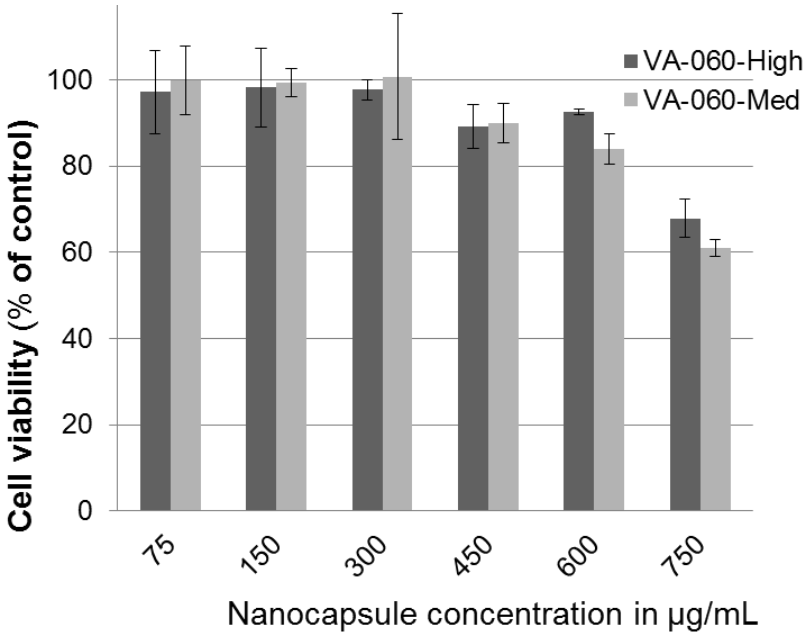

Figure 20. *Cell viability assay of $MnFe_2O_4$ loaded nanocapsules (VA-060-High and VA-060-Med) on HeLa cells. For lower concentrations (0-300 µg·mL^{-1}), no toxicity can be observed. At higher concentrations a toxic effect can be detected.*

To summarize the chapter, we have demonstrated the remote-controlled release of a model hydrophilic dye from polymer nanocapsules through application of an external alternating magnetic field. The high relaxivity value of the magnetic nanocapsules offers the possibility for their dual use as imaging agents and delivery transporters. Nanocapsules were functionalized with a thermolabile compound through covalent integration into the shell in order to allow for a thermal response. Water dispersible $MnFe_2O_4$ nanoparticles were integrated into the nanocontainers to act as heat generators through application of an external alternating magnetic field. The concentration of magnetic nanoparticles could be easily controlled due to the synthesis of the nanocapsules via miniemulsion polymerization inside of a "nanoreactor" droplet. High encapsulation efficiencies of active compounds and magnetic nanoparticles (up to 35 wt%) could be reached. The low cell toxicity of the $MnFe_2O_4$ loaded nanocapsules provides for their use as drug delivery systems with imaging properties and the possibility for a magnetically triggered release.

Future efforts will concentrate on the combination of the introduced magnetic functionality for a triggered magnetic release and MRI with a selective targeting of the nanocapsules *in-vitro* and *in-vivo*. In order to achieve the ambitious aim, the outer shell of the nanocapsules has to be modified in a way, that the interactions with proteins from blood serum and the shell are negligible. Then, the nanocapsule would possess a so called "stealth effect" which enables a long circulation within the blood stream. In other words, the nanocapsular drug shuttle has to have a high pharmacokinetic (PK) value. When further modifying the nanocapsule surface with selective targeting entities such as antibodies or microbodies, the nanocapsules specifically interact with the targeted cells such as cancer cells and are being taken up by them. In the ideal case, the nanocapsular drug delivery vehicle is traceable through MRI, targetable through surface functionalization and the drug releasable in remote control fashion.

In addition to the study on the magnetic field induce release of the nanocapsules, alternative ways of implementing iron oxide nanoparticles into the shell of the capsules and an additional way of functionalizing the nanocapsules with a thermoresponsive trigger was investigated. Those further efforts are described within the following two chapters. The described approaches however had drawbacks. In the case of introduction of iron oxide nanoparticles into the shell of capsules the preparation was too time-consuming for further investigations and the iron oxide loading was very low in all described examples. In the case of a polymer thermoresponsive shell material, the combination of thermoresponsive shell and iron oxide heat generators lead to a destabilization and precipitation of the iron oxide nanoparticles. Nevertheless, as a model system for the release of substances upon application of a thermal stimulus, the approach is very promising.

4.1.1.1 Other Possibilities for the Synthesis of Aqueous Dispersible Iron Oxide Nanoparticles and Their Encapsulation in Nanocapsules

The following chapters describe other possibilities for the surface functionalization of iron oxide nanoparticles and their encapsulation in polymeric capsules. In order to achieve a surface functionalization and stabilization of the iron oxide nanoparticles in aqueous environments, a variety of stabilizers was tested, including the amino acid L-lysine, carboxymethyl-dextran, the commercially available surfactant Lubrizol® U, and diethylene glycol. Because of the low solid content of magnetic particles, these

approaches were however not followed. The main strategy for the preparation of magnetically labeled nanocapsules presented in this thesis is the one described in chapter 4.1.1.2.

4.1.1.1.1 Water-Dispersible Lysine Coated Iron Oxide Nanoparticles

The challenges of stabilizing superparamagnetic nanoparticles in an aqueous dispersion are described in chapter 2.4.1, which deals with the synthesis and surface modification of superparamagnetic nanoparticles. The major drawback is the difficulty to prevent aggregation in highly concentrated dispersion. Most of the stabilizers known to efficiently prevent aggregation are based on quaternary amines and are not suitable for biomedical applications. Thus, natural stabilizers would be of high interest to stabilize superparamagnetic nanoparticles. Amino acids might be suitable because their carboxylic acid group has a binding affinity to iron oxide nanoparticles as it is the case for oleic acid and other ligands carrying carboxylic acid groups.[211-212] Additionally, the amino groups of the amino acid can electrostatically stabilize the nanoparticles in a certain pH range. Lysine, which carries two amino groups is therefore a promising stabilizer for our purpose.[35]

For the integration of superparamagnetic iron oxide nanoparticles in polyurea/urethane nanocapsules, a stabilization of the nanoparticles with an amine-carrying stabilizer is also tempting. Indeed, the amino group is highly reactive and quickly forms urea groups with isocyanates. Thus, it can easily react into the shell of the nanocapsules, anchoring the iron oxide nanoparticles to the shell and promoting a decomposition of the shell upon application of an external magnetic field to generate heat (see Figure 13).

The L-lysine functionalized nanoparticles were prepared following a literature recipe described in the experimental section (chapter 5.1.1.7.1). The analysis of the resulting nanoparticles dispersed in aqueous environment was performed *via* DLS measurements and TEM imaging. The light scattering measurement gave an average hydrodynamic diameter of 25 ± 5 nm. A TEM image of the nanoparticles is depicted in Figure 21a and shows nanoparticle sizes in the 3-5 nm range. On some parts of the grid, small clusters of iron oxide nanoparticles were present (~20 nm) in the size range of the hydrodynamic diameter as determined *via* DLS. However, the sizes of the aggregates were found to be in a reasonable range to still encapsulate them in nanocapsules (chapter 5.1.1.7.4). In order to check the encapsulation of the iron oxides into the nanocapsules, TEM imaging was performed (Figure 21b). The lysine-capped iron oxide nanoparticles were found to be encapsulated within the nanocapsules. However, only a small amount of iron oxide nanoparticles could be found encapsulated and due to an inhomogeneous

distribution of the iron oxide among the capsules, only some capsules contained nanoparticles. Due to the difficulty to increase the concentration of lysine functionalized iron oxides in aqueous dispersion and the therewith low loading of nanocapsules with iron oxide nanoparticles, further experiments were not carried out with this system.

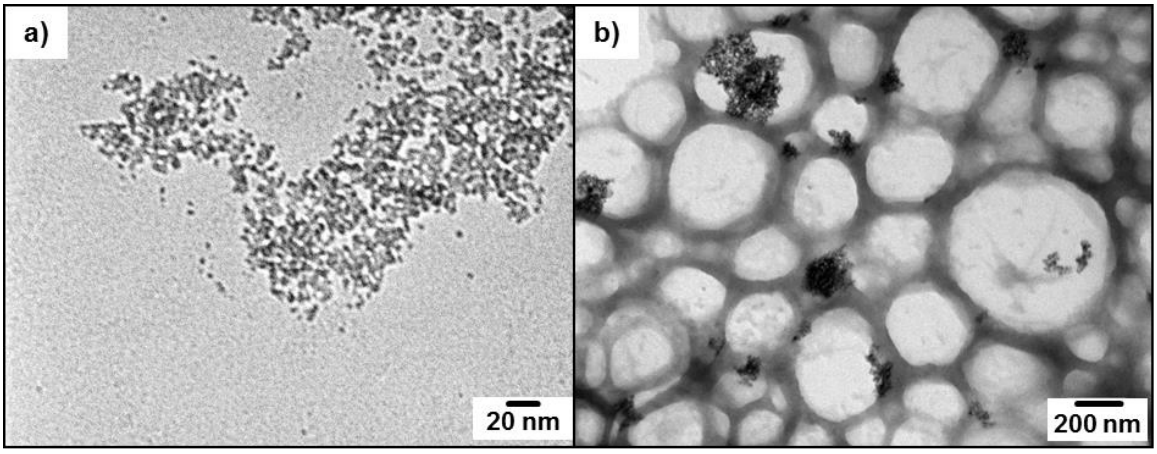

Figure 21. *TEM images of the lysine-stabilized iron oxide nanoparticles (a) and an image of encapsulated lysine-capped iron oxide nanoparticles in poly(urea/urethane) nanocapsules (b).*

4.1.1.1.2 Water-Dispersible, Carboxymethyl-dextran Coated Iron Oxide Nanoparticles

Commercially available iron oxide nanoparticles for applications for example as contrast agents in biomedicine (Endorem™, Lumirem®, Ferraspin™), are often coated with carboxymethyl-dextran.[213] The synthesis of such iron oxide nanoparticles can be also found in the literature.[214-215] The carboxymethyl-dextran is biocompatible and enables the iron oxide to be dispersed in aqueous media. Since the commercially available nanoparticles can only be ordered in very low solid content, we decided to synthesize iron oxide nanoparticles stabilized with carboxymethyl-dextran (chapter 5.1.1.7.2). A schematic illustration of the coating procedure with carboxymethyl-dextran is shown in Figure 22. Oleate-capped iron oxide nanoparticles were redispersed in dichloromethane. Sonication together with water yielded a direct miniemulsion with the droplets stabilized by carboxymethyl-dextran. Evaporation of the dichloromethane yielded carboxymethyl-dextran coated iron oxide nanoparticles.

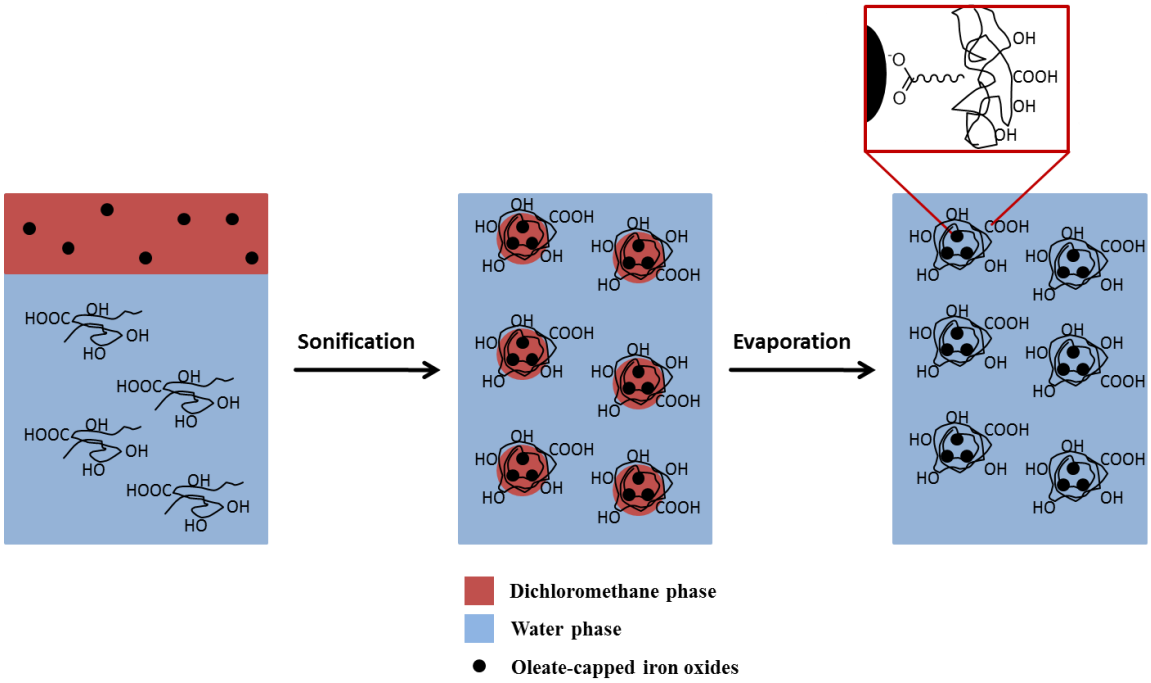

Figure 22. *Illustration of the synthesis of carboxymethyl-dextran coated iron oxide nanoparticles by the formation of carboxymethyl-dextran stabilized dichloromethane droplets containing iron oxides and the evaporation of the dichloromethane to yield iron oxide nanoparticles dispersed in aqueous medium.*

The synthesized carboxymethyl-dextran coated iron oxide nanoparticles were investigated by TEM (Figure 23a). Clearly, not only single iron oxide particles but clusters of iron oxides were observed. However the average cluster diameter of ~50-100 nm was still relatively small. In DLS, an average hydrodynamic diameter of 110 nm was determined. Owing to the relatively small size of the clusters, they were still suitable for the insertion into a capsule synthesis as described in chapter 5.1.1.7.4. Nevertheless, it has to be taken into account that the carboxymethyl-dextran coated iron oxides showed no long term stability and had to be used quickly (within a day). The capsule sizes were in the range of 200-800 nm as shown in Figure 23b. However, only in the larger sized capsules iron oxide could be found as shown in the TEM image.

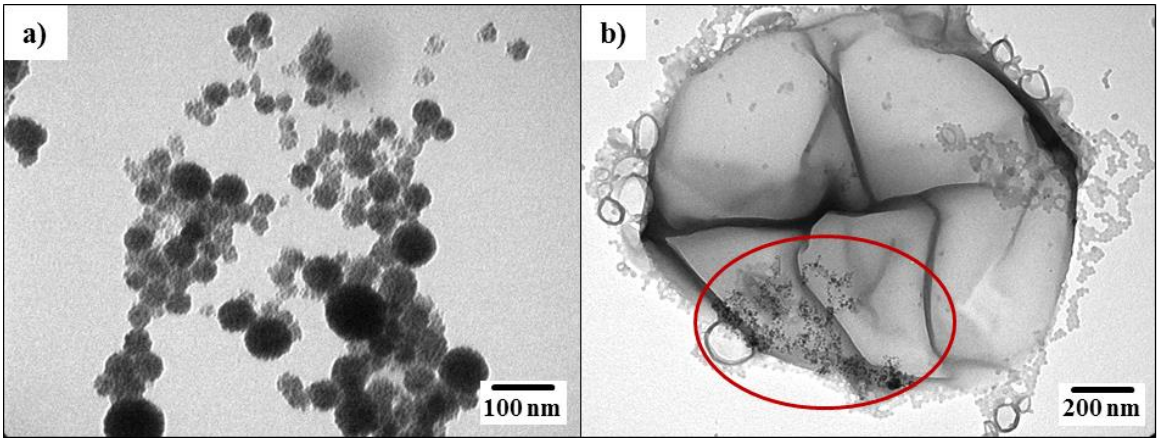

Figure 23. *TEM images of iron oxide nanoparticles stabilized by carboxymethyl-dextran drop-casted from aqueous dispersion (a) and encapsulated iron oxides inside of a poly(urethane/urea) nanocapsule (b). The iron oxide nanoparticles are marked with a red circle.*

In summary, a novel synthesis of carboxymethyl-dextran coated iron oxide nanoparticles was successfully carried out. However, the synthesis allows only low iron oxide concentrations to be prepared and the resulting particles coated with carboxymethyl-dextran are clusters with low stability in aqueous media. Because of the low concentration of the iron oxide and the low stabilization of the iron oxide through carboxymethyl-dextrane, it was not possible to obtain poly(urea/urethane) nanocapsules with high iron oxide content and no further experiments were carried out.

4.1.1.1.3 Water Dispersible Iron Oxide Nanoparticles Coated with Lubrizol®U

An alternative approach to synthesize iron oxide nanoparticles with an amino-functionality at the surface was performed using a surfactant double layer strategy as illustrated in Figure 24. A low amount of oleic acid capped iron oxide nanoparticles were dispersed in dichloromethane and a co-surfactant containing amino-groups (Lubrizol®U) was added (for detailed recipe see experimental section 5.1.1.7.3). Sonication together with water and subsequent evaporation of the dichloromethane resulted in iron oxide nanoparticles coated with a double layer of oleic acid and Lubrizol®U (Figure 24).

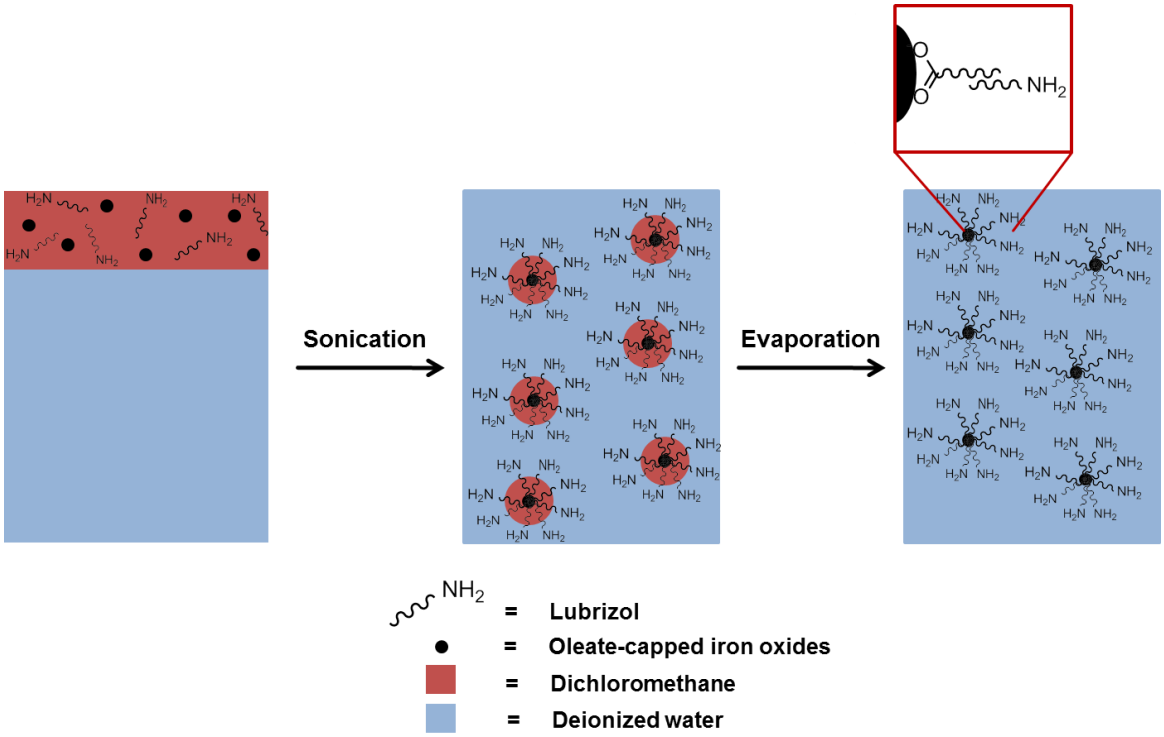

Figure 24. *Schematic illustration of the functionalization of iron oxide nanoparticles with a double layer of oleic acid and Lubrizol to give water stable, amino-functionalized nanoparticles.*

The obtained Lubrizol®U stabilized iron oxide nanoparticles were investigated *via* DLS measurements and TEM imaging. DLS results gave an average hydrodynamic diameter of ~50 nm, considerably higher than the average diameter of the particles observed by TEM (~8 nm). However, it has to be considered that three additional layers are on the top; the oleic acid, the Lubrizol®U and the water layer. TEM imaging mainly revealed singular iron oxide particles as can be seen in Figure 25a. Hence, the particles are suitable candidates for encapsulation.

The surface amino-group labeled iron oxide nanoparticles can then be inserted into poly(urea/urethane) nanocapsules as shown for the lysine and carboxymethyl-dextran coated particles. The concentration of the nanoparticles was firstly increased to ~5% by centrifugation and redispersion in small amounts of water. Then the nanocapsule synthesis was performed as described in the experimental section (chapter 5.1.1.7.3). DLS measurements gave an average hydrodynamic diameter of the capsules of 330 ± 70 nm. TEM images show the formation of capsules with a homogeneous distribution of the iron oxides among the capsules (Figure 25b+c). The location of the iron oxide nanoparticles within the capsules can only be assumed from the images due to possible drying effects. Therefore, the capsules were embedded in an epoxy resin and thin slices (~100 nm thick)

of the resin were investigated by TEM (Figure 25d). The TEM cuts show proof for the successful insertion of the iron oxide nanoparticles in the shell of the capsules.

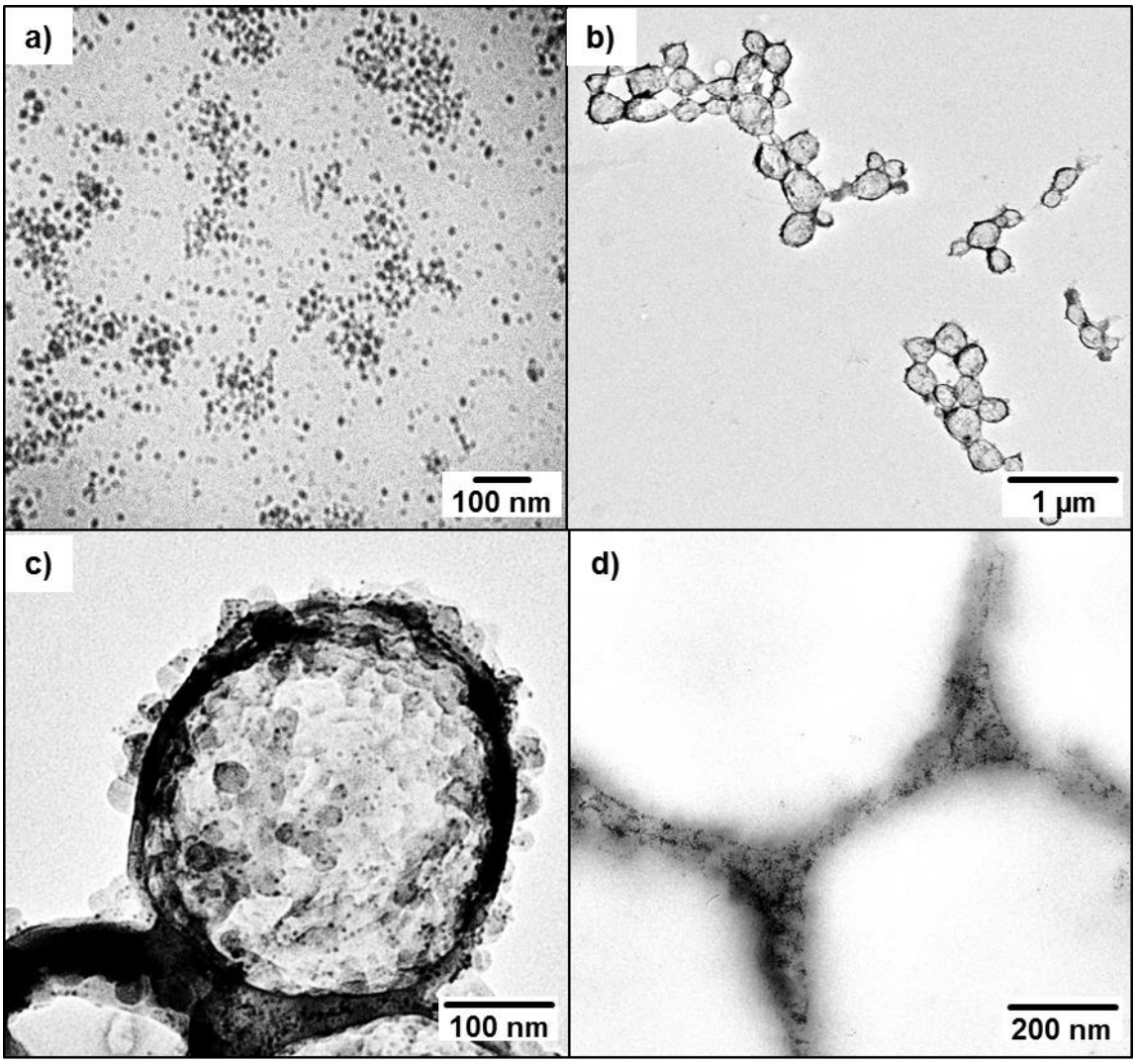

Figure 25. *TEM images of iron oxide nanoparticles stabilized by Lubrizol®U (a) and images of iron oxide nanoparticles encapsulated in poly(urea/urethane) capsules (b+c). d) TEM image of a thin slice of the same capsules loaded with iron oxide embedded in an epoxy resin.*

In addition to the demonstrated possibilities to synthesize and encapsulate iron oxide nanoparticles into poly(urea/urethane) nanocapsules, also diethylene glycol functionalized iron oxide nanoparticles were synthesized as reported by Hu et al.[216] However the particles were only very weakly magnetic and were not used for encapsulation reactions.

The demonstrated possibilities to introduce iron oxide nanoparticles (L-lysine, carboxymethyl-dextrane, Lubrizol®U, and diethylene glycol coated iron oxides) into capsules showed to be time-consuming and the loading with iron oxide nanoparticles not

homogeneous or high enough to use them for a magnetic field induced release study from the capsules. Nevertheless, these approaches can still be very useful for other applications. Exemplary, the iron oxide nanoparticles can be used as labels in order to trace the nanocapsules *via* MRI.

4.1.2 Thermoresponsive Capsules

The controlled encapsulation and triggered release of substances from nanocapsules offers potential applications in various areas such as drug delivery[217] and catalyst.[69] Not only temperature degradable compounds such as used in chapter 4.1.1.3 are suitable as thermal stimulus, often thermal stimulus responsive polymers are chosen.[218] The typical response of many polymers in solution to a change in temperature is a lower critical solution temperature (LCST).[219] Upon an increase in temperature, these polymers become insoluble at the LCST and precipitate (see chapter 2.4.2.1.3). Particles consisting of such polymers are suitable for a loading and release of entrapped compounds upon temperature increase by displaying a sponge-like response.[88, 220] At lower temperature, the crosslinked polymer interacts strongly with the surrounding liquid phase while at higher temperatures, the interaction is weaker and a contraction of the particle is observed. The mechanism of drug release then resembles the squeezing of a sponge. In order to obtain a temperature induced release in capsules, LCST polymers are not very suitable.[219] Here, polymers with an upper critical solution temperature (UCST) are required. However, only few examples are known.[221] Polymers known to show UCST behavior in aqueous solution are poly[oligo(ethylene glycol) methyl ether methacrylate] (POEGMA)[222] or zwitterionic polymers such as poly(3 dimethyl(methacryloxyethyl) ammonium propane sulfonate) (PdMMAEAPS).[223] However, these polymers that undergo UCST transitions are not easily accessible. One simple option to introduce a UCST-like behavior in a polyionic structure is the addition of a salt to the polymer solution. For poly(acrylic acid) (PAAc) in aqueous solution with high salt concentrations, such a behavior is observed.[224] Depending on the salt concentration, the UCST transition can be tailored. We make use of this system owing to the facile excess to an UCST behavior bearing polymer. Therefore, an aqueous solution with high content of salt containing poly(acrylic acid) was used for the formation of polymeric capsules. The capsule formation is schematically depicted in Figure 26 (for experimental details see chapter 5.1.2.1.1). Submicron aqueous miniemulsion droplets containing the salt and the PAAc were generated at temperatures > 60 °C by ultrasonication. At this temperature, the polymer is soluble. Cooling these miniemulsions to room temperature leads to precipitation of the acrylic acid at the water/cyclohexane interface. Addition of TDI enables a polyaddition reaction at the interface together with the HD monomer and,

probably partially, with the less reactive poly(acrylic acid). Transfer of the capsules from the cyclohexane phase into an aqueous phase is achieved by redispersion in surfactant carrying aqueous solution.

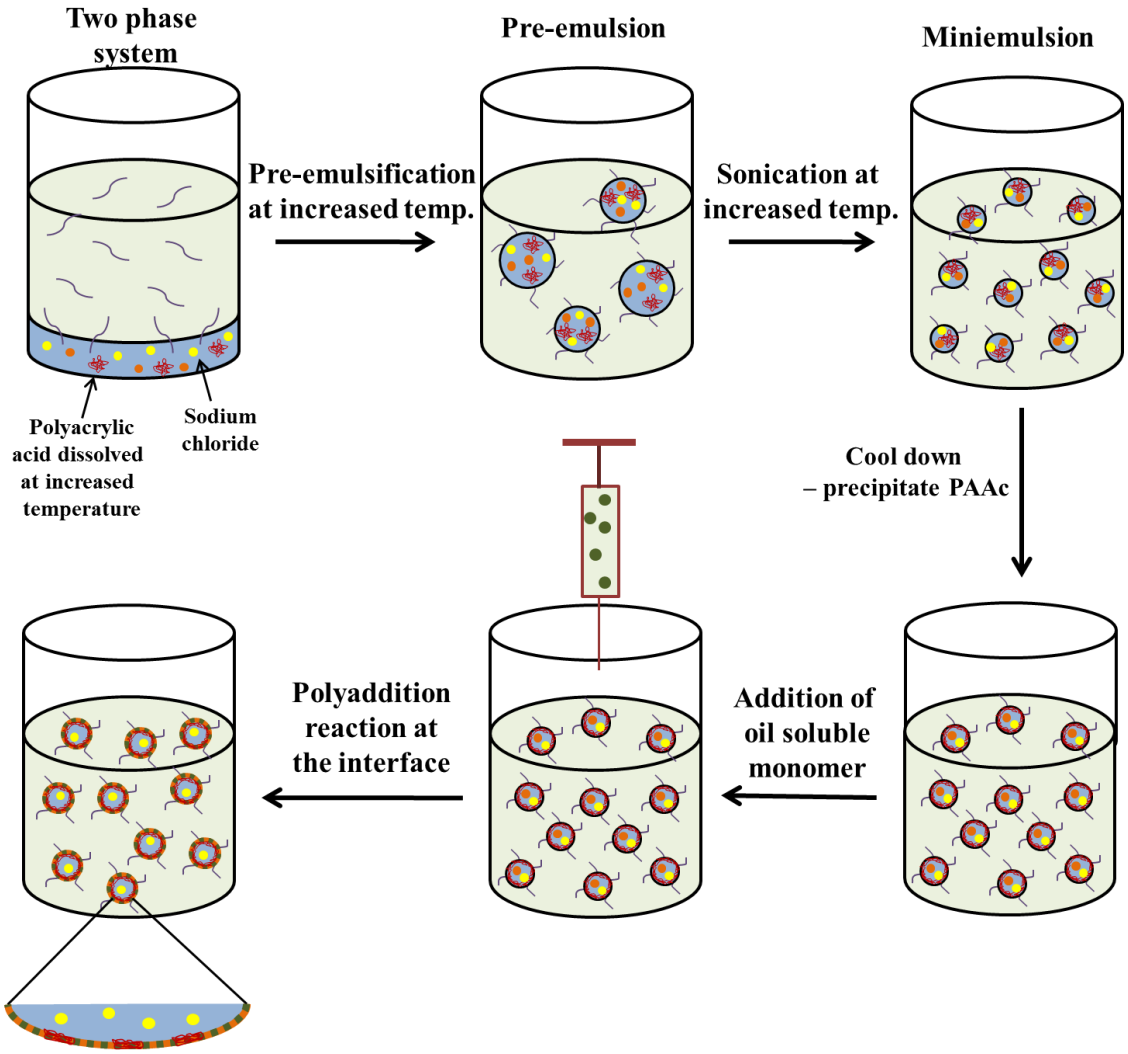

Figure 26. *Scheme of the capsule formation. The sonication of a two phase system at increased temperature yields an inverse miniemulsion which is cooled to room temperature. The PAAc precipitates inside of the nanodroplets and a polyaddition reaction at the interface is initiated by addition of a diisocyanate to give nanocapsules with aqueous core in an oil phase. Redispersion of the capsules is performed as illustrated in Figure 13.*

The formation of the capsules was followed by DLS and TEM imaging. DLS measurements gave an average hydrodynamic diameter of 620 ± 180 nm. The relatively large diameter of the capsules can be attributed to the high viscosity of the PAAc solution and therefore the high shear force needed to rupture one droplet into several droplets. For the release experiments, the fluorescent dye sulforhodamine 101 was encapsulated. Partial leakage of the dye was found after hours and days, but > 50% of the dye could be

encapsulated permanently within the capsules. Investigation of the thermoresponsive release of a model fluorescent dye from the capsules by increase in temperature was performed as described in the experimental part (chapter 5.1.2.1.2). Theoretically, the release is achieved by the dissolution of the poly(acrylic acid) at increased temperature and therefore pore creation. Indeed, an increase in fluorescent dye concentration in the continuous phase was detected when heating the capsule dispersion as shown in Figure 27b. Interestingly, the capsules can, by a decrease in temperature below the UCST, be "closed" again, enabling an interruption of the release. Cycles of heating and cooling therefore enable a stepwise release as shown in Figure 27b and as illustrated in Figure 27a.

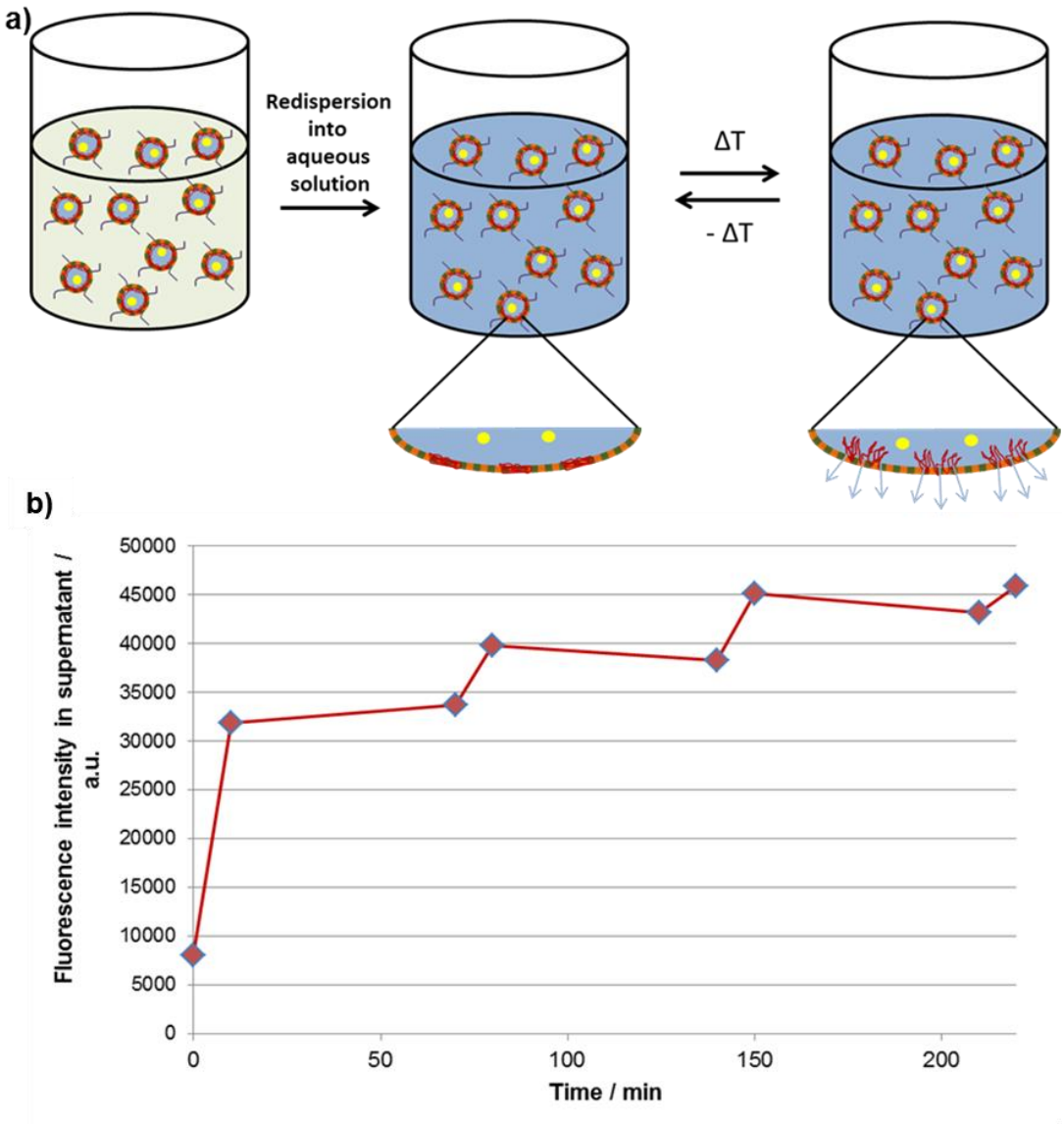

Figure 27. *a) Mechanism of the release by switching the temperature. b) Release profile of a model dye. Four heating intervals up to 80 °C for 10 min and three intermediate intervals over a time period of 60 min at room temperature are shown.*

In conclusion, capsules synthesized from very basic materials were produced in a simple way. Upon an increase in temperature, the capsules release their payload due to a thermo responsive polymer with UCST behavior as part of the shell. Not only the encapsulated material can be released, but the release can be stopped by decreasing the temperature. Hence, a stepwise release of hydrophilic compounds is provided.

4.1.3 Encapsulation of Gold Nanoparticles for the Triggered Release from Capsules by Irradiation

In the previously described chapters, the possibility of heat generation by the application of an alternating magnetic field and thermal energy dissipation by the excited magnetic nanoparticles was described. Another effective opportunity to generate heat is the irradiation of gold nanoparticles. Due to a high absorption coefficient in the near infrared area (NIR), efficient heat can be converted from electromagnetic energy to thermal energy.[225] The absorption of irradiation in the NIR area is low for tissue. Thus, the radiation can penetrate through the skin for several milli- to centimeters and the encapsulation of gold nanoparticles as heat generators can be lead to possibly release substances upon irradiation with NIR-light.[219, 226]

Therefore we tried not only to implement a magnetic stimulus into nanocapsules but also tag them with gold nanoparticles as NIR-responsive heat generators. The synthesis of the gold nanoparticles with citric acid as stabilizer was carried out as is described in chapter 5.1.3.1.1. Analysis of the optical properties of the citrate stabilized gold nanoparticles was carried out using UV-VIS spectroscopy. After the synthesis the particles are very dilute in aqueous solution (~100 $mg \cdot L^{-1}$). In order to get higher concentrations, the particles were centrifuged and redispersed to give a 10x higher concentration. TEM investigation of the gold nanoparticles reveal a diameter of 20 nm and no aggregates could be observed (Figure 28a). DLS measurements confirmed no larger aggregates and gave an average hydrodynamic diameter of 35 nm. The UV-Vis spectrum of the gold nanoparticles dispersion after the synthesis and after making the dispersion higher concentrated by centrifugation, are shown in Figure 28b.

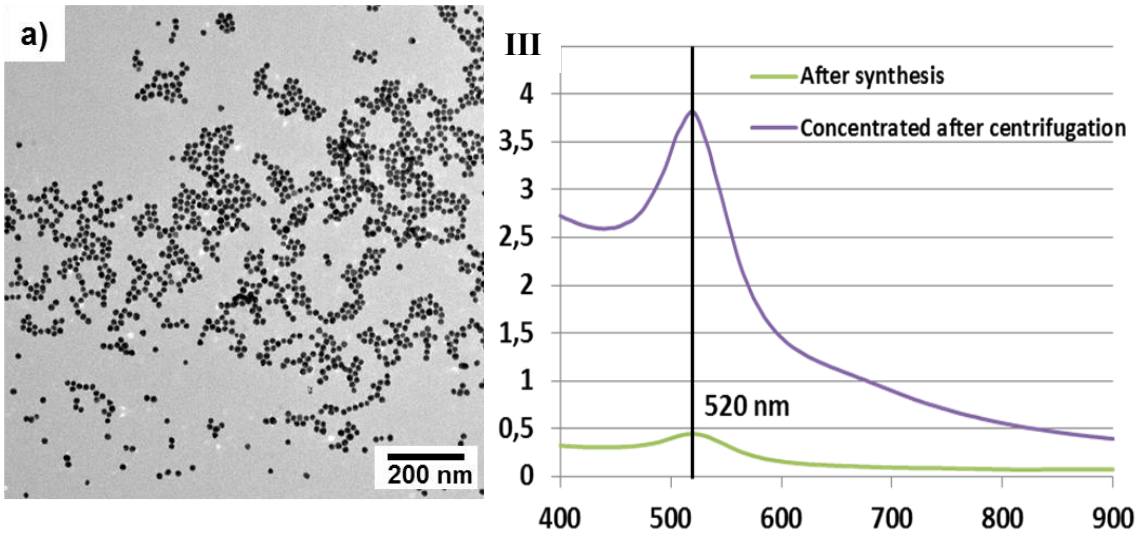

Figure 28. *a) TEM image of citrate coated gold nanoparticles drop-casted from aqueous dispersion. b) Absorption spectrum of citrate coated gold nanoparticles in pure water with two different concentrations.*

The UV-Vis spectrum of the gold nanoparticles shows the maximum absorption peak at around 520 nm, due to plasmon resonance of the gold. In the region of the near infrared light (700-800 nm), the absorption is very low. In order to increase the absorption in the near infrared region, the addition of salt can be very effective.[227] Once salt is added and the ionic strength of the dispersion is increased, the electrostatic stabilized gold nanoparticles tend to cluster together due to a decrease of the ionic stabilization of the nanoparticles (see chapter 5.1.3.1.2). Within the clustered nanoparticles, plasmons cannot only be excited in one single gold nanoparticle; additionally a whole cluster of particles can be excited by plasmon resonance. Thus, the amplitude of the plasmon resonance is shifted to lower energies and to higher wavelengths.[228] To investigate the effect of the salt concentration, two different concentrations were added (5 $mg \cdot mL^{-1}$ and 20 $mg \cdot mL^{-1}$ of sodium chloride) and the resulting clustering was investigated *via* UV-VIS spectroscopy, by TEM imaging and with DLS measurements (see Figure 29).

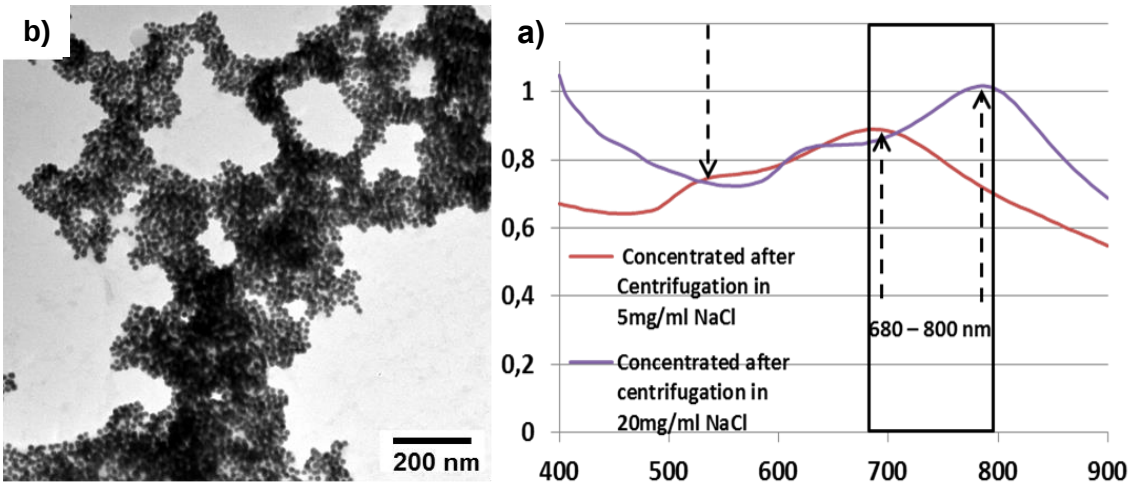

Figure 29. *a) TEM image of gold nanoparticles drop-casted from a 20 mg·mL^{-1} sodium chloride containing aqueous dispersion. b) Absorption spectrum of citrate coated gold nanoparticles in aqueous solution with 5 and 20 mg·mL^{-1} sodium chloride.*

The UV-Vis spectrum in Figure 29b shows, that after the addition of sodium chloride, the maximum absorption peak shifts to higher wavelengths as expected from theory (680 nm for 5 mg·mL^{-1} NaCl and 800 nm for 20 mg·mL^{-1} sodium chloride). DLS measurements confirm an increase in size (~ 120 nm for 5 mg·mL^{-1} and ~180 nm for 20 mg·mL^{-1}), due to cluster formation of the gold nanoparticles. Additionally, TEM imaging revealed clusters of gold nanoparticles after the addition of NaCl (Figure 29b depicts the image of 20 mg·mL^{-1} sodium chloride added).

The as synthesized and characterized citrate coated gold nanoparticles were introduced as aqueous dispersion into a typical synthesis of poly(urethane/urea) nanocapsules in inverse miniemulsion (see Figure 13 and chapter 5.1.3.1.2). The encapsulation was successful according to TEM images, however the amount of encapsulated gold was found to be very low as shown in Figure 30. Owing to the high density of the gold nanoparticles (19.32 g·cm^3)[229] and their relatively low concentration within the aqueous dispersion (which was increased to ~50 mg·mL^{-1} by centrifugation), the amount of nanoparticles per capsule is very low. In a first (quick) experiment no release upon irradiation was observed. Nevertheless, a release might still be possible by increasing the amount of gold nanoparticles. Therefore, an alternative synthetic procedure is recommended: Firstly the nanocapsules are synthesized and redispersed with cationic surfactants in aqueous solution. Then, in a second step, the gold nanoparticles are deposited onto a small amount of the nanocapsules by electrostatic interactions.[230]

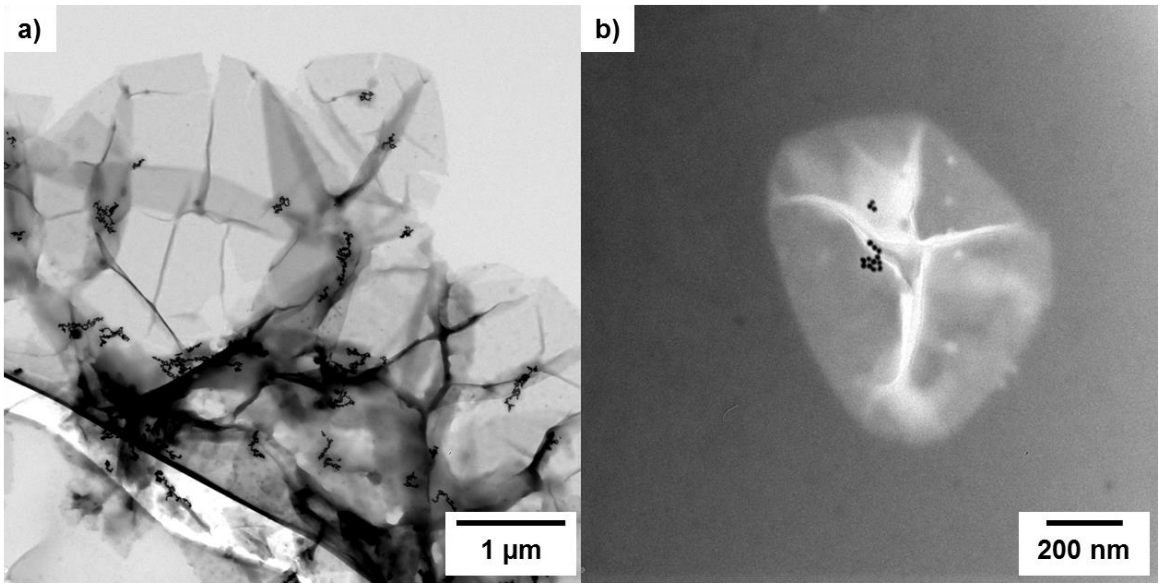

Figure 30. *TEM image of gold nanoparticles encapsulated in poly(urethane/urea) nanocapsules. a) Cluster of several nanocapsules. Various small gold aggregates can be observed within the nanocapsules. b) A single nanocapsule with a couple of encapsulated gold nanoparticles.*

4.1.4 Double Shell Polymer Hybrids Capsules - Towards Multiresponsive Systems

The preparation of a variety of smart capsules has already been described which can release encapsulated substances upon the influence of an external stimulus. Redox-,[231] light-,[232] pH-,[233] temperature responsive[234] release stimuli among others have already been shown. Additionally, multiple stimuli responsive systems have been demonstrated.[235] Here, a novel approach to combine two different stimuli responsive materials in a double shell capsules system is introduced. Release is then achieved either by application of both stimuli or upon application of one stimulus. Therefore, a polyaddition reaction of a thermally decomposing azo-initiator is performed on miniemulsion dropelts to obtain thermoresponsive nanocapsules (see chapter 4.1.1.3 and 5.1.4 for experimental details). Additionally, three different water-miscible monomers were encapsulated and upon temperature increase (not too long in order not to decompose the shell) and decomposition of the azo-initiator, polymerized. The influence of the radical "grafting form" polymerization of acrylic acid, N-vinylpyrrolidone, acryl amide as model monomers on the morphology of poly(urethane/urea) nanocapsules modified with an azo-diol initiator was investigated by SEM imaging as depicted in Figure 31.[207] Before heating the capsules are soft and collapse under the vacuum applied in the scanning electron microscope. After heating and the therewith going along grafting from

polymerization of the different monomers, the shell of the capsules becomes much harder in all cases and they do not easily shrink or collapse in the SEM. The harder shell indicates an additional stabilization of the shell which is most probably due to the generation of a second polymer layer, poly(acrylic acid), poly(acryl amide) or polyvinylpyrrolidone. The successful conversion of monomer was confirmed by freeze drying in order to determine the solid content. Table 4 lists the conversion of monomers in percentage.

Table 4. *Monomer conversion as determined by solid content.*

Sample	Theoretical solid content at 0% monomer conversion	Theoretical solid content at 100% monomer conversion	Experimentally determined solid content	Monomer conversion
AAc Before heating	3.94%		3.99%	
AAc After heating	3.94%	5.33%	4.16%	16%
AAm Before heating	3.94%		3.99%	
AAm After heating	3.94%	5.33%	4.50%	40%
VP Before heating	3.94%		3.92%	
VP After heating	3.94%	5.33%	4.54%	43%

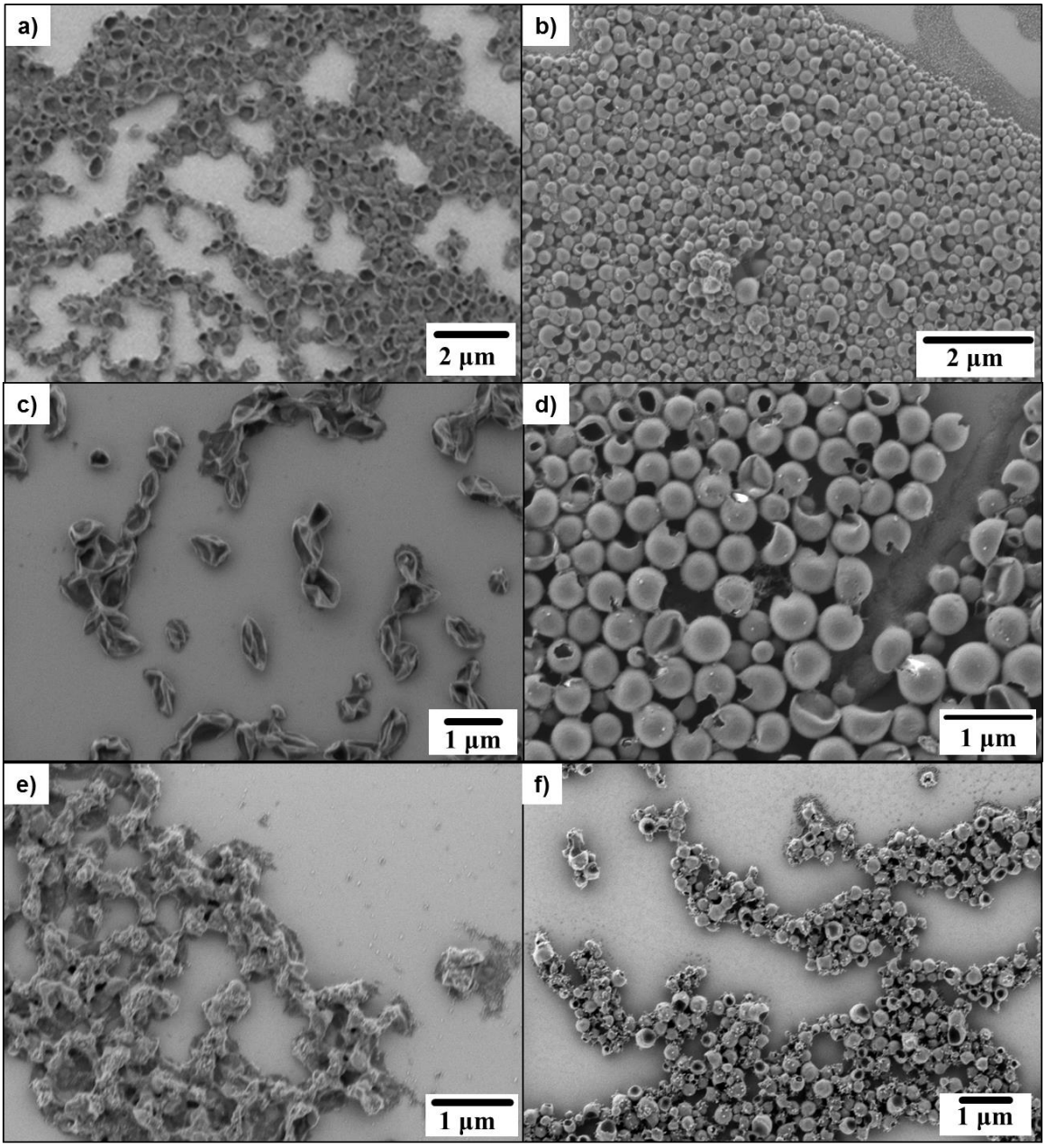

Figure 31. *SEM Images of nanocapsules before (a, c, e) and after (b, d, f) heating to induce "grafting from" polymerization. a+b) with encapsulated acrylic acid. c+d) Acryl amide. e+f) N-vinylpyrrolidone.*

Besides the morphological evidence, further investigations were carried out on a molecular level. The molecular weight of the different capsules was determined before and after the heating step *via* GPC analysis as displayed in Figure 32 and listed in Table 5.

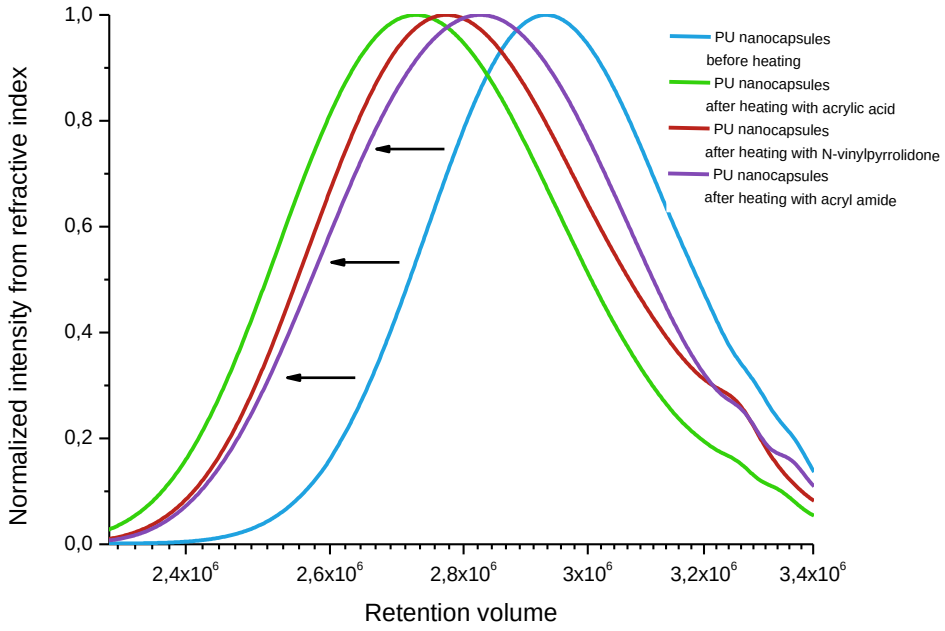

Figure 32. *GPC of M_w of PU-nanocapsules before (blue) and after heating for 16 h at 60 °C with different monomers (acrylic acid in green, N-vinylpyrrolidone in red, acryl amide in purple).*

Table 5. *Molecular weight and PDI of the resulting polymer form grafting from polymerization determined by GPC (in DMF with PS standard).*

Polymer	M_w / g·mol^{-1}	PDI (M_w/M_n)
Poly(acrylic acid)	16,400	2.7
Poly(acryl amide)	16,500	2.6
Poly(N-vinylpyrrolidone)	15,600	2.6

Determination of the molecular weight by GPC shows a clear shift for all of the three investigated radical “grafting from” polymerizations towards higher molecular weights (M_w). The increase in molecular weight is most probably due to a successful radical polymerization of the three different monomers onto the nanocapsules shell.

In summary, the successful synthesis of double shell capsules could be shown. For future experiments the encapsulation and stimuli responsive release could be investigated. Exemplary, double shell capsules consisting of an aqueous liquid core, an inner pH-responsive poly(acrylic acid) shell and a second thermoresponsive azo-diol shell could be investigated.

4.2 Multifunctional Magnetic Hybrid Nanoparticles

4.2.1 Anisotropic Magnetic Nanoparticles

In the present chapter, the synthesis of sulfonate functionalized iron oxide/polymer nanoparticles and their elongation is described to obtain anisotropic nanoparticles. The work was performed in collaboration with Christine Herrmann and Daniel Crespy and the presented results summarized from the publication: "*Re-dispersible Anisotropic and Structured Nanoparticles: Formation and Their Subsequent Shape Change*".[236] Generally, non-spherical nanoparticles are of interest due to an increase in surface area in comparison to spherical particles with the same volume. The enlarged surface area enables a potentially stronger surface interaction with their environment. In the case of stabilizing emulsions, quasi-ellipsoidal particles have been proven to be advantageous over spherical particles.[237] For nanoparticle-based imaging or drug delivery systems, the shape of the nanoparticles plays a major role in their interaction with cells.[238-239] When making use of such non-spherically shaped nanoparticles for applications in biomedicine, additional functionalities have to be integrated within the particles.

The nanoparticle synthesis was performed as shown in Figure 33 and as described in the experimental section (chapter 4.2). In contrast to other procedures, which involve only a miniemulsion as disperse phase,[240] here an additional diffusion step of monomers as in emulsion polymerization is used. The amount of iron oxide can then be increased from ~40 to ~80 wt%.[123] The styrene droplets act as monomer reservoirs and the iron oxide/octane miniemulsion droplets as seeds for the emulsion polymerization. A minority of nanoparticles containing no iron oxide is obtained from polymerized styrene reservoirs and by homogeneous nucleation. These non-magnetic particles can be easily separated by magnetic purification. Highly surface sulfonated polystyrene-co-styrene sulfonate nanoparticles with incorporated oleate-capped iron oxide nanoparticles are then obtained with an average hydrodynamic diameter of 193 ± 61 nm as determined *via* DLS. The zeta potential of -39 mV proofs the presence of the negatively charged sulfonated surface. The sulfonate-functionality on the surface is important, since the redispersion of particles with such functionality after elongation has been shown to work best.

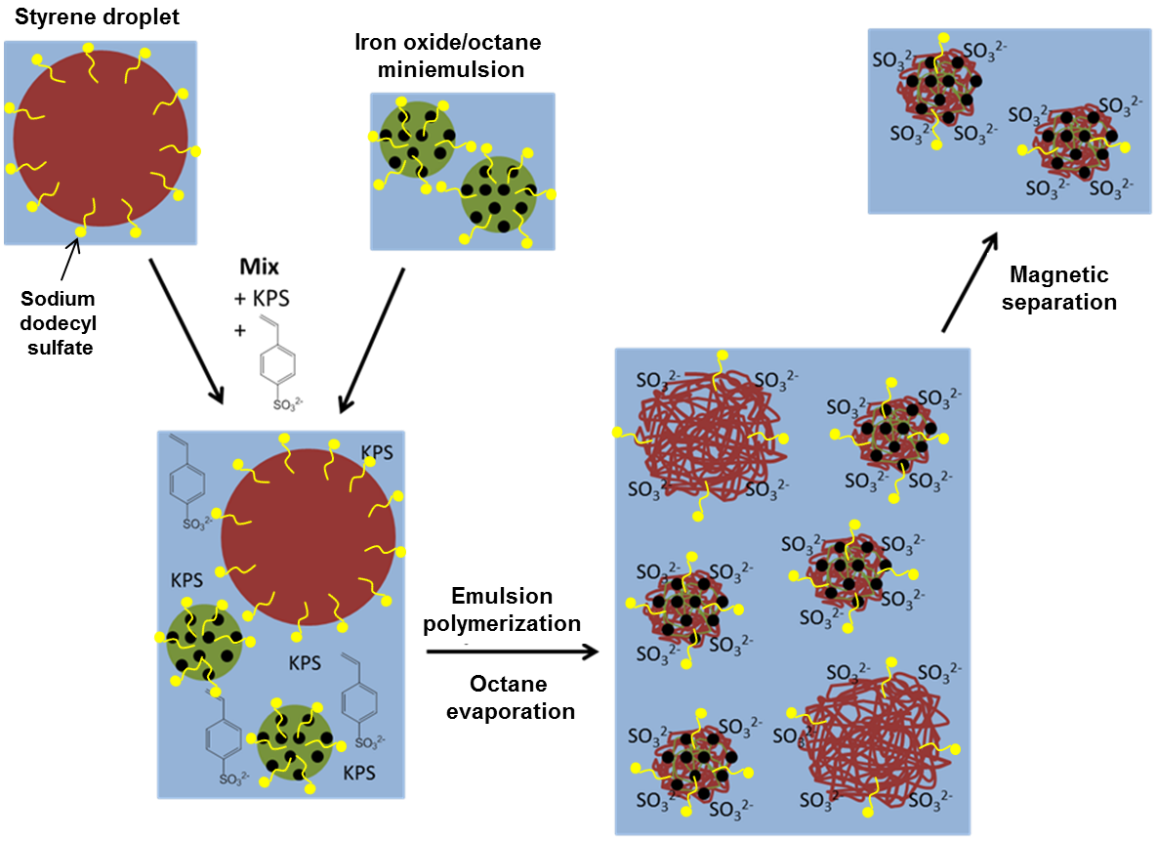

Figure 33. *Synthesis of spherical iron oxide/polystyrene nanoparticles with sulfonate surface functionality. Here, miniemulsion droplets of oleate-capped iron oxide nanoparticles in octane act as seeds for the emulsion polymerization of styrene. The covalently bond sulfonate surface functionality is introduced by the addition of styrene sulfonate monomer. Magnetic separation yields sulfonate decorated iron oxide/polystyrene nanoparticles.*

Stretching of the hybrid nanoparticles was achieved as demonstrated in Figure 34 and as described in detail in the experimental section (chapter 5.2.1.2). The nanoparticles dispersed in aqueous medium are mixed with a poly(vinyl alcohol) (PVA) containing solution and deposited onto a surface. After water evaporation, a film is formed. Heating the film up to ~140 °C, which is well above the T_g of the PVA, enables matrix flexibility and the film can be deformed mechanically. After deformation, the PVA matrix is removed and, after further purification, the nanoparticles dispersed in water.

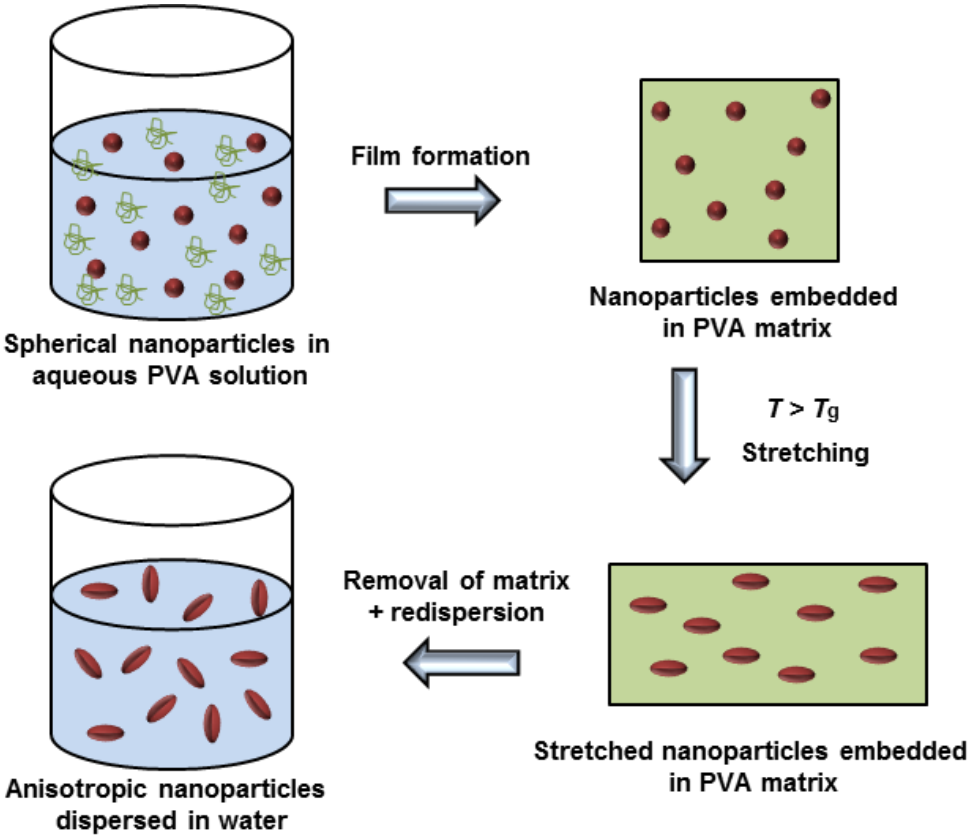

Figure 34. *Stretching procedure of the iron oxide labeled polymer nanoparticles. The aqueous dispersion of nanoparticles is combined with dissolved poly(vinyl alcohol) (PVA) and the composite film formed through evaporation of the water. The film is stretched upon temperature increase far above the glass transition temperature of PVA to ~140 °C and in a last step, the PVA matrix removed and the nanoparticles dispersed in aqueous medium.*[236]

After stretching, the obtained elongated nanoparticles were analyzed by TEM and SEM (Figure 35). The aspect ratio was determined from the images to be 2.5 ± 0.4 with an average length of the long axis of 216 ± 41 nm and of the short axis of 86 ± 14 nm. Approximately 43% of the inserted hybrid nanoparticles could be redispersed in aqueous dispersion. Before stretching, the iron oxide nanoparticles were distributed mainly homogeneous within the polymer nanoparticles. However, after stretching, a separation of iron oxide and polymer was observed. We believe that the separation is due to the heating, which is required to stretch the PVA film (140 °C) is far beyond the glass transition temperature of polystyrene or poly(styrene-*co*-styrene sulfonate). Thus, the polymer chain migration can occur and lead to a phase separation within the hybrid nanoparticles between the iron oxide and the polymer.

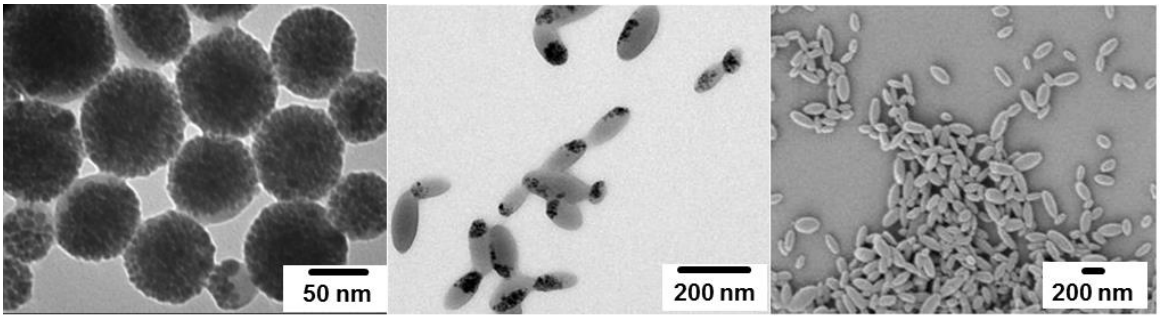

Figure 35. *TEM image of spherical nanoparticles of poly(styrene/styrene sulfonate) with incorporated iron oxide (a). SEM (b) and TEM (c) image of the same particles after stretching.*[236]

Observing, that after stretching, the iron oxide separates from the polymer (or the other way around), we performed a separate experiment with the inserted nanoparticles. An aqueous dispersion of the nanoparticles was heated to ~100 °C for 1 h and investigated *via* TEM imaging (Figure 36). We found similar results as for the stretching of the nanoparticles, meaning, that phase separation was observed. In order to change the morphology within the nanoparticle once more, *n*-octane was added and the dispersion sonicated to distribute the octane amoung the particles. The octane, a good solvent for oleate-capped iron oxide nanoparticles, enabled the iron oxide to distribute on the surface of the polymer particles when it is evaporated slowly. Further investigation using TEM imaging revealed that the morphology again had changed to a core-shell type arrangement. The polymer was found as core material with the iron oxide nanoparticles distributed on top as core material (Figure 36).

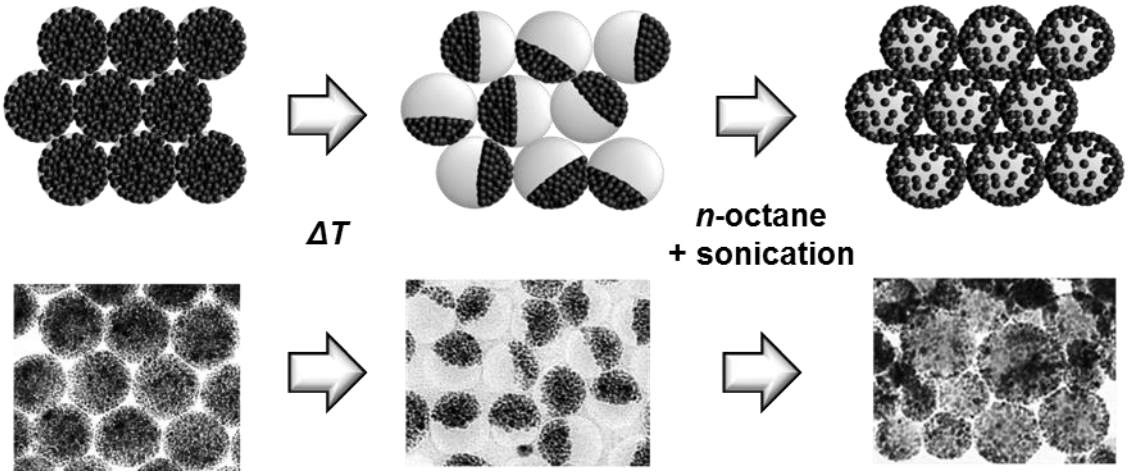

Figure 36. *Morphology change within iron oxide/polystyrene nanoparticles.*

An interesting additional feature discovered for the anisotropic nanoparticles is their ability to change their shape upon an increase in temperature above the T_g as described in detail in the published manuscript.[236] During mechanical stretching in the PVA matrix,

the polystyrene chains in the nanoparticles also elongate into an entropically unfavored conformation. Below the T_g the chains are in a "frozen state", but, once heating above the T_g, the entropic force drives the nanoparticles back into a spherical shape. Implementation of a superparamagnetic moiety into the nanoparticles opens the opportunity to trigger the shape change from anisotropic to spherical shape not only by an external temperature increase, but additionally by application of an external alternating magnetic field and local heating by the magnetic nanoparticles. Since the uptake of nanoparticles into cells is depending on their shape,[238] future experiments might be of high interest to investigate the triggered nanoparticle uptake into cells by applying an external alternating magnetic field and thus generating heat and changing their shape back to spheres.

4.2.2 Luminescent Magnetic Hybrid Nanoparticles

The implementation of a magnetic moiety into hybrid nanomaterials gives rise to a variety of different applications.[66] Here, the combination of magnetic with luminescent nanoparticles to yield hybrid nanoparticles with both properties is demonstrated. The work was conducted in collaboration with Viktor Fischer and Rafael Muñoz-Espí and the presented results are summarized from the publication: "*Luminescent and Magnetoresponsive Multifunctional Chalcogenide/Polymer Hybrid Nanoparticles"*.[244] The hybrid nanoparticles comprising an optically active compound with magnetically responsive entity are relevant for applications such as combined imaging agents,[245] cancer treatment[246] and catalysis,[247] among others. Typical approaches to combine luminescent and magnetic properties are to couple *ex-situ* synthesized quantum dots to a magnetic carrier nanoparticle[248] or the layer-by-layer assembly of one functional compound onto another.[249] However, such approaches can be time-consuming and give only small yields due to difficult functionalization procedures and the elaborate purification for the layer-by-layer assembly.

In our case, the use of phosphonate-functionalized polystyrene/magnetite nanoparticles as templates for the controlled crystallization of cadmium sulfide (CdS) onto the nanoparticle surface is described. The synthesis of polystyrene/magnetite nanoparticles with phosphonate surface functionality was performed as illustrated in Figure 37 and described in detail in the experimental section (Chapter 5.2.2). An especially designed surfmer (surfactant and monomer in one) was synthesized by Viktor Fischer. The surfmer carried a phosphonate head-group on one end and a polymerizable methacrylate group on the other end (Figure 37). The surfmer was used to stabilize *n*-octane droplets containing dispersed oleate-capped iron oxide nanoparticles. Using the droplets as seeds for an emulsion polymerization of styrene yielded in polystyrene

nanoparticles with incorporated iron oxide and phosphonate surface functionality. The phosphonate functionalities show strong interactions with cadmium ions according to the HSAB concept of Pearson.[250] Owing to the strong surface interactions, addition of a precipitating agent for cadmium can lead to crystal formation at the surface as demonstrated here. The cadmium ions then act as nucleation centers for the precipitation of the CdS.

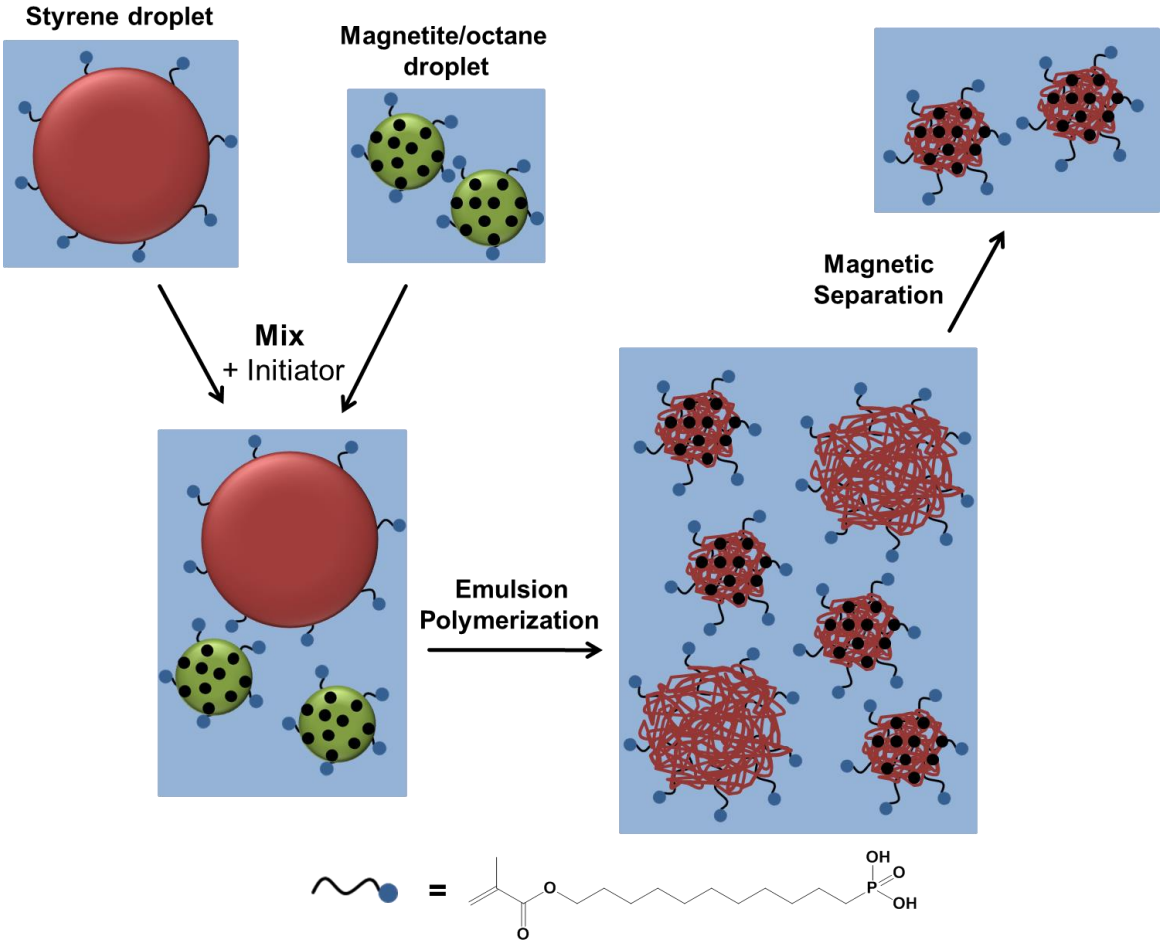

Figure 37. *Preparation of phosphonate-functionalized polystyrene particles loaded with magnetic iron oxide nanoparticles using a phosphonate surfmer. Hybrid nanoparticles are formed by an emulsion polymerization of styrene onto miniemulsion droplets of iron oxide in octane.*

The synthesized hybrid nanoparticles were analyzed by TEM before and after precipitation of CdS and element mapping was performed after the precipitation (Figure 38). The average hydrodynamic diameter as determined from DLS measurements was found to be 134 ± 44 nm before surface crystallization. The TEM image of the magnetic polymer nanoparticles shows that the iron oxide is mainly located within the polymer matrix, often in form of small clusters. The iron oxide content determined by TGA was 67 wt%, proving a high loading of the particles with iron oxide. The magnetic moiety was in more detail investigated by VSM measurements by Prof. Gerhard Jakob. The hysteresis

loop obtained revealed a superparamagnetic behavior at room temperature, since no retentivity was observed. Temperature dependent measurements showed a superparamagnetic behavior at least up to 300 K. Zeta potential measurements gave a value of −56 ± 8 mV, which is consistent with the presence of many anionic phosphonate groups on the surface of the particles. The visualization of the particles after crystallization revealed a thin layer on top of the particles (Figure 38).

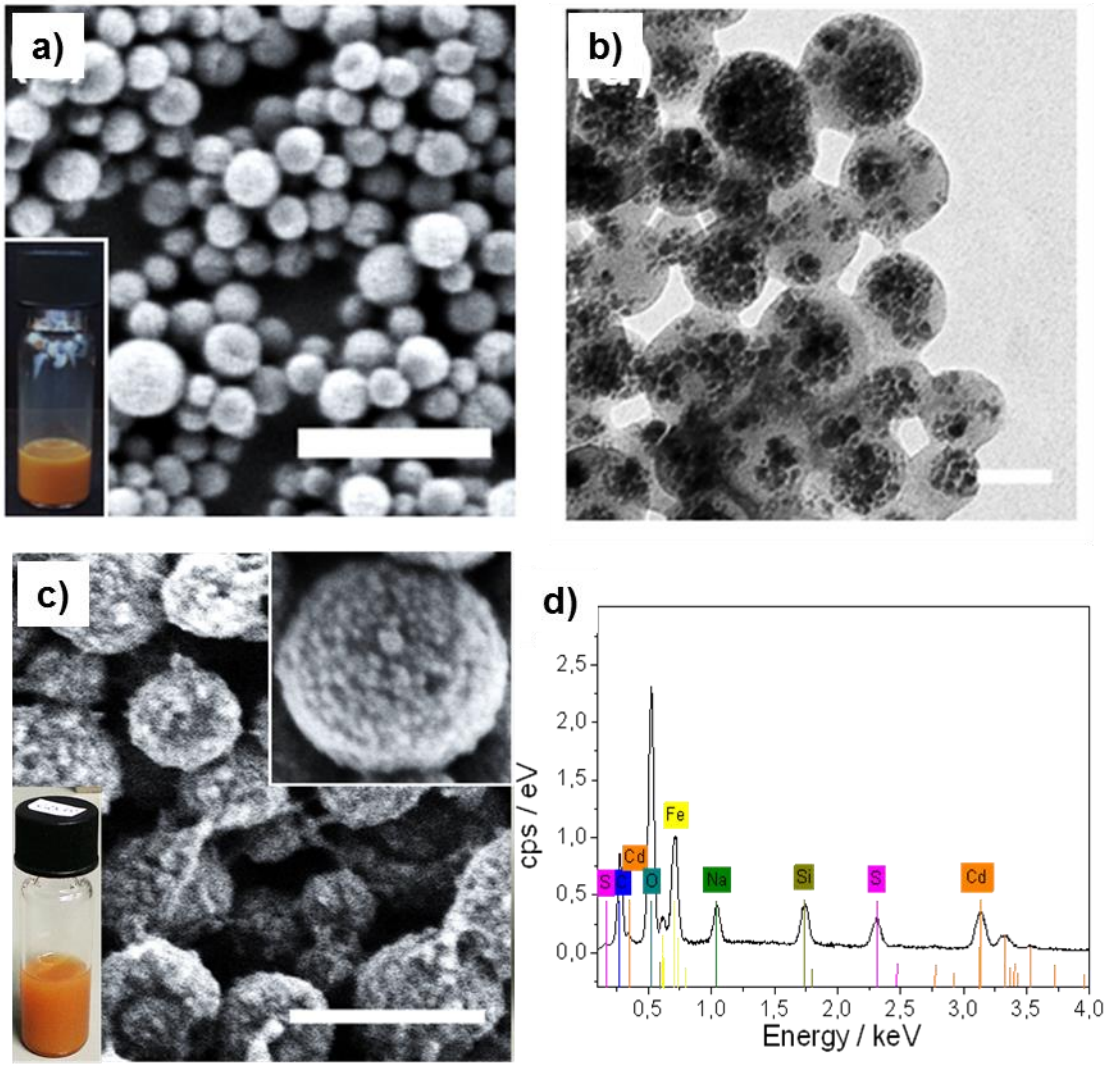

Figure 38. *SEM (a) and TEM (b) images of polystyrene/magnetite nanoparticles before crystallization of CdS onto the surface. c) SEM image after crystallization. d) EDX spectrum of the hybrid particles after surface crystallization. Iron as well as cadmium could be found in substantial amounts. Scale bar 450 nm in SEM image a, 300 nm in SEM image c and 100 nm in TEM image.*[244]

The surface layer was analyzed by energy-dispersive X-ray spectroscopy (EDX). EDX revealed the presence of mainly cadmium and sulfide which is consistent with the presence of a CdS layer. The zeta potential increased after surface crystallization to

values of −20 mV depending on the amount of added cadmium and sulfide, showing a partial coverage of the particles. TGA revealed a cadmium sulfide content of 26 wt%. The XRD patterns of the sample revealed the crystallization of CdS as hexagonal greenockite. The average crystallite size as determined using the Scherrer equation was determined to be ~13 nm. The optical activity of the CdS was investigated by fluorescence spectroscopy (Figure 39). The measurements revealed an emission band with a maximum at 620 nm.

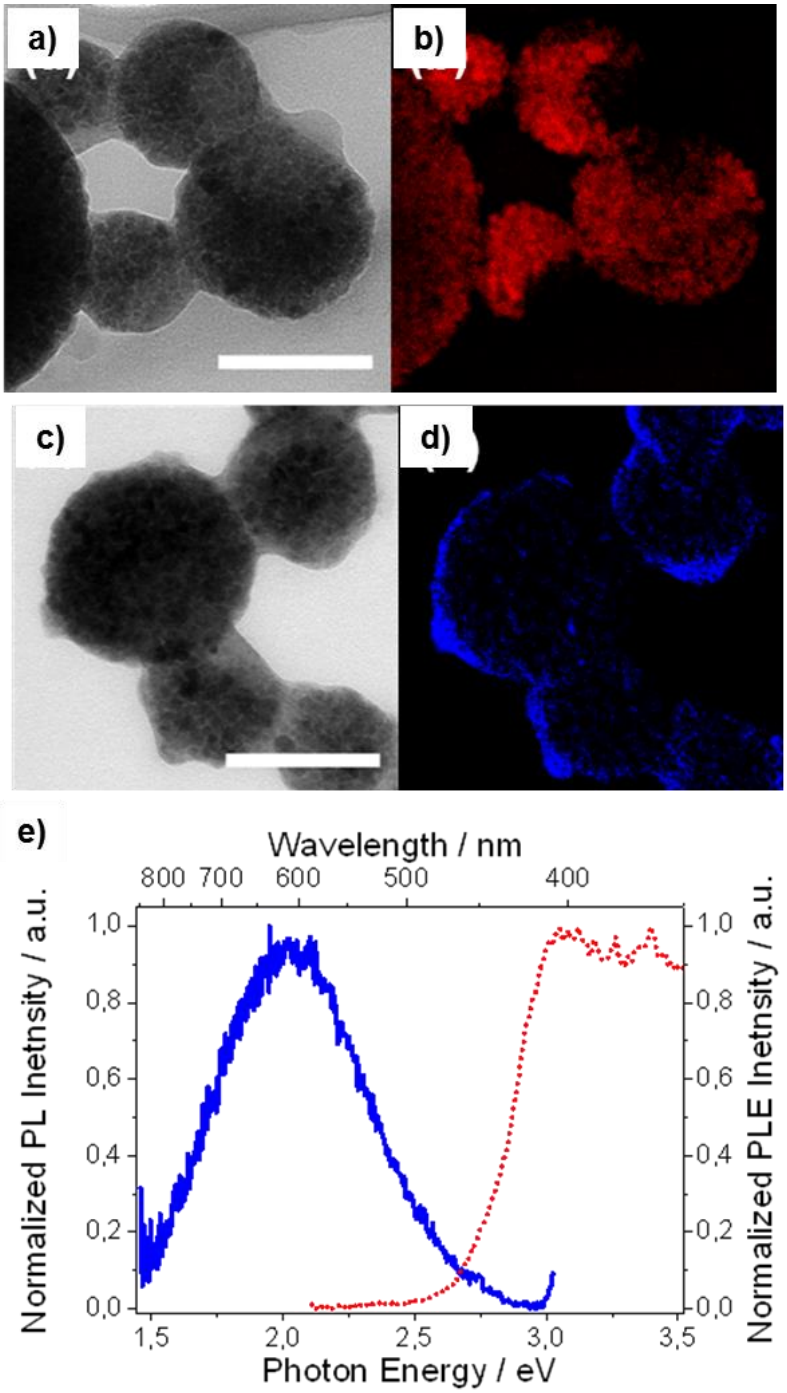

Figure 39. *Iron (b) and cadmium (d) element mapping performed via a transmission electron microscope. The corresponding image sections are shown as Figures a and c. Iron (in red) is revealed mainly within the core of the nanoparticles,*

cadmium (blue) is only present on the particle surface. e) Emission photoluminescence spectrum of the CdS/iron oxide/polymer nanoparticles (blue curve) with a maximum at ~610 nm. The red curve illustrates the excitation spectrum. Scale bar 100 nm.[244]

In summary, the synthesis of spacially defined hybrid nanoparticles could be demonstrated. Encapsulation of iron oxide was achieved by simultaneously implementing a phosphonate surface functionality. The phosphonate groups can then guide the precipitation of CdS onto the surface of the nanoparticles yielding in a dual-functionality consisting of a magnetic and a luminescent response.

4.3 Magnetic Polymer Hybrid Nanoparticles for MRI, as Labels for Cell Tracing and for Magnetic Field Guided Separation of Cell-Compartments

In a variety of collaborations, tailor made magnetic nanoparticles were synthesized for their use in biomedical systems for different purposes. I) Firstly, iron oxide labeled nanoparticles and capsules were used in a comparative way to study their T_2 relaxation time and their potential use as magnetic resonance imaging (MRI) contrast agents. The project was conducted together with Sandro Ebert. II) Secondly, biodegradable superparamagnetic nanoparticles were used as cell labels in order to trace cells *via* MRI. The cell tracing was done by Ina Vernikouskaya in Ulm. The presented results are based on the publication: "*Iron-Loaded PLLA (iPLLA) Nanoparticles as Highly Efficient Intracellular Markers for Visualization of Mesenchymal Stromal Cells by MRI, accepted for publication"*. III) In a third approach, highly superparamagnetic nanoparticles were applied for the magnetic separation of cell compartments to learn more about nanoparticle uptake pathways inside of cells. Investigation of the pathways was done by Daniel Hofmann.

As one of the major application areas in biomedicine, MRI has emerged as a powerful tool for the visualization of tissue owing to its non-invasive feature, its deep penetration into tissue in addition to a high resolution. Since it was first reported as one-dimensional MRI in 1952,[241] it took some years to discover the great potential of MRI, until in the early 70s, when it was shown, that cancer and healthy tissue can be distinguished *via* MRI.[242] Soon after, a two-dimensional image could be obtained and a few year after that, MRI could be used commercially. Even if MRI research has now been going on for decades, the contrast agents used are mainly based on the same materials. As positive contrast agent, mainly gadolinium complexes are used[243] and as negative contrast agent iron oxide nanoparticles. The use of iron oxide based contrast agents is due to their high natural abundance and therefore low cost and their facile synthesis going along with excellent superparamagnetic properties. However, even if the nanoparticles have been used for decades, there is still a lot of room for improvement in terms of surface functionalization of the particles and the understanding of the relationship between magnetic particle and its stabilizing shell with its relaxation time. Therefore, in collaboration with Sandro Ebert and Kerstin Münnemann, we have investigated in more detail the relationship between the structure of magnetic/polymer hybrid nanoparticles and their T_2 relaxation time. Furthermore, in an approach to establish biodegradable nanoparticles as cell tracer through MRI, we have collaborated together with Ina

Vernikouskaya and Hubert Schrezenmeier from Ulm University. Therefore, iron oxide labeled poly-L-lactide (PLLA) nanoparticles were synthesized in order to incubate cells with the nanoparticles. The incubated cells were then traced *in-vivo* by MRI. In a further study, superparamagnetic iron oxide/polystyrene nanoparticles were used to separate cell compartments together with Daniel Hofmann and Volker Mailänder. Therefore, cells were incubated with the magnetic nanoparticles. After cell uptake, the magnetic nanoparticles were removed and the accompanying proteins analyzed via mass spectrometry.

4.3.1 How Morphology Influences Relaxivity - A Comparative Study on Superparamagnetic Iron Oxide/Polymer Hybrid Nanostructures for MRI

Commonly used magnetic nanoparticles for MRI are the so called superparamagnetic iron oxide nanoparticles (SPIONs).[251] The synthesis of the core material, i.e. the superparamagnetic iron oxide with sizes commonly ranging from ~ 8-20 nm in diameter, can be done in high yields and with facile equipment in short time (see experimental section). The more challenging task however, is the functionalization of the small nanoparticles in aqueous dispersion to achieve long term colloidal stability. Many attempts have been made including the use of steric surfactants,[252] charged polymer surfactants,[253] and purely ionic surfactants.[254] However, the type and amount of stabilizer and the incorporation of the iron oxide within the matrix fundamentally changes the imaging capabilities in MRI applications. In order to investigate and understand this influence, different types of nanoparticles and nanocapsules carrying an iron oxide label for MRI were synthesized. We investigated the following model systems: a) Iron oxide nanoparticles of ~ 8 nm in diameter. b) Iron oxide nanoparticles of ~20 nm in diameter. c) Nanocapsules consisting of an iron oxide core (with ~8 nm nanoparticles) and a polyurethane shell. d) Nanocapsules consisting of an iron oxide core (with ~20 nm nanoparticles) and a polyurethane shell. e) Polystyrene nanoparticles with homogeneously distributed iron oxide nanoparticles. f) Iron oxide/poly(L-lactide) Janus nanoparticles. The TEM and SEM images of the hybrid structures are shown in Figure 40. Their hydrodynamic diameters as well as their abbreviations are listed in Table 6. The experimentally obtained relaxivities give rise to the following information: i) How does clustering of single superparamagnetic iron oxide nanoparticles affect the relaxivities? ii) What influence does the incorporation of the iron oxide nanoparticles into a diamagnetic polymer network have on the relaxivity? iii) How are the relaxivities influenced by the morphology of the iron oxide/polymer hybrid structure?

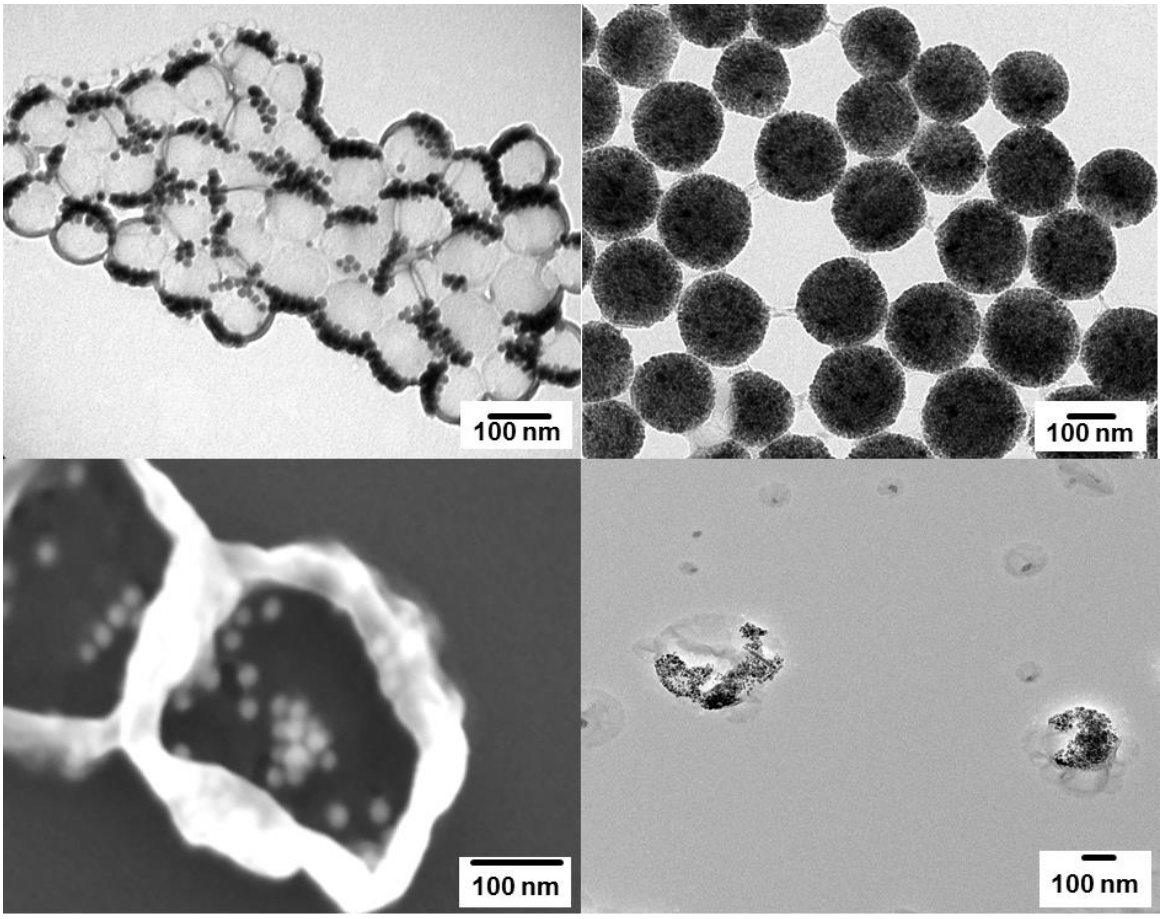

Figure 40. *TEM and SEM images of all the hybrid nanoparticles and nanocapsules.*

Table 6. *Hydrodynamic diameters and abbreviations for the different iron oxide/polymer hybrid nanostructures.*

System	Size [nm]	Synonym
SPION	8	S-8
SPION	20	S-20
PLLA nanoparticles loaded with 8 nm SPIONs	146	NP-146
PS nanoparticles loaded with 8 nm SPIONs	156	NP-156
PU nanocapsules loaded with 20 nm SPIONs	250	NC-250
PU nanocapsule loaded with 8 nm SPIONs	400	NC-400

Sandro Ebert made use of calculations based on the theory for agglomerated systems to predict the relaxivities for the different systems. The experimentally obtained T_2 values could be predicted for all morphologies within reasonable deviation. The results demonstrate that various morphologies can be described in one universal cluster as illustrated in Figure 41.

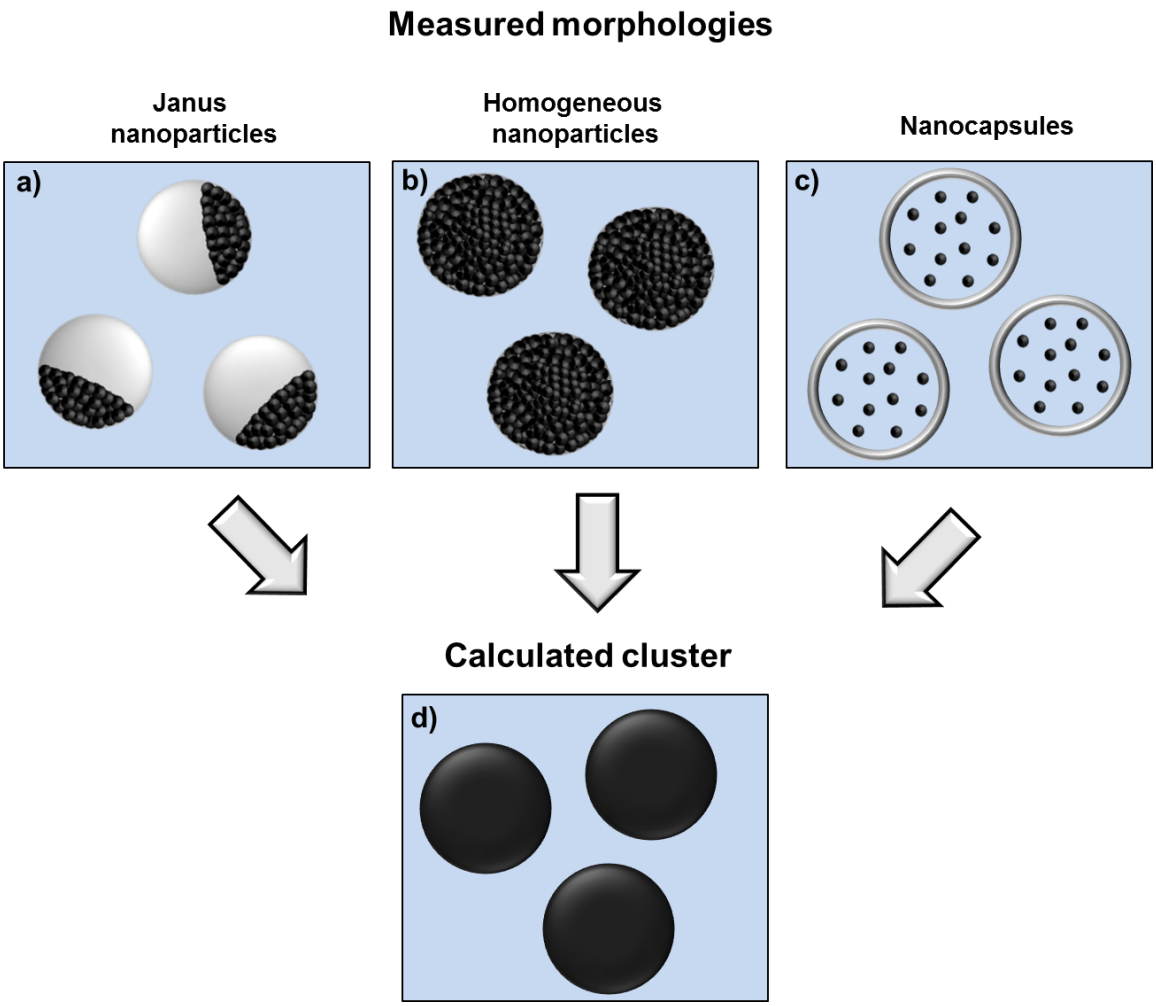

Figure 41. *Sketch of different morphologies of iron oxide/polystyrene hybrids. a) Janus nanoparticles. b) Homogeneous nanoparticles. c) Nanocapsules. All of them can be treated as weakly magnetized spheres with a hydrodynamic diameter determined by DLS.*

Not only were experimentally gained relaxivities compared with computations for agglomerated systems,[255] additionally calculations based on a unified equation found by Monte Carlo (MC) simulations were applied.[256] The experimental results and the results from calculations are listed in Table 7. The calculated values from both theoretical approaches follow the trend of the experimentally obtained results.

Table 7. *Experimentally obtained relaxivities, R-square of the line fit, calculated relaxivities based on the unified cluster approach and from MC simulations.*

System	r_2^{ex} [Hz/(mM·L)]	R^2	r_2^{calc} [Hz/(mM·L)]	r_2^{MC} [Hz/(mM·L)]
S-8	105 ± 8	0.97	89	55
S-20	167 ± 18	0.95	181	140
NP-146	216 ± 12	0.99	84	68
NP-156	165 ± 5	0.99	230	235
NC-250	43 ± 7	0.88	4	30
NC-400	114 ± 4	0.98	30	60

In summary, the relaxivities of different iron oxide/polymer hybrid nanoparticles and capsules with variable morphologies could be predicted by applying known theories with a semi-empirical approach and *ab initio* calculations.

4.3.2 SPIONS in Biodegradable Poly(L-Lactide) Nanoparticles with high Relaxivity for Cell Trafficking Visualized by MRI

For high resolution in *in-vivo* MRI imaging, the contrast agent has to be carefully chosen to fulfill major criteria such as biocompatibility and high relaxivity values.[257] One of the main uses of contrast agents, besides their clinical use to image tissue, is to improve the detection of diseases[258] or to label and trace cells,[259] especially stem cells.[63] It is of high interest to learn more about stem cell trafficking and to understand their pathways and in the end to know how to potentially pilot them.

We synthesized biocompatible poly(L-lactide) nanoparticles with incorporated oleate-capped iron oxide nanoparticles as labels for MR imaging. The particles were synthesized by applying the solvent-evaporation technique on miniemulsion droplets.[260] The hydrodynamic diameter of the PLLA particles that were used for the study was measured to be in the range of 133-148 nm as determined *via* DLS. Zeta potential measurements revealed a negative surface potential between -52 and -57 mV. Imaging of the iron oxide nanoparticles and the PLLA particles with encapsulated iron oxide was achieved *via* TEM (Figure 42). Cell toxicity experiments revealed no influence of the particles up to 300 $\mu g \cdot mL^{-1}$ on the cell viability of HeLa cells after 20 h of incubation.

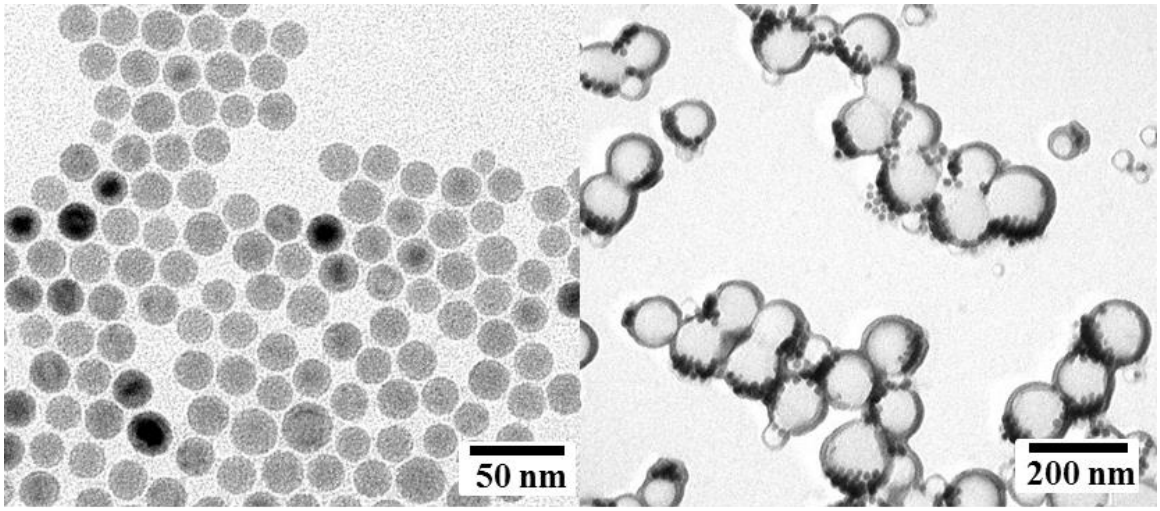

Figure 42. *TEM images of oleate capped iron oxide nanoparticles (left) and PLLA nanoparticles with incorporated iron oxide (right).*

PLLA nanoparticles of the obtained size and surface charge show rapid[261] and high[262] cell uptake.

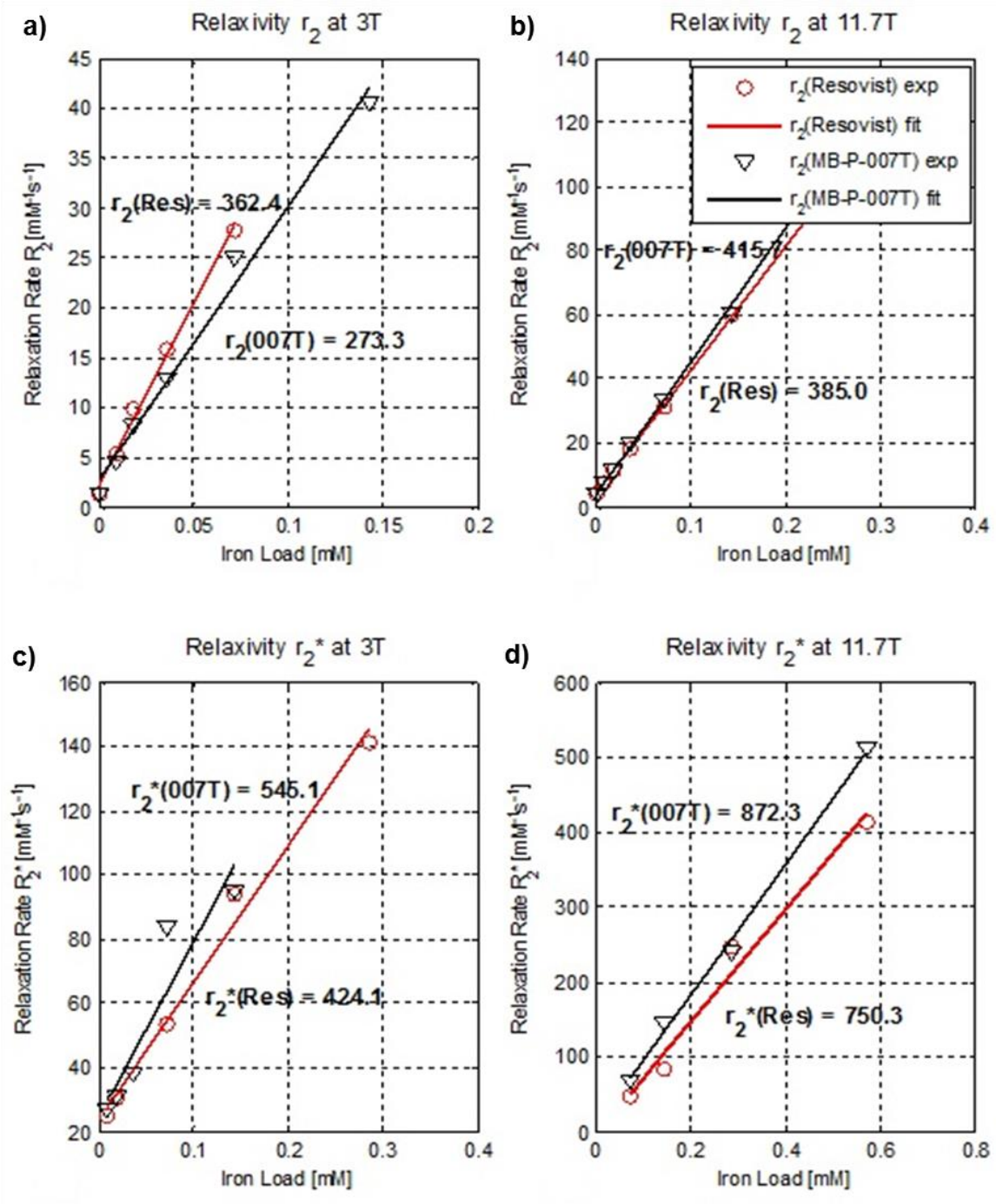

Figure 43. *r_2 and r_2^* relaxivity curves for Resovist® and iron oxide/PLLA nanoparticles measured at field strengths of 3T (a, c) and 11.7T (b, d).*

Further studies were done in collaboration with Ina Vernikouskaya and Natalie Fekete from the Institute for Clinical Transfusion Medicine and Immunogenetics in Ulm. Firstly, the use of the nanoparticles as imaging labels for stem cells was investigated. Besides their biocompatibility and good cell uptake, an additional property is needed: The relaxivity value in MRI has to be as high as possible to increase the contrast. In order to determine their relaxivity, an *in-vitro* relaxation rate mapping was conducted yielding

high values of r_2 = 273 $mM^{-1}s^{-1}$ at 3 T and r_2 = 416 $mM^{-1}s^{-1}$ at 11.7 T as shown in Figure 43.

In-vivo experiments in a rat model demonstrated the potential use of the particles as highly sensitive labels in stem cells for MRI. Only ~30,000 labeled cells were needed to trace them efficiently within the body of the rat. The movement of the MRI labeled cells could then be investigated on MRI cuts.

Further experiments using the iron oxide/PLLA nanoparticles were performed with the aim to trace stem cells *in-vivo* and follow their motion within a rat injury model. Stem cells labeled with the nanoparticles were injected approximately 1 cm away from the injury which was inflicted on the rats back. The motion of the stem cells and their potential targeting of the wounded tissue, with the ability to help healing the injury, was followed *via* MRI. It could be shown that the cells preferably get transported towards the wounded tissue and could support the healing process. To confirm these observations, the nanoparticles were further labeled with elemental tags (*e.g.* Pt), and fluorescent and IR dyes. However, the element tags that were inserted into the PLLA nanoparticles as platinum complexes (*e.g.* $Pt(acac)_2$) showed leakage from the polymer particles and could not be detected by ICP-OES in sufficient quantities. The dye signal was also found to be too weak to use it for quantitative *in-vivo* studies. Further efforts will focus on finding a more feasible element tag or on the improvement of the elemental analysis. The analysis was up to now performed using inductively coupled plasma optical emission spectroscopy (ICP-OES) but could also be done with inductively coupled plasma mass spectroscopy (ICP-MS) which can have a higher sensitivity by many orders of magnitude.

4.3.3 Magnetic Nanoparticles for Unraveling the Nanoparticle Endocytosis Trafficking

Nanoparticles uptake into cells has been intensively studied over the last decades. The uptake behavior of nanoparticles into cells is depending on the surface charge, surface roughness, size and shape of the nanoparticles.[238, 263] However, the pathways and fate of the nanoparticles within the cell is not so well understood, but of eminent importance for the understanding and improvement of drug delivery vehicles.[264] A major issue with studies on the intracellular nanoparticle trafficking (INT) performed so far is related to a disturbance of the cellular machinery during the visualization of the trafficking.[239, 265] Therefore, establishing a method to study INT non-invasively is of high importance. Such a non-invasive method is possible by using of a magnetic field. The magnetic field, when it is applied with reasonable strength, has no effect on the cellular trafficking, since the interaction between the applied magnetic field and the

mostly diamagnetic cell composition (except for very little ferromagnetic ions like *e.g.* iron) is negligible. To provide such a non-invasive method, fluorescently labeled superparamagnetic magnetite/polystyrene nanoparticles were designed and applied for a magnetic separation of endosomes containing the magnetic nanoparticles after their cell uptake. The synthesis was performed as described in the experimental section.

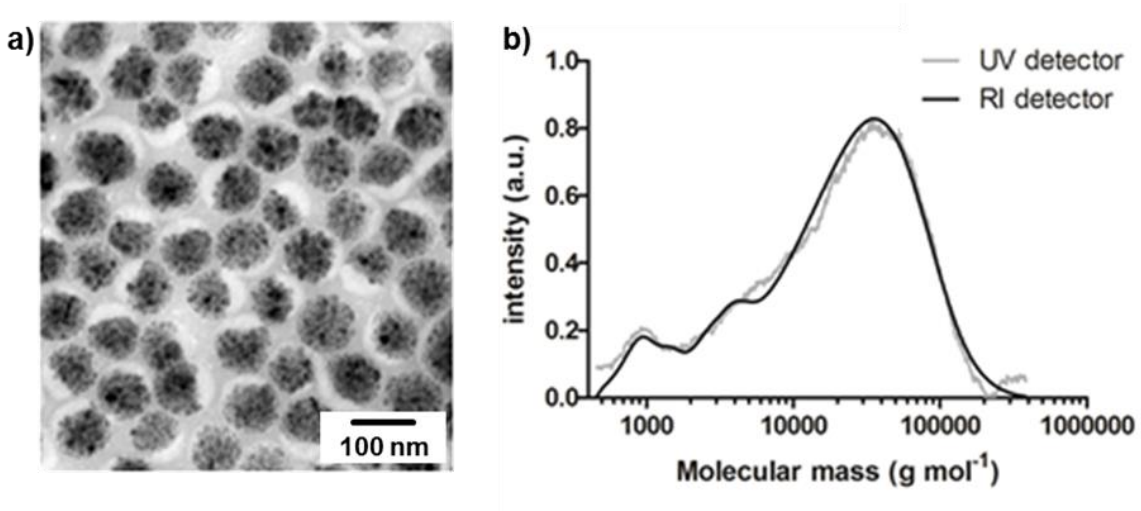

Figure 44. *a) TEM image of fluorescently labeled magnetite/polystyrene nanoparticles. b) GPC trace of the fluorescently labeled polystyrene. The refractive index and fluorescence signal detectors were used to prove the successful coupling of the fluorescent dye label.*

As dye label, the fluorescent dye BODIPY (B523-MA) was introduced. The synthesis of the dye was done by Andrey Turshatov using a procedure described elsewhere.[266] In order to prevent leakage of the dye from the nanoparticles into lipophilic vesicles, which has been a problem in previous studies, the dye was covalently linked to the polystyrene of the particles. The implemented BODIPY dye has a double bond, which is suitable for radical polymerization and therefore the dye gets copolymerized together with the styrene. The fluorescence properties of the dye do not get influenced by the polymerization. Covalent linkage of the dye was proven by GPC measurements, which show the same curves for both detectors, the reflective index (RI) detector and the fluorescent signal detector (Figure 44b).

Making use of miniemulsion polymerization, we obtained polystyrene nanoparticles with incorporated iron oxide as visualized by TEM imaging (Figure 44a). The iron oxide loading was determined to be 61 wt% according to TGA measurements (Table 8). The magnetization of the magnetite/polymer nanoparticles with fluorescent label was determined by VSM measurements to be 45 emu·g^{-1}. The high magnetization value of the hybrid nanoparticles is essential for their magnetic purification capabilities. The

nanoparticles display a hydrodynamic diameter of 126 ± 26 nm as determined from DLS measurements and a zeta potential value of -44 ± 12 mV. The negative surface charge as well as the small diameter of the particles is very suitable for cell uptake as previously studied.[267]

Table 8. *Characteristics of the fluorescently labeled magnetite/polystyrene nanoparticles.*

Information	Unit	Value
Diameter[a]	[nm]	126 ± 26
Zeta potential	[mV]	-44 ± 12
Magnetite content	[wt%]	61
Magnetization	[emu·g^{-1}]	45
Molecular weight M_w	[g·mol^{-1}]	44,000

a: Hydrodynamic diameter given as intensity average and standard deviation, determined by DLS.

In order to follow the INT pathways, HeLa cells were incubated with the hybrid nanoparticles for 20 h and the cell uptake was investigated via fluorescence activated cell sorting (FACS) measurements and confocal laser scanning microscopy (cLSM) imaging as done by Daniel Hofmann. With both methods, a high nanoparticle uptake could be observed. After the incubation for 20 h, the HeLa cells were disrupted, thereby releasing the intracellular vesicles. Superparamagnetic hybrid nanoparticles containing vesicles were then separated from other non-magnetic field responsive cell compartments by application of a static magnetic field and forwarded to peptide mass spectrometry analysis at the University Medical Center Mainz. From the peptides detected, conclusions could be drawn to further understand, in which compartments the hybrid nanoparticles had been present after endocytosis.

The demonstrated method holds great potential in understanding the INT pathways using a simple and non-invasive technique. Further experiments are currently carried out to use the method not only *in-vitro*, but also *in-vivo*.

4.4 Highly Magnetic Capsules for Biomedical and Self-Healing Applications

Capsules are ideal candidates for an efficient encapsulation and release of active compounds. Making use of the miniemulsion approach, a large amount of capsules in a facile preparation procedure is possible.[268] In the present chapter, miniemulsion in combination with emulsion polymerization is used in order to obtain highly iron oxide loaded capsules with a hydrophobic core. The capsules possess a high potential for their application as self-healing materials.[269-271] Encapsulation of self-healing agents into capsules and their controlled release upon a stimulus such as a mechanical disruption owing to a scratch in the coating holds great promises to reduce corrosion and the costs coming along. However, one major drawback, when integrating the capsules into the coating matrix, is their distribution within the matrix. Often inorganic coatings are used. Commonly, such coatings are produced in an electrochemical deposition process to which the capsules are not easily applicable to. Introduction of a strong magnetic field responsive moiety into the capsules would enable a parallel deposition together with the inorganic compound simply induced by application of a static magnetic field.

The synthesis of the magnetic nanocapsules is depicted in Figure 45 and described in detail in the experimental section (chapter 5.4). The basic elements of the synthesis are a mixture of miniemulsion droplets of iron oxide containing *n*-octane, which act as seeds and styrene droplets, which act as styrene reservoirs for an emulsion polymerization. Importantly, the octane content is high and the surfactant concentration low. Thus, the miniemulsion droplets are large. During the formation of polystyrene in the droplets, a phase separation takes place which leads to the formation of core-shell structures.[272] The hydrophobic octane forms a liquid core and the styrene a solid shell – hence, capsular structures are obtained.

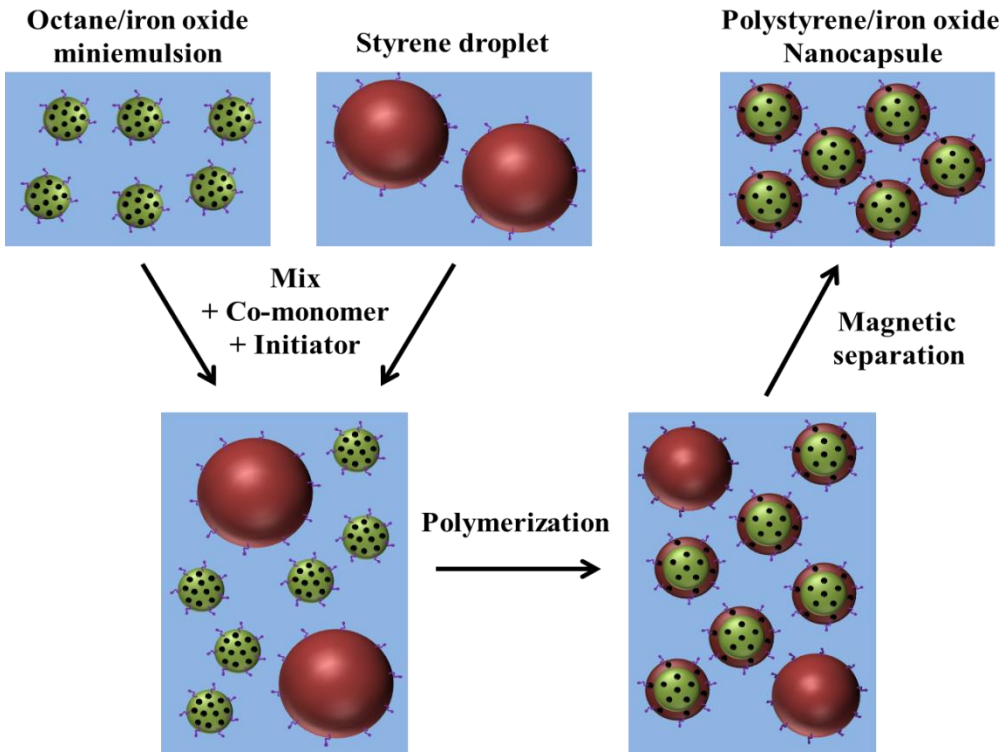

Figure 45 . *Schematic illustration of the synthetic procedure for the preparation of magnetic polystyrene nanoparticles.*

The formation of the polystyrene shell was investigated over time via TEM (Figure 46). After very short reaction times of 10 min, the capsular structures are hardly seen and loose magnetite is spread all over the TEM substrate. Already after half an hour, the capsules morphology can be visualized. However, they are still permeable for iron oxide nanoparticles, which leaks out. After 60 min, the capsules show no considerable leakage of iron oxide any more. Still, the shell is quite thin. As the reaction continues, after around 4 h, solid capsules with a thick shell can be observed. For longer reaction times, the capsules tend to form a more particle-like morphology owing to the ongoing evaporation of the liquid core of octane. It has to be mentioned that for all performed capsule formation, an additional fraction of small particles was obtained. However, the capsules can be separated with size selective methods, preferably centrifugation. DLS analysis revealed a hydrodynamic diameter of 370 ± 107 nm.

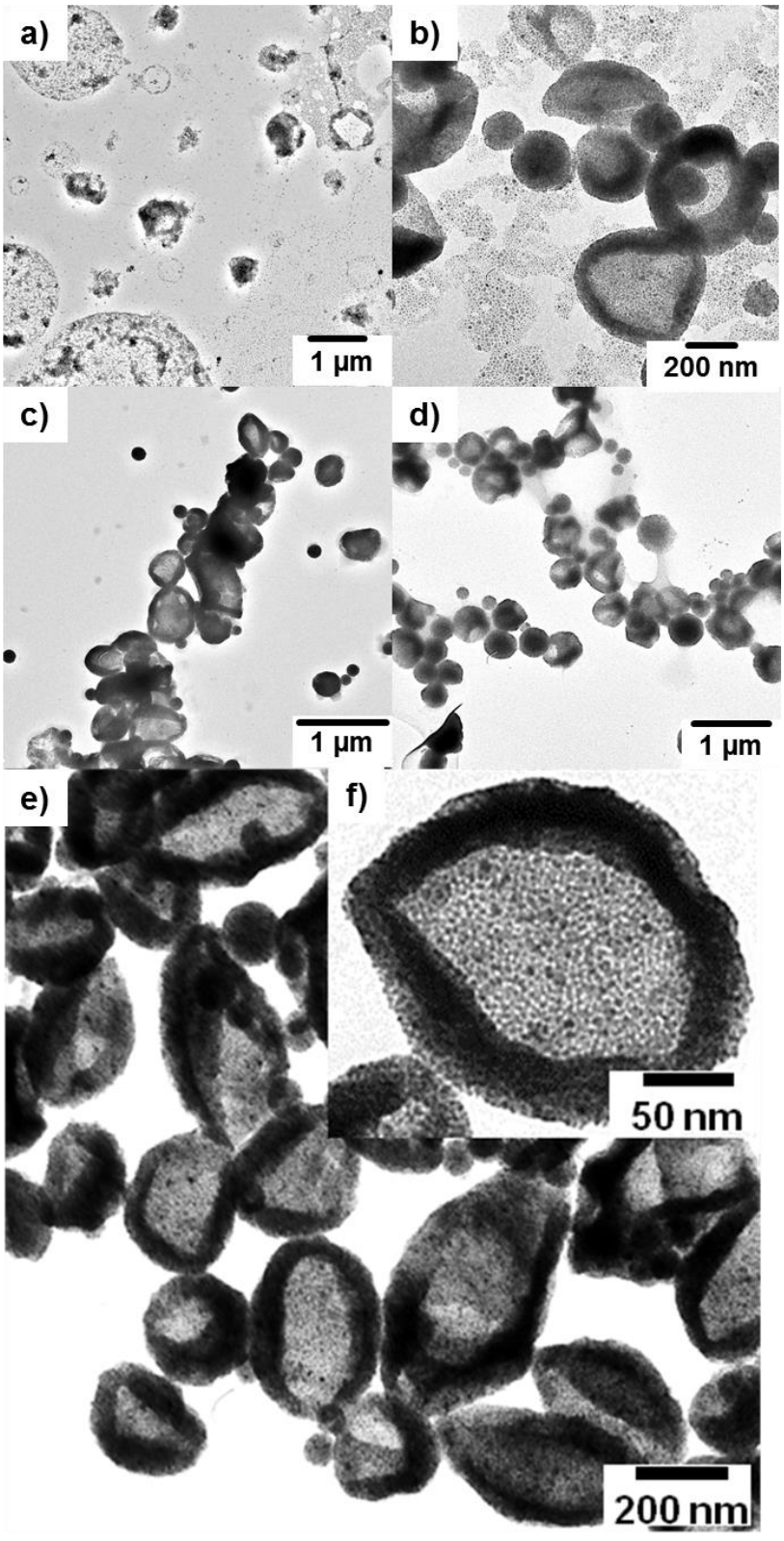

Figure 46. *Kinetic study of the formation of iron oxide/polystyrene hybrid nanocapsules. Samples were taken after certain reaction times, drop-casted on a copper grid and imaged via TEM. a) After 10 min reaction time the capsule structure can hardly be found and iron oxide is distributed all over the TEM grid. b) After 30 min weak walls have already formed, but magnetite is still leaking out. c) After 60 min the capsules wall has been growing and the interior doesn't leak out any more. d) After 120 min, all of the capsules are surrounded by a thin layer of polystyrene. Additionally, the formation of nanoparticles consisting of polystyrene and iron oxide is observed. e) After 240 min, stable capsules are obtained. f) Inset of capsules after 240 min.*

The synthesized highly magnetic capsules were then introduced into a coating in order to demonstrate the possibility to magnetically tailor their integration into the coating. Therefore, we show that for the use of an organic polymer based coating, the

destiny and density of the self-healing agent containing capsules can be magnetically controlled as done together with collaboration partners from Delft University. Figure 47 depicts two cases for the formation process of the coating. On the left side (a), when no magnetic field or only a weak field is applied, the polymer coating shows homogeneous distribution of the magnetic nanocapsules within the matrix. Under application of a strong external magnetic field (b), the nanocapsules can be forced to the destination of desire, in the described case, the bottom of the coating (the images are 180° inversed).

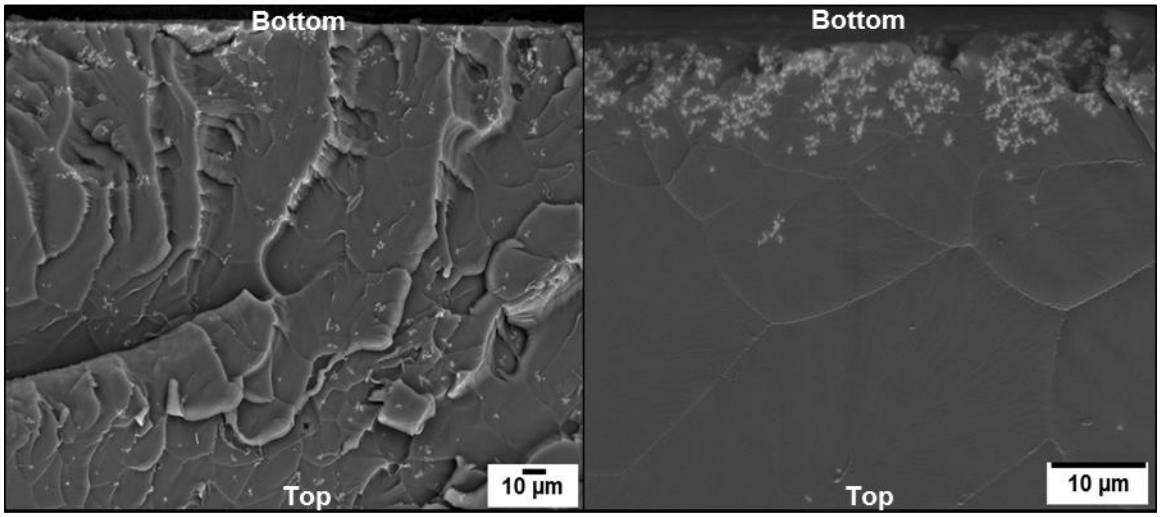

Figure 47. *SEM images which are 180° inversed. a) Polymer coating with magnetic nanocapsules distributed well among the matrix with little accumulation of the magnetic capsules at the bottom after application of an external magnetic field for 30 min. b) The application of an external magnetic field for 60 min yields a coating with magnetic nanocapsules present only in the top layer of the matrix.*

In conclusion, highly magnetic capsules could be produced *via* a simple process. The synthesized capsules possess potential applications whenever the encapsulation of hydrophobic compounds is needed (*e.g.* for drug delivery or self-healing materials). The ability of the magnetic compound to guide the capsule to a desired location was demonstrated by embedding the capsules in a polymer coating and directing it to the bottom of the coating by the application of a magnetic force.

4.5 Anisotropic Wetting on Magnetically Patterned Substrates

The following work has been conducted together with the RISE DAAD student Samuel Kazer from Columbia University, New York. Surface fluorinated polymer nanoparticles with encapsulated superparamagnetic iron oxide nanoparticles were synthesized in several steps including heterophase polymerization, silica coating, EDC coupling, and ATRP polymerization. The synthesized multifunctional nanoparticles were then deposited onto a substrate under external magnetic field application in order to obtain ribbon-like nanoparticle arrays which can be used for the anisotropic wetting of aqueous droplets when depositing them onto the modified substrate.

4.5.1 Motivation and Preparative Strategy

It is of fundamental interest to arrange nanostructures in a well-defined fashion to obtain macroscopically visible and applicable effects. Such an arrangement is especially of interest when manipulating surfaces in order to obtain optical[273-274] or liquid repellent properties.[275-276] Here, the deposition of ultrahydrophobic and magnetic hybrid nanoparticles onto a substrate is described with the purpose to form ribbon-like surface structures. Drying of the nanoparticles dispersion under application of an external magnetic field leads to alignment of the superparamagnetic hybrid nanoparticles and therefore ordered arrays on the substrates surface. The magnetically patterned surface can then be used to anisotropically deform aqueous droplets deposited on the substrate due to interaction with the ordered surface.[277-278] Depending on the time of wetting, different aspect ratios are obtained for the wetting droplets. As recent work on polymers and polymer coatings has turned to functional and useful surface design, various methods have been developed to better coat and functionalize surfaces. Of particular interest is the development and application of fluorinated polymers, given their impressive insolubility in most aqueous and organic solvents and related barrier properties.[279-280] The natural insolubility has led to extensive research developing fluorinated surfaces with ultra-hydrophobic properties as coatings for many materials.[281] Ultra-hydrophobic materials are those that, when wetted with water droplets, cause the droplets to exhibit a contact angle of 150º or larger with the surface (and a hysteresis < 5°), leaving the spherical nature of the droplet mostly intact.[276, 282] Recently, nanoparticles have been used as a functional intermediate to grow fluorinated polymers.[283] Controlled radical polymerizations such as atom transfer radical polymerization (ATRP) of fluorinated monomers[284] have been performed on functionalized nanoparticles. Then, the particles

have been attached to surfaces in various ways as a new method to create ultra-hydrophobic surfaces.[283]

Magnetic surface patterning has been very popular recently, gaining widespread attention as a method to assemble or assist the self-assembly of nano- and microparticles in various mediums and on surfaces.[4] Assisting in the creation of 1D and 2D nanostructures, superparamagnetic materials have vastly improved the architectural capabilities of nanoparticles under magnetic field application. A very common procedure incorporating superparamagnetic nanoparticles involves arranging them on a surface while drying in the presence magnetic fields.[285] After magnetic arrangement the nanoparticles and surface exhibit new properties on the nanoscale. However, what makes the structures so interesting are the effects that they demonstrate from a macroscopic view; net effects on the nano- and micro- scale can be seen on the deci- and centi- scale.

Here, by a combination of architectural control of superparamagnetic nanoparticles and the ultra-hydrophobicity of fluorinated polymers, an anisotropic, magnetic wetting surface has been developed. Therefore, an ultra-hydrophobic coating was created that enables access to non-symmetric wetting effects when adding an aqueous droplet due to its magnetically patterned surface. A multistep synthetic approach was chosen to obtain nanoparticles exhibiting superparamagnetic properties in combination with an ultra-hydrophobic, fluorinated surface (Figure 48). Firstly, superparamagnetic oleate-capped iron oxide nanoparticles were synthesized and implemented in a heterophase polymerization to result in iron oxide/polymer hybrid nanoparticles. Secondly, a PVP coating stabilizes the particles sterically and the addition of TEOS leads to the formation of a silica shell surrounding the polymer particles by a polycondensation reaction. The reaction is well known and many different combinations of silica/iron oxide/polystyrene have already been reported.[286] Additionally, a reaction of APS with the surface of the nanocolloids yielded in amino-functionalization. A coupling reaction promoted by EDC between the amino groups and an ATRP initiator enabled the surface polymerization of pentafluorostyrene on top of the colloids that resulted in an ultra-hydrophobic coating. Deposition of the multifunctional nanomaterials on a substrate under the influence of an external magnetic field induces a linear self-assembly and ribbon formation. When depositing an aqueous droplet on the substrate, anisotropic wetting becomes possible.

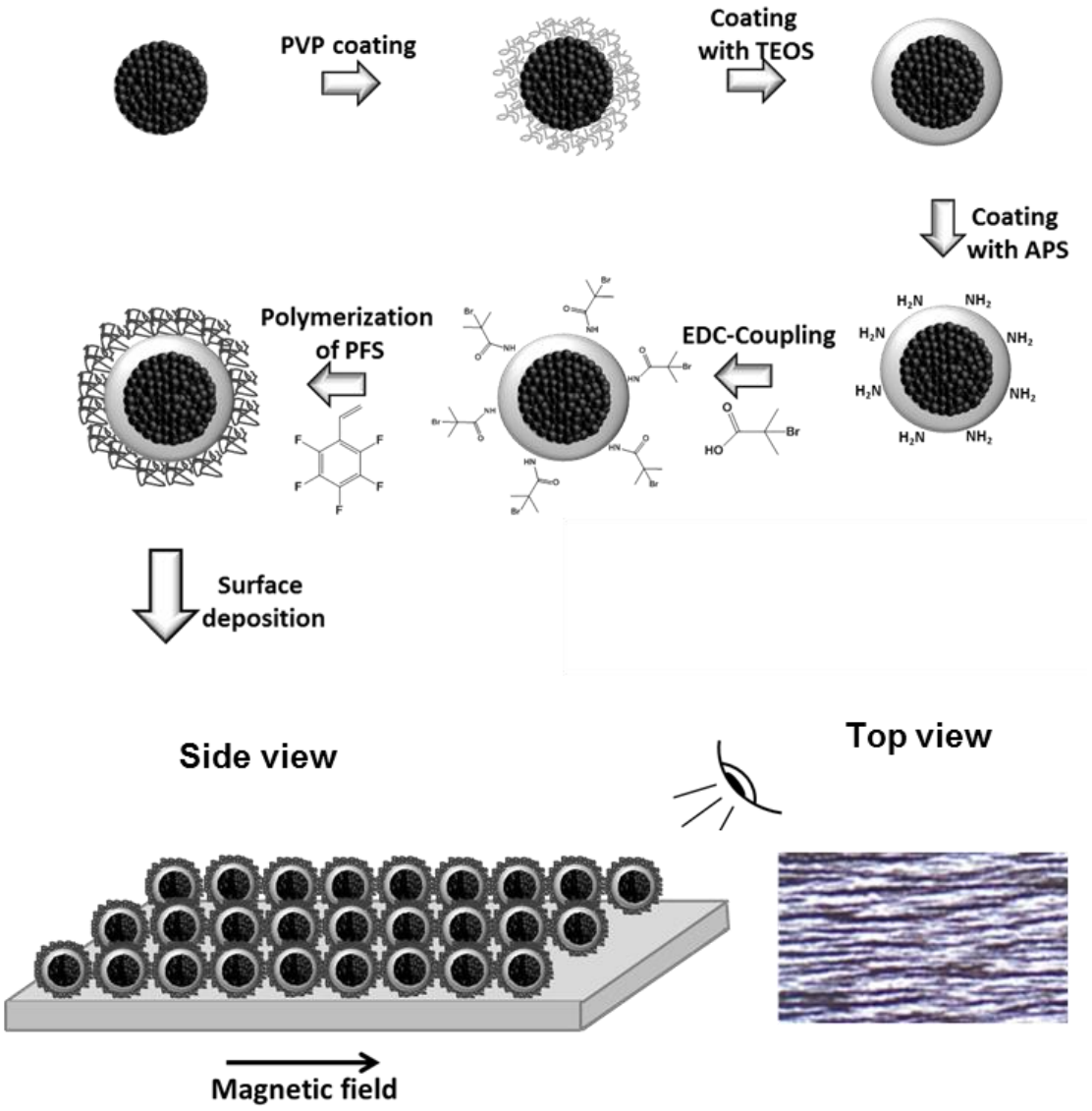

Figure 48. *Schematic illustration of the preparation of superparamagnetic iron oxide/polymer/silica nanoparticles with pentafluorostyrene surface functionality. Deposition of the particles onto a substrate under application of an external magnetic field causes linear assembly of the particles and therewith linear micrometer stripes of ultrahydrophobic coating.*

4.5.2 The Multifunctional Particles

The synthesis of oleate-capped iron oxide nanoparticles and their incorporation into a polystyrene matrix has already been intensively described in other chapters and is given with all details in the experimental section. The implemented iron oxide/polystyrene nanoparticles were characterized to have a hydrodynamic diameter of 177 ± 54 nm as measured by DLS and an iron oxide content of 80 wt% as determined from

thermogravimetric analysis (TGA). The successful coating and surface polymerization of PFS on the iron oxide/polystyrene nanoparticles was followed by several intermediate experiments to prove the success of each step of the procedure. TEM images of the particles after TEOS coating confirm the successful synthesis of silica shells around the particles and the absence of formation of silica-only nanoparticles after magnetic washing (Figure 49). Additionally TGA measurements confirmed the coating with silica since a significant increase in inorganic compounds could be detected. APS coating was confirmed by zeta potential measurements. After silica coating, the zeta potential value was detected to be -52 mV. When adding APS, the value increased significantly to -11 mV due to the presence of positively charged amino groups on the surface of the nanoparticles. The zeta potential measurements were performed at neutral pH. To indicate the presence of the fluorinated polymer on the surface of the particles, TGA was performed. The amount of fluorinated polymer present on the particles can thereby be calculated to be 2-3 wt%. A simple qualitative test was also performed to test the successful polymerization of the fluorinated monomer on the surface of the particles: 10 μL of the particle suspension in TFT was added to 1.0 mL of de-ionized water. After mixture in water and subsequent washing, the particles would not form a suspension in water after stirring, mixing and sonication, remaining as visible aggregates. The failure of the particles to re-suspend in water indicates a coating of fluorinated polymer around the particles.

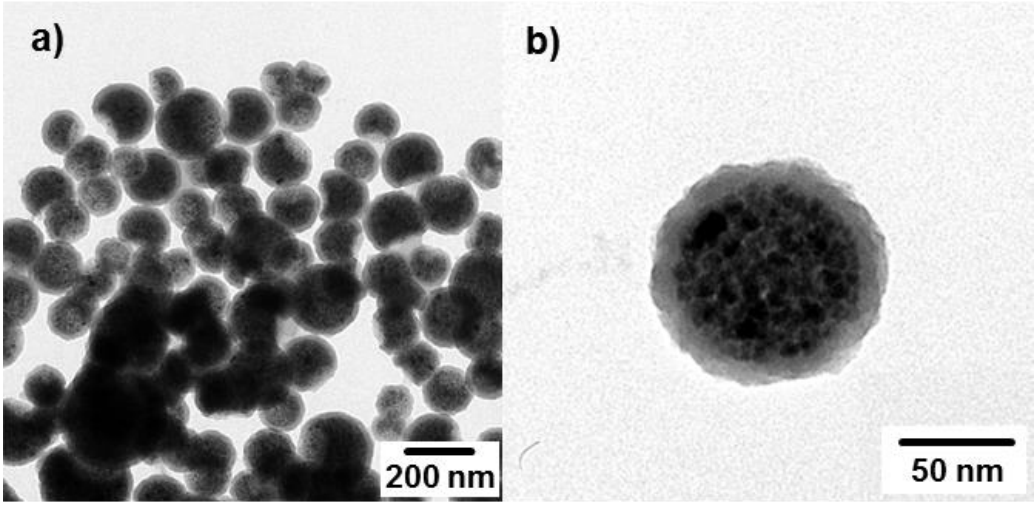

Figure 49. *a) TEM image of many individual silica coated particles. b) TEM image of a single polystyrene/magnetite particle coated with silica and reacted with APS.*

4.5.3 Magnetic Surface Patterning

A precise description of the deposition of water onto the patterned substrate is given in chapter 5.5.5. Initial testing of the magnetically aligned anisotropic surfaces was conducted using light microscopy in order to visually confirm the anisotropic nature of water droplets on the surface. Figure 50 shows the successful anisotropic nature of the surfaces, revealing deformed, but elongated water droplets on the aligned nanoparticles. It seems that the chains/lines formed by the fluorinated nanoparticles create ultra-hydrophobic barriers which the water droplet has difficulty to overcome. Thus, the water droplet spreads parallel to the ribbons of fluorinated nanoparticles. The spreading of the droplet occurs relatively slowly, over a period of minutes, allowing a viewer to watch the faster growth along the lines of ultra-hydrophobic particles and slower growth across them.

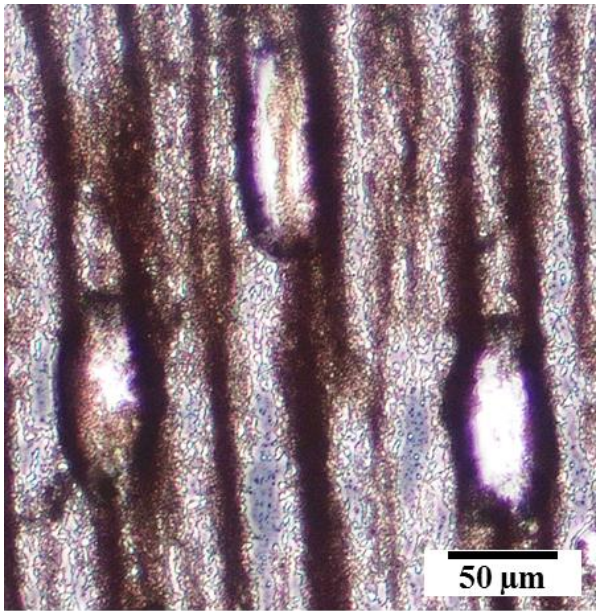

Figure 50. *Light microscopic image of micrometer sized water droplets growing in the direction of the pattered stripes of ultra-hydrophobic particles and thus elongating along the patterned axis. In the image, the aspect ratio of the droplets is 2.6:1 along the patterned stripes.*

In conclusion, an anisotropic, magnetically patterned surface was successfully created solely by means of nanoparticle chemistry starting with superparamagnetic hybrid nanoparticles. The end product has exhibited promising results as an ultra-hydrophobic surface and as an anisotropic surface. Water droplets applied to the surface exhibit large contact angles parallel to the patterned fluorinated nanoparticle chains while slowly spreading perpendicular to the chains. Over time, the droplets become anisotropic,

exhibiting an ellipsoid shape with their major axis along the deposited nanoparticle chains.

Further experiments were conducted in order to not only guide an aqueous droplet into a non-spherical shape, but as well deform cells in a desired direction. Therefore, a dispersion of cells was injected into a paint gun and sprayed onto a modified substrate. Investigations of the cells on the substrate revealed that the cells had been disrupted during the spraying process. However, in future experiments it might still be possible to guide cells within a water droplet into a desired direction using a milder deposition method.

4.6 From Particles to Fibers - Well-defined Nanofibers with Tunable Morphology from Spherical Colloidal Building Blocks

The present chapter describes the work related to the creation of nanofibers with tunable morphology form spherical colloidal building blocks. Parts of the presented results in this chapter have been published as "*Well-defined Nanofibers with Tunable Morphology from Spherical Colloidal Building Blocks"*.[133] To get access to spherical nanomaterials is far easier then to achieve a one dimensionality (see chapter 2.4.3). However, stable linear nanoarrangements with defined periodicity are attractive for many fields of application ranging from energy conversion[287-288] and storage[289-290] over life science[291-292] to surface patterning,[293-294] and coatings[295] and are therefore of high interest. The linear structure can provide for instance a directed transport of electrons or heat[296] or can provide interesting mechanical properties.[297] Further modification through introduction of a magnetic iron oxide moiety into linear nanostructures enables their use for hyperthermia treatment,[132] high performance lithium storage[298] or catalysis of oxygen reduction reaction.[299] Desired properties often include a nanometric scale, versatile labeling and functionalization, a high stability, and magnetic loading with homogeneous distribution. In order to fulfill the criteria, organic-inorganic hybrid nanofibers are needed. Common approaches used nowadays for the production of linear nanostructures include electrospinning,[300-301] magnetic-field assisted electrospinning,[10c-d] self-assembly,[135-139, 302] or template-assisted methods.[303-304] However, the approaches suffer drawbacks when it comes to achieving combinations of the aforementioned desired properties. In contrast, the synthesis of spherical hybrid nanoparticles with multifunctionality is comparably easy and has been shown in many different ways.[16] A plethora of polymer particles can be implemented for a two dimensional film formation process by sintering the particles together. Recently, one dimensional (1D) as well as 2D arrangements of microparticles were fabricated by making use of thermal annealing.[151] With the help of an elaborate templating matrix, more complex arrangements such as rings are possible.[305] However, with the use of a templating matrix only small amounts can be produced. A template-free fabrication of polymer hybrid nanofibers in solution with defined architecture is therefore highly desirable.

4.6.1 Description of the Process for Fiber Formation

Here, a method for the facile and versatile linear fusion of magnetic polymer nanoparticles in an aqueous dispersion by a directed sintering of linear self-assembled

magnetic nanoparticles is demonstrated. The strategy hence allows for the fabrication of hybrid polymer/inorganic nanofibers with tunable corrugation. The linear arrangement and the alignment of the particles are realized by their assembly upon an external magnetic field and a moderate flow of water. The environmental temperature is controlled to favor polymer chain diffusion so that the neighboring particles in contact with each other can fuse together.

The axial fusion of magnetic polymer colloids into nanofibers can be realized with a simple setup (see Figure 51 and chapter 5.6.1.1.4). The setup includes a thermostat and a pump for controlling the temperature and the flow speed, respectively. The functional particles are injected and carried to a permanent ring magnet (field strength 25–200 mT). The external magnetic field induces a magnetic dipole in each superparamagnetic nanoparticle. Due to attractive dipole-dipole interaction, the particles assemble in linear fashion.[306-309] A particles fusion is achieved when the surrounding temperature of the aqueous environment is above the glass transition temperature (T_g) of the polymer. The formed fibers can be collected by increasing the flow speed and thereby displacing them away from the magnet. The benefits of the process comprise a fast fabrication of nanofibers (fusion within milliseconds to seconds time range), simple equipment, and the fact that the surrounding medium used to process the particles is water.

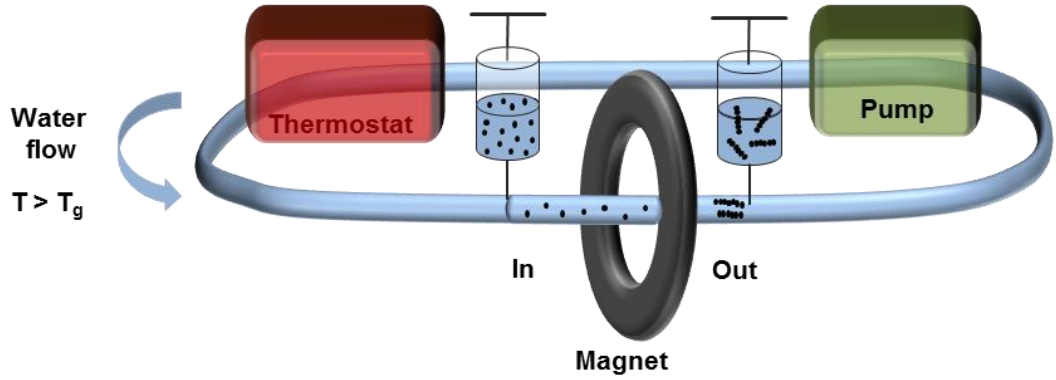

Figure 51. *Experimental flow setup for the fabrication of nanofibers through magnetic field induced self-assembly and linear fusion of magnetic polymer nanoparticles in aqueous dispersion.*

Alternatively to this process, instead of pumping the aqueous dispersion, the magnet can be moved along the tube mechanically. When the aqueous dispersion inside of the tube is heated above the T_g, one dimensional fibers can be obtained as well. Since the largest magnetic nanochains are attracted the highest by the static magnet, the method allows to obtain very long magnetic fibers when they are collected directly next to the magnet.

4.6.2 Characteristics of the Iron Oxide/Polystyrene Nanoparticles

As magnetic moiety superparamagnetic magnetite nanoparticles capped with oleic acid were introduced (chapter 5.6.1.1.1). The synthesized oleic acid capped iron oxide nanoparticles displayed an average particle size of 8 nm in diameter according to transmission electron microscopy micrographs (Figure 52a). The saturation magnetization of the nanoparticles (under subtraction of the oleic acid layer) was determined to be 84 $emu \cdot g^{-1}$ according to vibrating sample magnetometer (VSM) measurements (Figure 52b). Their X-Ray diffraction (XRD) pattern is consistent with the crystal structure of magnetite (Figure 52c). Since the magnetization value is very high, *i.e.* close to the saturation bulk magnetization value for magnetite 92 $emu \cdot g^{-1}$, the particles are ideal candidates as magnetic moiety for the linear assembly of the magnetic polymer hybrid colloids. Owing to their superparamagnetic properties, attractive forces between the magnetic particles are only present when an external magnetic field is applied. Thus, after fiber formation of the magnetic polymer colloids, no interaction between the fibers is observed when the external magnetic field is removed. As a consequence, a permanent linkage has to be generated while aligning the particles. By introduction of a polymer matrix, polymer chain migration upon temperature increase provides such a linkage. Therefore, polystyrene nanoparticles with encapsulated magnetite were employed as a model polymer particle for the fiber formation.

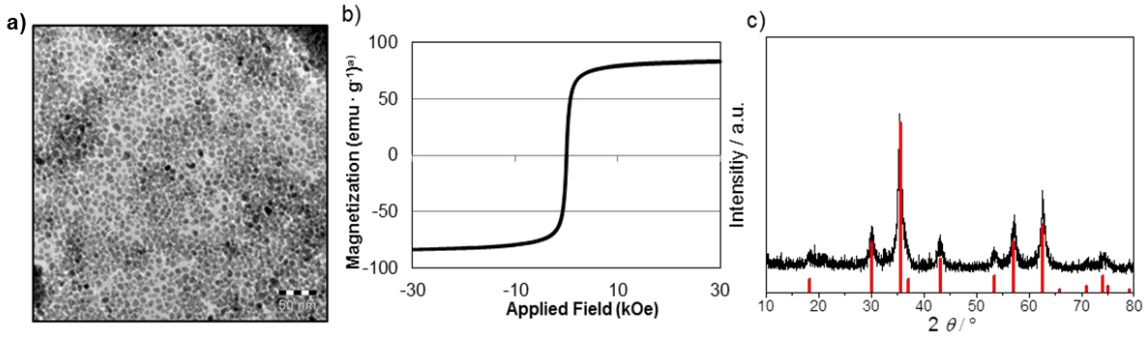

Figure 52. *Characterization of oleate capped iron oxide nanoparticles: a) TEM micrograph. b) VSM magnetization curve related to the mass of iron oxide. c) XRD diffractogram. d) Illustration of the interaction between a dispersion of iron oxide loaded polystyrene nanoparticles and an external magnet.*

For the synthesis, miniemulsion droplets with dispersed magnetic nanoparticles were used as seeds for the emulsion polymerization of styrene as illustrated earlier in chapter 4.2. Choosing miniemulsion droplets offers the possibility for a facile and versatile modification through integration of functional moieties (*e.g.* dyes, inorganic nanoparticles, functional monomers) into the droplets and therefore into the resulting nanoparticles.[16, 204] To verify the feasibility of a linear sintering of self-assembled

polymer particles, we first synthesized polystyrene nanoparticles with homogeneously distributed magnetite (PS-Mag-H). The magnetite content was chosen to be high (70 wt% according to thermogravimetric analysis - TGA measurements) in order to achieve a large magnetic dipole in each particle under application of an external magnetic field and thus a strong inter-particles attraction.

4.6.3 Hybrid Nanoparticle Synthesis and Linear Fusion – From Necklaces to Smooth Fibers

For the process of linear fusion, the topology of the nanofibers surface can be controlled by varying the degree of fusion of the spherical functional particles as schematically depicted in Figure 53. Because the fusion is highly dependent on the temperature, the degree of fusion and therefore the surface topology is tuned by the temperature of the aqueous medium. Necklace-like architectures are obtained by weakly fusing the particles whereas almost uniform nanofibers are created for a larger extent of fusion. In the latter case, the identity of the single nanoparticles is lost, *i.e.* the initial magnetic nanoparticles cannot be identified anymore in the final nanofibers.

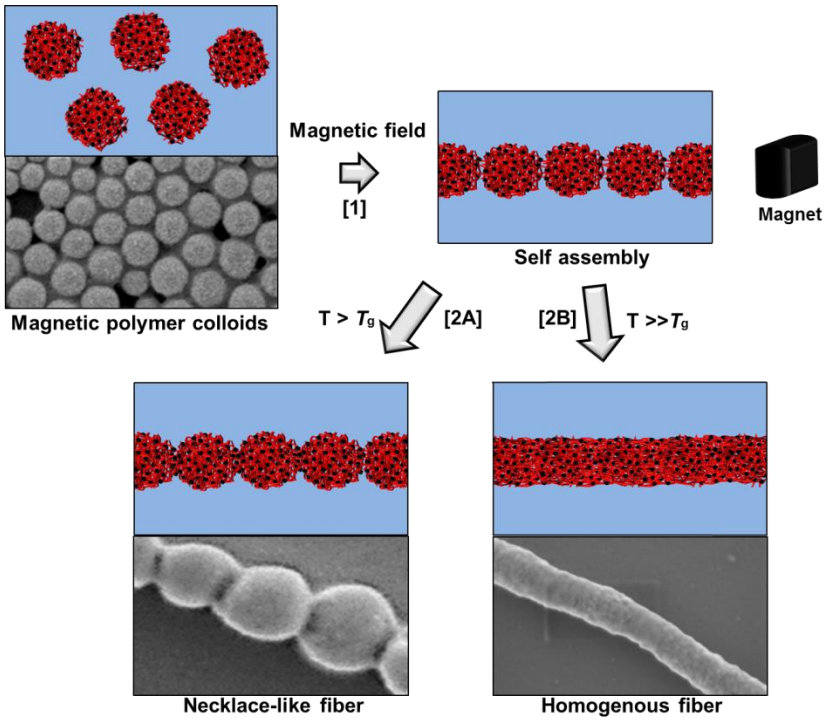

Figure 53. *Magnetic self-assembly [1] and fusion [2] of magnetic polymer colloids in water. Increasing the temperature above the glass transition temperature (T_g) provides enough polymer chain flexibility and enables a linear sintering process. Temperatures close to the T_g yields a low extent of fusion and a necklace-like morphology [2A]. For*

temperatures well above the T_g, fusion is observed to a larger extent and completely merged particles give a homogeneous fiber containing well-distributed iron oxide nanoparticles [2B].

Whereas the attraction between the particles can be tuned by the amount of magnetite inside the hybrid particles, the process of merging is mainly controlled by the nature of the polymer for a defined continuous phase, *e.g.* water, and a given temperature. Thus, it is mandatory to have a closer investigation on the composition and properties of the particles with special emphasis on the polymer chains. During the process of merging, several events are sequentially occurring: i) Deformation of the particles due to minimization of the interfacial energy between polymer and water leads to an increase in contact area between neighboring particles. The deformation is strongly dependent on the size of the particles;[310] ii) The diffusion of the polymer chains enables material exchange between the particles and merges the particles together. The molecular weight of the polymer chains and their polydispersity plays a very important role for the kinetics of chain diffusion.[145]

The employed nanoparticles (PS-Mag-H) display a hydrodynamic diameter of 127 ± 8 nm as determined by DLS (see Table 9 for details and chapter 5.6.1.1.2). Their TEM and SEM images are displayed in Figure 54. The relatively small diameter allows for a strong contribution of retarded elastic deformation to the sintering process and thus supports the colloid fusion.[310]

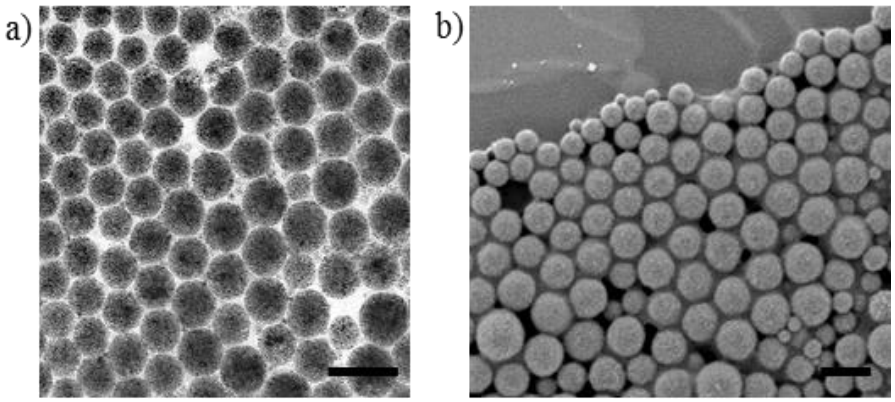

Figure 54. *TEM (a) and SEM (b) micrographs of polystyrene nanoparticles with homogeneously distributed iron oxide nanoparticles (PS-Mag-H). Scale bar 200 nm.*

Additionally, it offers the advantage that the resulting fibers are small in diameter and therefore have a large surface to volume ratio. In order to allow a facile merging of the hybrid nanoparticles, no crosslinker was used. The weight average molecular weight (M_w) of the polymer was determined to be 29,400 g·mol^{-1} with a polydispersity index (PDI) of 2.8. The relatively small molecular weight enables a fast chain diffusion which is accelerated by the large PDI.[145] The T_g of the hybrid particles was measured to be 56 °C

as determined by differential scanning calorimetry (DSC). The T_g of pure polystyrene (~ 100 °C[311]) was found to be significantly reduced due to the presence of oleic acid from the oleate capped magnetic nanoparticles (Figure 55).

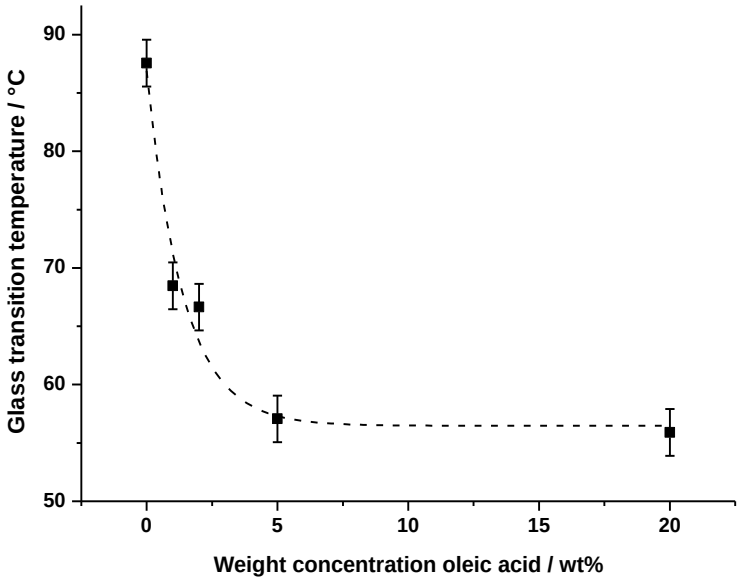

Figure 55. *Influence of oleic acid content on the glass transition temperature of polystyrene nanoparticles synthesized via miniemulsion technique.*

Table 9. *Characteristics of polystyrene nanoparticles with homogeneous distribution of iron oxide.*

Information	Unit	PS-Mag-H
D_h[a]	[nm]	127 (15)
Zeta potential	[mV]	-57
Iron oxide content	[wt%]	70
Magnetization	[emu·g^{-1}]	59
M_w	[g ·mol^{-1}]	29,400 (PDI[b] of 2.8)
T_g	[°C]	56

a: Hydrodynamic diameter given as intensity average and standard deviation, determined by DLS;

b: Polydispersity index $M_w \cdot M_n^{-1}$

To obtain highly stable nanoparticles, the charged comonomer styrene sulfonate was added during the polymerization to introduce a covalently bonded negative surface charge. The negatively charged surface (zeta potential of -51 mV) provides additional stabilization of the colloids by electrostatic repulsion between the particles to prevent their aggregation. Without the functional comonomer, the polymer particles could still be merged together, but large non-linear aggregates of particles were observed.

The length and structure of the formed nanofibers were investigated by scanning electron microscopy (SEM) and transmission electron microscopy (TEM) as depicted in Figure 56. Analysis of the single fibers was done for 100 fibers for which the number of particles per fiber was counted. For typical conditions (magnetic field of 200 mT, T = 85 °C, 10 s fusion time), the average length of the fibers was determined to be 6.4 ± 2.5 µm for PS-Mag-H. An average number of 55 ± 22 nanoparticles can be assigned to the fibers. The average length of the fibers can be controlled by varying the time of fusion (Figure 57). After a fast increase in length with time of fusion, the length converges towards a maximum.

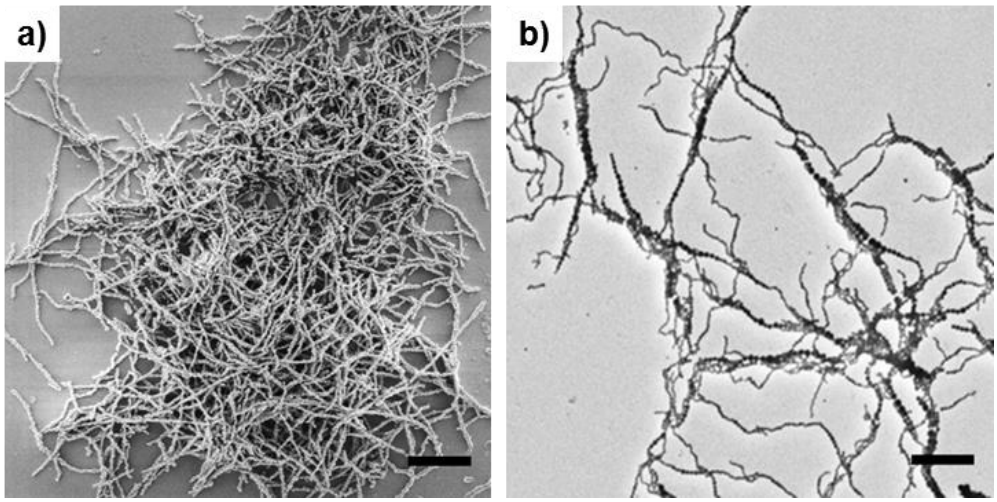

Figure 56. *SEM (a) and TEM (a) micrographs of nanofibers formed from homogeneously iron oxide loaded polystyrene nanoparticles. Scale bar 2 µm.*

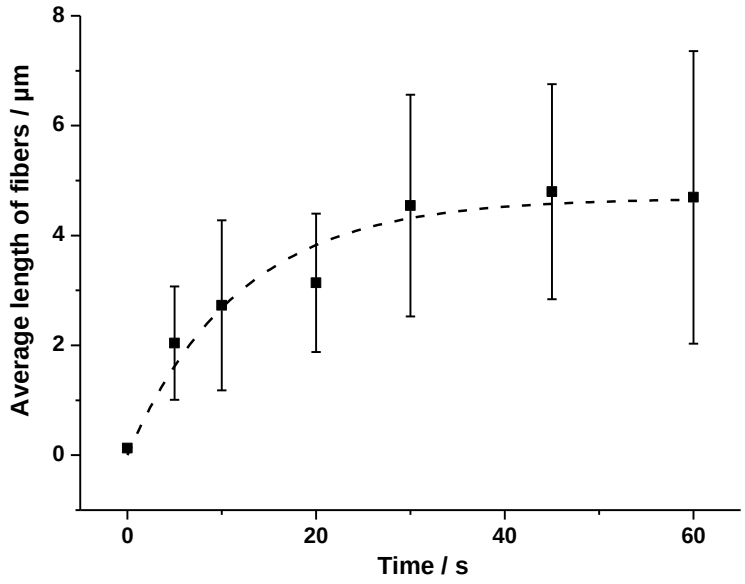

Figure 57. *Development of the average fiber length with merging time (determined from TEM micrographs). The fiber formation proceeded at 80 °C and with an applied external magnetic field strength of 25 mT. Under such conditions the fusion is slow (due to the relatively low temperature) and the chain length is limited.*

Additionally, we found that the amplitude of the magnetic field has an influence on the chain length. Application of a weaker field of 25 mT leads to the formation of shorter fibers (20-50% shorter). A flow velocity in the range between 0.3-2 $mm \cdot s^{-1}$ was found to be ideal. Once the fibers are formed, a breaking of the fibers upon application of moderate sonication or vigorous stirring cannot be observed. In a surfactant solution, the colloidal stability of the nanofibers can be maintained for several hours and it takes several days for the fibers to precipitate.

By setting the environmental temperature above but close to the T_g of the polymer, the nanoparticle merging is slow and allows for a more detailed investigation of the merging kinetics. Therefore the average interparticle merging diameter for PS-Mag-H was investigated as a function of the time of merging (Figure 58). For different fusion times the interparticle diameter of 100 fibers was counted. According to Frenkel's theory of sintering, the interparticle radius (or diameter) between two particles is proportional to the square root of the sintering time.[312] Because the merging kinetics of the particles PS-Mag-H could be described by Frenkel's theory, the interparticle diameter can be controlled and predicted by means of the fusion time.

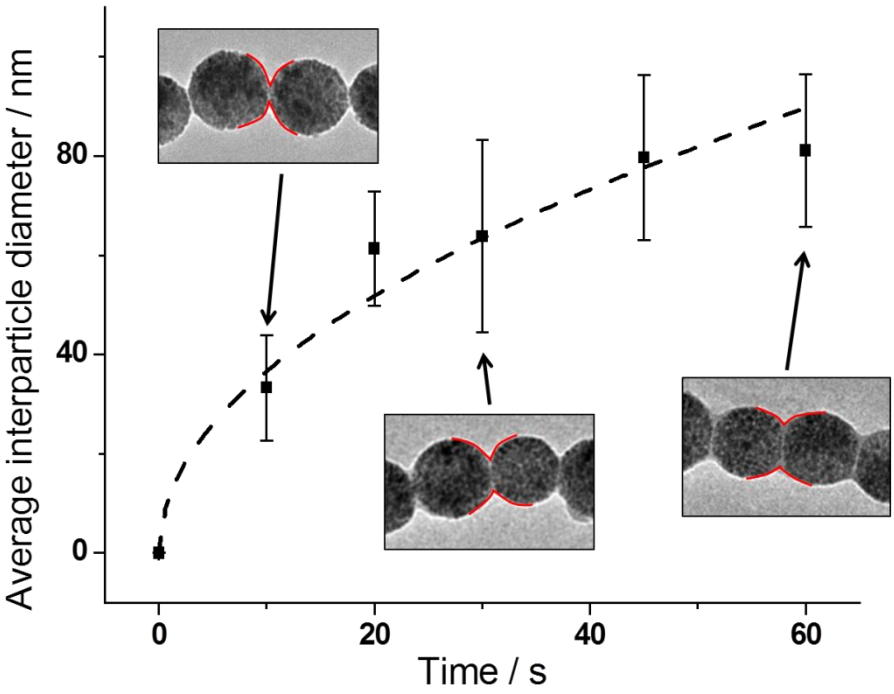

Figure 58. *Temporal evolution of the interparticle diameter for the merging of PS-Mag-H particles.*

Detailed investigations of the internal fiber morphology and distribution of magnetic nanoparticles inside the polymer matrix were carried out by TEM imaging (Figure 59). Figure 59a shows the TEM micrograph of a necklace-like nanofibers with weakly merged particles. The contact area between neighboring particles displays mainly polystyrene and only very little amount of magnetite. The particle shape is slightly elongated along the fiber axis (aspect ratio of 1.07:1.00). For completely merged particles (Figure 59b), the inorganic nanoparticles are homogeneously distributed along the polymer fiber. The complete merging and homogeneous distribution of the iron oxides indicates, that the mechanism of particle merging is composed of different steps depending on the temperature: i). For temperatures close to the T_g, elastic deformation of the particles leads to a weak overlap of the particles and a slight particle anisotropy. Inter-particle diffusion of single polymer chains and entanglements provides the possibility to link neighboring particles together. The iron oxide remains mainly static. ii) At higher fusion temperatures, a higher flexibility and stronger deformation of the particles is observed. The large deformation increases the contact area of neighboring particles, which leads to enhanced exchange of material between the particles. Additionally, the polymer chain diffusion is increased and enables the iron oxide nanoparticles to distribute along together with the polymer chains. In consequence, nanofibers with homogeneously distributed iron oxide nanoparticles are obtained. With a further increase in temperature, a slight increase in the average diameter of the fibers can be observed. The increasing

diameter can be attributed to the reduction of interfacial energy between the hybrid material and water by decreasing the aspect ratio of the nanofibers.

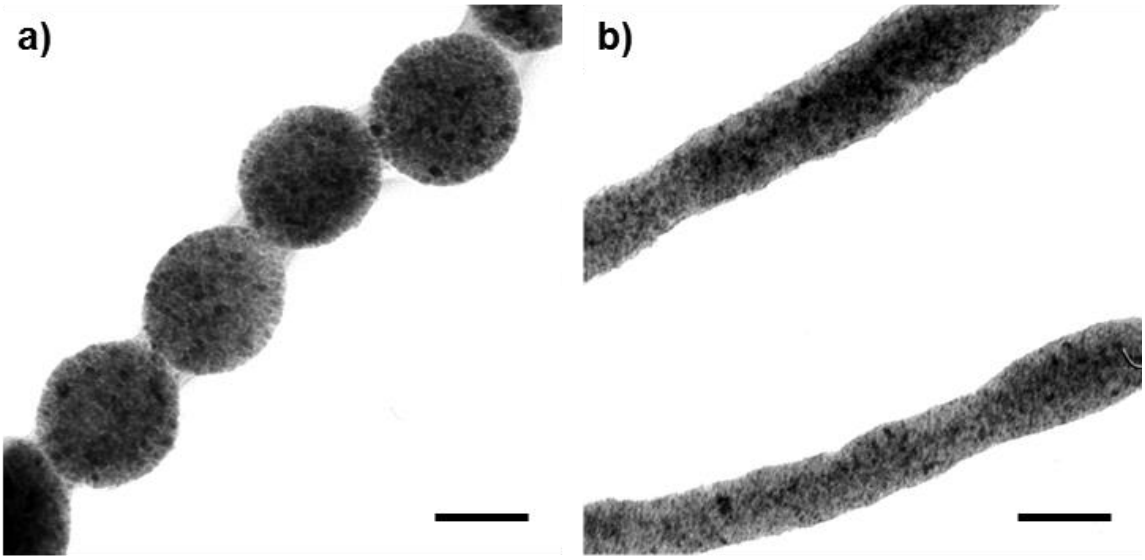

Figure 59. *TEM micrographs of linear merged polystyrene nanoparticles loaded with iron oxide. Weak merging of PS-Mag-H particles leads to necklace-like structures (a), larger extent of merging yields relatively smooth nanofibers where single particles cannot be identified anymore (b). Scale bar 100 nm (a, b).*

4.6.4 Iron Oxide Nanorods through Calcination

The hybrid fibers can be further calcinated to obtain inorganic nanofibers and nanorods (Figure 60). When calcinating the completely merged particles PS-Mag-H, the homogeneously distributed iron oxide nanoparticles prevent cracking of the wires and iron oxide nanostructures with high aspect ratio (~ 22) can be obtained. However, at certain points in the fibers, the calcination leads to breaking points to yield magnetic inorganic nanorods.

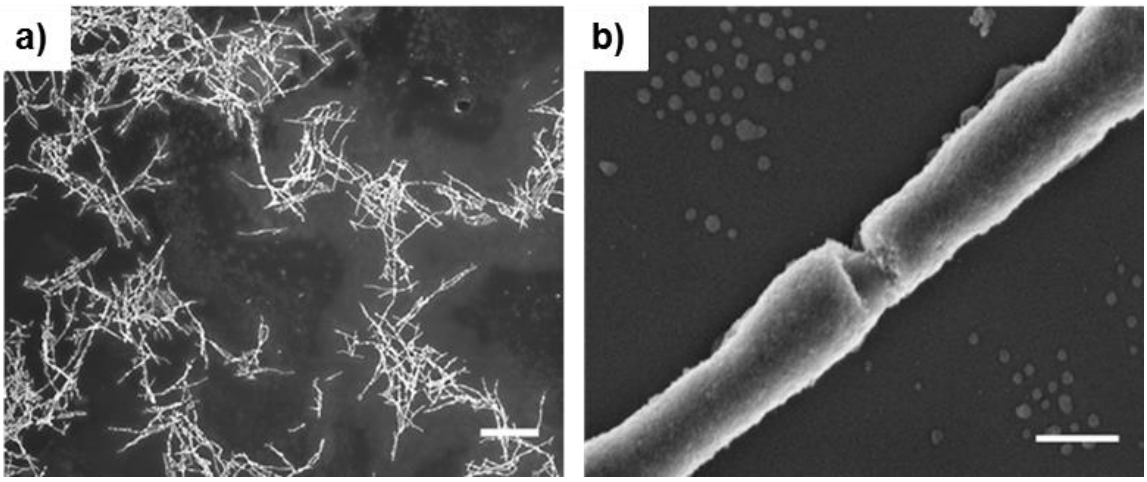

Figure 60. *SEM micrographs of calcinated strongly fused PS-Mag-H nanofibers. Overview picture (a) and close-up view (b). Scale bar 100 nm (b); 5 µm (a).*

A more detailed investigation of the nanorod element composition was done by EDX analysis (Figure 61). Only very little carbon can be observe and it becomes clear, that the rods consists almost exclusively of iron and oxide.

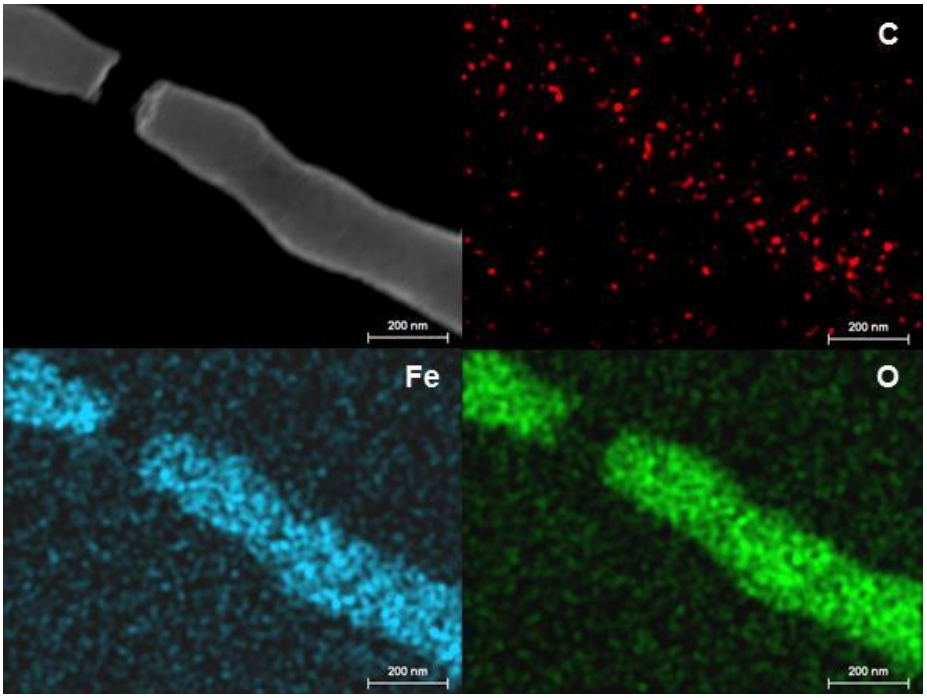

Figure 61. *SEM image (upper left) and element mapping (including carbon, iron and oxygen) of a calcinated fiber including a cracking point. For calcination, the fiber was calcinated for 4 h at 600 °C. In the upper right corner of the images the corresponding element is given.*

Since many of the rods combined can be seen as a porous three dimensional (tissue-like) network, many applications become possible. Owing to the high aspect ratio, the

thin diameter and the porous structure of the single rods, they are promising candidates to be used as building blocks for the catalysis of oxygen reduction reaction[299] or for high performance lithium storage.[298]

4.6.5 Tunable Corrugation of Zigzag Fibers Arranged from Janus Nanoparticles

Going one step further, we synthesized nanoparticles with a more complex Janus morphology (PS-Mag-J, see chapter 5.6.1.1.3 for experimental details) and applied the aforementioned process (see Figure 62 for SEM and TEM micrographs). For further characteristics of the particles see Table 10.

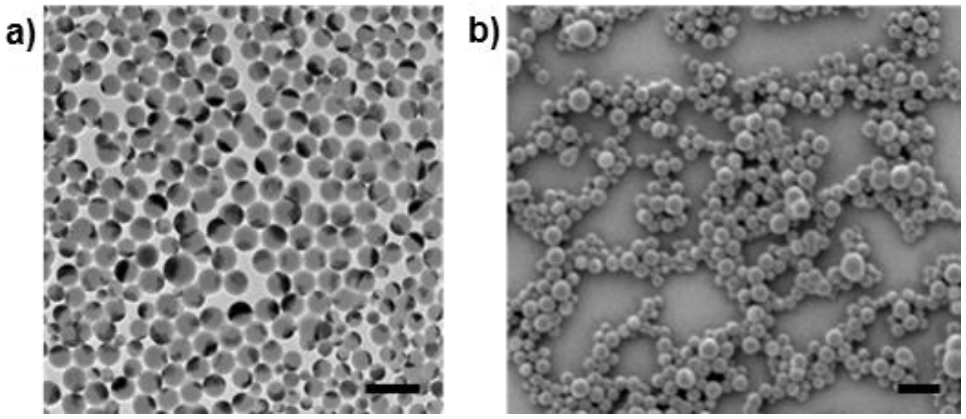

Figure 62. *TEM (a) and SEM (b) micrographs of iron oxide/polystyrene nanoparticles with Janus morphology (PS-Mag-J). Scale bar 500 nm.*

Table 10. *Characteristics of polystyrene nanoparticles with Janus-like distribution of iron oxide.*

Information	Unit	PS-Mag-J
D_h[a]	[nm]	237 (27)
Zeta potential	[mV]	-51
Iron oxide content	[wt%]	34
Magnetization	[emu·g^{-1}]	29
M_w	[g ·mol^{-1}]	158,000 (PDI[b] of 5.0)
T_g	[°C]	54

By letting a Janus nanoparticle dispersion dry on a TEM grid in the presence of an external magnetic field, the Janus particles align linearly and the formation of magnetic and non-magnetic domains can be observed as depicted in Figure 63a. The formation of domains was observed when pure aqueous dispersions were used. The addition of DMSO (1 wt%) was found to be beneficial for the formation of the linear structures The formation of domains is due to a zigzag arrangement of the particles as can be better seen in Figure 63b. However, in the process the particles are not linked permanently. They are also not in dispersed phase anymore and thus, not applicable for further applications.

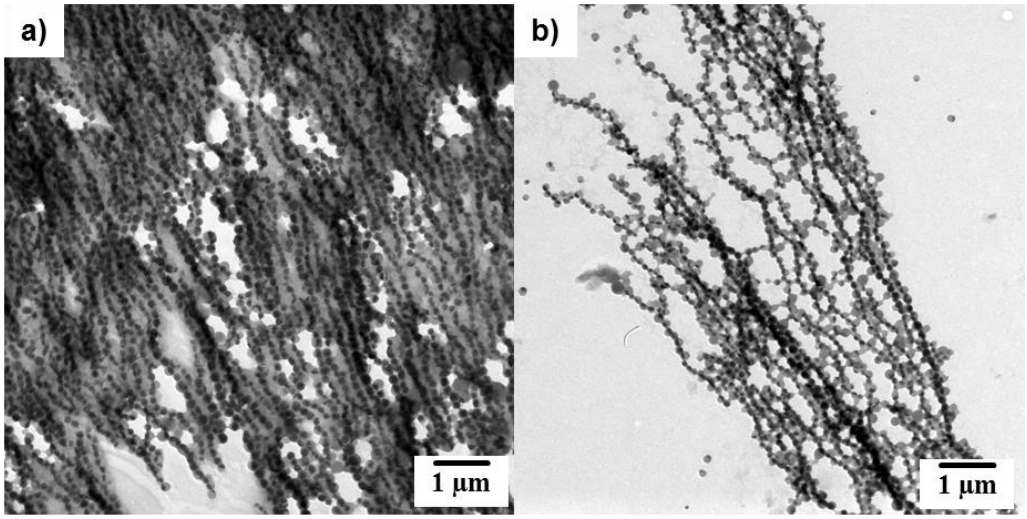

Figure 63. *TEM images of magnetic Janus nanoparticles. The dispersion of Janus nanoparticles was dried on the TEM grid under the application of an external magnetic field (with 1 wt% DMSO added to the dispersion).*

When introducing the Janus particles to the above mentioned fusion process, the variation of colloidal morphology induces an alignment of the particles in a zigzag fashion as well. Under certain conditions, even more complicated arrangements under application of an external magnetic field are possible, at least theoretically predicted.[164, 313] The conditions for merging the Janus particles are, compared to PS-Mag-H, more challenging. The reasons are the lower iron oxide loading (34 wt%) leading to a weaker interaction of the particles under magnetic field, the larger particles size (237 ± 27 nm) that slows down the particle deformation, and the higher molecular weight of the polymer (M_w = 158,000 g·mol^{-1}, PDI = 5.0) that enhances the viscosity of the heated particles. Nevertheless, the particles can be successfully merged together (Figure 64b,c,d). The obtained zigzag architectures have an average length of 3.0 ± 1.1 µm with an average number of particles per fiber of 13 ± 4. The zigzag fibers are significantly shorter and consist of fewer particles than PS-Mag-H because of the lower magnetic attraction force and the difficult zigzag arrangement. Such an arrangement not only demands diffusion of

the particles into linear structures, but additionally rotation into the right orientation. The particles merge together in a two-dimensional plane and therefore have only one orientation possibility in the plane.

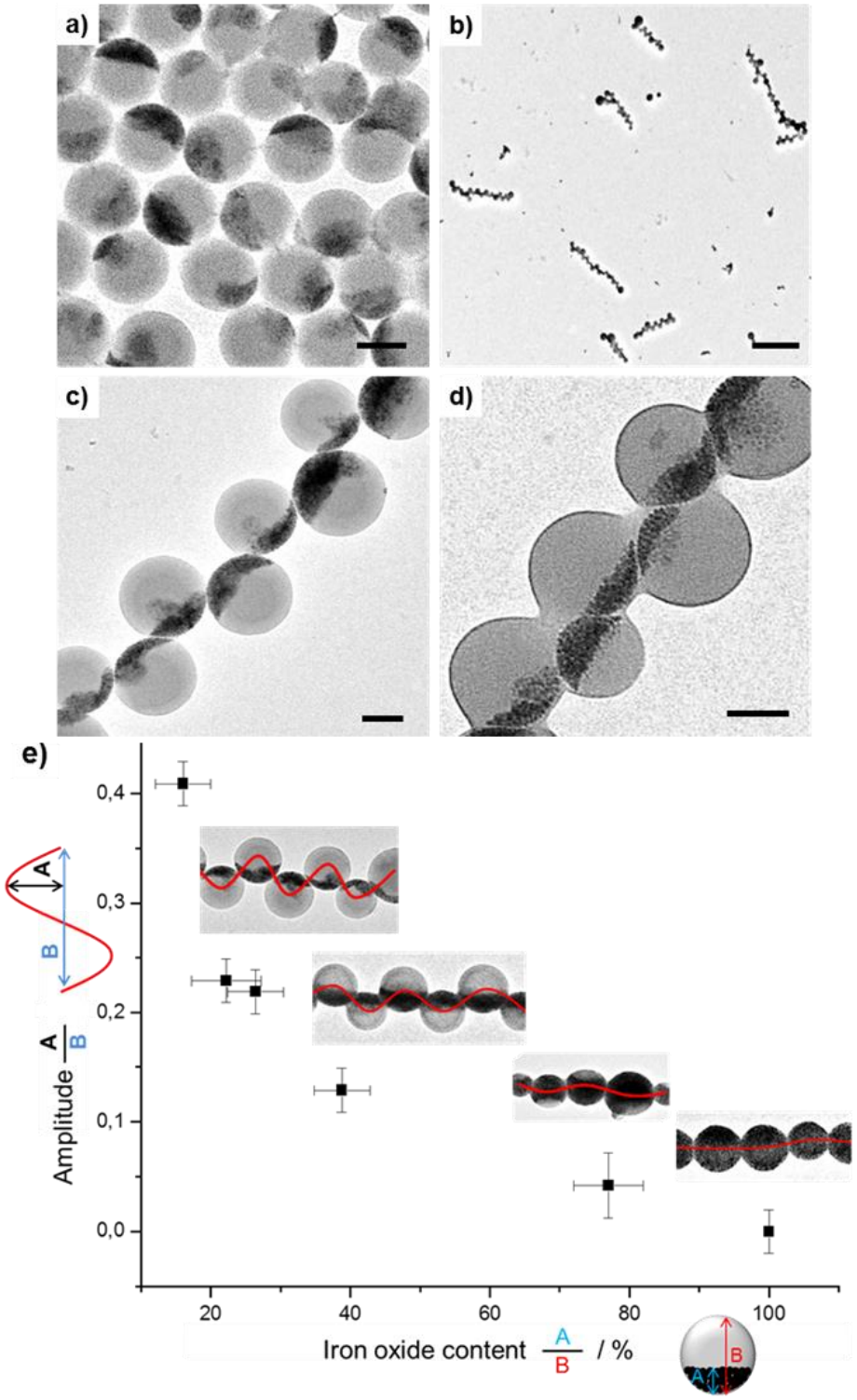

Figure 64. *TEM micrographs of inserted PS-Mag-J nanoparticles (a) and resulting zigzag fibers (b, c, d) after fusion of the particles. Weakly fused zigzag fiber (c) and*

stronger fused fiber (d). Scale bar 200 nm (a, c, d): 2 µm (b). Control of corrugation amplitude by variation of iron oxide content (e).

For the Janus nanoparticles, a weak (c) and a stronger (d) fusion can be observed as for PS-Mag-H. However, for the case of a stronger fusion, the particles do not form smooth cylindrical fibers. The difference in comparison to PS-Mag-H can be explained by the significantly higher molecular weight of the polymer in the Janus nanoparticles and the resulting higher viscosity of the polymer chains,[314] which slows down the diffusion significantly.

Furthermore, the zigzag corrugation can be controlled by the ratio of iron oxide to polystyrene inside the Janus particles (Figure 64e). Indeed, decreasing the iron oxide content yield larger corrugation in the zigzag fibers. Thus, the morphology of the inserted 0D colloids accounts for the complexity in terms of corrugation of the obtained fibers.

Additionally another possibility to arrange Janus particles was found. Interestingly, when inserting Janus particles with a low T_g and fusing them rapidly at high temperature yields undefined linkage in contrast to the above described case. Figure 65a illustrates the two major steps to obtain zigzag fibers: (I) The perfect linear arrangement and attachment of a particle to the growing fiber by directed diffusion caused by magnetic attraction. (II) The orientation of the Janus particle in space by rotation. In the case of a large difference between fusion temperature and T_g, the particles fuse fast. Thus, rotation in space cannot always take place fast enough and the particles are linked first. As a result, the particles are not able to form a zigzag arrangement and instead fuse chaotically. Such a chaotic fusion causes junctions at several points of the growing architecture as investigated *via* TEM imaging (Figure 65b). The orientation of the single Janus particles is random and several junction points can be observed. The Janus particles are fused very strongly and their single identity is not revealed very clearly.

Further opportunities arise from the aforementioned observations. Indeed, the formation of blocks is observed when using homogeneously distributed iron oxide and Janus-like distributed iron oxide (PS-Mag-H and PS-Mag-J), (Figure 65c). The particles with homogeneously distributed iron oxide form linear arrangements, while the Janus particles arrange in a rather chaotic fashion to form a highly branched structure. The combination of both features yields a structure which resembles a linear-branched copolymer with one linear block and a highly branched block.

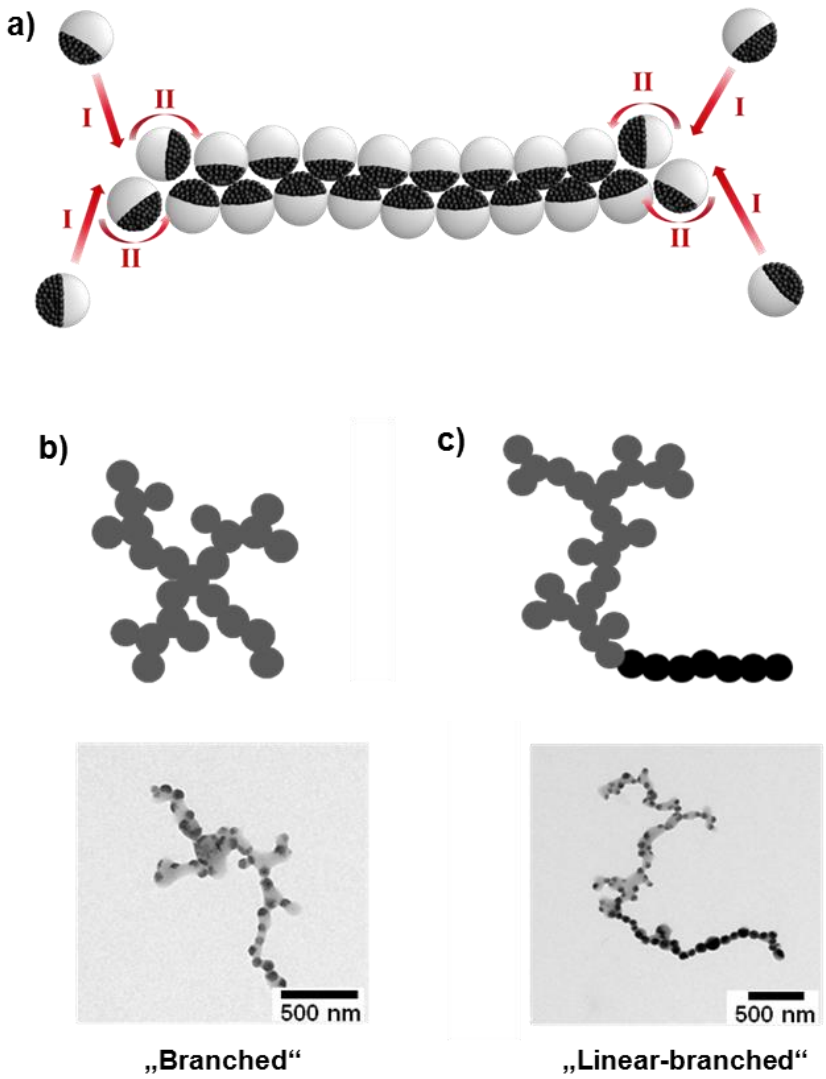

Figure 65. *a) Schematic illustration of the formation of zigzag fibers from Janus particles by magnetic dipole-dipole induced diffusion of the particles to the growing chain (I) and rotation in space to achieve the preferred orientation (II). b) TEM image of a highly branched architecture of fused Janus particles. c) TEM image of a "linear-branched" architecture obtained from two types of particles forming a linear tail and a branched head.*

In conclusion, a novel method for the preparation of hybrid and inorganic fibers and nanorods in aqueous environments was demonstrated. Spherical magnetic building blocks of hybrid nanoparticles are assembled under flow and an external magnetic field without any templating agent. The fast fusion speed (0.5-50 s), the facile synthetic procedure and the aqueous fusion medium are important advantages of the novel process. The morphology of the obtained fibers, ranging from necklace-like to smooth cylindrical structures, *i.e.* with a tuneable corrugation, can be controlled by the process parameters such as time of fusion, temperature and morphology of the magnetic nanoparticles. Indeed, the assembly of Janus nanoparticles yields zigzag structures. Moreover,

implementation of magnetic/polymer nanocapsules into the fusion process enables the generation of linear structures with core-sheath morphology. The complexity of the 0D initial structure is therefore used for inducing a complexity into the obtained 1D structure. It is expected that novel supraparticular assemblies with high stability will be created by using spherical building blocks of different sizes and with increased complexity of colloidal structures.

The hereby established novel process offers further possibilities. Future investigations should be focused on two main tasks: Firstly, the structure of the obtained nanofibers was found to be variable with respect to cross-linking of the fibers and the sequence of small and large particles. The different structures will be analyzed in the following chapter in more details. Secondly, the use of the nanofibers for different applications can be evaluated. In particular, they could be introduced as Fe_3O_4 materials for catalytic reactions. A nitrogen containing compound could be introduced into the nanoparticles. After magnetic aligning and sintering, a calcination step could form nanorods of Fe_3O_4 containing aromatic systems doped with nitrogen atoms. Such systems have been proven to be excellent for catalytic reactions.[299, 315] An additional application could be possible when sintering the nanofibers onto the surface of a substrate in order to obtain hedgehog-like coatings. Fluorination could yield superamphiphilic surfaces. Strong repellent properties for any fluid have especially been found for “snowman-like” piles on surfaces, which makes their elaborate synthesis from spherical colloidal building blocks worthwhile.[276, 316]

4.6.6 Tubes from Magnetic Polymer Capsules

Furthermore, it was possible to form nanotubular structures by using nanocapsules instead of nanoparticles (see chapter 4.4 and 5.4 for synthetic details of the capsules and the fusion process) in the process described above (see Figure 66a). When two neighbouring nanocapsules are merged, the contact area increases. The polymer chain diffusion and the motion of the magnetic nanoparticles can lead to a complete fusion of the capsules to form a linear tubular morphology with a liquid *n*-octane core and a solid polystyrene/magnetite sheath (see chapter 5.6.4 for experimental details). Some examples for the obtained structures are shown in Figure 66c+d. The TEM images give only a 2D image and thus do not reveal all information about the 3D structure. However, a core-sheath structure can be assumed from the TEM image in Figure 66d. A fusion of capsules to form tubes has never been reported (at least never from dispersions) and is therefore of high interest and worthwhile to investigate further.

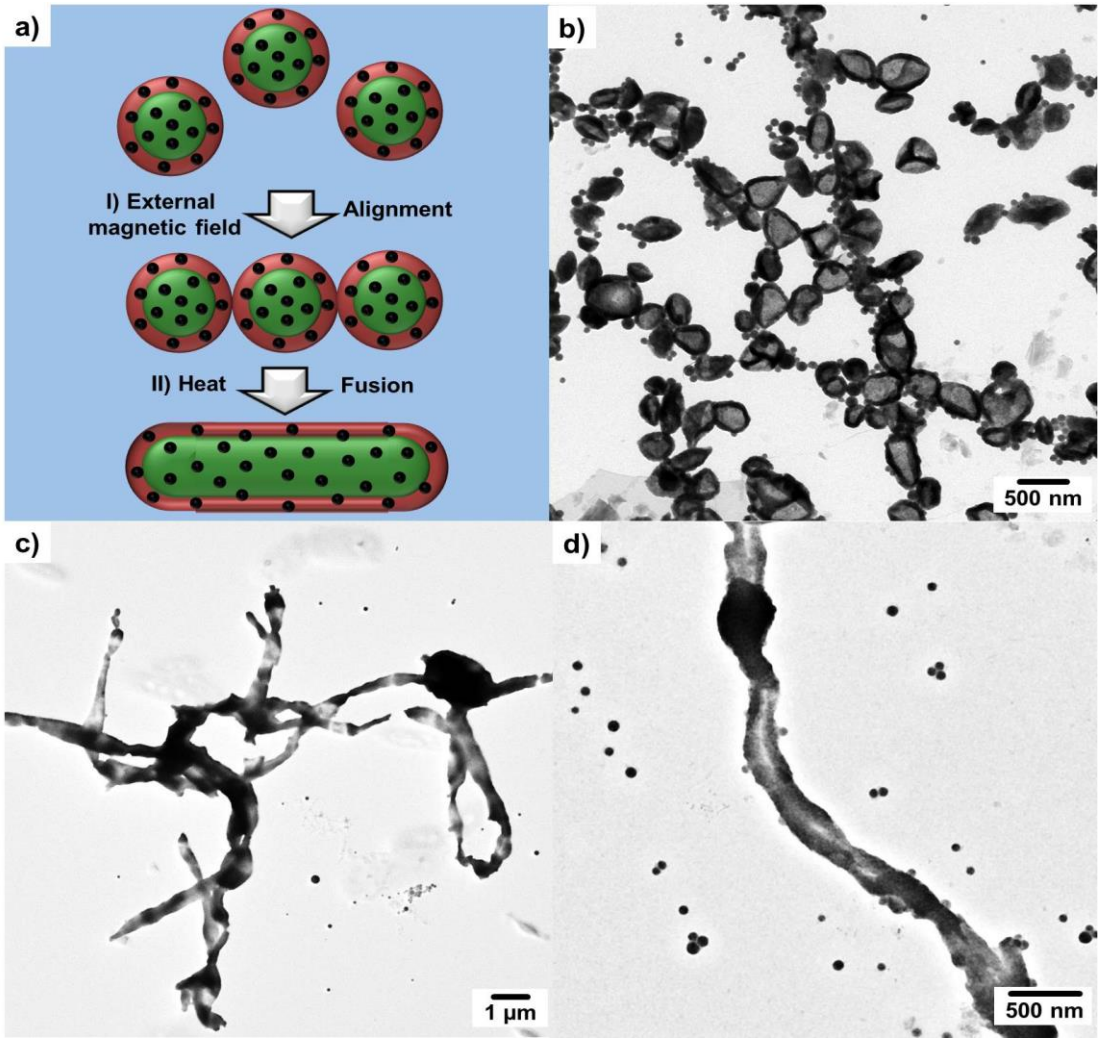

Figure 66. *a) Preparation of nanotubular structures from magnetic polymer nanocapsules through magnetic alignment (I) and thermal sintering (II). TEM images of magnetic polystyrene nanocapsules (b) and tubes (c, d).*

4.7 Colloidal Building Blocks for Polymer-like Architectures - From Block Copolymers to Tailorable Degrees of Branching

The basic laws of physics have created a tool kit of extremely well-defined building blocks, the elements of the periodic table. Well-connected with each other in molecules, the atoms account for all known structures in nature, no matter how complex they are. Owing to the precise structure of atoms, interactions between them are highly specific. Stable arrangements with defined binding properties and thus, architecture can evolve under defined conditions. Large efforts have been made in the past to use colloids as building blocks for defined colloid arrangements as well. Recently, it was shown that colloids can be shaped in a precise fashion. The defined colloidal building block can then be used to achieve a specific binding between colloids.[317] When the site specific reactivity is implemented in the colloids, defined colloidal arrangements with astonishing precision can be created.[166, 318]

A less precise arrangement of atoms is known for polymers. They vary in chain length (PDI), monomer composition or the position and amount of junction points. Even so, they are of high interest for materials applications owing to their unique bulk properties. The bulk properties originate from the average composition of the polymer chains. The average composition can mainly be tuned by the employed monomer composition, the sequencing of the monomer within the polymer chain, the average molecular weight (and molecular weight distribution) and the crosslinking density. Even if polymer-like assemblies of colloidal building blocks in one dimensional (1D) or 2D fashion have been shown for different particles through electrostatic interactions,[167, 319-320] magnetic interactions,[160, 321-322] van der Waals forces,[302, 323-324] hydrogen bonding[166] and surface roughness[325] among others, a control over sequencing of different colloids or a control over junction points in the arrangements was not reported. Because the assembled colloids have applications *e.g.* in photonics,[326-327] electronics[328] or robotics,[163] many applications might be possible for more complex polymer-like colloid assemblies as well.

Within the following chapter, the linkage of superparamagnetically labeled polystyrene nanoparticles in polymer-like fashion is demonstrated. The synthesis of superparamagnetic nanoparticles and their incorporation into a polystyrene matrix to obtain iron oxide/polystyrene nanoparticles is described in the experimental section. Assembly under application of an external magnetic field and temperature annealing of the nanocolloids provided stable nanoparticle chains as shown in chapter 4.6.[133] When nanocolloids of the same size were used, linear nanoparticle chains were obtained. Investigating the growth of the chains gives an insight into the assembly mechanism of the building blocks. The growth analysis revealed a preferred chain growth mechanism. When using dispersions with different nanoparticle sizes, further polymer-like

architectures can be achieved. Viewing the different nanoparticle sizes as different types of monomers, the reactivity and valency of the nanoparticles can be tailored to a certain degree. On the one side, a variation of size composition could be used to control the sequence of small and large colloids in block-like fashion. Under certain conditions, the self-organization by size was observed, resulting in the formation of block copolymer-like structures. In addition, changes in the velocity of the magnetic field application can lead to a rather statistical assembly of the different sizes. Furthermore, the particles with large size differences can be used to introduce junction points. The junction points cause branching of the single nanoparticle chain, and for high concentrations, even whole networks are obtained. Introduction of the junction points is well tailorable under suitable conditions like the polydispersity of the particle dispersion or the increase of the external magnetic field.

The different possibilities to achieve polymer-like architectures through controlled nanocolloids assembly are depicted in Figure 67. In the upcoming chapters 4.7.1-4.7.3, three main topics are being investigated in detail according to the scheme. First, more insight into the length of linear chains is given with respect to a polymer-growth mechanism. Secondly, the variable reactivity of differently sized nanoparticles is investigated in more details. Accounting for the formation of either statistical or block copolymer-like arrangements with respect to their size, the reactivity of the single building blocks is a key parameter to obtain elaborate arrangements of nanoparticles. Finally, the introduction of junction points within the nanochains is investigated. With the help of the junction points, branched chains are possible as well as highly crosslinked networks of nanoparticles.

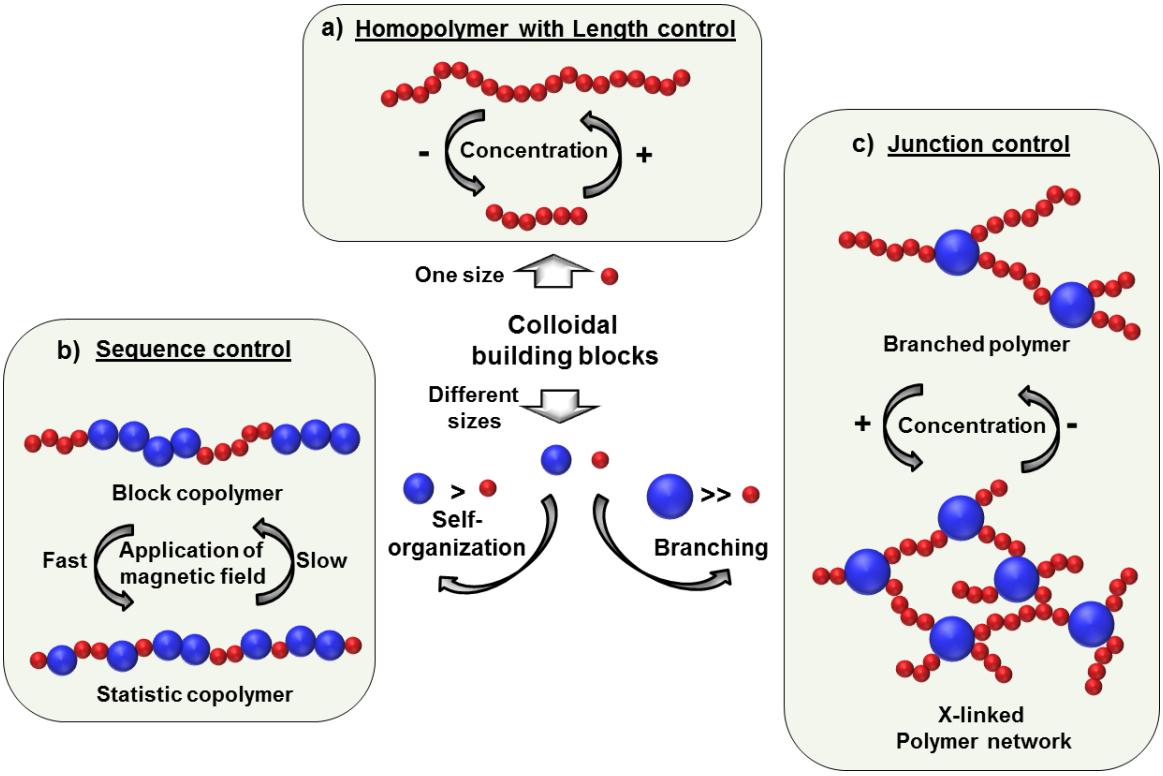

Figure 67. *Overview of the different possibilities to assemble superparamagnetic polystyrene nanoparticle under influence of an external magnetic field to form "colloidal polymers" of various architectures. a) Insertion of a monodisperse nanoparticle dispersion yields linear nanochains. Depending on the concentration of the nanoparticle dispersion (and the time), longer or shorter chains can be obtained. b) When using a polydisperse sample, the different sized particles can self-organize into blocks of larger and smaller particles, resulting in colloidal block copolymers. Applying the magnetic field faster strings the particles in a rather statistical fashion together. c) The insertion of particles with large size differences enables the controlled introduction of junction points. Several small nanoparticles can assemble around a large particle which then has a triple or even quadruple valency. High concentrations of nanoparticles lead to networks of colloidal polymers.*

4.7.1 Linear Assembly and Fusion of Magnetic Polymer Hybrid Nanoparticles

The principles behind the fusion of the single nanoparticles were already described in the previous chapter 0. Details concerning the growth of the chains have been neglected so far and will be discussed now. With respect to the formation and growth mechanism of the chains, an analogy to the growth of polymers can be drawn. Here, two main growth mechanisms are possible: Chain and step growths. In the first case, single monomers are

attached to the growing chain. Each growing polymer chain can only react with monomers, not with other polymers. In the step growth mechanism, growing polymer chains can react with other chains. The two different mechanisms result in very different temporal evolutions for the average chain length and the monomer conversion. For the step growth mechanism, the degree of polymerization (DP) increases slowly with time. Only for a high conversion, high DPs can be achieved. Step growth of nanoparticles could be demonstrated for the linear assembly of bifunctional gold rods by hydrophobic interactions as shown by the group of Kumacheva.[302]

Monitoring the DP with time for the assembly and fusion of the iron oxide/polystyrene nanoparticles, a different kinetic is found as shown in Figure 68b. The average length of the chains increases fast and then plateaus; a rather typical behavior for chain growth. The mechanism is depicted in Figure 68a. Large chains coexist together with many monomer particles during the assembly and fusion reaction. For the ideal case where all nanoparticles are considered to have two binding sites and assuming that the binding sites are of the same reactivity, one would expect a step growth. Here, a different kinetic is observed. A rather chain growth-like mechanism is additionally underpinned by the occurrence of single nanoparticles together with very long chains (in the case for which the "polymerization" is not yet finished) as depicted in Figure 68e.

The difference in the kinetic growth behavior can only be explained by a different reactivity of the growing chain in comparison to the single nanoparticles. One reasonable explanation that can be given to understand the phenomenon is the increasing magnetic force of the chains F_{mag} with the mass of magnetite m_{mag} and thus, with the number of particles per chain N_p. The increasing field attracts magnetic nanoparticles faster. Therefore, it is less likely for single particles to come together than for single particles with a chain.

$$N_P \sim m_{mag} \sim F_{mag} \tag{6}$$

It has to be taken into account that step growth will also occur, however chain growth is predominant when considering the fast increase of the DP of single chains.

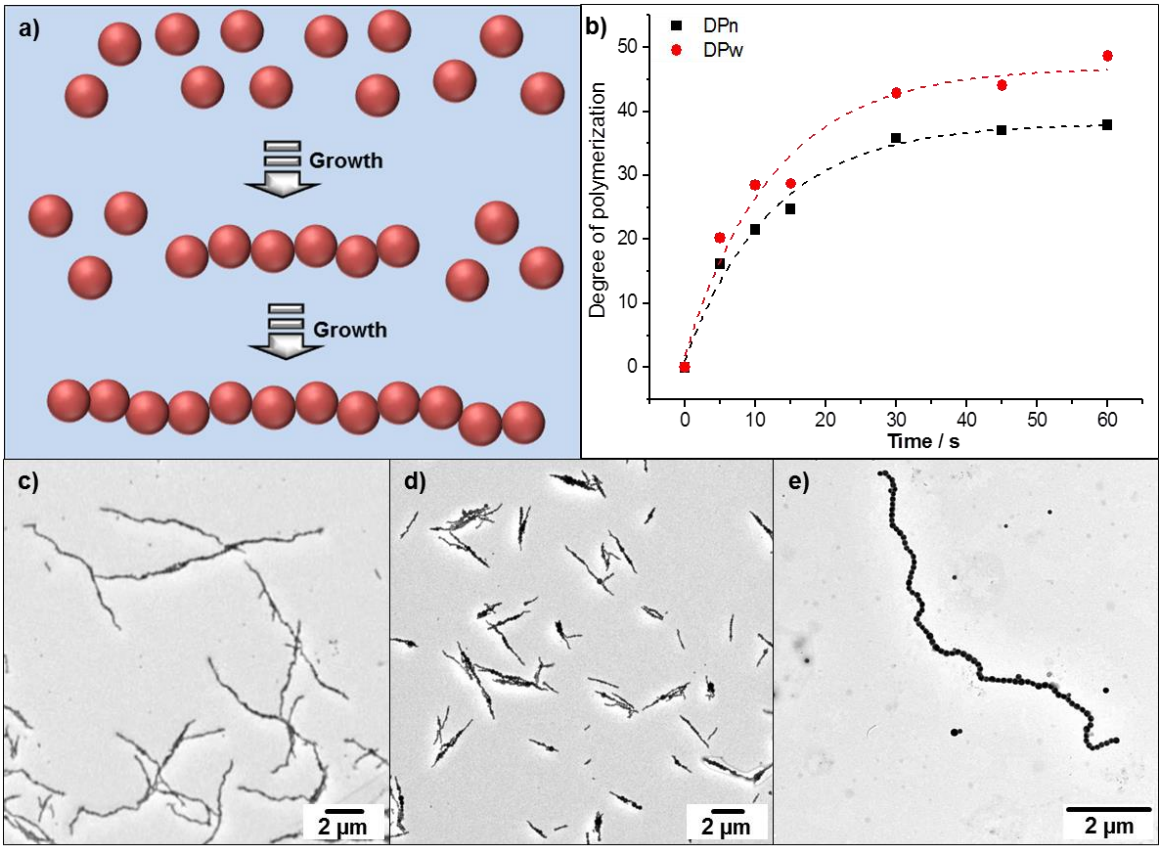

Figure 68. *Formation of linear chains of nanoparticles upon self-assembly and thermal annealing. a) Schematic illustration of the linear assembly and fusion of monodisperse nanoparticles. b) Graph illustrating the growth kinetics of the chains. The degree of polymerization (DPn for number weighing and DPw for weight weighing) increases fast in the early stages and plateaus at longer times. c) TEM image depicting several long linear chains of nanoparticles at higher concentrations of nanoparticles. d) TEM image of short linear nanochains as obtained for lower concentrations. e) TEM image of one chain prepared from nanoparticle "monomers" with narrow monodispersity of the single nanoparticle diameters.*

Besides the aforementioned possibility to tune the length of the chains with time (also see 4.6.3), there is another option related to the concentration of particles in the dispersion. With an increasing concentration of the particles in dispersion, the resulting chains decrease in length. Shorter chains from lower concentrated nanoparticle dispersions are depicted in Figure 68d, longer chains from higher concentrated dispersions are shown in Figure 68c.

4.7.2 Control over Self-Assembly by Particle Sizes to Form Block Copolymers

Often two different monomers are polymerized together to obtain a copolymer which comprises properties of the two homopolymers. Furthermore, the properties depend highly on the sequence of the monomers within the polymer chain. Depending on the relative monomer reactivities, a statistical, an alternating, or a block copolymer sequence of the monomers is obtained in the resulting chain.

In the present chapter, we address the question about how nanoparticles of different sizes interact and assemble with each other, or more precisely: How does the velocity of the nanoparticle assembly and thus, the reactivity correlate with the size of the nanoparticles? The introduction of a facile and stable linkage into self-assembled magnetic nanoparticle chains could not be shown up to now. Thus, common investigations on their assembly are limited to large particles (≥ 1 µm) which can be studied by optical microscopy. The method described in the thesis to assemble and fuse particles provides a perfect tool to study the assembly of magnetic nanoparticles in more detail because the particles can be monitored by TEM in a "frozen" state after their fusion in dispersion.

The TEM images show a tendency of different sized particles to come together and form blocks of similar sized neighboring particles (Figure 69b+c). An astonishing separation between the large particles and the small particles within the chains can be observed. The size-separation is observed for large (Figure 69c) and short chains (Figure 69b). However, not under all conditions such a self-assembly by size is observed. When the magnetic field is applied fast, a rather random or statistical assembly is observed (Figure 69d). Thus, the velocity with which the magnetic field is applied is the key parameter to obtain an order in block-like fashion or a disorder in statistical fashion of differently sized nanoparticles when they assemble (Figure 69a). On the basis of the made observations, a more detailed investigation was carried out. The degree of order was quantitatively analyzed with respect to the water flow (see Figure 69e) and therefore with the velocity of magnetic field application. The size deviation (25, 50, 75 and 100%) of neighboring nanoparticles was analyzed and the degree of order (DO) plotted against the flow (Figure 69e). The DO describes the percentage of neighboring particles which have a similar size (< than the set size deviation) as described in Figure 69e. The DO was calculated for a completely statistical arrangement of the nanoparticles with the given size distribution and the values added as dashed lines. When the flow is increased, the DO converges towards the dashed line of the statistical arrangement. However, the DO is considerably higher when the flow is very slow. The probability for neighboring particles to have a size deviation of 100% or more is approximately 5-6 times higher for a fast flow than for a slow flow.

In conclusion, the sequence of larger and smaller particles within a nanochain can be controlled by the flow and thus, by the velocity of magnetic field application. Owing to the simple relationship, the formation of block-like or statistical copolymers can be very well controlled by the flow of the dispersion in the device. The flow is the key parameter to tailor the assembly of differently sized particles with each other.

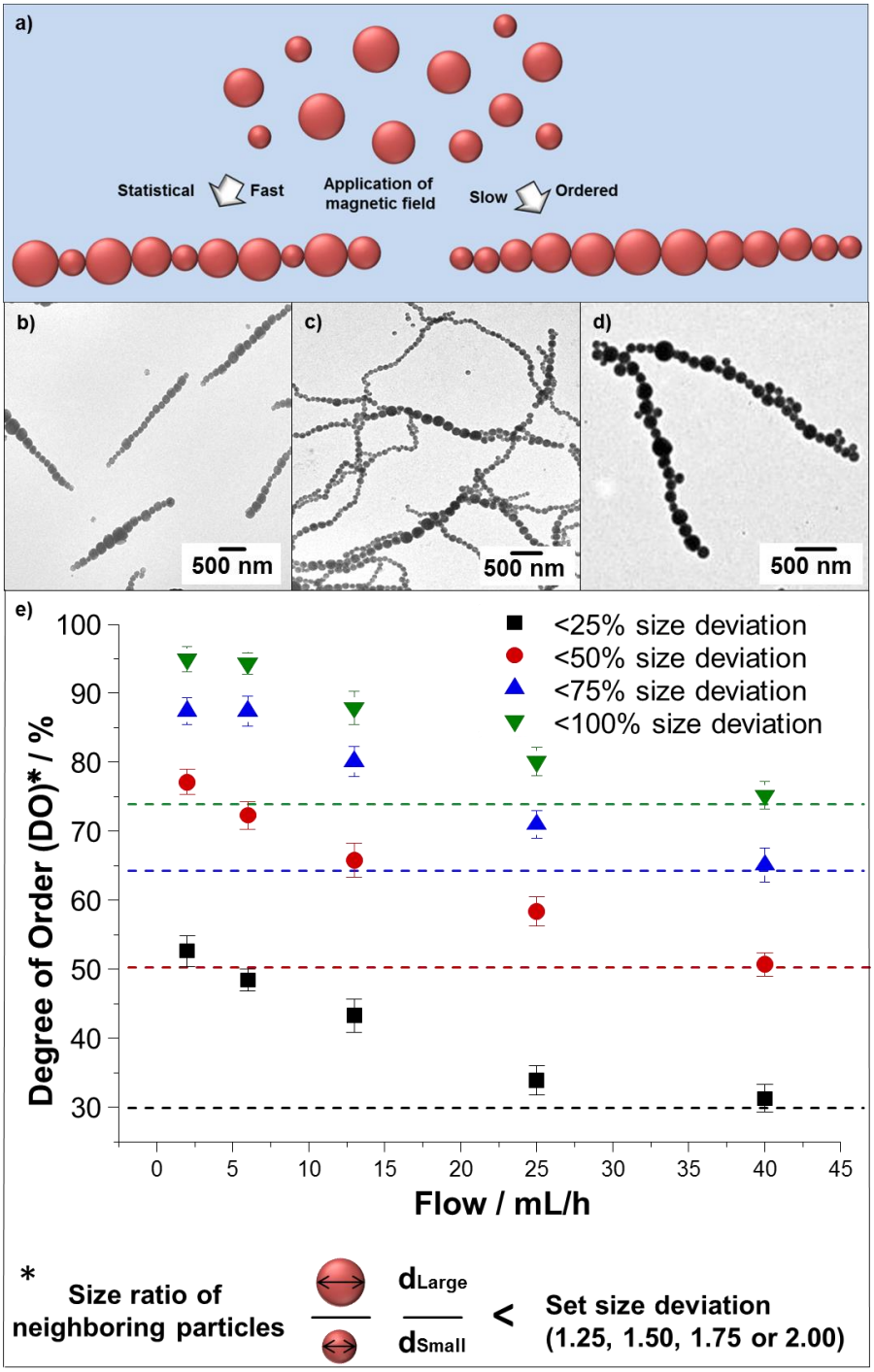

Figure 69. *Control of the sequence of large and small nanoparticles into linear chains of nanoparticles. a) Schematics depicting the two possibilities to align a polydisperse sample of nanoparticles. When all particles have the same reactivity, a statistical*

assembly occurs. In the case of a faster assembly of larger particles, an order results with larger particles in the middle and smaller particles at the edges of the chain. b) TEM image of short chains of nanoparticles. c) TEM image of larger chains with block-like areas of larger and smaller particles. d) TEM image of statistically assembled nanoparticles into chains. e) Graph illustrating the probability that neighboring particles have similar sizes with respect to the flow conditions.

Now we have to direct our attention towards the question why there is such a distinct difference in the assembly of a polysdisperse sample depending on the velocity of magnetic field application. Considering that all nanoparticles, no matter how big they are, are mainly composed of inorganic iron oxides (as can be suggested from TGA measurements and TEM analysis), the saturation magnetization of the particles increases linearly with their volume. Thus, the amount of magnetite is proportional to the diameter of the particles to a power of three. The pronounced dependency of the size on the magnetite content and therefore the induced magnetic field of each particle is the main reason for the size dependent assembly. It has to be kept in mind that a particle twice the size has eight times the amount of magnetite. The larger particles generate a larger magnetic field and can assemble first. The faster assembly for larger particles is favored by employing a weak external field and thus, a weak field generated by the particles. Here, at first the large particles come together and then assembly from both sides of the growing chain. Then, smaller and smaller particles assemble at the edges and fuse. Figure 69b shows a TEM image of short chains where the particles are assembled depending on their size. As theoretically assumed, the outer parts of the chains consist mainly of small particles whereas the middle part often consists of the largest particles. It has to be kept in mind that the ordered sequence is not occurring in all chains. Nevertheless it is clearly the predominant arrangement. When the magnetic field is applied very fast, all particles generate a large field and immediately align independently on their size. Thus, the size-separation process cannot take place. A rather statistical arrangement of the nanoparticles results from the chaotic assembly.
In summary, the results presented here give rise to control the sequences of assembled particles with different sizes by a simple parameter and enable the production of linear nanoparticle arrangements with defined sequences of differently sized particles.

4.7.3 Introducing Junctions to Control the Degree of Branching and Form Networks

In polymer chemistry, the introduction of monomers which have a valency (number of binding sites) higher than two are of high importance to obtain various architectures with

tunable properties[329] and to gain access to whole networks of polymer chains.[330] The following chapter is related to the introduction of junction points in the nanochains.

For the introduction of junction points, the size difference of neighboring particles plays a crucial role. The mechanism of the formation of a junction with triple or quadruple valency is schematically depicted in Figure 70a. The combination of a large particle with several small binding partners provides the basis for such a junction. The reason for the high probability to form junctions whenever the size ratio of neighboring particles is large originates mainly from steric considerations: The larger the size ratio of two particles, the more small particles "fit" next to a large particle. The occurrence of junctions as a function of the large to small ratio of neighboring particles was analyzed from TEM images and quantified as shown in Figure 70e. For neighboring particles with the same size, almost no junctions can be observed. When however increasing the size ratio between neighboring particles, the probability to obtain a junction increases significantly. At large size ratios of the neighboring nanoparticles, the probability to obtain a junction point drops again. The drop in probability can be assigned to the decreasing occurrence of very large and very small particles in dispersion that can fulfill the size ratio criterion to form a junction point. Two examples for a junction point are shown as TEM images in the Figure 70b and c. The first image shows a triple valency, the second image a quadruple valency.

In the previous chapter, the influence of the flow on the sequence of large and small particles within the chain was discussed. With increasing flow, neighboring particles tend to arrange in statistical fashion and do not self-assemble by size. In order to obtain junction points, a rather statistical sequencing of larger and smaller particles is mandatory and promotes the probability to obtain junction points. The dependency of the probability to obtain junction points was quantified with respect to the flow of the particle dispersion as shown in Figure 70f. The quantification clearly underlines the dependency of the probability to obtain junction points on the flow conditions. Thus, the introduction of junctions can be tailored not only by the size difference (polydispersity) of the particles as described earlier, but additionally by the flow.

Not only is it possible to generate branched chains by the introduction of junction points, additionally it is possible to form a network of the nanoparticle chains (Figure 70d). The occurrence of a network can be easily tuned based on the probability of a junction point per particle p_j (let us assume only triple valency) and the amount of particles per chain, the degree of polymerization (DP). The critical extent for the formation of a network is reached when:[331]

$$p_j \approx \frac{1}{DP} \tag{7}$$

The relationship between the DP and p_j provides a perfect tool to calculate and predict the formation of a network. Based on the possibility to tune the chain length with time and

concentration and to introduce junction points by controlling the flow and polydispersity, nanoparticle networks can be created.

In conclusion it could be shown that junctions are easily introduced into the chains and can be tailored by the flow conditions and the polydispersity of the sample. Introduction of single junction points into chains as well as the fabrication of whole networks of particles becomes possible.

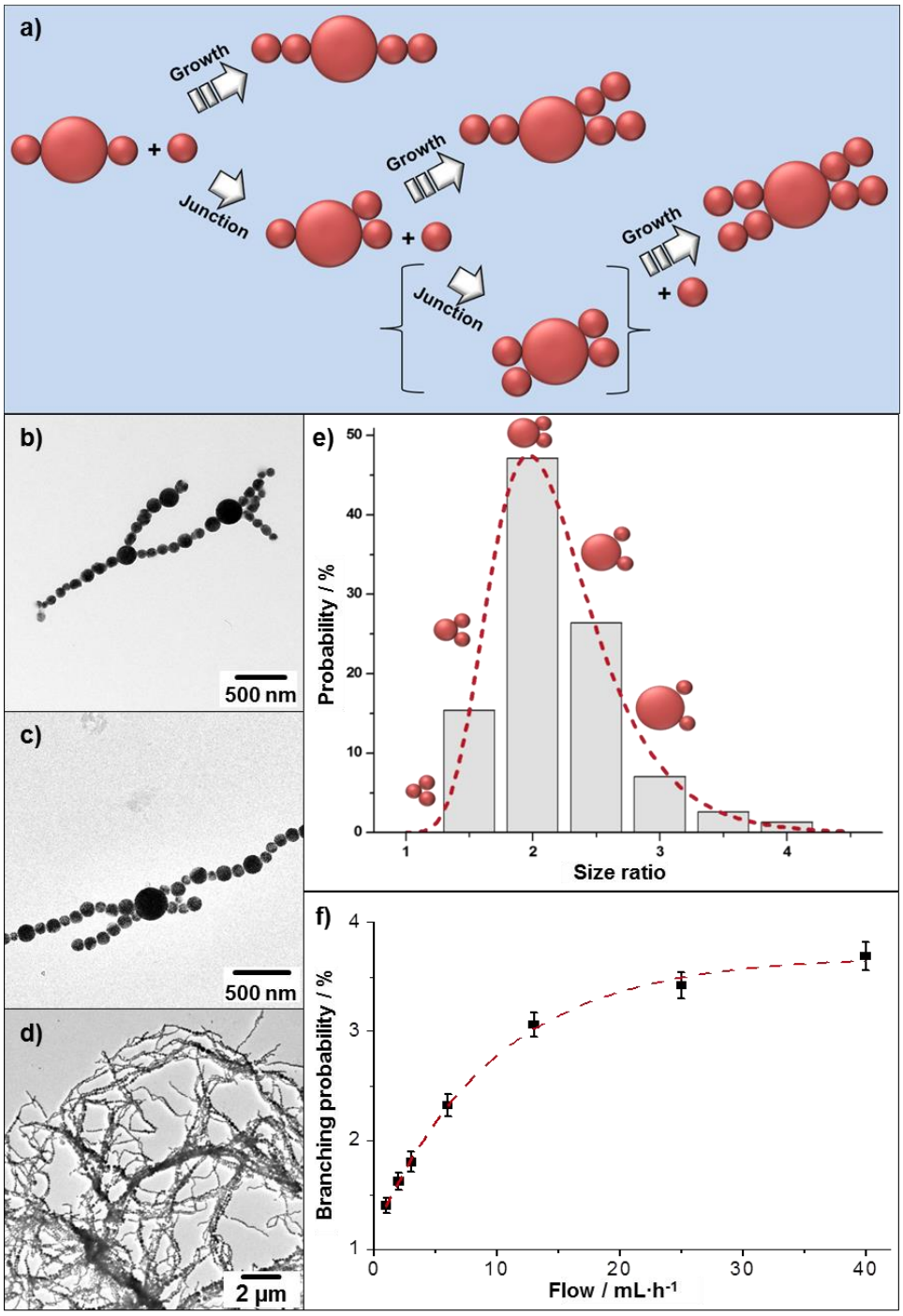

Figure 70. *Introduction of junction points into a growing chain of nanoparticles. a) Scheme illustrating the possibility for creating one or two junctions when a large particle*

meet several small particles. b) TEM image of a branched nanoparticles chain with larger particles of triple valency. c) TEM image of a branched chain with a larger particle of quadruple valency. d) TEM image of a whole network of crosslinked nanoparticle chains by a combination of large chains with high branching probability. e) Graph illustrating the probability to obtain a junction point with respect to the size ratio of neighboring particles. f) Dependency of the percentage of branching points with the flow speed.

4.8 Redoxresponsive Complexes as Reversible Linkers for Smart Nanoparticle Chains – Towards Mimicking Cooperative Behavior of Bacteria

In the present chapter, the synthesis and linear linkage of especially designed nanoparticles is demonstrated in order to mimic the cooperative behavior of some bacteria that form linear colonies. The nanoparticles are built with two functional modules. Firstly, the superparamagnetic magnetite moieties inside the nanoparticles are used as structure-directing agents to create chains of nanoparticles under an external magnetic field resembling arrangements of *streptococci*. Secondly, the surface of the nanoparticles is decorated with bioinspired ligands allowing for interparticle crosslinking with trivalent cations. The crosslinking reaction is reversible and is controlled by a chemical redox-stimulus. Thus, the surface functionality is used as lock/unlock mechanism for the assembly and disassembly of the nanoparticles. The model system shows the possibility to mimic naturally occurring bacterial assemblies. The concept can be used for applications where the shape of the nanomaterials plays a major role in their performance, *i.e.* drug-delivery *in-vivo* and cell uptake, or to separate easily the assembly of the nanoparticles from the reactive medium after their use in their discrete form. The presented results have been accepted for publication in *Chemistry of Materials* as "*Redox-Responsive Nanoparticles and their Reversible Assembly/Disassembly to Mimick Bacteria Cooperative Behavior".*

4.8.1 Motivation and Basic Idea

Since Feynman´s vision of nanobots performing tasks at the micro- and nanoscale[332] it is the dream of many chemists to develop complex materials that adapt their properties in function of their environments and/or intended use.[333] A promising approach is to learn from biology to design synthetic systems with high level of complexity.[334] Bacteria are fascinating organisms that count among the first form of life on Earth. One striking characteristic of bacteria is the variety of shapes they can adapt - from spheroids to rods, spirals, and filaments. Modeled through evolution, the specific shape of a bacterium is largely influenced by their motility, resistance to desiccation and osmotic shock, aptitude to build biofilms, and ability to avoid predation.[335] The morphology of a single species of bacteria is also not static and there is evidence that shape change such as filamentation in stressful environments is a key part of the survival strategy of many pathogenic bacteria.[336-337] The assembly of bacteria into larger

aggregates is of fundamental interest *e.g.* for the understanding of biofilm formation or its prevention.[338] In the case of *bacillus subtilis*, the bacteria form linear chains, then larger structures, and finally form a biofilm.[339-340] A control over disassembly of the bacteria is highly desirable to prevent biofilm formation.

Herein, the synthesis of singular nanoparticle species and their arrangement into chains of several particles *via* a lock/unlock mechanism based on a chemistry used in bacteria to capture and enrich their iron content is described (for experimental details of the multifunctional nanoparticle synthesis and the linear alignment and linkage see chapter 5.8). Unlike the previously reported methods that describe the supraparticular assembly driven by electric field,[150] magnetic field,[120] temperature,[341] pH change,[342-344] entropic or van der Waals interactions,[154, 302] response to biomolecules,[345-346] deformation by irradiation,[347] or coordination chemistry,[348] our strategy is to the best of our knowledge the first to rely on a reversible lock/unlock mechanism of nanoparticles controlled by a redox reaction.

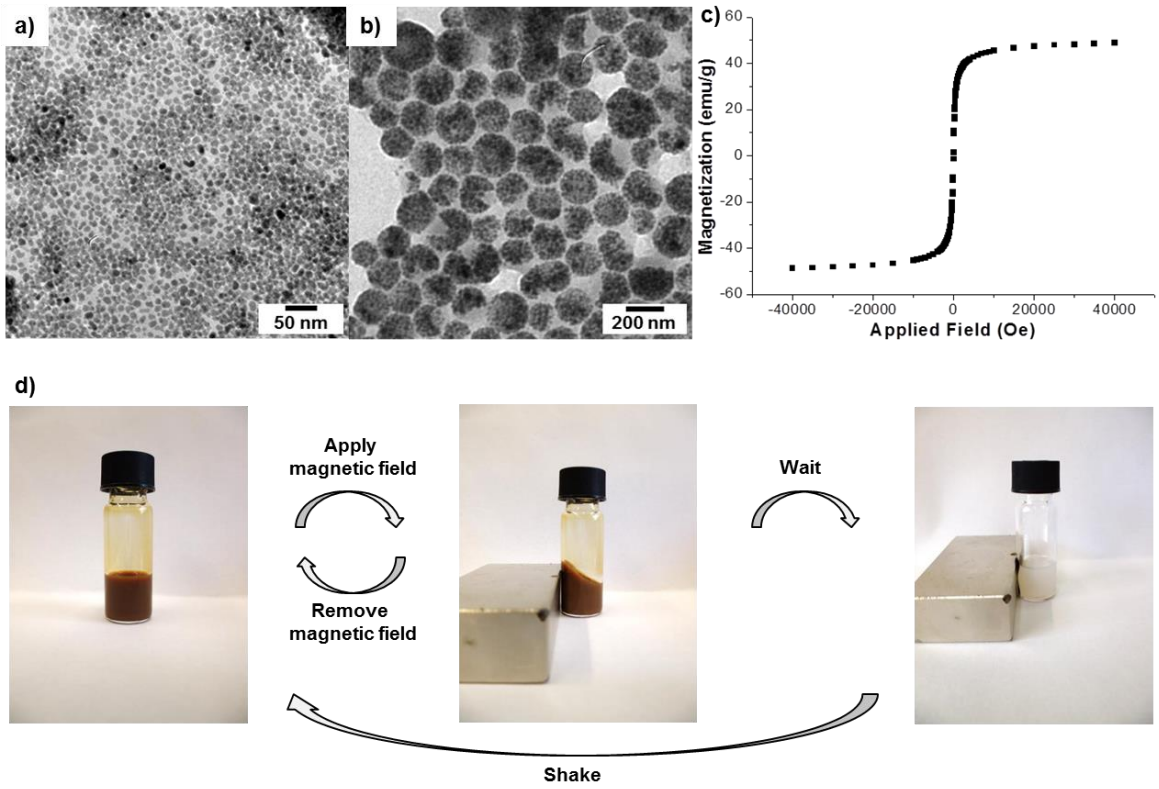

Figure 71. *TEM images of oleate capped iron oxide nanoparticles (a) and polystyrene nanoparticles with encapsulated iron oxide (b). Magnetization curve of the iron oxide loaded polystyrene nanoparticles as determined from SQUID measurements.*

The nanoparticles were designed to display two essential but independent properties: The ability to assemble upon application of an external magnetic field and the lock/unlock mechanism triggered by a redox stimulus. Magnetite nanoparticles with sizes

of 10.2 ± 2.0 nm were employed as structure directing modules in the nanoparticles to drive the supraparticular assembly. An amount of 66 wt% of magnetite was encapsulated in larger (hydrodynamic diameter 152 ± 65 nm) polystyrene nanoparticles by seeded miniemulsion polymerization (see Figure 71) for TEM images of oleate coated magnetite before and after encapsulation into polystyrene nanoparticles). The zeta potential value at neutral pH was determined to be -72 ± 8 mV.

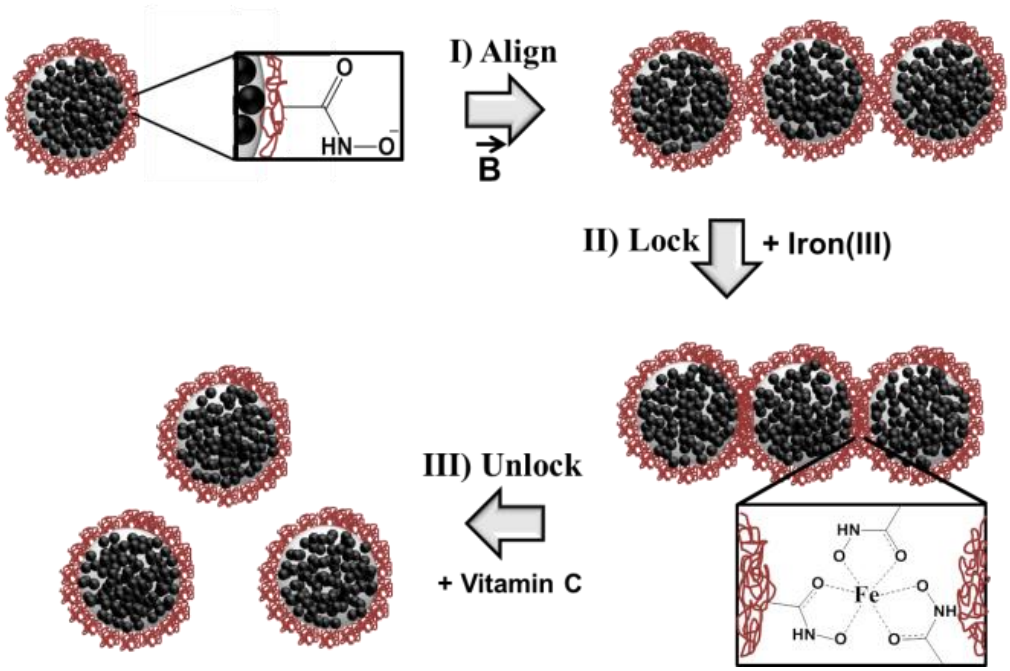

Figure 72. *Schematics depicting the assembly/disassembly of the nanoparticles. Supraparticular assembly is achieved upon application of an external magnetic field (I) followed by interparticle locking through crosslinking of the hydroxyamic acid decorated nanoparticles with ferric ions (II). The suprastructure can be reversed to singular nanoparticles by the addition of a reducing agent, e.g. vitamin C and hence unlocking of the suprastructure (III).*

The locking mechanism was inspired by the formation of polymers by suprapolymer chemistry (Figure 72).[349-350] One prominent example is described by the addition of salt to a solution containing multicoordinating ligands, leading to the formation of an organometallic complex between the coordinating building blocks summing up to a supramolecular polymer.[351] The implementation of the lock/unlock mechanism was achieved by copolymerizing the styrene with synthesized methacrylhydroxamic acid, a comonomer presenting a hydroxyamic functionality. The very high formation constant of hydroxamato-complexes with iron(III) ions ($\log\beta_3 \sim 30^{20}$) and the fast complexation kinetic provide predestined properties for the use of the complex as efficient lock between neighboring particles.[352-353] The high capturing affinity of hydroxamates is observed in the form of natural siderophores,[354-355] *i.e.* iron

chelating compounds that are produced by bacteria to transport ferric ions.[356] In our case, the addition of ferric ions shall ensure an efficient interparticle crosslinking mediated by the biosinspired surface functionalized with hydroxamic acid groups. When reducing the iron(III) to ferrous ions, the complex stability dramatically decreases. The less stable complex is not able to ensure particle cross-linking. An unlocking is hence achieved and the particles disassemble. In analogy, in bacteria, the hydroxamato complex of iron(III) is reduced to iron(II) to release the iron from its manacle, the hydroxamic acid ligands.[357]

4.8.2 Locking and Unlocking

The lock/unlock mechanism was first investigated with methacrylhydroxamic acid in aqueous solution. The synthesized methacrylhydroxamic acid was mixed at pH ~9-10 with a 10 mmol aqueous solution of the hydoxyamic acid and a 5 mmol aqueous solution of $FeCl_3$. A red color appeared instantaneously with an absorption maximum at ~480 nm identified by UV-Vis spectroscopy (Figure 73a). The reversibility of the complex formation was verified by adding a 20 mmol vitamin C solution to the iron(III) complex. The color disappeared. The magnitude of electric charges at the double layer of the poly(styrene-*co*-methacrylhydroxyamic acid)/magnetite hybrid nanoparticles was monitored as a function of the pH by zeta potential measurements (Figure 73b). A significant decrease of the zeta potential was observed around the pK_a of hydroxyamic acids (~8-9) due to the deprotonation of the acidic group, revealing the presence of the functional groups on the nanoparticles surface.[352] The magnetic properties of the iron oxide/polymer hybrid nanoparticles were investigated *via* SQUID measurements. The nanoparticles show a superparamagnetic behavior (only minute hysteresis at room temperature) with a saturation magnetization of 49 $emu \cdot g^{-1}$ (Figure 71).

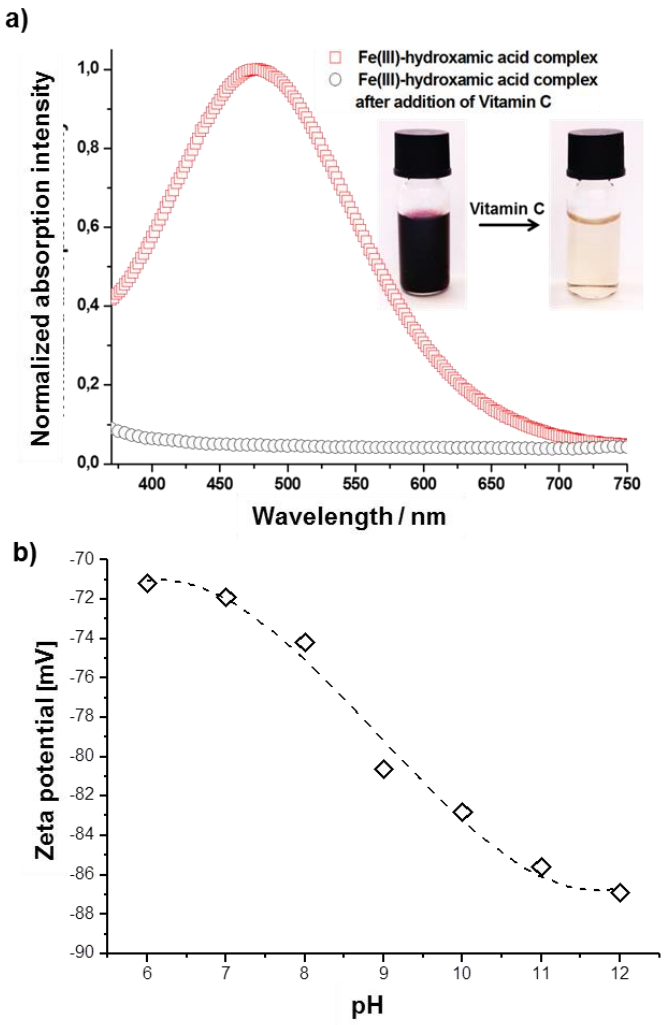

Figure 73. *a) Absorption spectrum of iron(III) complexed with hydroxamic acid (red curve) and after addition of vitamin C (black curve). b) Deprotonation of hydroxamic acid functionalized nanoparticles monitored by zeta potential measurements.*

The supraparticular assembly was achieved by passing a controlled flow of nanoparticles dispersions through a static ring magnet. The suprastructure was chemically locked by complex formation by addition of an aqueous solution containing 1 $mg \cdot L^{-1}$ $FeCl_3$ that was also passed through the static magnet. It is important to carefully control the concentration of iron(III) salt. When the salt concentration is too high (> 2 $mg \cdot L^{-1}$ $FeCl_3$), precipitation due to collapse of the electrostatic stabilization of the nanoparticles is observed. The locked supraparticular structures can be obtained by fast removal of the ring magnet. Analysis of the size and shape of the obtained suprastructures were evaluated by dynamic light scattering (DLS) and transmission electron microscopy (TEM), respectively (Figure 74). The average hydrodynamic diameter of the locked suprastructure was ~1 µm, *i.e.* much larger than the initial singular nanoparticles. Most of the nanoparticles were arranged in a linear or pseudo-linear fashion in twisted chains of nanoparticles (Figure 74b), resembling arrangement of *streptococci* (Figure 74d).

The disassembly or unlocking of the suprastructure was realized by adding 1 $g \cdot L^{-1}$ of an aqueous vitamin C containing solution and therewith forming a reducing medium. Removal of the interparticle crosslinking and disassembly onto mostly singular entities was shown by TEM and DLS. When aggregating the particles without the presence of a magnet through addition of larger quantities of iron(III) (> 10 $mg \cdot L^{-1}$ $FeCl_3$), the particles form 3-dimensional aggregates, owing to a collapse of the electrostatic stabilization. Upon addition of vitamin C, hardly any disassembly can be observed since the particles are not explicitly connected by hydroxamato-complexes and the reversibility of the linear arrangement is not possible by simply unlocking the complex. Thus, the size of the linear nanoparticles aggregates can be molecularly controlled through complex formation/destruction which is mediated by electrostatic crosslinking and redox stimulus for the assembly and disassembly processes, respectively.

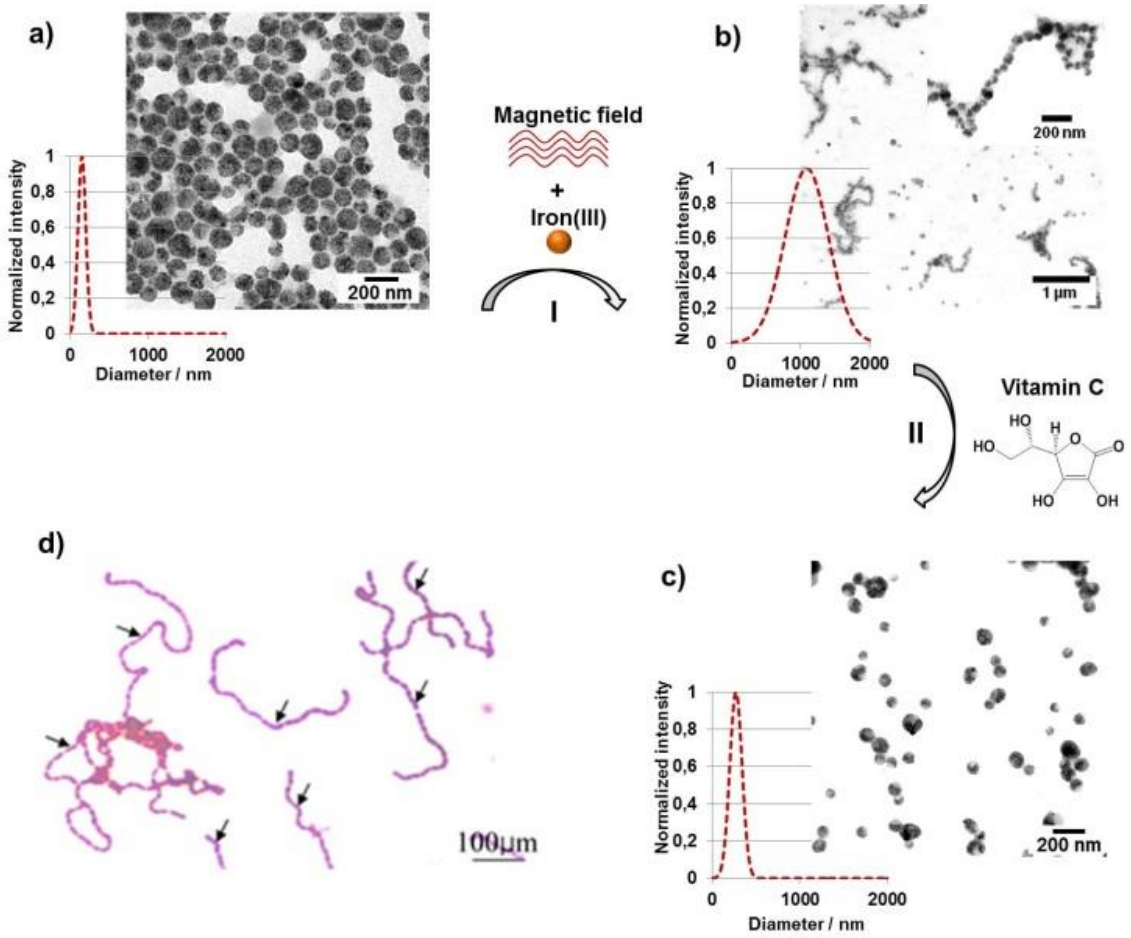

Figure 74. *I) Supraparticular assembly of magnetic nanoparticles (a) in a pseudo-linear fashion and locking of the suprastructure by crosslinking with ferric ions to form stable suprastructures (b). II) Unlocking of the suprastructure by reduction of iron(III) to iron(II) by vitamin C, leading to a disassembly into singular nanoparticles (c). d) Optical microscopy image of Streptococci arrangements.*[358]

In conclusion, a novel strategy for the synthesis of nanoparticles displaying supraparticular assemblies mimicking the cooperative arrangement of *streptococci* bacteria has been demonstrated. The magnetic functionality of the nanoparticles was used for the non-permanent formation of pseudo-linear suprastructures. Because the nanoparticles surface was decorated with bioinspired hydroxyamic acid ligands, the obtained structures could be locked by electrostatic crosslinking with ferric ions. By reducing the ferric ions to ferrous ions with vitamin C, the cohesion between individual nanoparticles in the suprastructure becomes loose and singular nanoparticles are recovered. The model system shows the possibility to mimic naturally occurring bacterial assemblies. The concept can be used for applications where the shape of the nanomaterials plays a major role in their performance, *i.e.* drug-delivery *in-vivo* and cell uptake, or to separate easily the assembly of the nanoparticles from the reactive medium after their use in their discrete form. It is known that phagocytosis of particles is inhibited when they display high aspect ratios (> 20).[359] Therefore the formation of ~1 μm suprastructures can be a strategy to avoid phagocytosis *in-vivo* and release individual nanoparticles as drug-delivery carriers suitable for cell uptake in a reducing medium. Additionally, the portfolio of functionality of such nanoparticles could be widened by using other hydroxyamic acid derivatives due to their additional use as antibacterial substances.

5 Experimental Section

Materials

All chemicals were used as received unless otherwise stated. All solvents were purchased from Sigma Aldrich and used without further purification. The monomers methyl methacrylate, acrylic acid, pentafluorostyrene, and styrene were passed through an aluminum oxide column before use to remove the stabilizer.

Acrylamide (> 99%, Sigma Aldrich), acrylic acid (99%, Sigma Aldrich), agarose (Top vision low melting point agarose from Fermentas), (3-aminopropyl)trimethoxysilane (97%, Sigma Aldrich), ammonium hydroxide (28% solution in water, VWR), ascorbic acid (> 99%, Sigma Aldrich), 2,2'-azobis[2-[1-(2-hydroxyethyl)-2-imidazolin-2-yl]propane]dihydrochloride (VA-060, Wako) recrystallized from 2-propanol before use, biomer ® L9000 (Mw = 130 000 g/mol, determined by GPC in chloroform; Biomer), 2,2`-bipyridine (> 99%, Sigma Aldrich), bromoacetic acid (99%, Sigma-Aldrich), α-bormoisobutyric acid (> 98%, Sigma Aldrich), carboxymethyl-dextran sodium salt (Sigma-Aldrich), copper(II) bromide (99%, Sigma Aldrich), 1-ethyl-3-(3-dimethylaminopropyl) carbodiimide (> 98%, Sigma Aldrich), ferric chloride hexahydrate ($FeCl_3 \cdot 6H_2O$, 99%, Acros), ferrous chloride tetrahydrate ($FeCl_2 \cdot 4H_2O$, 99%, Merck), gold(III) chloride hydrate (> 99%, Sigma Aldrich), *n*-hexadecane (99%, Fisher), 1,2-hexadecanediol (90%, Sigma-Aldrich), 1,6-hexanediol (99%, Sigma-Aldrich), hydroxyethyl starch (HES, M_w = 200,000 g·mol^{-1}, Fresenius kabi), hydroxylamine hydrochloride (> 99%, Sigma Aldrich), IR-780 iodide (> 98%, Sigma Aldrich), iron(III)acetylacetonate ($Fe(acac)_3$, 97%, Sigma-Aldrich), Lubrizol®U (Polyisobutylenesuccinimidopentamine, M_w = 384 - 875 g·mol^{-1} as determined from SEC, HLB-Value < 7, Lubrizol, France), L-lysine hydrochloride (> 98%, Sigma Aldrich), manganese(II)acetylacetonate ($Mn(acac)_2$, Sigma-Aldrich), methyl methacrylate (99%, Sigma Aldrich), *N*-(2,6-diisopropylphenyl)-perylene-3,4-dicarbonacidimide (PMI, BASF), 1-octadecene (92%; Merck), oleic acid (58%, Riedel-de Haen), oleylamine (70%, Sigma-Aldrich), 2,3,4,5,6.pentafluorostyrene (> 99%, Sigma Aldrich), poly(acrylic acid) (M_w = 450,000 g·mol^{-1}, 35$_{wt.}$% solution in water, Sigma Aldrich), poly[(ethylene-*co*-butylene)-*b*-(ethylene oxide)] (KLE, (P(E/B-*b*-EO), with M_w = 3,700 g·mol^{-1} for P(E/B) and M_w = 3,600 g·mol^{-1} for P(EO) unless otherwise stated), polyglycerol polyriccinolate (PGPR 90, Danisco), polyoxyethylene (20) sorbitan monooleate (Tween 80, Sigma-Aldrich), polyvinylalcohol (PVA, 88% hydrolyzed, M_w ~ 25,000 g·mol^{-1}, Sigma-Aldrich), poly(vinyl pyrrolidone) (M_w = 40.000 g·mol^{-1}, Sigma Aldrich), potassium persulfate

(99%, Aldrich), sodium chloride (99%, Fischer), sodium hydroxide (99%, Riedel-de Haen), sodium *n*-dodecyl sulfate (SDS, 99%, Merck), styrene (> 99%, Aldrich), sodium *p*-styrenesulfonate, (> 90%, Aldrich), sulforhodamine 101 (95%, Sigma-Aldrich), tetraethyl orthosilicate (> 99%, Sigma Aldrich), tetramethylammonium hydroxide (TMAOH, 10% solution in water, Merck), toluene 2,4-diisocyanate (TDI, 98%, Aldrich), triethylamine (> 98%, Sigma Aldrich), α,α,α-trifluorotoluene (> 99%, Sigma Aldrich), trisodium citrate dihydrate (Sigma Aldrich), 1-vinyl-2-pyrrolidinone (> 99%, Sigma Aldrich).

Instrumentation

Determination of the hydrodynamic radii was done by dynamic light scattering (DLS) on a NICOMP Zetasizer at an angle of 90°. The dispersion was diluted with the corresponding continuous phase and measured at 25 °C. Zeta potential was measured using a Malvern Instruments Zeta Nanosizer at a detection angle of 173°. All samples were highly diluted in an aqueous 10^{-3} M KCl solution before measurement. The solid content was determined gravimetrically, typically by weighing the samples before and after freeze drying. Scanning electron microscopy (SEM) micrographs were performed on a Hitachi SU8000 microscope at an extractor voltage of 3.0 kV. For energy dispersive X-ray spectroscopy (EDX) and element mapping, a Hitachi SU8000 microscope equipped with a Bruker Quantax 5010 spectrometer at an operation voltage of 5 kV was used. The nanocapsules dispersions were diluted with the corresponding continuous phase, drop-casted on a silicon wafer, and air dried under ambient conditions. Transmission electron microscopy (TEM) was performed on a Zeiss EM912 at 80 kV working voltage. For sample preparation, the sample dispersions were diluted with the corresponding solvent and drop-casted on a carbon coated mesh 300 or 400 copper grid. The determination of the inorganic content in the samples was done by thermogravimetric analysis (TGA) on a thermobalance Mettler Toledo TGA/SDTA 851. The freeze dried sample was heated from room temperature to 1000 °C with a heating rate of 10 °C·min^{-1} under nitrogen atmosphere. Size exclusion chromatography (SEC) was used for the determination of molecular mass distributions with a PSS SecCurity (Agilent Technologies 1260 Infinity). THF or DMF were used as solvents at a flow rate of 1 mL·min^{-1} and a column temperature of 30 °C and the calibration was carried out with polystyrene standards purchased from Polymer Standard Service GmbH (PSS). A UV S3702 detector at 254 nm wavelength or a refractive index (RI) detector was used. Potassium bromide pellets containing 1 wt% of sample were used for FTIR measurements conducted on a BX spectrometer from Perkin Elmer. X-Ray Diffraction (XRD) measurements were

performed on a Philips PW 1820 diffractometer with monochromatic CuKα radiation (λ = 1.5418 Å, 40 kV, 30 mA, 5 s, $\Delta\theta$ = 0.02). A vibrating sample magnetometer (VSM, Oxford Instruments Maglab) was used to investigate magnetic properties of the manganese ferrite and iron oxide nanoparticles. Field cooled (FC) and zero field cooled (ZFC) temperature dependent measurements were performed in a 15 mT magnetic field to determine the blocking temperature. The size of the magnetic moment was determined by measurement of hysteresis loops in fields up to 4 T at room temperature (300 K). Quantitative determination of released dye by measuring the fluorescence intensity was done using a Tecan Infinite M1000 Reader. Absorption measurements were also performed using the same Tecan Reader. Nuclear magnetic resonance (^{1}H-NMR) spectra were measured using a 300 MHz Bruker spectrometer. Application of an alternating magnetic field was achieved using a home-built high frequency induction device (HIG) which is placed at the University of Ulm. The apparatus is equipped with four copper wire coils covering a frequency range from 150 to 820 kHz. The magnetic field can be varied between 0.3 and 5.0 kA·m^{-1}. The teflon tube sample holders (height 12 cm, i.d. 0.7 cm, o.d. 1.0 cm) are filled with 2 ml of sample dispersion. The temperature of the samples can be measured with a non-metallic temperature probe (GaAs) equipped with teflon coated fiber optics from OPTOcon GmbH (Dresden, Germany). For or T_1 and T_2 measurements, a 1.5 T magnet in vertical design from Bruker (Karlsruhe, Germany) was used. The magnet was equipped with a Maran DRX spectrometer from Oxford Instruments (Oxfordshire, UK). Temperature control during measurement was achieved in the NMR coil by application of a heated stream of nitrogen gas using a home-built liquid nitrogen evaporator and a VT-1000 temperature controller from Bruker (Karlsruhe, Germany). Sonication of all samples to form a miniemulsion was done on a ½ inch tip Branson Sonifier W-450-Digital. Glass transition temperatures were determined from DSC measurements performed on a DSC 822 Mettler Toledo in a temperature range from -140 to 200 °C with a heating rate of 10 °C.

5.1 Encapsulation and Stimuli-Responsive Release from Polymer Nanocapsules

5.1.1 Magnetic Tracing and Releasing from Nanocapsules for Combined Imaging and Therapy

5.1.1.1 The Magnetic Stimulus

5.1.1.1.1 Synthesis of Manganese Ferrite Nanoparticles

The synthesis of superparamagnetic $MnFe_2O_4$ nanoparticles was performed according to a slightly modified procedure described in literature.[41, 360] 0.942 g (3 mmol) oleic acid, 1.15 g (3 mmol) oleylamine, 0.253 g (1 mmol) $Mn(acac)_2$, 0.706 g (2 mmol) $Fe(acac)_3$ and 1.438 g (5 mmol) hexadecanediol were added to 10 ml *n*-octadecene. After drying for 1 h at 50 °C under vacuum, the flask was purged two times with nitrogen. Under nitrogen atmosphere, the mixture was heated slowly to 200 °C and kept at the temperature for 45 min. The temperature was increased steadily to 315 °C (heat rate of 1.5 $°C \cdot min^{-1}$) and held at the temperature for 30 min. The heat source was removed and the mixture was cooled down to room temperature. Isopropanol was added to precipitate the nanoparticles which were then separated from the reaction solution by centrifugation. Purification was achieved by redispersion of the nanoparticles in *n*-hexane, precipitation through addition of acetone and centrifugation. The purification procedure was repeated two times and the black precipitate dried overnight under vacuum to give a black powder of ~10 nm in diameter $MnFe_2O_4$ nanoparticles. Larger, ~14 nm sized $MnFe_2O_4$ nanoparticles were obtained by adding the 10 nm $MnFe_2O_4$ nanoparticles as seeds to the above described procedure. Using the 14 nm $MnFe_2O_4$ nanoparticles as seeds to the above described procedure, ~16 nm $MnFe_2O_4$ nanoparticles were obtained.

5.1.1.1.2 Synthesis of Carboxymethylated Poly(vinyl alcohol) (CMPVA)

A procedure published by Liong et al. was used for the synthesis of CMPVA.[41] 3 g (61 mmol based on monomer) of low molecular weight PVA (preferably M_w = 25,000 $g \cdot mol^{-1}$, 88% hydrolysed) were dissolved in 90 mL deionized water at 80 °C. 5.04 g (126 mmol) of sodium hydroxide was dissolved in 10 mL water and the solution was added dropwise to the PVA solution under vigorous stirring followed by the

slow addition of 10.1 g (72.9 mmol) of bromoacetic acid. The reaction mixture was stirred for 3 days at room temperature and filtered. The solution was neutralized to pH 6 with 1N hydrochloric acid and 500 mL of ethanol added followed by stirring for 30 min. After centrifugation, the product was dried at 45 °C under vacuum overnight to give 2.77 g of a colorless solid.

5.1.1.1.3 Transfer of the Manganese Ferrite Nanoparticles into Aqueous Environment

50 mg (or alternatively 100 mg) of 16 nm oleate- and oleylamine-capped $MnFe_2O_4$ nanoparticles were added to 5 mL of an aqueous TMAOH solution (10 wt%) followed by sonication for 1 h in an ultrasonication bath. Most of the TMAOH could be removed through centrifugation and the particles were redispersed in 50 mL water (containing 0.1 wt% TMAOH). For a further purification, the centrifugation was be repeated several times. For the stabilizer exchange, 50 mg of CMPVA were dissolved in 50 mL of hot water and slowly added to the $MnFe_2O_4$ dispersion followed by sonication for 10 min using an ultrasonication bath. The dispersion was stirred overnight and centrifuged. After redispersion in aqueous solution the magnetic nanoparticles are suitable for encapsulation into polymer nanocapsules.

5.1.1.2 Thermolabile Nanocapsules[207]

In order to study the reaction of a thermolabile azo-diol monomer into the shell of nanocapsules, the following synthesis was performed and the inserted monomers as well as the resulting polymer analyzed *via* ^{1}H-NMR spectroscopy. Therefore, 3.5 mg (0.06 mmol) NaCl, 38 mg (0.321 mmol) 1,6-hexanediol and 132 mg (0.321 mmol) VA-060 were dissolved in 750 mg of demineralized water. Separately, 70 mg of P(E/B-*b*-EO) with a molecular weight of ~11,000 g·mol^{-1} (consisting of P(E/B) of ~3,700 g·mol^{-1} and P(EO) of 7,300 g·mol^{-1}) were dissolved in 6 g of cyclohexane at increased temperature (60 °C). The two phases were mixed and pre-emulsified in a beaker by high magnetic stirring (1400 rpm) followed by sonication at a 1/2 inch tip sonifier for 3 min under ice cooling (70% amplitude, 10 s pulse, 5 s pause). After sonication, a solution containing 168 mg (0.965 mmol) of 2,4-toluenediisocyanate in 4 g cyclohexane was added dropwise and the reaction mixture stirred over night at room temperature. For ^{1}H-NMR analysis, the dispersion was purified from excess surfactant by centrifugation and redispersion in cyclohexane. The purification step was repeated two times and the nanocapsules freeze dried and dissolved in d_7-DMF for ^{1}H-NMR studies.

5.1.1.3 Magnetic Nanocapsules with Thermolabile Shell

Nanocapsules with incorporated $MnFe_2O_4$ nanoparticles were prepared through a polyaddition reaction at the interface of inverse miniemulsion droplets. Therefore, different amounts of $MnFe_2O_4$ nanoparticles (50 mg, 100 mg and 200 mg) were redispersed in 1 mL deionized water through sonication for 5 min. 132 mg of VA-060 (thoroughly purified by recrystallization!) and 38 mg of 1,6-hexanediol were dissolved in 0.5 mL deionized water and both aqueous phases combined. Separately, 75 mg of PGPR were dissolved in 6 g cyclohexane. All phases were combined, mechanically stirred for 1 h to obtain a pre-emulsified system and sonified under ice-cooling for 3 min (1/2 inch tip, 70% amplitude, 10 s pulse, 5 s pause). To the resulting miniemulsion, a solution of 80 mg of TDI in 6 g cyclohexane was added dropwise under vigorous stirring. After stirring overnight, the nanocapsules were separated from free surfactant by centrifugation and discarding of the supernatant was followed by redispersion in cyclohexane. For redispersion in water, 0.5 ml of the nanocapsule dispersion in cyclohexane were added to 5 mL of a 0.2 wt% Tween 80 containing aqueous solution under vigorous stirring. After vigorous stirring for 4 h at room temperature in an open vessel to evaporate the cyclohexane, the capsule dispersion was purified magnetically.

5.1.1.4 Magnetic Field Induced Release Studies

For release studies from the magnetic nanocapsules with thermolabile shell, the hydrophilic model dye Sulforhodamine 101 was encapsulated in a typical nanocapsule synthesis as described in chapter 5.1.1.3. In order to study the release of the fluorescent dye, 2 mL of the aqueous capsule dispersion (0.1 wt% solid content) were inserted into a teflon tube. An alternating magnetic field with a frequency of 720 kHz and a field strength of 4.5 $kA \cdot m^{-1}$ was applied. Samples of 0.2 mL of capsule dispersion were drawn after 0, 5, 15, 30 and 60 min. Separation of the nanocapsules from the continuous aqueous phase was achieved by putting the sample on a permanent magnet in order to precipitate the magnetic nanocapsules. The supernatant was then analyzed *via* fluorescence spectroscopy to quantify the dye.

5.1.1.5 Relaxivity Measurements for MRI

All relaxivity measurements including interpretation of the results were done by Sandro Ebert (subgroup of Kerstin Münnemann). For the measurements the sample dispersions were embedded in a 1 wt% agarose phantom. Therefore, the sample

dispersion was mixed with a 2 wt% agarose solution (1:1 ratio), filled into a 5 mm NMR tube and cooled to room temperature. The agarose matrix prevents the nanoparticles from settlement and does not influence the relaxivities r_1 and r_2.[361] For measurement, all samples were heated to 37 °C in a tempered water bath and kept at the temperature during measurement. The transverse relaxation time ^{1}H-T_2 was measured with a Carr Purcell Meiboom Gill (CPMG) echo train. The echos were integrated and the resulting data points fitted with a mono-exponential curve in order to determine the T_2 times. For each sample, five different concentrations were measured to determine the relaxivity values.

5.1.1.6 Cell Toxicity Assay

The cell toxicity assays were conducted by Stephanie Tomcin (subgroup of Volker Mailänder). In order to determine the effect of $MnFe_2O_4$ loaded nanocapsules on cells, a cell toxicity assay was conducted similarly to an assay described in literature.[362] Therefore, HeLa cells were incubated in Dulbecco´s Modified Eagle Medium (DMEM, Invitrogen, Germany, supplemented with 10 vol% fetal calf serum, 100 units·mL^{-1} penicillin together with 100 mg·mL^{-1} streptomycin, and 2 mM GlutaMAX^{TM}, all supplements are from Invitrogen, Germany) without phenol Red and with different amounts of $MnFe_2O_4$ loaded nanocapsules (75, 150, 300, 450, 600 and 750 µg·mL^{-1}) for 24 h in a humidified incubator containing 5% CO_2 atmosphere at 37 °C. Incubation was followed by an MTS assay in medium according to the protocol of the manufacturer of CellTiter 96 Aqueous One Solution Cell Proliferation Assay (Progema, USA).

5.1.1.7 Other Possibilities for the Synthesis of Aqueous Dispersible Iron Oxide Nanoparticles and Their Encapsulation into Nanocapsules

The basic iron oxide nanoparticles for the surface functionalization described in the following chapters were all oleate-capped and were synthesized as reported in chapter 5.6.1.1.1.

5.1.1.7.1 Water-Dispersible Iron Oxide Nanoparticles Coated with L-lysine

The synthesis of L-lysine coated iron oxide nanoparticles was done as described in the procedure described by Patel et al.[35] Briefly, 338 mg (1.25 mmol) of iron(II)chloride tetrahydrate and 497 mg (2.5 mmol) of iron(III)chloride hexahydrate were dissolved in 2 M hydrochloric acid aqueous solution. Separately, 50 mL of a 0.15 M aqueous sodium

chloride solution was prepared. This solution was placed in a three necked flask, flushed with Argon and heated to 80 °C. 1.83 g (10 mmol) of the amino acid (L-lysine hydrochloride) was added and the mixture was stirred until a clear solution was obtained. Then the iron(II, III) chloride solutions were added followed by the addition of an aqueous 28% ammonium hydroxide solution under vigorous stirring until pH 9-10 was reached. Vigorous stirring was continued for 24 h.

During the reaction, a precipitate appeared which could be isolated by magnetic separation and the supernatant was discarded. Demineralized water was added and the magnetic particles were separated again by applying an external magnet. The purification procedure was repeated three times. The analysis of the obtained iron oxides was done by DLS measurements and TEM imaging.

5.1.1.7.2 Water-Dispersible Iron Oxide Nanoparticles Coated with Carboxymethyl-dextran

Typically, 50 mg of oleate-coated iron oxide nanoparticles were redispersed in 2 g of dichloromethane. Separately, 100 mg of carboxymethyl-dextran ($M_w \leq 40{,}000$ g·mol^{-1}) was dissolved in 10 mL demineralized water. Both phases were mixed and sonicated for 10 min under water cooling (~25 °C) using a ½ inch tip sonifier (50% amplitude, 5 s pulse, 5 s pause). The obtained miniemulsion was then stirred in an open vial for 1 h at 40 °C. The resulting iron oxide nanoparticles stabilized by carboxymethyl-dextran were analyzed *via* DLS measurements and TEM imaging. In order to concentrate the dispersion, the iron oxide nanoparticles were separated by centrifugation from the continuous phase and redispersed in a small volume of demineralized water.

5.1.1.7.3 Water-Dispersible Iron Oxide Nanoparticles Coated with Lubrizol®U

For the coating procedure, 50 mg of the oleate-capped iron oxide nanoparticles were redispersed in 2 g of dichloromethane containing 50 mg of Lubrizol®U. 10 mL of demineralized water were added and the two phase system was sonified with a ½ inch tip sonifier for 15 min at 25 °C (50% amplitude, 5 s pulse, 5 s pause). After sonication, the miniemulsion was stirred for 2 h at 40 °C. Analysis of the nanoparticles coated with Lubrizol®U was done as described in chapter 5.3.1.7.2.

5.1.1.7.4 Encapsulation of the Aqueous Dispersions of Iron Oxide Nanoparticles into Polymer Capsules

50 mg of iron oxide nanoparticles with different functionalizations (chapters 5.1.1.7.1-5.1.1.7.3) were introduced into a typical capsule synthesis at the interface of inverse miniemulsion droplets. The synthesis was carried out as described in chapter 5.1.3.1.2 with slight changes. The gold nanoparticles were replaced by the iron oxide nanoparticles and the co-monomers were not VA-060 and hexanediol, but 100 mg of hydroxyethylstarch (HES) with M_w = 200,000 g·mol^{-1}.

5.1.2 Thermoresponsive Capsules

5.1.2.1.1 Capsule Synthesis

For the disperse phase, 200 mg of poly(acrylic acid) with M_w = 250,000 g·mol^{-1}, 1 mg of sulforhodamine 101, and 100 mg of sodium chloride were dissolved in 1.4 g of water at 80 °C for 1 h. Separately, 70 mg of PGPR was dissolved in 7.5 g of cyclohexane (continuous phase I) and 15 mg of PGPR together with 120 mg of TDI was dissolved in 5 g cyclohexane (continuous phase II). The dispersed phase and the continuous phase I were combined and stirred for 1 h at 1400 rpm at 80 °C in a closed vial. Then, the pre-emulsion was sonicated with a Branson ½ inch tip Sonifier for 3 min at 60 °C (70% amplitude, 10 s pulse, 5 s pause). After sonication, the miniemulsion was cooled to room temperature and the continuous phase II was added dropwise within 5 min. The reaction mixture was stirred overnight and the resulting nanocapsules investigated via DLS and TEM. Purification was achieved by centrifugation. Redispersion was performed as follows: 0.5 mL of the nanocapsules dispersion in cyclohexane was mixed with 10 mL of a 0.1 wt% SDS aqueous solution and stirred at 2000 rpm for 5 h in an open vial at room temperature.

5.1.2.1.2 Release Experiments

The aqueous nanocapsule dispersion was heated quickly from room temperature to 80 °C in a preheated oil bath and kept at that temperature for 10 min. A sample was taken and the dispersion was quickly cooled down to room temperature and kept at room temperature for 50 min. Another sample was taken and the dispersion heated to 80 °C again. The procedure was repeated several times and the drawn samples centrifuged. The

supernatant after centrifugation was analyzed *via* fluorescence spectroscopy in order to quantify the released dye.

5.1.3 Encapsulation of Gold Nanoparticles for the Triggered Release from Nanocapsules by Irradiation

5.1.3.1.1 Synthesis of Gold Nanoparticles

Before performing the synthesis, all the glasswares were washed with *aqua regia* and rinsed several times with demineralized water. For the synthesis, 200 mg of trisodium citrate was dissolved in 700 mL of demineralized water and the solution heated to reflux. Then, 60 mg of chloroauric acid in 10 mL of demineralized water was added instantly and the solution was vigorously stirred under reflux for an additional 15 min. After cooling to room temperature, the gold nanoparticles were centrifuged in order to increase the concentration of the particles in dispersion.

5.1.3.1.2 Encapsulation of Gold Nanoparticles into Capsules

The gold nanoparticles were concentrated by centrifugation up to 50 $mg \cdot mL^{-1}$. For the synthesis, 1 mL of the gold dispersion was mixed with 132 mg of VA-060 and 38 mg of 1,6-hexanediol in 0.5 mL of demineralized water. Separately, 60 mg of KLE (see chapter 5.1.1.2) was dissolved in 6 g of cyclohexane (continuous phase I) and 168 mg TDI was mixed with 4 g of cyclohexane (continuous phase II). The continuous phase I was mixed with the gold dispersion and stirred to form a macroemulsion. Then the two phase system was sonified for 3 min under ice cooling (70% amplitude, 10 s pulse, 5 s pause) using a 1/2 inch tip sonifier. The obtained miniemulsion was vigorously stirred and the continuous phase II was added dropwise within 5 min, and stirred overnight at room temperature. The analysis of the dispersion was done by DLS measurements and TEM imaging.

5.1.4 Double Shell Polymer Hybrid Capsules - Towards Multiresponsive Systems

The nanocapules were prepared similar to the recipe described in chapter 5.1.1.2. Instead of 750 mg of demineralized water, only 600 mg were used and 150 mg of acrylic

acid, acrylamide, or *N*-vinylpyrrolidone were added. After capsule formation, the monomer was grafted to the shell. Therefore, an argon stream was bubbled through the dispersion for 10 min and the dispersion was heated to 60 °C for 16 h. For analysis of the double shell structure, TEM and SEM imaging was used for visualization. The monomer conversion was determined from the solid content. Molecular weights were determined *via* GPC analysis.

5.2 Multifunctional Hybrid Nanoparticles

5.2.1 Anisotropic Magnetic Nanoparticles

5.2.1.1 Synthesis of the Polystyrene Nanoparticles Loaded with Iron Oxide

The inserted oleate-capped iron oxide nanoparticles were synthesized as described in chapter 5.6.1.1.2. The hybrid polymer/magnetite nanoparticles were prepared as published earlier.[236] Briefly, 1 g of oleic acid coated magnetite nanoparticles were redispersed in 0.5 g *n*-octane by sonication for 30 min in an ultrasound bath. Then, the dispersion was stirred with 24 ml of a 0.5% aqueous solution of SDS for 30 min mechanically. The two-phase system was sonified with a ½ inch tip Branson W-450-D sonifier for 1 min at 50% amplitude (5 s pulse, 5 s pause) and further mechanically stirred at 200 rpm, creating an emulsion A. The emulsion B is created by combining the oil phase consisting of 1.2 g of styrene and 20 mg of *n*-hexadecane with an aqueous solution of 25 mg SDS and 50 mg sodium styrene sulfonate in 24 g water. The miniemulsion was homogenized by sonication with the same parameter as for emulsion A, except that the amplitude was reduced to 10%. 25.5 g of emulsion A and 25.3 g of emulsion B are then added into a 50 ml flask and mechanically-stirred at 250 rpm for 60 min, with an initial Argon bubbling for 10 min. 10 mg KPS was then added and the flask heated to 80 °C and stirred further for 20 h. Purification was performed magnetically. Analysis was done *via* TEM imaging, DLS measurements, solid content determination, TGA and VSM.

5.2.1.2 Uniaxial Stretching of the Hybrid Nanoparticles

The stretching procedure is described in literature in more detail.[236, 363] 3.5 wt% of PVA was dissolved at 80 °C in demineralized water. After cooling to room temperature,

the solution was mixed with the colloid dispersion (5-8 wt% of colloids with respect to PVA) and stirred for 2 h. The obtained dispersion was then spread on a substrate and let dry overnight. The film was heated to 140 °C in an oil bath and stretched to the desired length. After stretching, the film was cooled down to room temperature and purified by dissolving the film in a mixture of isopropanol and water (3/7 v/v). Purification from excess PVA was achieved by centrifugation of the particles and their redispersion in the same solvent mixture several times. Analysis of the stretched particles was done by TEM and SEM imaging and by determination of the solid content.

5.2.2 Luminescent Magnetic Hybrid Nanoparticles

The surfmer was synthesized by Viktor Fischer as described elsewhere.[244] The oleate-capped iron oxide nanoparticles were synthesized as described in chapter 5.6.1.1.2. Surface-functionalized polystyrene nanoparticles with a magnetic core were prepared from two miniemulsions. The first miniemulsion was obtained by mixing of water (24 g) containing a small amount of the phosphonate surfmer (25 mg, 0.210 mmol) with a dispersion of oleic acid-capped magnetite particles (1 g of magnetite particles in 0.5 g *n*-octane). Afterwards, the two phase system was homogenized by ultrasound for 3 min. (50% intensity, pulse 10 s, pause 5 s). For the second miniemulsion, water (24 g) containing phosphonate surfmer (5 mg, 0.042 mmol) and sodium styrene sulfonate (50 mg) was mixed with a solution of styrene (1.2 g) and hexadecane (20 mg). The two-phase mixture was homogenized by ultrasonication for 1 min (10% intensity, pulse 5 s, pause 5 s). Subsequently, both miniemulsions were combined and degased by bubbling argon for 10 min. Afterwards, KPS (20 mg) was added under mechanical stirring (250 rpm). For polymerization, the mixture was heated at 80 °C for 16 h. After complete polymerization, the dispersion was purified magnetically.

The crystallization of CdS was performed by Viktor Fischer. The experiments were carried out at room temperature using 5 mmol of metal salt per gram of latex. Briefly, cadmium acetate dehydrate was dissolved in ethanol, 100 µL of latex dispersion added at once and the dispersion stirred for 2 h. 1 mL of a 0.1 M alcoholic $Na_2S{\cdot}9H_2O$ was added slowly using a syringe pump (2 $mL{\cdot}h^{-1}$). After crystallization, the particles were purified magnetically. Analysis of the particles was done by performing DLS, VSM, TGA and zeta potential measurements and using TEM as imaging tool.

5.3 Magnetic Polymer Hybrid Nanoparticles for MRI, as Labels for Cell Tracing, and for Magnetic Field Guided Separation of Cell-Compartments

5.3.1 How Morphology Influences Relaxivity - A Comparative Study on Superparamagnetic Iron Oxide/Polymer Hybrid Nanostructures for MRI

The different synthetic steps are described in the following chapters. For relaxivity measurements, the procedure described in chapter 5.1.1.5 was used.

5.3.1.1 Synthesis of Iron Oxide Nanoparticles

Two sets of oleate-capped iron oxide nanoparticles were synthesized in order to determine their relaxivity and the relaxivity of their hybrids with different morphologies. The synthesis of the iron oxide nanoparticles with a diameter ~8 nm were synthesized as described in chapter 5.6.1.1.1. For the synthesis of iron oxide nanoparticles with a diameter of ~20 nm, the procedure described in chapter 5.3.2.1 was followed.

5.3.1.2 Synthesis of Iron Oxide Labeled Poly(L-Lactide) Nanoparticles

The synthesis of PLLA nanoparticles loaded with was done as described in chapter 5.3.2. The particles were analyzed *via* VSM and DLS measurements and by TEM imaging.

5.3.1.3 Synthesis of Iron Oxide/Polystyrene Hybrid Nanoparticles with Homogeneous Distribution

The synthesis of iron oxide loaded polystyrene nanoparticles was performed as described in chapter 5.6.1.1.2. The particles were analyzed *via* VSM and DLS measurements and by TEM imaging.

5.3.1.4 Synthesis of Nanocapsules Loaded with 8 or 20 nm in Diameter Sized Iron Oxide Nanoparticles

For the synthesis of iron oxide loaded nanocapsules, 100 mg of oleate-capped iron oxide nanoparticles with different sizes (~8 and ~20 nm diameter) were added to 5 mL of an aqueous TMAOH solution (10 wt%) followed by sonication for 1 h in an ultrasonication bath. The TMAOH was removed by several centrifugations and the particles were redispersed in 50 mL deionized water. Finally, the iron oxide nanoparticles were redispersed in 1 mL deionized water which contained 76 mg of 1,6-hexanediol. Separately, 60 mg of P(E/B-*b*-EO) was dissolved in 6 g cyclohexane. Both phases were combined, mechanically stirred for 1 h at 1400 rpm to obtain a pre-emulsified system, and sonified under ice-cooling using a Branson sonifier W450 Digital with ½ inch tip diameter for 3 min (70% amplitude, 10 s pulse, 5 s pause). The obtained miniemulsion was stirred at 500 rpm while adding dropwise a solution of 80 mg of TDI in 6 g cyclohexane. Stirring overnight yielded a brown dispersion which was centrifuged twice to remove the excess surfactant. For the redispersion of the capsules in water, 0.5 ml of the nanocapsules dispersion was added to 5 mL of a 0.1 wt% SDS aqueous solution under vigorous stirring. The mixture was vigorously stirred for 4 h at room temperature in an open vial. Removal of excess surfactant was done magnetically.

5.3.2 Biodegradable Iron Oxide/Poly(L-Lactide) Nanoparticles with High Relaxivity for MRI Visualized Cell Trafficking

5.3.2.1 Synthesis of Oleate-capped Iron Oxide Nanoparticles of ~20 nm Diameter

The synthesis of oleate-capped iron oxide nanoparticles was performed according to a procedure reported by Jana et al.[364] Briefly, 2.4 g NaOH were dissolved in 200 mL methanol and added dropwise to a solution of 5.4 g $FeCl_3 \cdot 6\ H_2O$ in 17 mL oleic acid and 100 mL methanol. The obtained brown precipitate was washed five times with methanol and dried under reduced pressure overnight. For the nanoparticle synthesis, the brown solid was dissolved in 100 mL of 1-octadecene and three equivalents of oleic acid were added. The solution was heated slowly to 310 °C (heating rate: 3.3 $°C \cdot min^{-1}$) under stirring in an argon atmosphere and kept at 310 °C temperature for 35 min. After cooling to room temperature, addition of a mixture of acetone and methanol (1:1) and centrifugation gave a black precipitate. Dissolving the nanoparticles in small amount *n*-

octane, addition of acetone and methanol (1:1), and centrifugation was repeated two times. The black precipitate was dried under reduced pressure overnight.

5.3.2.2 Synthesis of Poly(L-Lactide) Nanoparticles Labeled with Iron Oxide

For the synthesis of PLLA nanoparticles with incorporated iron oxide nanoparticles, 300 mg PLLA, 0.22 mg *N*-(2,6-diisopropylphenyl)-perylene-3,4-dicarbonacidimide (PMI), 1 mg IR-780 iodide, and 150 mg oleate-coated iron oxide nanoparticles were dispersed in 13 g chloroform by ultrasonication for 30 min and combined with a solution of 72 mg SDS in 24 g milliQ water. The two phase system was pre-emulsified for 1 h at 1400 rpm, ultrasonicated for 3 min (70%, 10 s pulse, 5 s pause) using a Branson sonifier W450 Digital with 6.5 mm tip diameter, and stirred at 300 rpm for 16 h at 40 °C in an open 50 mL flask to obtain a greyish dispersion. Purification was achieved by centrifugation for 5 min at 600 rpm (Eppendorf 5417C microcentrifuge) followed by dialysis (MWCO 14,000 membrane).

5.3.3 Magnetic Nanoparticles for Unraveling the Nanoparticle Endocytosis Trafficking

The synthesis of oleate-capped iron oxide nanoparticles was done as described in chapter 5.6.1.1.2. The synthesis of the iron oxide containing polystyrene nanoparticles was performed similar to a procedure published earlier.[236] In detail, 1g of oleic acid capped iron oxide nanoparticles was redispersed in 0.5g *n*-octane for 30min in a sonication bath followed by the addition of 2 mg of BODYPY dye. BODIPY was synthesized by Andrey Turshatov as described elsewhere.[266] Separately, 25 mg of SDS was dissolved in 24 g deionized water, combined with the disperse octane phase, and sonified with a tip sonifier for 3 min (70% amplitude, 10s pulse, 5s pause) under ice cooling. The resulting miniemulsion was stirred (non-magnetically) at room temperature. For a second emulsion, *n*-hexadecane (20 mg; 0.088 mmol) and styrene (1 g; 9.6 mmol) were mixed with a 0.04 wt% aqueous SDS solution. The two phase system was sonified with a tip sonifier for 1 min (10% amplitude, 5s pulse, 5s pause) under ice cooling and added to the magnetic miniemulsion. Nitrogen was bubbled through the combined dispersions for 5 min. KPS (25 mg; 0.092 mmol) and sodium styrenesulfonate (30 mg ; 0.145 mmol) were added and the reaction mixture heated to 80 °C under stirring and kept at the temperature for 6 h. Purification of the magnetic polystyrene particles was done magnetically. Investigation of the obtained nanoparticles was done by DLS, TEM, zeta

potential and TGA. The nanoparticles were also tested for their cell viability by Daniel Hofmann.

5.4 Highly Magnetic Nanocapsules for Biomedical and Self-Healing Applications

The synthesis of magnetic nanocapsules was performed similarly to the synthesis of iron oxide/polystyrene hybrid nanoparticles as schematically illustrated in chapter 4.4 and as described in chapter 5.6.1.1.2. As a major difference to the synthesis of nanoparticles, the amount of *n*-octane is significantly increased to 10 g while all the other amounts and parameters are kept constant. The higher amount of octane leads to larger droplets and a prolonged evaporation of the octane. In the case of nanoparticles composed of iron oxide and polystyrene, the octane evaporates completely during the emulsion polymerization. For the capsule synthesis, only a minor amount evaporates and most of the octane remains as liquid core in the capsules. Purification of the capsules was done by centrifugation and magnetic separation. Morphology analysis was done by TEM imaging and size determination by DLS measurements.

5.5 Anisotropic Wetting on Magnetically Patterned Substrates

5.5.1 Iron Oxide Nanoparticle Synthesis and Incoorporation into Polystyrene Nanoparticles

The synthesis of the oleate-capped iron oxide nanoparticles was carried out as described in chapter 5.6.1.1.1. The incorporation of the iron oxide nanoparticles into polystyrene nanocolloids was done following the procedure in chapter 5.6.1.1.2. Analysis of the oleate-capped iron oxide nanoparticles and the polystyrene hybrid nanoparticles was done by TEM imaging and DLS measurements.

5.5.2 Silica Coating on the Iron Oxide/Polystyrene Hybrid Nanoparticles

A procedure was in part borrowed from publications of Graf et al. and Ge et al.[365],[366] Briefly, 1.0 mL of a polymer dispersion of polystyrene/magnetite particles in 0.1 wt% SDS were mixed with 1.0 mL of a polyvinylpyrrolidone (PVP) solution

(6.5 $g \cdot L^{-1}$) and was shaken overnight to coat the particles with PVP. An initial PVP coating has been shown to reduce the particle aggregation during the Stöber process for silica coatings.[367] After washing with deionized water five times (by magnetic purification), a modified Stöber process was used to coat the particles and functionalize them with amine groups. The particles were first diluted to 2.0 mL total volume in water followed by the addition of 4.0 mL 2-propanol and 250 μL ammonium hydroxide (28% w/w). 3.00 μL tetraethoxysilane (TEOS) was added every 20 min to a maximum of 12 μL while shaking for a total of 2 h at 400 rpm. After the coating with TEOS, the particles were washed 3 times in ethanol and re-suspended in 6 mL ethanol. 4.00 μL (3-aminopropyl)triethoxysilane (APS) was then added and the dispersions were shaken at 80 ºC and 400 rpm for 1 h. After shaking, the suspension was washed 4 times in ethanol to give a suspension of amino-functionalized silica coated polystyrene/magnetite nanoparticles. The silica coated particles as well as the amino-functionalized particles were analyzed *via* TEM imaging and DLS.

5.5.3 Initiator Coupling

In order to allow a polymerization at the particle surface, an initiator was coupled by EDC coupling to the APS shell on the particles. Following the procedure outlined by Berger et al.[368], α-bromoisobutyric acid was coupled via the following method. For each suspension of particles described above, a vial was placed at 0 ºC (in ice bath). 180 μL α-bromoisobutyric acid and 330 μL 1-ethyl-3-(3-dimethylaminopropyl) carbodiimide (EDC) were added in the vial, and mixed by shaking by hand. Note: The reactants solidified when mixed. To the solid mixture, at 0 ºC, the suspension of coated nanoparticles was added. Finally, 125 μL of triethylamine (molar equivalent of α-bromoisobutyric acid) was added to the reaction to de-protonate the carboxylic acid in the initiator for coupling. The reaction was then shaken at 400 rpm at room temperature overnight. The product was purified by magnetic purification and washing 3 times in ethanol followed by 3 times in water to remove any residual initiator. The final suspension was then freeze-dried by high vacuum at room temperature overnight to yield a brown powder of initiator coupled, silica coated polystyrene/magnetite particles (typically yields ~3–7 mg).

5.5.4 ATRP-Surface Polymerization of Pentafluorostyrene

The final step for the preparation of ultrahydrophobic, magnetic polymer suspensions was the surface polymerization of fluorinated monomer on the

polystyrene/magnetite particles. The fluorinated monomer of choice was 2,3,4,5,6-pentafluorostyrene (PFS), referencing its successful ATRP reaction conducted by Jankova and Hvilsted.[284] Typically, the vacuum dried particles (~5 mg) were placed in a 50 mL Schlenk round bottom flask to which 3.0 mL of PFS (purified by aluminum oxide column) was added. The mixture was then sonicated for 30 s and stirred with a magnetic stir bar in an oil bath at room temperature. Then, 1.0 mg $CuBr_2$ and 4.0 mg of 2,2'-bipyridine (bipy) were added, and the flask was put under argon atmosphere and heated to 105 ºC while refluxing. Once heated to reaction temperature, 300 μL of tin (II) ethylhexanoate was added and the reaction put under an Argon atmosphere and stirred overnight. The product was then suspended and washed 5 times in α-trifluorotoluene (TFT) with a final volume of 2.0 mL.

5.5.5 Coatings of Substrates and their Analysis

Both glass slides and silica SEM plates were used as substrates to test the anisotropic wetting properties of the synthesized particles. Various distances between the drying suspension and the static magnet were tested to determine the optimal magnetic alignment of the nanoparticles on a substrate. Drying the particle dispersion 4.0 cm away from the magnet was found to create the best macroscopic alignment. Usually, a glass slide cut into dimensions of 12 mm x 26 mm was set long-way perpendicular to the center of the magnet with a distance of 4.0 cm between the center of the glass and the edge of the magnet (Figure 48). 10 μL of the fluorinated particles suspension was then dropped on the center of the glass and let to dry. Afterwards, the glass substrate was rotated 180º and another 10 μL was added. Depending on the concentration of the nanoparticle suspension, the coating procedure was repeated 0–2 times. A macroscopic view of the surface coatings was then achieved using an optical microscope. Preliminary experiments and pictures with anisotropic wetting consisted either of dropping 0.20 – 2.00 μL droplets of deionized water on the coated surface or spraying the surface with a deionized water mist in a gel box followed by imaging with amicroscope. Contact angle experiments were also conducted to determine the hydrophobicity of the obtained surfaces.

5.6 From Particles to Fibers - Well-defined Nanofibers with Tunable Morphology from Spherical Colloidal Building Blocks

5.6.1 Synthesis of Hybrid Nanoparticles and their Linear Fusion - From Necklaces to Smooth Fibers

5.6.1.1.1 Synthesis of Fe_3O_4 Nanoparticles with Average Diameter ~8 nm

Oleic acid capped iron oxide nanoparticles with an average diameter of ~8 nm were synthesized after a slightly modified procedure described by Ramirez et al.[122] 12.01 g (60 mmol) ferrous chloride tetrahydrate and 24.36 g (90 mmol) ferric chloride hexahydrate were dissolved in 100 ml deionized water followed by the dropwise addition of 40 ml of a 28% aqueous ammonium solution within 5 min under constant stirring at room temperature. 4.0 g (14.2 mmol) oleic acid were added, the reaction mixture heated to 70 °C for 1 h and afterwards to 110 °C for 2 h. The evaporating water was constantly refilled with deionized water. Within the heating step, clustering and precipitation of the iron oxide nanoparticles was observed. After cooling the reaction mixture, the resulting black residue was rinsed several times with deionized water followed by drying under vacuum at 40 °C overnight.

5.6.1.1.2 Synthesis of Polystyrene Nanoparticles with Homogeneously Distributed Iron Oxide Nanoparticles

The synthesis of polystyrene nanoparticles with homogeneously distributed magnetic iron oxide nanoparticles (PS-Mag-H) was performed as described previously.[236] 1 g of oleate-capped iron oxide nanoparticles was redispersed in 2 g *n*-octane for 30 min in a sonication bath followed by the addition of 24 g of an aqueous solution containing 25 mg of SDS. The two phase system was sonified with a tip sonifier for 3 min under ice cooling (70% amplitude, 10 s pulse, 5 s pause) and stirred non-magnetically (KPG-stirrer) at room temperature. Separately, 1 g of styrene was mixed with 30 mg *n*-hexadecane and 24 g of a 10 mg SDS containing aqueous solution. After sonication with a tip sonifier for 1 min under ice cooling (10% amplitude, 5 s pulse, 5 s pause), the dispersion was added to the magnetite containing dispersion. Nitrogen was bubbled through the combined dispersions for 5 min, 20 mg of KPS and 30 mg of sodium styrene sulfonate were added, and the reaction mixture was heated to 80 °C under stirring for 8 h. Purification of the magnetic polystyrene particles was carried out magnetically

and by centrifugation. The obtained nanoparticles were analyzed *via* DLS, TGA and zeta potential measurements, by solid content determination, and SEM as well as TEM imaging.

5.6.1.1.3 Synthesis of Iron Oxide/Polystyrene Nanoparticles with Janus-like Morphology

Magnetic Janus nanoparticles (PS-Mag-J) were synthesized following the same procedure described in the chapter 5.6.1.1.3 with slight modifications as described earlier.[133] There are two major differences in the synthesis of iron oxide loaded polystyrene nanoparticles with Janus morphology in comparison to the homogenous distribution of the iron oxides in the polystyrene matrix. First of all, a higher styrene amount is used for Janus particles. The higher amount of styrene leads to a higher amount of polystyrene in the resulting magnetic nanoparticles. Secondly, no *n*-hexadecane is used in the styrene droplets. As a result, hexadecane, which is an osmotic pressure agent, does not counter the diffusion of styrene through the continuous phase. Due to the faster diffusion of styrene in the absence of hexadecane, styrene mainly enters droplets of *n*-octane in which magnetic nanoparticles are dispersed. Then, a Janus morphology is obtained.[369] When the diffusion is slowed down in the presence of hexadecane, the octane is evaporated and its content is lower or it has already evaporated once the styrene enters the miniemulsion. Homogenous distribution of magnetic nanoparticles is observed. The obtained nanoparticles were analyzed *via* DLS, TGA and zeta potential measurements, by solid content determination and SEM as well as TEM imaging.

5.6.1.1.4 Description of the Process of Fiber Formation

The setup shown in Figure 75 was used for fiber formation from homogeneously distributed iron oxide/polymer hybrid nanoparticles. Therefore, an aqueous solution containing 0.05 wt% sodium dodecyl sulfate (SDS) was heated to a defined temperature between 80 and 98 °C and pumped through a silicone tube with a flow of 10-30 $mm \cdot s^{-1}$ (Postnova analytics PN 1610 syringe closing system). The tube contains a static ring magnet, through which the dispersion is passed and can be collected afterwards. Either the nanoparticle dispersion is inserted as shown in Figure 75, or it is injected into a silicon tube directly. In both cases, the magnetic colloid dispersion (1 wt% solid content) is stabilized with 0.1 wt% SDS. The injection site of the colloid dispersion or the syringe pump is placed at least 5 cm away from the ring magnet. The particle dispersion is then pumped towards the magnet. Merging of the single particles occurred as soon as the particles are forming linear arrangements due to the influence of the external magnetic

field. The magnetic field measured closest to the magnet was determined to be 200 mT. The resulting linearly merged fibers and necklaces could be collected by either removing the magnet and collecting the dispersion or by increasing the flow speed and displacing the magnetic dispersion away from the magnet (in some cases, the flow is already strong enough and does not have to be increased). In the continuous setup shown in Figure 75, the fiber dispersion can directly be collected at the exit of the tubing. Imaging of the obtained fibers was then done by TEM and SEM imaging.

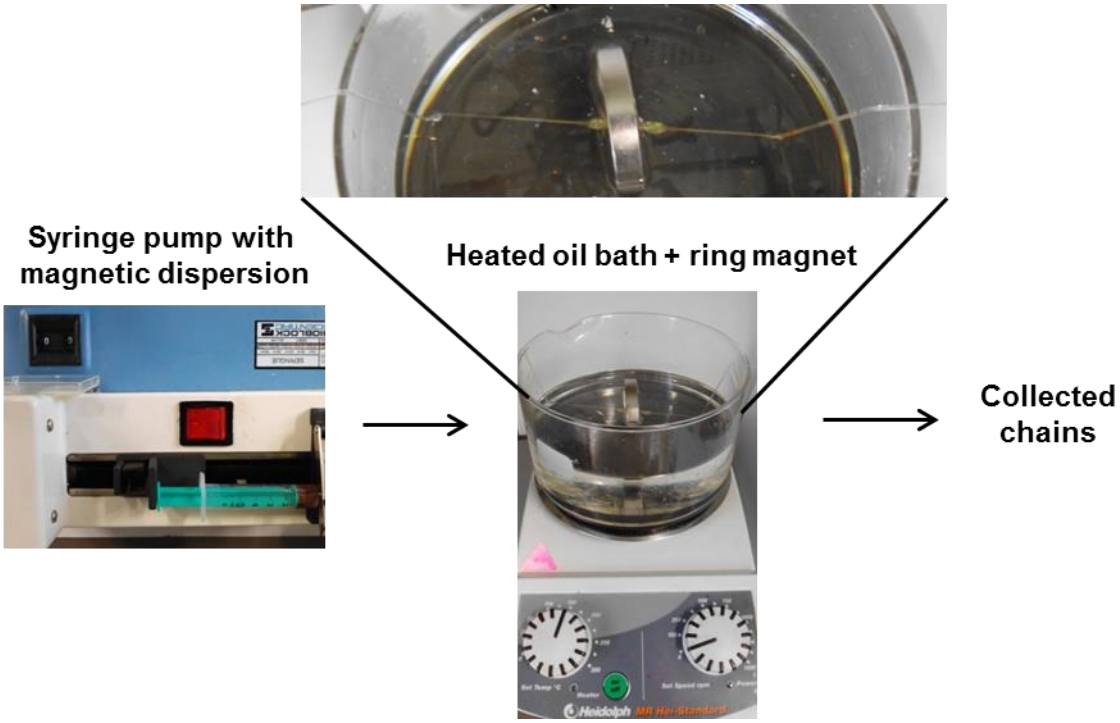

Figure 75. *Experimental setup for the fabrication of nanofibers through magnetic self-assembly and linear fusion of magnetic polymer nanoparticles in aqueous dispersion. The setup comprises a syringe pump with the iron oxide/polystyrene nanoparticle dispersion and an oil bath with a ring magnet. Syringe, bath and a collecting vial are connected through tubes (plastic outside of the oil bath and glass in the heated oil bath.*

5.6.2 Formation of Iron Oxide Nanorods through Calcination

For the calcination of the fibers, a dispersion of smooth fibers (0.01% solid content) was drop-casted on a silicon wafer, heated with a rate of 10 °C·min^{-1} to 400 °C, and kept at 400 °C for 5 h under oxygen atmosphere. Analysis of the calcinated fibers was then done by SEM imaging in combination with EDX for elemental analysis.

5.6.3 Tunable Corrugation of Zigzag Fibers Prepared from Janus Nanoparticles

For the formation of zigzag fibers from iron oxide/polymer Janus nanoparticles, the particles described in chapter 5.6.1.1.3 were used. The particles were employed in setup shown in Figure 75 under the conditions described in chapter 5.6.1.1.4. The only difference that has to be taken into account is the flow speed, which was chosen to be slow (5-10 $mm \cdot s^{-1}$) for the Janus nanoparticles. Alternatively, the dispersion can be simply injected into a heated tube filled with water and a static magnet guided along the hot tube. After sintering, the zigzag fibers were investigated *via* TEM and SEM imaging.

5.6.4 Formation of Tubes from Magnetic Polymer Capsules

For the formation of tubes from iron oxide/polymer hybrid capsules, the synthesis of capsules was performed as described in chapter 5.4. The capsules were separated by weak centrifugation and magnetically from smaller particles which were also present in the dispersions. However, some small particles still remained in the purified dispersions. For the linear sintering of the magnetic capsules, the equipment described in chapter 5.6.1.1.4 or 5.6.3 was used under the there mentioned conditions. The formed tubes were investigated under the TEM microscope.

5.7 Colloidal Building Blocks for Polymer-like Architectures - From Block copolymers to Tailorable Degrees of Branching

The synthesis of oleate-capped iron oxide nanoparticles, which are then introduced as magnetic moiety was done as described in chapter 5.6.1.1.1. The particles were then used to form iron oxide/polystyrene hybrid nanoparticles following the experimental procedure described in the chapters 5.6.1.1.2 and 5.6.1.1.3. The resulting particles were analyzed *via* DLS and TEM. To lower the particle size distribution, the particles were separated by size by centrifugation (between 800-2500 rpm).

5.7.1 Linear Assembly and Fusion of Magnetic Polymer Hybrid Nanoparticles

For the fusion of the hybrid nanoparticles, the experimental setup shown and described in chapter 5.6.1.1.4 or the procedure in chapter 5.6.3 were used. Different types of particles were inserted and their assembly and fusion behavior studied depending on the size distribution of the particles and the flow speed (going along with the speed of applying the external magnetic field) during the sintering process. Analysis of the particle chains after fusion was done mainly *via* TEM imaging.

5.7.2 Control over Self-Assembly by Particle Sizes to Form Block Copolymers

In order to investigate the assembly of particles with different average diameters, the setup from chapter 5.6.1.1.4 was used. The same particle dispersion was inserted under different flow conditions as shown in Figure 69e. The diameter of the particles was determined *via* ImageJ. For the determination of the degree of order, > 500 particles were counted from TEM images.

5.7.3 Introducing Junction Points to Control the Degree of Branching and Form Networks

The chain formation was achieved with the setup of chapter 5.6.1.1.4. Different flow speeds were investigated (1-40 $mL \cdot h^{-1}$) to determine the influence of the flow on the branching probability. Analysis was done on TEM images using ImageJ to calculate the particle diameters. For the study of the branching probability with respect to the size ratio of neighboring particles, 300 junction points were analyzed from TEM images.

5.8 Redox-Responsive Nanoparticles and their Reversible Assembly/Disassembly to Mimic Bacteria Cooperative Behavior

5.8.1 Synthesis of Superparamagnetic Iron Oxide Nanoparticles

Oleate-capped iron oxide nanoparticles were prepared following a procedure of Fischer et al.[244] and as reported in chapter 5.6.1.1.1. Briefly, 90 mmol $FeCl_3 \cdot 6H_2O$ and 60 mmol $FeCl_2 \cdot 4H_2O$ were dissolved in 50 ml deionized water followed by the slow addition of 40 ml of a ammonium hydroxide solution (28%). 21.2 mmol oleic acid were added and the mixture heated to 70 °C and then 110 °C. The reaction mixture was kept at 70 °C for 1 h and 110 °C for 2 h, respectively. After cooling, the nanoparticles were purified by washing several times with deionized water. The nanoparticles were analyzed *via* VSM measurements and TEM imaging.

5.8.2 Synthesis of Methacrylhydroxamic acid

The monomer methacrylhydroxamic acid was synthesized by Thomas Weidner with a procedure described in the literature.[370] 45 mmol of hydroxylamine hydrochloride was dissolved in 30 ml of deionized water. At room temperature and under an inert atmosphere, 105 mmol of sodium hydroxide dissolved in 15 ml of deionized water was added dropwise. Subsequently, 30 mmol methyl methacrylate in 15 ml dioxane was slowly added under vigorous magnetic stirring. The mixture was let stirring at room temperature for 18 h and reduced to half its initial volume using a rotary evaporator. Addition of concentrated hydrochloric acid resulted in a colorless precipitate, which was separated by filtration. The solution was completely evaporated using a rotary evaporator. The residue was mixed with water followed by extraction with ethyl acetate. The extraction was repeated several times and the ethyl acetate evaporated. ^{1}H-NMR (DMSO-d6): δ = 1.9 (s, 3H), 5.35 (s, 1H), 5.65 (s, 1H), 10.4 (s, 1H), 10,8 (s, 1H). FT-IR (KBr, λ^{-1} / cm^{-1}): 3412 (m), 3193 (m), 2963 (s), 1659 (s), 1614 (s).

5.8.3 Preparation of Magnetic Polystyrene Nanoparticles Decorated with Hydroxamic acid

The synthesis of magnetically labeled polystyrene nanoparticles with methacrylhydroxamic acid surface functionality was carried out similarly to the procedure

described in chapter 5.6.1.1.2 or as published earlier.[133] Briefly, 1 g of oleate capped iron oxide nanoparticles was dispersed in 0.5 g octane by sonication in an ultrasonication bath for 30 min and mixed with 24 ml water containing 0.17 mmol sodium dodecyl sulfate. The two phase system was first sonicated for 3 min under ice cooling (6,5 mm tip size, 70% amplitude, 10 s pulse, 5 s pause) with a Branson sonifier 450 W Digital and then mechanically stirred. Separately, 9.6 mmol of styrene was mixed with 0.1 mmol hexadecane and added to a solution of 0.04 mmol sodium dodecyl sulfate in 24 ml deionized water. The mixture was sonicated under ice cooling using the aforementioned sonication conditions (10% amplitude, 5 s pulse, 5 s pause). After mixing with the magnetic miniemulsion, argon was bubbled through the emulsion for 5 min followed by the addition of 0.3 mmol of potassium persulfate and heating to 80 °C. After 30 min, 20 mg of methacrylhydroxamic acid were added and the mixture stirred at 80 °C for an additional 16 h. The methacrylhydroxamic acid functionalized magnetic polystyrene nanoparticles were purified from water soluble initiator and non-reacted methacrylhydroxamic acid through magnetic precipitation of the nanoparticles and discarding of the supernatant followed by redispersion of the nanoparticles in an aqueous 10^{-3} M SDS solution. The purification procedure was repeated three times. Analysis of the nanoparticles was done by TEM for imaging, DLS measurements for the determination of the hydrodynamic radius and pH dependent zeta potential measurements to detect the hydroxamic acid surface functionality.

5.8.4 Supraparticular Assembly and Locking of the Structures by Complex Formation

Suprastructures from nanoparticles were obtained by passing a controlled flow of the nanoparticles dispersion (0.1 wt% solid content) through a static ring magnet in a setup described in chapter 5.6.1.1.4. The applied magnetic field on the nanoparticles was determined to be 40-60 mT using a larger ring magnet than the one described in the chapter 5.6.1.1.4. Interparticle crosslinking was achieved by addition of a 1 $mg \cdot L^{-1}$ $FeCl_3$ aqueous solution which was also passed through the static magnet. The obtained chains were analyzed *via* DLS measurements and TEM imaging.

5.8.5 Redox-triggered Disassembly of the Suprastructures

The dispersions of locked suprastructures were treated with a 1 $g \cdot L^{-1}$ vitamin C containing aqueous solution. After addition of vitamin C, the dispersion was weakly shaken overnight and analyzed by DLS and TEM.

6 Summary and Outlook

In summary, the thesis highlights promising perspectives for aqueous dispersions of superparamagnetic/polymer hybrid nanoparticles and capsules. It was shown, that the implementation of a superparamagnetic moiety enables an efficient magnetic field triggered heat generation to induce a release of active compounds from polymer nanocapsules in a remote-controlled fashion. Furthermore, the preparation of defined magnetic nanohybrid particles and capsules was presented. In different collaborations, the nanohybrids were used for various applications such as MRI cell tracing or magnetic separation of cell compartments. Additionally it could be demonstrated, that the magnetic entity is suitable as structuring agent to form defined supraparticular assemblies. Spherical particles could be aligned with an external magnetic field and fused to create linear nanofibers. Not only linear nanofibers, additionally highly defined architectures in polymer-analogy could be generated from the colloidal building blocks. Finally, a process could be described in which the nanoparticles were locked in their linear assembly by complex formation and - upon addition of a reducing agent – could be disassembled again.

Magnetic switchable nanocontainers

In the first part of the thesis, several possibilities for the introduction of superparamagnetic nanoparticles into nanocapsules were demonstrated. The superparamagnetic nature of the nanoparticles allowed for a response towards an external magnetic field. It could be shown that the magnetic response enabled a bi-functionality: Firstly, tracing of the magnetically labeled particles *via* MRI became possible. Secondly, a release of encapsulated hydrophilic compounds upon application of an external alternating magnetic field could be achieved. Because the nanocapsules present additionally a high T_2 relaxivity, they are very well suited as contrast agents for MRI. Thanks to their multifunctionality, the described nanocapsules could be used as a novel drug delivery vehicle. Additionally supported by the high encapsulation efficiency and the biocompatibility of the capsules, the promising drug delivery vehicles are currently under *in-vivo* investigation.

Multifunctional magnetic hybrid nanoparticles

Multifunctional nanoparticles were synthesized together with two collaborative partners. Together with Viktor Fischer, nanoparticles with a superparamagnetic iron oxide core and a luminescent cadmium sulfide shell were prepared in several steps. The dual-functionality can be interesting especially for biomedical applications, in which the particles can act as magnetically separable, fluorescently detectable nanocolloids *e.g.* for the selective separation and detection of biomolecules.
In collaboration with Christine Herrmann, anisotropic nanoparticles with a magnetic moiety could be prepared. Here, the dual-functionality of an elongated shape in combination with the superparamagnetism can be interesting for biomedical applications as well. Indeed, the cell uptake of nanoparticles is highly dependent on the shape of the particles. Since the elongated particles relax back into their original spherical shape upon heating, an external excitation with a magnetic field and thus, heat generation could do so too. The change in shape could then enable a magnetically triggered cell interaction.

Magnetic polymer hybrid nanoparticles for MRI, as labels for cell tracing and for magnetic field guided separation of cell-compartments

The multifunctional use of biocompatible superparamagnetic nanoparticles and capsules could be demonstrated in the described chapter. Besides the common use as contrast agents for MRI they were suitable as labels for cell tracing or as magnetic field responsive dispersions for the separation of cell compartments. As in the last two cases, the particles could be used to elucidate non-invasively pathways within an organism, which is the basis for a better understanding and a targeted intervention in the body.

Highly magnetic capsules

In a facile procedure, highly iron oxide loaded polymer capsules were prepared by heterophase polymerization. The obtained capsules in the submicron range can be of interest as self-healing compartments which can be magnetically introduced in coatings. Additionally, they can be of interest for biomedical applications to store and release hydrophobic components.

Anisotropic wetting on magnetic patterned substrates

The cooperative behavior of superparamagnetic nanoparticles to form linear arrangements was shown in the described chapter. Nanoparticles with a magnetic core and a poly(pentafluorostyrene) shell were prepared and deposited on a substrate under the application of an external magnetic field. Linear self-assembly of the magnetic dispersion and evaporation of the continuous phase left a ribbon-like patterning of the particles on the substrate. The ribbons of ultrahydrophobic coating were then used to achieve an anisotropic wetting of aqueous droplets. Thus, it could be shown that substrate patterning is possible by making use of magnetic forces on superparamagnetic dispersions.

From spherical colloids to nanofibers

Besides stimulating a single superparamagnetic particle (*e.g.* to induce a release), the cooperative response of superparamagnetic nanoparticles to an externally applied magnetic field was demonstrated. Spherical model nanoparticles consisting of superparamagnetic iron oxides and a polystyrene matrix were synthesized. The self-assembly of the superparamagnetic particles by magnetic field application and the fusion of the polymer moiety upon temperature increase led to permanently linked supraparticular assemblies. When monodisperse particles were inserted, linear nanofibers resulted from the process. The corrugation of the nanofibers could be tuned either by the fusion time or temperature. After calcination, the resulting inorganic nanorods could potentially be used as a platform for catalytic purposes. Furthermore, the insertion of Janus nanoparticles led to more elaborate linear arrangements in zigzag fashion. Moreover, the insertion of iron oxide/polystyrene capsules into the process and their fusion provided the possibility to make tubular structures. The described process holds great potential for the synthesis of well-defined nanofibers with tunable morphology and corrugation from easily accessible spherical nanoparticles.

Towards polymer-like colloidal architectures

Using the aforementioned process of fiber formation, the fusion of the nanoparticles provided an image of the “frozen state” of magnetically self-assembled nanoparticles. By insertion of a polydisperse nanoparticle dispersion into the process, various polymer-like architectures were generated. Two major factors for the formation of defined architectures could be isolated and investigated: I) The introduction of junction points by a variation of neighboring nanoparticle sizes. II) The faster assembly of larger nanoparticles with high iron oxide content by slowly applying the external field and thus, the creation of blocks of

nanoparticles of different sizes. In contrary, a fast application of the external field did not result in a distinct separation of different particle sizes within the particle assembly. The two options provided a suitable tool kit for the creation of various polymer-like architectures: Following from option I, the introduction of defined junction points, arrangements ranging from linear over branched structures to whole networks could be generated. Additionally, by tailoring the interaction of differently sized particles, as in the case of option II, enabled the preparation of nanoparticle arrangements ranging from statistical to block copolymer-like.

Responsive assembly/disassembly of nanocolloids in bacteria-like fashion

Reversible assembly and linkage of nanoparticles was demonstrated following a lock/unlock mechanism. The superparamagnetic iron oxide/polystyrene nanoparticles were decorated with hydroxyamic acid groups. Upon application of an external magnetic field, the particles assembled linearly and could be linked by addition of iron(III) ions, locking the particles in their position by the formation of a stable iron(III) hydroxamato-complex. Reversibility of the locked supraparticular assembly was achieved by addition of a mild reducing agent (*e.g.* vitamin C), causing reduction of the complex centering iron ion. A less stable iron(II) complex was formed, which led to unlocking and disassembly of the nanoparticles.

7 Zusammenfassung und Ausblick

Zusammenfassend kann gesagt werden, dass die Arbeit vielversprechende Perspektiven für superparamagnetische Hybridnanopartikel und Kapseln aufzeigt. Es konnte gezeigt werden, dass das Einbringen einer superparamagnetischen Komponente eine effiziente Erwärmung unter Anlegen eines externen alternierenden Magnetfeldes und somit eine ferngesteuerte Freisetzung von aktiven Substanzen ermöglicht. Des Weiteren konnten definierte, multifunktionale, magnetische Hybridparikel und Kapseln im Nanometer-Bereich hergestellt werden. Diese konnten in zahlreichen Kollaborationen für vielfältige Anwendungen genutzt werden z.B. für die Magnetresonanztomographie, zur Zell-Markierung oder für die magnetische Separation von Zell-Kompartimenten. Zusätzlich wurde gezeigt, dass die magnetische Komponente als strukturgebendes Element geeignet ist um definierte suprapartikuläre Anordnungen zu bilden. Sphärische Nanopartikel konnten unter Anlegen eines externen Magnetfeldes angeordnet und zusammengeschmolzen werden, woraus sich lineare Nanofasern oder komplexere Architekturen in Polymer-Analogie ergaben. Außerdem konnten die Partikel in einem alternativen Prozess durch Bildung eines Metall-Komplexes vernetzt werden und anschließend - unter Zugabe eines Reduktionsmittels - wieder entkoppelt werden.

Magnetisc schaltbare Nanokapseln

Im ersten Teil der Arbeit wurden verschiedene Möglichkeiten aufgezeigt, wie Nanokapseln mit superparamagnetischen Nanopartikeln markiert werden können. Die superparamagnetische Eigenschaft der Nanopartikel bedingte eine Reaktion auf ein externes Magnetfeld. Diese Reaktion ermöglichte eine Bifunktionalität: Zum einen wurde durch eine solche Markierung eine Bildgebung im MRT ermöglicht. Zum anderen konnte eine Freisetzung von eingekapselten, hydrophilen Stoffen durch Anlegen eines alternierenden externen Magnetfeldes erreicht werden. In Kombination mit den guten T_2 Relaxationswerten, und der damit verbundenen Möglichkeit den Aufenthaltsort der Nanokapseln im MRT zu visualisieren, sind diese Nanokapseln vielversprechende neuartige Nanotransporter für Medikamente. Unterstützt durch eine hohe Einkapselungseffizienz und die Biokompatibilität der Kapseln, werden die vielversprechenden Kapseln derzeit in *in-vivo* Versuchen eingesetzt.

Multifunktionale magnetische Hybrid-Nanopartikel

Im Rahmen zweier Kollaborationen wurden Nanopartikel mit dualer Funktionalität hergestellt. Zusammen mit Viktor Fischer konnten Nanopartikel mit superparamagnetischem Eisenoxid-Kern und lumineszenter CdS-Hülle in mehreren Schritten hergestellt werden. Die zweifache Funktionalität ist vor allem für biomedizinische Anwendungen von Interesse. Magnetische separierbare, fluoreszenz-markierte Nanopartikel könnten zum Beispiel für die Abtrennung und Detektion von Biomolekülen eingesetzt werden.

In einer weiteren Kollaboration mit Christine Hermann wurden anisotrope Nanopartikel mit superparamagnetischem Kern hergestellt. Auch hier sind die Partikel vor allem für biomedizinische Anwendungen von Interesse. Da die Zellaufnahme von Nanopartikeln stark von deren Form abhängt, könnten die elongierten Partikel speziell hierfür interessant sein. Die elongierten Partikel gehen in ihre Ursprungsform zurück, wenn man sie erwärmt. Daher könnte ein Erwärmen im externen Magnetfeld dazu genutzt werden die elongierten Partikel in sphärische zu überführen und somit ihre Zell-Interaktion zu steuern.

Hybrid-Nanopartikel für MRT, als Marker zur Zell-Verfolgung und für Magnetfeld-gesteuerte Separation von Zell-Kompartimenten

Die multifunktionale Anwendung von biokompatiblen superparamagnetischen Nanopartikeln und Kapseln konnte in diesem Kapitel gezeigt werden. Neben ihrer allgegenwärtigen Anwendung als Kontrastmittel für MRT können die Partikel auch als Marker für die Zell-Verfolgung oder als Magnetfeld-sensitive Dispersionen für die Separation von Zell-Kompartimenten eingesetzt werden. In den beiden letzten Fällen dienen die Partikel der Aufklärung von Transportwegen im Organismus. Dies bildet die Grundlage für ein besseres Verständnis und ein gezieltes Eingreifen im Körper.

Superparamagnetische Kapseln

In einem einfachen Prozess konnten superparamagnetische Eisenoxid beladene Kapseln über eine Heterophasen-Polymerisation hergestellt werden. Die erhaltenen Kapseln könnten als magnetisch-deponierbare selbstheilende Kompartimente in Beschichtungen eingesetzt werden. Zusätzlich sind die Kapseln auch für biomedizinische Anwendungen von Interesse für die Einkapselung und Freisetzung von hydrophoben Komponenten.

Anisotropes Benetzen von magnetisch-strukturierten Substraten

Das kooperative Verhalten von superparamagnetischen Nanopartikeln, welches zu linearen Anordnungen führt, konnte in diesem Kapitel gezeigt werden. Nanopartikel mit magnetischem Kern und einer ultrahydrophoben Poly(pentafluorstyrol)-Hülle wurden hierfür hergestellt und unter Einwirken eines externen Magnetfeldes auf einem Substrat deponiert. Dies führte zu einer linearen Ausrichtung der Partikel und unter Trocknen der kontinuierlichen Phase bildete sich ein Streifenmuster auf dem Substrat. Die Streifen aus der ultrahydrophoben Beschichtung konnten anschließend genutzt werden, um das Substrat mit Wassertropfen anisotrop zu Benetzen. Somit konnte gezeigt werden, dass eine Oberflächenstrukturierung von Substraten mit magnetischen Dispersionen möglich ist.

Von sphärischen Kolloiden zu Nanofasern

Neben dem Anregen eines einzelnen superparamagnetischen Partikels (z.B. um eine Freisetzung zu erzielen), konnte das kooperative Verhalten solcher Partikel auf ein externes Magnetfeld untersucht werden. Hierfür wurden sphärische Modelpartikel bestehend aus einer superparamagnetischen Eisenoxid Komponente und einer Polystyrol-Matrix hergestellt. Mit diesen Partikeln konnte gezeigt werden, dass stabile suprapartikuläre Anordnungen durch Anlegen eines externen Magnetfeldes und somit einer linearen Anordnung der Partikel und Erhöhung der Temperatur, wodurch die Partikel verschmelzen, erzielt werden kann. Durch Einbringen von monodispersen Partikeln resultierten lineare Nanofasern aus dem Prozess. Die Riffelung der Nanofasern konnte über die Fusionszeit und Temperatur gesteuert werden. Nach Kalzinieren könnten die anorganischen nanofasern für katalytische Anwendungen interessant werden. Zusätzlich konnte gezeigt werden, dass durch das Einbringen von komplexeren 0D Kolloiden, wie im Fall von Janus Partikeln, kompliziertere lineare Anordnungen möglich sind, so wie beispielsweise zigzag-Fasern. Außerdem konnte gezeigt werden, dass durch das Einbringen von Eisenoxid beladenen Polystyrol-Kapseln in dem Fusionsprozess Kanal-analoge Strukturen erhalten werden können. Der beschriebene Prozess könnte in Zukunft genutzt werden, um wohl-definierte Nanofasern mit steuerbarer Morphologie aus leicht zugänglichen Hybrid-Nanopartikeln zu gewinnen.

Kolloidale Polymere mit komplexen Architekturen

Wenn man von dem oben beschriebenen Prozess Gebrauch macht, lassen sich nicht nur lineare Nanofasern herstellen. Durch ein „einfrieren“ der angeordneten Nanopartikel, wenn die Partikel zusammengeschmolzen werden, kann der Anordnungsprozess im Detail untersucht werden. Wurden polydisperse Proben in dem Prozess verwendet, so konnen verschiedenste Polymer-analoge Architekturen erhalten werden. Hierfür sind zwei Punkte hauptverantwortlich: I) Die Möglichkeit Verzweigungspunkte durch eine Größenvariation von Nachbarpartikeln einzuführen. II) Die Möglichkeit größere Partikel mit hohem Eisenoxid-Gehalt schneller anordnen zu können, wenn das Magnetfeld langsam angelegt wird. Hierdurch konnten Blöcke aus unterschiedlich großen Partikeln erhalten werden. Im Gegensatz hierzu führte das schnelle Anlegen des externen Magnetfeldes zu einer statistischen Anordnung der Partikelgrößen. Diese zwei Möglichkeiten boten ein ausreichendes Werkzeug für die Herstellung verschiedenster kolloidaler Polymere: Mit Hilfe von Möglichkeit I konnten durch das Einführen von Verzweigungspunkten Anordnungen von linearen über leicht-verzweigte bis hin zu netzwerkartigen Strukturen zugänglich gemacht werden. Zusätzlich konnte durch Steuerung der internen Struktur, wie durch Möglichkeit II beschrieben, eine statistische oder blockähnliche Anordnung von unterschiedlichen Partikelgrößen erreicht werden.

Gesteuertes Anordnen/Auseinanderbringen von Nanokolloiden in Bakterien-Analogie

Über eine alternative Route konnten superparamagnetische/polymere Nanopartikel reversibel angeordnet werden. Hierzu wurden die superparamagnetischen Polystyrol Nanopartikel mit einer Hydroxamsäure-Oberflächenfunktionalität versehen. Durch Anlegen eines externen Magnetfeldes ordneten sich die Partikel linear an und konnten durch Zugabe von Eisen(III) permanent verknüpft werden. Hierbei bildete sich ein stabiler Komplex aus. Eine Reversibilität der Verknüpfung konnte durch Zugabe eines milden Reduktionsmittels erreicht werden (z.B. Vitamin C). Hierdurch wurde der Komplex reduziert und es bildete sich ein weniger stabiler Eisen(II)-Komplex, was zu einer Destabilisierung der Verknüpfung und schließlich einem Verstreuen der einzelnen Partikel führte.

8 List of Abbreviations

AAc	Acrylic acid
AAm	Acryl amide
APS	(3-Aminopropyl)-trimethoxysilane
ATRP	Atom transfer radical polymerization
bipy	2,2'-Bipyridine
BODIPY	Boron-dipyrromethene
CCD	Charge coupled device
CdS	Cadmium(II) sulfide
cLSM	Confocal laser scanning microscopy
CMPVA	Carboxymehtylated poly(vinyl alcohol)
CPMG echo	Carr Purcell Meiboom Gill echo
$CuBr_2$	Cupper(II) bromide
D_h	Hydrodynamic diameter
DLS	Dynamic light scattering
DMSO	Dimethyl sulfoxide
DNA	Deoxyribonucleic acid
DP_N	Number average degree of polymerization
DP_W	Weight average degree of polymerization
DSC	Differential scanning calorimetry
EDC	1-Ethyl-3-(3-dimethyl-aminopropyl) carbodiimide
EDX	Energy-dispersive x-ray spectroscopy
EPR	Enhanced permeability and retention
FACS	Fluorescence activated cell sorting
FTIR	Fourier transform infrared spectroscopy
ΔG	Gibbs energy
GPC	Gel permeation chromatography
HD	1,6-Hexanediol
HES	Hydroxyethyl starch
HSAB	Hard and soft acids and bases
ICP-MS	Inductive coupled plasma mass spectrometry
ICP-OES	Inductive coupled plasma optical emission spectrometry

INT	Intracellular nanoparticle trafficking
KBr	Potassium bromide
kDa	Kilodaltons
KLE	Poly[(ethylene-*co*-butylene)-*b*-(ethylene oxide)], (P(E/B-*b*-EO))
KPS	Potassium persulfate
LCST	Lower critical solution temperature
MACS	Magnetic Cell Seperation System
MC	Monte Carlo
M_c	Critical molecular weight
M_e	Entanglement molecular weight
MMA	Methyl methacrylate
M_n	Number average molecular weight
MPI	Magnetic particle imaging
MRI	Magnetic resonance imaging
MTS	3-(4,5-dimethylthiazol-2-yl)-5-(3-carboxy-methoxyphenyl)-2-(4-sulfophenyl)-2H-tetrazolium
M_w	Weight average molecular weight
MWCO	Molecular weight cutoff
NaCl	Sodium chloride
NMR	Nuclear magnetic resonance
PDI	Polydispersity index
PdMMAEAPS	Poly(3 dimethyl(meth-acryloxyethyl) ammonium propane sulfonate)
PEG	Poly(ethylene glycol)
PFS	Pentafluorostyrene
PGPR 90	Poly(glycerol polyriccinolate)
PK	Pharmacokinetic
PLLA	Poly(L-lactide)
PMI	N-(2,6-diisopropyl-phenyl)-perylene-3,4-dicarbonacidimide
POEGMA	Poly[oligo(ethylene glycol) methyl ether methacrylate]
PPV	Poly(*p*-phenylene vinylene)
PVA	Poly(vinyl alcohol)
PVP	Poly(vinyl pyrrolidone)
RI	Refractive index

SEC	Size exclusion chromatography
SEM	Scanning electron microscopy
SDS	Sodium dodecyl sulfate
SPIONS	Superparamagnetic iron oxide nanoparticles
SQUID	Superconducting quantum interference device
TBE	1,1,2,2-Tetrabromethan
TDI	2,4-Toluenediiso-cyanate
TEM	Transition electron microscopy
TEOS	Tetraethyl orthosilicate
TFT	α,α,α-Trifluorotoluene
T_g	Glass transition temperature
TGA	Thermogravimetric analysis
TMAOH	Tetramehyl ammonium hydroxide
TWEEN 80	Polyoxyethylene (20) sorbitan monooleate
UCST	Upper critical solution temperature
UV-Vis	Ultraviolet-visible spectroscopy
VA-060	2,2'-Azobis[2-[1-(2-hydroxyethyl)-2-imidazolin-2-yl]propane] dihydrochloride
VP	Vinylpyrrolidone
VSM	Vibrating sample magnetometer
XRD	X-ray diffraction

9 Bibliography

[1] R. P. Feynman, *Microelectromechanical Systems, Journal of* **1992**, *1*, 60-66.

[2] D. E. Lee, H. Koo, I. C. Sun, J. H. Ryu, K. Kim, I. C. Kwon, *Chemical Society Reviews* **2012**, *41*, 2656-2672.

[3] M. Elsabahy, K. L. Wooley, *Chemical Society Reviews* **2012**, *41*, 2545-2561.

[4] Z. H. Nie, A. Petukhova, E. Kumacheva, *Nature Nanotechnology* **2010**, *5*, 15-25.

[5] L. B. Wang, L. G. Xu, H. Kuang, C. L. Xu, N. A. Kotov, *Accounts of Chemical Research* **2012**, *45*, 1916-1926.

[6] D. H. Martin, *Magnetism in Solids*, M.I.T. Press, **1967**.

[7] D. P. Gesellschaft, *Annalen der Physik*, Wiley-VCH, **1834**.

[8] H. P. Myers, *Introductory Solid State Physics, Second Edition*, Taylor & Francis, **1997**.

[9] W. Nolting, *Grundkurs Theoretische Physik 3*, Springer, **2001**.

[10] B. L. Cushing, V. L. Kolesnichenko, C. J. O'Connor, *Chemical Reviews* **2004**, *104*, 3893-3946.

[11] B. Aslibeiki, P. Kameli, H. Salamati, *Journal of Magnetism and Magnetic Materials* **2012**, *324*, 154-160.

[12] R. Lacmann, A. Herden, C. Mayer, *Chemical Engineering & Technology* **1999**, *22*, 279-289.

[13] D. Turnbull, *J. Chem. Phys.* **1950**, *18*, 198-203.

[14] L. Batet, J. Fradera, E. M. d. l. Valls, L. A. Sedano, *Fusion Engineering and Design* **2011**, *86*, 421-428.

[15] D. Gebauer, A. Volkel, H. Colfen, *Science* **2008**, *322*, 1819-1822.

[16] K. Landfester, *Angewandte Chemie-International Edition* **2009**, *48*, 4488-4507.

[17] J. M. Asua, *Progress in Polymer Science* **2002**, *27*, 1283-1346.

[18] W. D. Harkins, *J. Am. Chem. Soc.* **1947**, *69*, 1428-&.

[19] C. K. Weiss, K. Landfester, in *Hybrid Latex Particles: Preparation With, Vol. 233* (Eds.: A. M. VanHerk, K. Landfester), **2010**, pp. 185-236.

[20] J. G. Zhang, S. Q. Xu, E. Kumacheva, *J. Am. Chem. Soc.* **2004**, *126*, 7908-7914.

[21] V. Fischer, I. Lieberwirth, G. Jakob, K. Landfester, R. Muñoz-Espí, *Advanced Functional Materials* **2013**, *23*, 451-466.

[22] X. F. Liu, M. Zhu, S. H. Chen, M. J. Yuan, Y. B. Guo, Y. L. Song, H. B. Liu, Y. L. Li, *Langmuir* **2008**, *24*, 11967-11974.

[23] C. Holtze, A. C. Rowat, J. J. Agresti, J. B. Hutchison, F. E. Angile, C. H. J. Schmitz, S. Koster, H. Duan, K. J. Humphry, R. A. Scanga, J. S. Johnson, D. Pisignano, D. A. Weitz, *Lab on a Chip* **2008**, *8*, 1632-1639.

[24] E. J. W. Verwey, J. T. G. Overbeek, *Theory of the Stability of Lyophobic Colloids*, Dover Publications, **1999**.

[25] D. H. Napper, *Industrial & Engineering Chemistry Product Research and Development* **1970**, *9*, 467-&.

[26] D. N. Thomas, S. J. Judd, N. Fawcett, *Water Research* **1999**, *33*, 1579-1592.

[27] D. H. Napper, *Journal of Colloid and Interface Science* **1977**, *58*, 390-407.

[28] C. J. Xu, S. H. Sun, *Advanced Drug Delivery Reviews* **2013**, *65*, 732-743.

[29] W. S. Seo, J. H. Lee, X. M. Sun, Y. Suzuki, D. Mann, Z. Liu, M. Terashima, P. C. Yang, M. V. McConnell, D. G. Nishimura, H. J. Dai, *Nature Materials* **2006**, *5*, 971-976.

[30] D. K. Kim, Y. Zhang, W. Voit, K. V. Rao, M. Muhammed, *Journal of Magnetism and Magnetic Materials* **2001**, *225*, 30-36.

[31] A. Petri-Fink, H. Hofmann, *Ieee Transactions on Nanobioscience* **2007**, *6*, 289-297.

[32] Z. P. Chen, *Synthesis and Reactivity in Inorganic Metal-Organic and Nano-Metal Chemistry* **2012**, *42*, 1040-1046.

[33] M. Levy, A. Quarta, A. Espinosa, A. Figuerola, C. Wilhelm, M. Garcia-Hernandez, A. Genovese, A. Falqui, D. Alloyeau, R. Buonsanti, P. D. Cozzoli, M. A. Garcia, F. Gazeau, T. Pellegrino, *Chemistry of Materials* **2011**, *23*, 4170-4180.

[34] P. C. Papaphilippou, A. Pourgouris, O. Marinica, A. Taculescu, G. I. Athanasopoulos, L. Vekas, T. Krasia-Christoforou, *Journal of Magnetism and Magnetic Materials* **2011**, *323*, 557-563.

[35] D. Patel, Y. M. Chang, G. H. Lee, *Current Applied Physics* **2009**, *9*, S32-S34.

[36] S. Jiang, A. A. Eltoukhy, K. T. Love, R. Langer, D. G. Anderson, *Nano Letters* **2013**, *13*, 1059-1064.

[37] V. S. Wilms, H. Bauer, C. Tonhauser, A. M. Schilmann, M. C. Muller, W. Tremel, H. Frey, *Biomacromolecules* **2013**, *14*, 193-199.

[38] B. H. Kim, N. Lee, H. Kim, K. An, Y. I. Park, Y. Choi, K. Shin, Y. Lee, S. G. Kwon, H. B. Na, J. G. Park, T. Y. Ahn, Y. W. Kim, W. K. Moon, S. H. Choi, T. Hyeon, *J. Am. Chem. Soc.* **2011**, *133*, 12624-12631.

[39] C. Rodriguez-Navarro, L. G. Benning, *Elements* **2013**, *9*, 203-209.

[40] L. Babes, B. Denizot, G. Tanguy, J. J. Le Jeune, P. Jallet, *Journal of Colloid and Interface Science* **1999**, *212*, 474-482.

[41] M. Liong, H. Shao, J. B. Haun, H. Lee, R. Weissleder, *Advanced Materials* **2010**, *22*, 5168-+.

[42] M. Mahmoudi, S. Sant, B. Wang, S. Laurent, T. Sen, *Advanced Drug Delivery Reviews* **2011**, *63*, 24-46.

[43] R. Gans, *Physikalische Zeitschrift* **1908**, *9*, 10-13.

[44] J. V. I. Timonen, M. Latikka, L. Leibler, R. H. A. Ras, O. Ikkala, *Science* **2013**, *341*, 253-257.

[45] K. Katagiri, Y. Imai, K. Koumoto, *Journal of Colloid and Interface Science* **2011**, *361*, 109-114.

[46] S. H. Hu, S. Y. Chen, X. H. Gao, *Acs Nano* **2012**, *6*, 2558-2565.

[47] E. Amstad, J. Kohlbrecher, E. Muller, T. Schweizer, M. Textor, E. Reimhult, *Nano Letters* **2011**, *11*, 1664-1670.

[48] S. D. Kong, W. Z. Zhang, J. H. Lee, K. Brammer, R. Lal, M. Karin, S. H. Jin, *Nano Letters* **2010**, *10*, 5088-5092.

[49] W. H. Chong, L. K. Chin, R. L. S. Tan, H. Wang, A. Q. Liu, H. Chen, *Angewandte Chemie International Edition* **2013**, *52*, 8570-8573.

[50] A. M. Schmidt, *Macromol. Rapid Commun.* **2006**, *27*, 1168-1172.

[51] M. Zrinyi, L. Barsi, A. Buki, *J. Chem. Phys.* **1996**, *104*, 8750-8756.

[52] T. Gelbrich, M. Feyen, A. M. Schmidt, *Macromolecules* **2006**, *39*, 3469-3472.

[53] H. Wang, Q. W. Chen, Y. F. Yu, K. Cheng, *Dalton Transactions* **2011**, *40*, 4810-4813.

[54] A. S. Lubbe, C. Alexiou, C. Bergemann, *Journal of Surgical Research* **2001**, *95*, 200-206.

[55] S. Pagoti, S. Surana, A. Chauhan, B. Parasar, J. Dash, *Catalysis Science & Technology* **2013**, *3*, 584-588.

[56] S. Y. Wei, Z. P. Dong, Z. Y. Ma, J. Sun, J. T. Ma, *Catalysis Communications* **2013**, *30*, 40-44.

[57] M. Stein, J. Wieland, P. Steurer, F. Tolle, R. Mulhaupt, B. Breit, *Advanced Synthesis & Catalysis* **2011**, *353*, 523-527.

[58] R. D. Ambashta, M. Sillanpaa, *Journal of Hazardous Materials* **2010**, *180*, 38-49.

[59] S. Laurent, S. Dutz, U. O. Hafeli, M. Mahmoudi, *Advances in Colloid and Interface Science* **2011**, *166*, 8-23.

[60] S. Miltenyi, W. Muller, W. Weichel, A. Radbruch, *Cytometry* **1990**, *11*, 231-238.

[61] H. W. Gu, K. M. Xu, C. J. Xu, B. Xu, *Chemical Communications* **2006**, 941-949.

[62] J. Weizenecker, B. Gleich, J. Rahmer, H. Dahnke, J. Borgert, *Physics in Medicine and Biology* **2009**, *54*, L1-L10.

[63] M. Mahmoudi, H. Hosseinkhani, M. Hosseinkhani, S. Boutry, A. Simchi, W. S. Journeay, K. Subramani, S. Laurent, *Chemical Reviews* **2011**, *111*, 253-280.

[64] M. D. Fox, M. E. Raichle, *Nature Reviews Neuroscience* **2007**, *8*, 700-711.

[65] E. L. Que, C. J. Chang, *Chemical Society Reviews* **2010**, *39*, 51-60.

[66] J. Thevenot, H. Oliveira, O. Sandre, S. Lecommandoux, *Chemical Society Reviews* **2013**.

[67] H. Ringsdorf, *Journal of Polymer Science Part C-Polymer Symposium* **1975**, 135-153.

[68] R. Langer, *Chemical Engineering Communications* **1980**, *6*, 1-48.

[69] Y. Lu, Y. Mei, M. Drechsler, M. Ballauff, *Angewandte Chemie International Edition* **2006**, *45*, 813-816.

[70] K. E. Uhrich, S. M. Cannizzaro, R. S. Langer, K. M. Shakesheff, *Chemical Reviews* **1999**, *99*, 3181-3198.

[71] D. A. Fluri, C. Kemmer, M. D. E. Baba, M. Fussenegger, *Journal of Controlled Release* **2008**, *131*, 211-219.

[72] A. K. Patri, J. F. Kukowska-Latallo, J. R. Baker, *Advanced Drug Delivery Reviews* **2005**, *57*, 2203-2214.

[73] Y. N. Zhao, J. L. Vivero-Escoto, Slowing, II, B. C. Trewyn, V. S. Y. Lin, *Expert Opinion on Drug Delivery* **2010**, *7*, 1013-1029.

[74] P. Gupta, K. Vermani, S. Garg, *Drug Discovery Today* **2002**, *7*, 569-579.

[75] M. Nakayama, T. Okano, T. Miyazaki, F. Kohori, K. Sakai, M. Yokoyama, *Journal of Controlled Release* **2006**, *115*, 46-56.

[76] C. Park, K. Oh, S. C. Lee, C. Kim, *Angewandte Chemie-International Edition* **2007**, *46*, 1455-1457.

[77] K. Niikura, N. Iyo, Y. Matsuo, H. Mitomo, K. Ijiro, *Acs Applied Materials & Interfaces* **2013**, *5*, 3900-3907.

[78] A. P. R. Johnston, G. K. Such, F. Caruso, *Angewandte Chemie-International Edition* **2010**, *49*, 2664-2666.

[79] R. P. Liburdy, R. L. Magin, *Radiation Research* **1985**, *103*, 266-275.

[80] J. Ge, E. Neofytou, T. J. Cahill, R. E. Beygui, R. N. Zare, *Acs Nano* **2012**, *6*, 227-233.

[81] K. Katagiri, M. Nakamura, K. Koumoto, *Acs Applied Materials & Interfaces* **2010**, *2*, 768-773.

[82] C. Alexiou, A. Schmidt, R. Klein, P. Hulin, C. Bergemann, W. Arnold, *Journal of Magnetism and Magnetic Materials* **2002**, *252*, 363-366.

[83] S. Louguet, B. Rousseau, R. Epherre, N. Guidolin, G. Goglio, S. Mornet, E. Duguet, S. Lecommandoux, C. Schatz, *Polymer Chemistry* **2012**, *3*, 1408-1417.

[84] C. Y. Liu, J. Guo, W. L. Yang, J. H. Hu, C. C. Wang, S. K. Fu, *Journal of Materials Chemistry* **2009**, *19*, 4764-4770.

[85] S. D. Kong, W. Z. Zhang, J. H. Lee, C. Choi, J. Khamwannah, M. Karin, S. H. Jin, *Journal of Vacuum Science & Technology B* **2012**, *30*.

[86] H. Oliveira, E. Perez-Andres, J. Thevenot, O. Sandre, E. Berra, S. Lecommandoux, *Journal of Controlled Release* **2013**, *169*, 165-170.

[87] S. A. Rovers, R. Hoogenboom, M. F. Kemmere, J. T. F. Keurentjes, *Soft Matter* **2012**, *8*, 1623-1627.

[88] J. Zhang, R. D. K. Misra, *Acta Biomaterialia* **2007**, *3*, 838-850.

[89] A. M. Schmidt, *Colloid and Polymer Science* **2007**, *285*, 953-966.

[90] M. Feyen, E. Heim, F. Ludwig, A. M. Schmidt, *Chemistry of Materials* **2008**, *20*, 2942-2948.

[91] A. Lendlein, S. Kelch, *Angewandte Chemie-International Edition* **2002**, *41*, 2034-2057.

[92] A. Lendlein, R. Langer, *Science* **2002**, *296*, 1673-1676.

[93] C. Mangold, B. Obermeier, F. Wurm, H. Frey, *Macromol. Rapid Commun.* **2011**, *32*, 1930-1934.

[94] I. C. Sanchez, R. H. Lacombe, *Macromolecules* **1978**, *11*, 1145-1156.

[95] P. Brown, A. Bushmelev, C. P. Butts, J. Cheng, J. Eastoe, I. Grillo, R. K. Heenan, A. M. Schmidt, *Angewandte Chemie-International Edition* **2012**, *51*, 2414-2416.

[96] H. Wang, Q. W. Chen, Y. B. Sun, M. Y. He, *Journal of Physical Chemistry C* **2010**, *114*, 19660-19666.

[97] H. Maeda, K. Greish, J. Fang, in *Polymer Therapeutics Ii: Polymers as Drugs, Conjugates and Gene Delivery Systems, Vol. 193* (Eds.: R. SatchiFainaro, R. Duncan), **2006**, pp. 103-121.

[98] Y. Matsumura, H. Maeda, *Cancer Research* **1986**, *46*, 6387-6392.

[99] R. Haag, F. Kratz, *Angewandte Chemie* **2006**, *118*, 1218-1237.

[100] L. Borsi, B. Carnemolla, E. Balza, P. Castellani, L. Zardi, M. Friebe, C.-S. Hilger, **2013**.

[101] F. Kratz, *Pharmazie in unserer Zeit* **1995**, *24*, 14-26.

[102] C. Alexiou, W. Arnold, R. J. Klein, F. G. Parak, P. Hulin, C. Bergemann, W. Erhardt, S. Wagenpfeil, A. S. Lubbe, *Cancer Research* **2000**, *60*, 6641-6648.

[103] S. J. Zhu, M. H. Hong, G. T. Tang, L. L. Qian, J. Y. Lin, Y. Y. Jiang, Y. Y. Pei, *Biomaterials* **2010**, *31*, 1360-1371.

[104] G. Baier, D. Baumann, J. M. Siebert, A. Musyanovych, V. Mailander, K. Landfester, *Biomacromolecules* **2012**, *13*, 2704-2715.

[105] H. Freichels, M. Wagner, P. Okwieka, R. G. Meyer, V. Mailander, K. Landfester, A. Musyanovych, *Journal of Materials Chemistry B* **2013**, *1*, 4338-4348.

[106] J. L. Zhang, Z. Y. Feng, X. Q. Jia, M. L. Liang, Z. W. Men, Y. Zhang, Y. F. Bu, W. Li, *Chemical Engineering Science* **2013**, *99*, 28-37.

[107] A. Pavía-Sanders, S. Zhang, J. A. Flores, J. E. Sanders, J. E. Raymond, K. L. Wooley, *Acs Nano* **2013**, *7*, 7552-7561.

[108] H. M. Moon, J. W. Kim, *Biotechnology Progress* **2010**, *26*, 179-185.

[109] Z. R. Yurkovetsky, J. M. Kirkwood, H. D. Edington, A. M. Marrangoni, L. Velikokhatnaya, M. T. Winans, E. Gorelik, A. E. Lokshin, *Clinical Cancer Research* **2007**, *13*, 2422-2428.

[110] A. I. Abdelrahman, S. Dai, S. C. Thickett, O. Ornatsky, D. Bandura, V. Baranov, M. A. Winnik, *J. Am. Chem. Soc.* **2009**, *131*, 15276-15283.

[111] W. A. Bonner, R. G. Sweet, H. R. Hulett, Herzenbe.La, *Review of Scientific Instruments* **1972**, *43*, 404-&.

[112] N. Harbeck, S. Schwarze, E. Schuren, N. Yamamoto, N. Moniwa, M. Schmitt, P. Dettmar, W. Nathrath, F. Janicke, H. Hofler, H. Graeff, *International Journal of Oncology* **1995**, *6*, 1249-1254.

[113] M. Imbeault, R. Lodge, M. Ouellet, M. J. Tremblay, *Virology* **2009**, *393*, 160-167.

[114] A. Matsumine, K. Takegami, K. Asanuma, T. Matsubara, T. Nakamura, A. Uchida, A. Sudo, *International Journal of Clinical Oncology* **2011**, *16*, 101-108.

[115] A. Jordan, R. Scholz, P. Wust, H. Fahling, R. Felix, *Journal of Magnetism and Magnetic Materials* **1999**, *201*, 413-419.

[116] O. Veiseh, J. W. Gunn, M. Q. Zhang, *Advanced Drug Delivery Reviews* **2010**, *62*, 284-304.

[117] S. Ganta, H. Devalapally, A. Shahiwala, M. Amiji, *Journal of Controlled Release* **2008**, *126*, 187-204.

[118] M. Liong, J. Lu, M. Kovochich, T. Xia, S. G. Ruehm, A. E. Nel, F. Tamanoi, J. I. Zink, *Acs Nano* **2008**, *2*, 889-896.

[119] B. Gleich, R. Weizenecker, *Nature* **2005**, *435*, 1214-1217.

[120] J. Y. Yuan, Y. Y. Xu, A. H. E. Muller, *Chemical Society Reviews* **2011**, *40*, 640-655.

[121] K. Y. van Berkel, A. M. Piekarski, P. H. Kierstead, E. D. Pressly, P. C. Ray, C. J. Hawker, *Macromolecules* **2009**, *42*, 1425-1427.

[122] L. P. Ramirez, K. Landfester, *Macromolecular Chemistry and Physics* **2003**, *204*, 22-31.

[123] H. Xu, L. L. Cui, N. H. Tong, H. C. Gu, *J. Am. Chem. Soc.* **2006**, *128*, 15582-15583.

[124] D. L. Shi, H. S. Cho, Y. Chen, H. Xu, H. C. Gu, J. Lian, W. Wang, G. K. Liu, C. Huth, L. M. Wang, R. C. Ewing, S. Budko, G. M. Pauletti, Z. Y. Dong, *Advanced Materials* **2009**, *21*, 2170-+.

[125] S. Bhattacharya, F. Eckert, V. Boyko, A. Pich, *Small* **2007**, *3*, 650-657.

[126] S. Park, J. H. Lim, S. W. Chung, C. A. Mirkin, *Science* **2004**, *303*, 348-351.

[127] H. Wang, A. J. Patil, K. Liu, S. Petrov, S. Mann, M. A. Winnik, I. Manners, *Advanced Materials* **2009**, *21*, 1805-+.

[128] X. Youyong, Y. Jiayin, F. Bing, M. Drechsler, M. Mullner, S. Bolisetty, M. Ballauff, A. Muller, *Advanced Functional Materials* **2010**, *20*, 4182-4189.

[129] D. Nyamjav, J. M. Kinsella, A. Ivanisevica, *Applied Physics Letters* **2005**, *86*.

[130] Z. M. Huang, Y. Z. Zhang, M. Kotaki, S. Ramakrishna, *Composites Science and Technology* **2003**, *63*, 2223-2253.

[131] S. Agarwal, A. Greiner, J. H. Wendorff, *Progress in Polymer Science* **2013**, *38*, 963-991.

[132] C. Huang, S. J. Soenen, J. Rejman, J. Trekker, L. Chengxun, L. Lagae, W. Ceelen, C. Wilhelm, J. Demeester, S. C. De Smedt, *Advanced Functional Materials* **2012**, *22*, 2479-2486.

[133] M. B. Bannwarth, S. W. Kazer, S. Ulrich, G. Glasser, D. Crespy, K. Landfester, *Angewandte Chemie International Edition* **2013**, *52*, 10107-10111.

[134] M. Ma, Q. Zhang, J. Dou, H. Zhang, D. Yin, W. Geng, Y. Zhou, *Journal of Colloid and Interface Science* **2012**, *374*, 339-344.

[135] K. S. Khalil, A. Sagastegui, Y. Li, M. A. Tahir, J. E. S. Socolar, B. J. Wiley, B. B. Yellen, *Nature Communications* **2012**, *3*.

[136] Z. Junfeng, M. Lingjie, F. Xinliang, Z. Xiaoke, L. Qinghua, *Angewandte Chemie International Edition* **2010**, *49*, 8476-84798479.

[137] H. Singh, P. E. Laibinis, T. A. Hatton, *Langmuir* **2005**, *21*, 11500-11509.

[138] R. Sheparovych, Y. Sahoo, M. Motornov, S. M. Wang, H. Luo, P. N. Prasad, I. Sokolov, S. Minko, *Chemistry of Materials* **2006**, *18*, 591-593.

[139] A. J. Amali, P. Saravanan, R. K. Rana, *Angewandte Chemie International Edition* **2011**, *50*, 1318-1321.

[140] Y. Xin, Z. H. Huang, L. Peng, D. J. Wang, *Journal of Applied Physics* **2009**, *105*.

[141] J. M. Kinsella, A. Ivanisevic, *J. Am. Chem. Soc.* **2005**, *127*, 3276-3277.

[142] O. Kriha, M. Becker, M. Lehmann, D. Kriha, J. Krieglstein, M. Yosef, S. Schlecht, R. B. Wehrspohn, J. H. Wendorff, A. Greiner, *Advanced Materials* **2007**, *19*, 2483-+.

[143] J. L. Keddie, *Materials Science & Engineering R-Reports* **1997**, *21*, 101-170.

[144] M. Soleimani, J. C. Haley, D. Majonis, G. Guerin, W. Lau, M. A. Winnik, *J. Am. Chem. Soc.* **2011**, *133*, 11299-11307.

[145] M. Soleimani, S. Khan, D. Mendenhall, W. Lau, M. A. Winnik, *Polymer* **2012**, *53*, 2652-2663.

[146] Y. C. Wang, M. A. Winnik, *Macromolecules* **1990**, *23*, 4731-4732.

[147] B. Hatton, L. Mishchenko, S. Davis, K. H. Sandhage, J. Aizenberg, *Proceedings of the National Academy of Sciences of the United States of America* **2010**, *107*, 10354-10359.

[148] A. J. Hart, A. H. Slocum, *Nano Letters* **2006**, *6*, 1254-1260.

[149] J. Bang, U. Jeong, D. Y. Ryu, T. P. Russell, C. J. Hawker, *Advanced Materials* **2009**, *21*, 4769-4792.

[150] H. R. Vutukuri, A. F. Demirörs, B. Peng, P. D. J. van Oostrum, A. Imhof, A. van Blaaderen, *Angewandte Chemie International Edition* **2012**, *51*, 11249-11253.

[151] H. R. Vutukuri, J. Stiefelhagen, T. Vissers, A. Imhof, A. van Blaaderen, *Advanced Materials* **2012**, *24*, 412-+.

[152] A. Ruditskiy, B. Ren, I. Kretzschmar, *Soft Matter* **2013**, *9*, 9174-9181.

[153] G. M. Whitesides, J. P. Mathias, C. T. Seto, *Science* **1991**, *254*, 1312-1319.

[154] K. J. M. Bishop, C. E. Wilmer, S. Soh, B. A. Grzybowski, *Small* **2009**, *5*, 1600-1630.

[155] C. B. Murray, C. R. Kagan, M. G. Bawendi, *Science* **1995**, *270*, 1335-1338.

[156] B. Moulton, M. J. Zaworotko, *Chemical Reviews* **2001**, *101*, 1629-1658.

[157] M. E. Leunissen, C. G. Christova, A. P. Hynninen, C. P. Royall, A. I. Campbell, A. Imhof, M. Dijkstra, R. van Roij, A. van Blaaderen, *Nature* **2005**, *437*, 235-240.

[158] E. P. K. Currie, W. Norde, M. A. C. Stuart, *Advances in Colloid and Interface Science* **2003**, *100*, 205-265.

[159] D. A. Christian, A. W. Tian, W. G. Ellenbroek, I. Levental, K. Rajagopal, P. A. Janmey, A. J. Liu, T. Baumgart, D. E. Discher, *Nature Materials* **2009**, *8*, 843-849.

[160] A. F. Demirors, P. P. Pillai, B. Kowalczyk, B. A. Grzybowski, *Nature* **2013**, *advance online publication*.

[161] B. W. Brooks, *Chemical Engineering & Technology* **2010**, *33*, 1737-1744.

[162] N. Vogel, L. de Viguerie, U. Jonas, C. K. Weiss, K. Landfester, *Advanced Functional Materials* **2011**, *21*, 3064-3073.

[163] A. Snezhko, I. S. Aranson, *Nat Mater* **2011**, *10*, 698-703.

[164] J. Yan, M. Bloom, S. C. Bae, E. Luijten, S. Granick, *Nature* **2012**, *491*, 578-581.

[165] Q. Chen, S. C. Bae, S. Granick, *Nature* **2011**, *469*, 381-384.

[166] Y. F. Wang, Y. Wang, D. R. Breed, V. N. Manoharan, L. Feng, A. D. Hollingsworth, M. Weck, D. J. Pine, *Nature* **2012**, *491*, 51-U61.

[167] F. Li, D. P. Josephson, A. Stein, *Angewandte Chemie International Edition* **2011**, *50*, 360-388.

[168] A. Perro, E. Duguet, O. Lambert, J. C. Taveau, E. Bourgeat-Lami, S. Ravaine, *Angewandte Chemie-International Edition* **2009**, *48*, 361-365.

[169] K. W. Urban, *Science* **2008**, *321*, 506-510.

[170] Z. L. Wang, *Advanced Materials* **2003**, *15*, 1497-1514.

[171] W. J. Deruijter, *Micron* **1995**, *26*, 247-275.

[172] S. Roath, D. Newell, A. Polliack, E. Alexander, P. S. Lin, *Nature* **1978**, *273*, 15-18.

[173] D. C. Joy, J. B. Pawley, *Ultramicroscopy* **1992**, *47*, 80-100.

[174] D. A. Muller, *Nature Materials* **2009**, *8*, 263-270.

[175] W. Schärtl, *Light Scattering from Polymer Solutions and Nanoparticle Dispersions*, Springer, Berlin, **2007**.

[176] A. Sze, D. Erickson, L. Q. Ren, D. Q. Li, *Journal of Colloid and Interface Science* **2003**, *261*, 402-410.

[177] R. J. Hunter, *Journal of Physical Chemistry* **1962**, *66*, 1367-&.

[178] S. Foner, *Review of Scientific Instruments* **1959**, *30*, 548-557.

[179] M. Hesse, H. Meier, B. Zeeh, *Spektroskopische Methoden in der organischen Chemie*, Thieme Georg Verlag, **2005**.

[180] R. H. Hashemi, W. G. Bradley, C. J. Lisanti, *Mri: The Basics*, Lippincott Williams & Wilkins, **2004**.

[181] J. J. Liu, R. Horst, V. Katritch, R. C. Stevens, K. Wuthrich, *Science* **2012**, *335*, 1106-1110.

[182] Y. J. Wang, L. Hosta-Rigau, H. Lomas, F. Caruso, *Physical Chemistry Chemical Physics* **2011**, *13*, 4782-4801.

[183] Y. Zhao, J. Fickert, K. Landfester, D. Crespy, *Small* **2012**, *8*, 2954-2958.

[184] J. Fickert, P. Rupper, R. Graf, K. Landfester, D. Crespy, *Journal of Materials Chemistry* **2012**, *22*, 2286-2291.

[185] I. G. Loscertales, A. Barrero, I. Guerrero, R. Cortijo, M. Marquez, A. M. Ganan-Calvo, *Science* **2002**, *295*, 1695-1698.

[186] S. Svenson, *European Journal of Pharmaceutics and Biopharmaceutics* **2009**, *71*, 445-462.

[187] J. Jansen, E. M. M. Debrabandervandenberg, E. W. Meijer, *Science* **1994**, *266*, 1226-1229.

[188] C. E. Mora-Huertas, H. Fessi, A. Elaissari, *International Journal of Pharmaceutics* **2010**, *385*, 113-142.

[189] L. J. De Cock, S. De Koker, B. G. De Geest, J. Grooten, C. Vervaet, J. P. Remon, G. B. Sukhorukov, M. N. Antipina, *Angewandte Chemie-International Edition* **2010**, *49*, 6954-6973.

[190] T. R. Hoare, D. S. Kohane, *Polymer* **2008**, *49*, 1993-2007.

[191] R. Langer, *Nature* **1998**, *392*, 5-10.

[192] A. K. Bajpai, S. K. Shukla, S. Bhanu, S. Kankane, *Progress in Polymer Science* **2008**, *33*, 1088-1118.

[193] C. Sun, J. S. H. Lee, M. Q. Zhang, *Advanced Drug Delivery Reviews* **2008**, *60*, 1252-1265.

[194] M. Arruebo, R. Fernandez-Pacheco, M. R. Ibarra, J. Santamaria, *Nano Today* **2007**, *2*, 22-32.

[195] P. Cherukuri, E. S. Glazer, S. A. Curleya, *Advanced Drug Delivery Reviews* **2010**, *62*, 339-345.

[196] C. Kumar, F. Mohammad, *Advanced Drug Delivery Reviews* **2011**, *63*, 789-808.

[197] K. Katagiri, Y. Imai, K. Koumoto, T. Kaiden, K. Kono, S. Aoshima, *Small* **2011**, *7*, 1683-1689.

[198] S.-H. Hu, B.-J. Liao, C.-S. Chiang, P.-J. Chen, I. W. Chen, S.-Y. Chen, *Advanced Materials* **2012**, *24*, 3627-3632.

[199] E. M. Rosenbauer, M. Wagner, A. Musyanovych, K. Landfester, *Macromolecules* **2010**, *43*, 5083-5093.

[200] H. M. Kim, H. Lee, K. S. Hong, M. Y. Cho, M. H. Sung, H. Poo, Y. T. Lim, *Acs Nano* **2011**, *5*, 8230-8240.

[201] H. Yang, C. X. Zhang, X. Y. Shi, H. Hu, X. X. Du, Y. Fang, Y. B. Ma, H. X. Wu, S. P. Yang, *Biomaterials* **2010**, *31*, 3667-3673.

[202] E. W. Peng, E. S. G. Choo, P. Chandrasekharan, C. T. Yang, J. Ding, K. H. Chuang, J. M. Xue, *Small* **2012**, *8*, 3620-3630.

[203] Z. X. Tang, C. M. Sorensen, K. J. Klabunde, G. C. Hadjipanayis, *Journal of Applied Physics* **1991**, *69*, 5279-5281.

[204] K. Landfester, *Annual Review of Materials Research* **2006**, *36*, 231-279.

[205] D. Crespy, M. Stark, C. Hoffmann-Richter, U. Ziener, K. Landfester, *Macromolecules* **2007**, *40*, 3122-3135.

[206] U. Paiphansiri, J. Dausend, A. Musyanovych, V. Mailander, K. Landfester, *Macromolecular Bioscience* **2009**, *9*, 575-584.

[207] M. Bannwarth, Diplomarbeit, Johannes Gutenberg Universität (Mainz), **2010**.

[208] W. K. Johnson, C. Stoupis, G. M. Torres, E. B. Rosenberg, P. R. Ros, *Magnetic Resonance Imaging* **1996**, *14*, 43-49.

[209] F. Hu, H. M. Joshi, V. P. Dravid, T. J. Meade, *Nanoscale* **2010**, *2*, 1884-1891.

[210] J. Qin, S. Laurent, Y. S. Jo, A. Roch, M. Mikhaylova, Z. M. Bhujwalla, R. N. Muller, M. Muhammed, *Advanced Materials* **2007**, *19*, 1874-1878.

[211] E. Amstad, T. Gillich, I. Bilecka, M. Textor, E. Reimhult, *Nano Letters* **2009**, *9*, 4042-4048.

[212] E. Amstad, M. Textor, E. Reimhult, *Nanoscale* **2011**, *3*, 2819-2843.

[213] Y.-X. J. Wang, *Quantitative Imaging in Medicine and Surgery* **2011**, *1*, 35-40.

[214] R. Lawaczeck, H. Bauer, T. Frenzel, M. Hasegawa, Y. Ito, K. Kito, N. Miwa, H. Tsutsui, H. Volger, H. J. Weinmann, *Acta Radiologica* **1997**, *38*, 584-597.

[215] O. Lunov, T. Syrovets, C. Rocker, K. Tron, G. U. Nienhaus, V. Rasche, V. Mailander, K. Landfester, T. Simmet, *Biomaterials* **2010**, *31*, 9015-9022.

[216] F. Q. Hu, K. W. MacRenaris, E. A. Waters, T. Y. Liang, E. A. Schultz-Sikma, A. L. Eckermann, T. J. Meade, *Journal of Physical Chemistry C* **2009**, *113*, 20855-20860.

[217] T. G. Park, A. S. Hoffman, *Journal of Biomedical Materials Research* **1990**, *24*, 21-38.

[218] M. A. C. Stuart, W. T. S. Huck, J. Genzer, M. Muller, C. Ober, M. Stamm, G. B. Sukhorukov, I. Szleifer, V. V. Tsukruk, M. Urban, F. Winnik, S. Zauscher, I. Luzinov, S. Minko, *Nature Materials* **2010**, *9*, 101-113.

[219] E. Amstad, S.-H. Kim, D. A. Weitz, *Angewandte Chemie International Edition* **2012**, *51*, 12499-12503.

[220] N. Bhuchar, R. Sunasee, K. Ishihara, T. Thundat, R. Narain, *Bioconjugate Chemistry* **2012**, *23*, 75-83.

[221] J. Seuring, S. Agarwal, *Macromol. Rapid Commun.* **2012**, *33*, 1898-1920.

[222] P. J. Roth, F. D. Jochum, P. Theato, *Soft Matter* **2011**, *7*, 2484-2492.

[223] Y. Maeda, H. Mochiduki, I. Ikeda, *Macromol. Rapid Commun.* **2004**, *25*, 1330-1334.

[224] R. Buscall, T. Corner, *European Polymer Journal* **1982**, *18*, 967-974.

[225] A. O. Govorov, H. H. Richardson, *Nano Today* **2007**, *2*, 30-38.

[226] G. Han, C. C. You, B. J. Kim, R. S. Turingan, N. S. Forbes, C. T. Martin, V. M. Rotello, *Angewandte Chemie-International Edition* **2006**, *45*, 3165-3169.

[227] D. V. Volodkin, A. G. Skirtach, H. Mohwald, *Angewandte Chemie-International Edition* **2009**, *48*, 1807-1809.

[228] S. K. Ghosh, T. Pal, *Chemical Reviews* **2007**, *107*, 4797-4862.

[229] H. P. Latscha, M. Mutz, *Chemie der Elemente*, Springer, **2011**.

[230] L.-P. Lv, Y. Zhao, N. Vilbrandt, M. Gallei, A. Vimalanandan, M. Rohwerder, K. Landfester, D. Crespy, *J. Am. Chem. Soc.* **2013**.

[231] R. H. Staff, M. Gallei, M. Mazurowski, M. Rehahn, R. Berger, K. Landfester, D. Crespy, *Acs Nano* **2012**, *6*, 9042-9049.

[232] L. L. del Mercato, E. Gonzalez, A. Z. Abbasi, W. J. Parak, V. Puntes, *Journal of Materials Chemistry* **2011**, *21*, 11468-11471.

[233] G. F. Luo, X. D. Xu, J. Zhang, J. Yang, Y. H. Gong, Q. Lei, H. Z. Jia, C. Li, R. X. Zhuo, X. Z. Zhang, *Acs Applied Materials & Interfaces* **2012**, *4*, 5317-5324.

[234] C. Schaffer, H. Bogge, A. Merca, I. A. Weinstock, D. Rehder, E. T. K. Haupt, A. Muller, *Angewandte Chemie-International Edition* **2009**, *48*, 8051-8056.

[235] J. Dong, Y. N. Wang, J. Zhang, X. W. Zhan, S. Q. Zhu, H. Yang, G. J. Wang, *Soft Matter* **2013**, *9*, 370-373.

[236] C. Herrmann, M. B. Bannwarth, K. Landfester, D. Crespy, *Macromolecular Chemistry and Physics* **2012**, *213*, 829-838.

[237] B. Madivala, S. Vandebril, J. Fransaer, J. Vermant, *Soft Matter* **2009**, *5*, 1717-1727.

[238] L. Florez, C. Herrmann, J. M. Cramer, C. P. Hauser, K. Koynov, K. Landfester, D. Crespy, V. Mailander, *Small* **2012**, *8*, 2222-2230.

[239] S. E. A. Gratton, P. A. Ropp, P. D. Pohlhaus, J. C. Luft, V. J. Madden, M. E. Napier, J. M. DeSimone, *Proceedings of the National Academy of Sciences of the United States of America* **2008**, *105*, 11613-11618.

[240] K. Landfester, L. P. Ramirez, *Journal of Physics-Condensed Matter* **2003**, *15*, S1345-S1361.

[241] H. Y. Carr, *Physics Today* **2004**, *57*, 83-83.

[242] R. Damadian, *Science* **1971**, *171*, 1151-&.

[243] S. Sharma, U. Paiphansiri, V. Hombach, V. Mailander, O. Zimmermann, K. Landfester, V. Rasche, *Contrast Media & Molecular Imaging* **2010**, *5*, 59-69.

[244] V. Fischer, M. B. Bannwarth, G. Jakob, K. Landfester, R. Muñoz-Espí, *The Journal of Physical Chemistry C* **2013**, *117*, 5999-6005.

[245] E. Q. Song, J. Hu, C. Y. Wen, Z. Q. Tian, X. Yu, Z. L. Zhang, Y. B. Shi, D. W. Pang, *Acs Nano* **2011**, *5*, 761-770.

[246] H. S. Cho, Z. Y. Dong, G. M. Pauletti, J. M. Zhang, H. Xu, H. C. Gu, L. M. Wang, R. C. Ewing, C. Huth, F. Wang, D. L. Shi, *Acs Nano* **2010**, *4*, 5398-5404.

[247] M. J. Jin, D. H. Lee, *Angewandte Chemie-International Edition* **2010**, *49*, 1119-1122.

[248] A. Riedinger, M. P. Leal, S. R. Deka, C. George, I. R. Franchini, A. Falqui, R. Cingolani, T. Pellegrino, *Nano Letters* **2011**, *11*, 3136-3141.

[249] P. T. Hammond, *Materials Today* **2012**, *15*, 196-206.

[250] R. G. Pearson, *J. Am. Chem. Soc.* **1963**, *85*, 3533-&.

[251] E. Terreno, D. Delli Castelli, A. Viale, S. Aime, *Chemical Reviews* **2010**, *110*, 3019-3042.

[252] Y. Ding, Y. Hu, L. Y. Zhang, Y. Chen, X. Q. Jiang, *Biomacromolecules* **2006**, *7*, 1766-1772.

[253] G. Liu, J. Xie, F. Zhang, Z. Wang, K. Luo, L. Zhu, Q. Quan, G. Niu, S. Lee, H. Ai, X. Chen, *Small* **2011**, *7*, 2742-2749.

[254] V. Salgueirino-Maceira, L. M. Liz-Marzan, M. Farle, *Langmuir* **2004**, *20*, 6946-6950.

[255] S. Laurent, D. Forge, M. Port, A. Roch, C. Robic, L. V. Elst, R. N. Muller, *Chemical Reviews* **2008**, *108*, 2064-2110.

[256] Q. L. Vuong, P. Gillis, Y. Gossuin, *Journal of Magnetic Resonance* **2011**, *212*, 139-148.

[257] A. K. Gupta, M. Gupta, *Biomaterials* **2005**, *26*, 3995-4021.

[258] L. Frullano, C. Catana, T. Benner, A. D. Sherry, P. Caravan, *Angewandte Chemie International Edition* **2010**, *49*, 2382-2384.

[259] V. Mailander, M. R. Lorenz, V. Holzapfel, A. Musyanovych, K. Fuchs, M. Wiesneth, P. Walther, K. Landfester, H. Schrezenmeier, *Molecular Imaging and Biology* **2008**, *10*, 138-146.

[260] M. Urban, A. Musyanovych, K. Landfester, *Macromolecular Chemistry and Physics* **2009**, *210*, 961-970.

[261] G. Schmidtke-Schrezenmeier, M. Urban, A. Musyanovych, V. Mailander, M. Rojewski, N. Fekete, C. Menard, E. Deak, K. Tarte, V. Rasche, K. Landfester, H. Schrezenmeier, *Cytotherapy* **2011**, *13*, 962-975.

[262] A. Musyanovych, J. Schmitz-Wienke, V. Mailander, P. Walther, K. Landfester, *Macromolecular Bioscience* **2008**, *8*, 127-139.

[263] A. Hocherl, M. Dass, K. Landfester, V. Mailander, A. Musyanovych, *Macromolecular Bioscience* **2012**, *12*, 454-464.

[264] U. J. Choe, A. R. Rodriguez, B. S. Lee, S. M. Knowles, A. M. Wu, T. J. Deming, D. T. Kamei, *Biomacromolecules* **2013**, *14*, 1458-1464.

[265] D. Vercauteren, H. Deschout, K. Remaut, J. F. J. Engbersen, A. T. Jones, J. Demeester, S. C. De Smedt, K. Braeckmans, *Acs Nano* **2011**, *5*, 7874-7884.

[266] I. Nikiforow, J. r. Adams, A. M. König, A. Langhoff, K. Pohl, A. Turshatov, D. Johannsmann, *Langmuir* **2010**, *26*, 13162-13167.

[267] V. Holzapfel, M. Lorenz, C. K. Weiss, H. Schrezenmeier, K. Landfester, V. Mailander, *Journal of Physics-Condensed Matter* **2006**, *18*, S2581-S2594.

[268] K. Landfester, C. K. Weiss, in *Modern Techniques for Nano- and Microreactors/-Reactions, Vol. 229*, Springer-Verlag Berlin, Berlin, **2010**, pp. 1-49.

[269] B. J. Blaiszik, N. R. Sottos, S. R. White, *Composites Science and Technology* **2008**, *68*, 978-986.

[270] L.-P. Lv, Y. Zhao, N. Vilbrandt, M. Gallei, A. Vimalanandan, M. Rohwerder, K. Landfester, D. Crespy, *J. Am. Chem. Soc.* **2013**, *135*, 14198-14205.

[271] Z. Yi, J. Fickert, K. Landfester, D. Crespy, *Small* **2012**, *8*, 2954-2958.

[272] C. Wohnhaas, A. Turshatov, V. Mailander, S. Lorenz, S. Baluschev, T. Miteva, K. Landfester, *Macromolecular Bioscience* **2011**, *11*, 772-778.

[273] M. Srinivasarao, *Chemical Reviews* **1999**, *99*, 1935-1962.

[274] Y. Bai, J. Feng, Y. F. Liu, J. F. Song, J. Simonen, Y. Jin, Q. D. Chen, J. Zi, H. B. Sun, *Organic Electronics* **2011**, *12*, 1927-1935.

[275] P. Roach, N. J. Shirtcliffe, M. I. Newton, *Soft Matter* **2008**, *4*, 224-240.

[276] H.-J. Butt, C. Semprebon, P. Papadopoulos, D. Vollmer, M. Brinkmann, M. Ciccotti, *Soft Matter* **2013**, *9*, 418-428.

[277] D. Y. Xia, L. M. Johnson, G. P. Lopez, *Advanced Materials* **2012**, *24*, 1287-1302.

[278] D. Y. Xia, S. R. J. Brueck, *Nano Letters* **2008**, *8*, 2819-2824.

[279] A. Bruno, *Macromolecules* **2010**, *43*, 10163-10184.

[280] M. Delucchi, S. Turri, A. Barbucci, M. Bassi, S. Novelli, G. Cerisola, *Journal of Polymer Science Part B-Polymer Physics* **2002**, *40*, 52-64.

[281] B. Ameduri, B. Boutevin, G. Kostov, *Progress in Polymer Science* **2001**, *26*, 105-187.

[282] D. Oner, T. J. McCarthy, *Langmuir* **2000**, *16*, 7777-7782.

[283] S. Berger, L. Ionov, A. Synytska, *Advanced Functional Materials* **2011**, *21*, 2338-2344.

[284] K. Jankova, S. Hvilsted, *Macromolecules* **2003**, *36*, 1753-1758.

[285] B. D. Korth, P. Keng, I. Shim, S. E. Bowles, C. Tang, T. Kowalewski, K. W. Nebesny, J. Pyun, *J. Am. Chem. Soc.* **2006**, *128*, 6562-6563.

[286] M. Feyen, C. Weidenthaler, F. Schuth, A. H. Lu, *J. Am. Chem. Soc.* **2010**, *132*, 6791-6799.

[287] P. Reineck, G. P. Lee, D. Brick, M. Karg, P. Mulvaney, U. Bach, *Advanced Materials* **2012**, *24*, 4750-4755.

[288] D. L. Long, E. Burkholder, L. Cronin, *Chemical Society Reviews* **2007**, *36*, 105-121.

[289] D. H. Wang, R. Kou, D. Choi, Z. G. Yang, Z. M. Nie, J. Li, L. V. Saraf, D. H. Hu, J. G. Zhang, G. L. Graff, J. Liu, M. A. Pope, I. A. Aksay, *Acs Nano* **2010**, *4*, 1587-1595.

[290] S. Cavaliere, S. Subianto, I. Savych, D. J. Jones, J. Roziere, *Energy & Environmental Science* **2011**, *4*, 4761-4785.

[291] Y. Z. Long, M. Yu, B. Sun, C. Z. Gu, Z. Y. Fan, *Chemical Society Reviews* **2012**, *41*, 4560-4580.

[292] G. F. Zheng, F. Patolsky, Y. Cui, W. U. Wang, C. M. Lieber, *Nature Biotechnology* **2005**, *23*, 1294-1301.

[293] J. Y. Cheng, C. T. Rettner, D. P. Sanders, H. C. Kim, W. D. Hinsberg, *Advanced Materials* **2008**, *20*, 3155-3158.

[294] M. Paven, P. Papadopoulos, S. Schöttler, X. Deng, V. Mailänder, D. Vollmer, H.-J. Butt, *Nat Commun* **2013**, *4*.

[295] S. Srinivasan, V. K. Praveen, R. Philip, A. Ajayaghosh, *Angewandte Chemie-International Edition* **2008**, *47*, 5750-5754.

[296] S. Shen, A. Henry, J. Tong, R. T. Zheng, G. Chen, *Nature Nanotechnology* **2010**, *5*, 251-255.

[297] F. Natalio, T. P. Corrales, M. Panthofer, D. Schollmeyer, I. Lieberwirth, W. E. G. Muller, M. Kappl, H. J. Butt, W. Tremel, *Science* **2013**, *339*, 1298-1302.

[298] S. Yang, Y. Sun, L. Chen, Y. Hernandez, X. Feng, K. Müllen, *Sci. Rep.* **2012**, *2*.

[299] Z. H. Wen, S. Q. Ci, F. Zhang, X. L. Feng, S. M. Cui, S. Mao, S. L. Luo, Z. He, J. H. Chen, *Advanced Materials* **2012**, *24*, 1399-1404.

[300] A. Greiner, J. H. Wendorff, *Angewandte Chemie-International Edition* **2007**, *46*, 5670-5703.

[301] D. Crespy, K. Friedemann, A. M. Popa, *Macromol. Rapid Commun.* **2012**, *33*, 1978-1995.

[302] K. Liu, Z. H. Nie, N. N. Zhao, W. Li, M. Rubinstein, E. Kumacheva, *Science* **2010**, *329*, 197-200.

[303] L. Shi, C. J. Pei, Y. M. Xu, Q. Li, *J. Am. Chem. Soc.* **2011**, *133*, 10328-10331.

[304] P. N. Martinho, T. Lemma, B. Gildea, G. Picardi, H. Muller-Bunz, R. J. Forster, T. E. Keyes, G. Redmond, G. G. Morgan, *Angewandte Chemie-International Edition* **2012**, *51*, 11995-11999.

[305] Y. N. Xia, Y. D. Yin, Y. Lu, J. McLellan, *Advanced Functional Materials* **2003**, *13*, 907-918.

[306] Y. Lin, A. Boker, J. B. He, K. Sill, H. Q. Xiang, C. Abetz, X. F. Li, J. Wang, T. Emrick, S. Long, Q. Wang, A. Balazs, T. P. Russell, *Nature* **2005**, *434*, 55-59.

[307] C. B. Mao, D. J. Solis, B. D. Reiss, S. T. Kottmann, R. Y. Sweeney, A. Hayhurst, G. Georgiou, B. Iverson, A. M. Belcher, *Science* **2004**, *303*, 213-217.

[308] S. Y. Park, H. Handa, A. Sandhu, *Nano Letters* **2010**, *10*, 446-451.

[309] R. M. Erb, H. S. Son, B. Samanta, V. M. Rotello, B. B. Yellen, *Nature* **2009**, *457*, 999-1002.

[310] S. Mazur, R. Beckerbauer, J. Buckholz, *Langmuir* **1997**, *13*, 4287-4294.

[311] H. Gausepohl, *Kunststoff-Handbuch*, Hanser Verlag, München, **1996**.

[312] R. E. Dillon, L. A. Matheson, E. B. Bradford, *Journal of Colloid Science* **1951**, *6*, 108-117.

[313] D. Zerrouki, J. Baudry, D. Pine, P. Chaikin, J. Bibette, *Nature* **2008**, *455*, 380-382.

[314] W. M. Kulicke, R. Kniewske, *Rheologica Acta* **1984**, *23*, 75-83.

[315] W. Wei, S. B. Yang, H. X. Zhou, I. Lieberwirth, X. L. Feng, K. Mullen, *Advanced Materials* **2013**, *25*, 2909-2914.

[316] X. Deng, L. Mammen, H. J. Butt, D. Vollmer, *Science* **2012**, *335*, 67-70.

[317] S. Sacanna, M. Korpics, K. Rodriguez, L. Colón-Meléndez, S.-H. Kim, D. J. Pine, G.-R. Yi, *Nat Commun* **2013**, *4*, 1688.

[318] H. Ejima, J. J. Richardson, F. Caruso, *Angewandte Chemie International Edition* **2013**, *52*, 3314-3316.

[319] B. Bharti, G. H. Findenegg, O. D. Velev, *Scientific Reports* **2012**, *2*.

[320] M. G. Warner, J. E. Hutchison, *Nat Mater* **2003**, *2*, 272-277.

[321] C. T. Yavuz, J. T. Mayo, W. W. Yu, A. Prakash, J. C. Falkner, S. Yean, L. L. Cong, H. J. Shipley, A. Kan, M. Tomson, D. Natelson, V. L. Colvin, *Science* **2006**, *314*, 964-967.

[322] Y. Yang, L. Gao, G. P. Lopez, B. B. Yellen, *Acs Nano* **2013**, *7*, 2705-2716.

[323] Y. Min, M. Akbulut, K. Kristiansen, Y. Golan, J. Israelachvili, *Nat Mater* **2008**, *7*, 527-538.

[324] A. H. Groschel, A. Walther, T. I. Lobling, F. H. Schacher, H. Schmalz, A. H. E. Muller, *Nature* **2013**, *advance online publication*.

[325] D. J. Kraft, R. Ni, F. Smallenburg, M. Hermes, K. Yoon, D. A. Weitz, A. van Blaaderen, J. Groenewold, M. Dijkstra, W. K. Kegel, *Proceedings of the National Academy of Sciences of the United States of America* **2012**, *109*, 10787-10792.

[326] O. Benson, *Nature* **2011**, *480*, 193-199.

[327] L. He, M. Wang, J. Ge, Y. Yin, *Accounts of Chemical Research* **2012**, *45*, 1431-1440.

[328] L. Wang, L. Xu, H. Kuang, C. Xu, N. A. Kotov, *Accounts of Chemical Research* **2012**, *45*, 1916-1926.

[329] S. E. Stiriba, H. Kautz, H. Frey, *J. Am. Chem. Soc.* **2002**, *124*, 9698-9699.

[330] P. J. Flory, J. Rehner, *J. Chem. Phys.* **1943**, *11*, 512-520.

[331] P. C. Hiemenz, T. P. Lodge, *Polymer Chemistry*, CRC PressINC, **2007**.

[332] R. P. Feynman, *Engineering and Science* **1960**, 22-36.

[333] G. A. Ozin, I. Manners, S. Fournier-Bidoz, A. Arsenault, *Advanced Materials* **2005**, *17*, 3011-3018.

[334] G. M. Whitesides, R. F. Ismagilov, *Science* **1999**, *284*, 89-92.

[335] K. D. Young, *Current Opinion in Microbiology* **2007**, *10*, 596-600.

[336] S. S. Justice, D. A. Hunstad, L. Cegelski, S. J. Hultgren, *Nat Rev Micro* **2008**, *6*, 162-168.

[337] K. Kerksiek, *Infectionresearch* **2009**.

[338] I. Kolodkin-Gal, S. G. Cao, L. Chai, T. Bottcher, R. Kolter, J. Clardy, R. Losick, *Cell* **2012**, *149*, 684-692.

[339] H. Vlamakis, Y. R. Chai, P. Beauregard, R. Losick, R. Kolter, *Nature Reviews Microbiology* **2013**, *11*, 157-168.

[340] D. Volfson, S. Cookson, J. Hasty, L. S. Tsimring, *Proceedings of the National Academy of Sciences of the United States of America* **2008**, *105*, 15346-15351.

[341] Y. D. Liu, X. G. Han, L. He, Y. D. Yin, *Angewandte Chemie-International Edition* **2012**, *51*, 6373-6377.

[342] D. X. Li, Q. He, Y. Cui, J. B. Li, *Chemistry of Materials* **2007**, *19*, 412-417.

[343] M. Motornov, Y. Roiter, I. Tokarev, S. Minko, *Progress in Polymer Science* **2010**, *35*, 174-211.

[344] D. Suzuki, S. Tsuji, H. Kawaguchi, *J. Am. Chem. Soc.* **2007**, *129*, 8088-8089.

[345] J. M. Hu, G. Q. Zhang, S. Y. Liu, *Chemical Society Reviews* **2012**, *41*, 5933-5949.

[346] L. Xu, W. Ma, L. Wang, C. Xu, H. Kuang, N. A. Kotov, *Chemical Society Reviews* **2013**, *42*, 3114-3126.

[347] Z. C. Zhu, E. Senses, P. Akcora, S. A. Sukhishvili, *Acs Nano* **2012**, *6*, 3152-3162.

[348] Y. Wang, A. D. Hollingsworth, S. K. Yang, S. Patel, D. J. Pine, M. Weck, *J. Am. Chem. Soc.* **2013**, *135*, 14064-14067.

[349] J. M. Lehn, *Chemical Society Reviews* **2007**, *36*, 151-160.

[350] J. M. Lehn, *Science* **2002**, *295*, 2400-2403.

[351] L. Brunsveld, B. J. B. Folmer, E. W. Meijer, R. P. Sijbesma, *Chemical Reviews* **2001**, *101*, 4071-4097.

[352] B. Monzyk, A. L. Crumbliss, *J. Am. Chem. Soc.* **1979**, *101*, 6203-6213.

[353] G. Schwarzenbach, K. Schwarzenbach, *Helvetica Chimica Acta* **1963**, *46*, 1390-&.

[354] M. J. Miller, *Chemical Reviews* **1989**, *89*, 1563-1579.

[355] R. Codd, *Coordination Chemistry Reviews* **2008**, *252*, 1387-1408.

[356] J. D. Faraldo-Gomez, M. S. P. Sansom, *Nature Reviews Molecular Cell Biology* **2003**, *4*, 105-116.

[357] Z. Rappoport, J. F. Liebman, *The Chemistry of Hydroxylamines, Oximes and Hydroxamic Acids*, Wiley, **2008**.

[358] J. Q. Tang, C. J. Wang, Y. J. Feng, W. Z. Yang, H. D. Song, Z. H. Chen, H. J. Yu, X. Z. Pan, X. J. Zhou, H. R. Wang, B. Wu, H. L. Wang, H. M. Zhao, Y. Lin, J. H. Yue, Z. Q. Wu, X. W. He, F. Gao, A. H. Khan, J. Wang, G. P. Zhao, Y. Wang, X. Wang, Z. Chen, G. F. Gao, *Plos Medicine* **2006**, *3*, 668-676.

[359] J. A. Champion, S. Mitragotri, *Pharmaceutical Research* **2009**, *26*, 244-249.

[360] S. H. Sun, H. Zeng, D. B. Robinson, S. Raoux, P. M. Rice, S. X. Wang, G. X. Li, *J. Am. Chem. Soc.* **2004**, *126*, 273-279.

[361] L. Josephson, J. Lewis, P. Jacobs, P. F. Hahn, D. D. Stark, *Magnetic Resonance Imaging* **1988**, *6*, 647-653.

[362] A. Kelsch, S. Tomcin, K. Rausch, M. Barz, V. Mailander, M. Schmidt, K. Landfester, R. Zentel, *Biomacromolecules* **2012**, *13*, 4179-4187.

[363] J. A. Champion, Y. K. Katare, S. Mitragotri, *Journal of Controlled Release* **2007**, *121*, 3-9.

[364] N. R. Jana, Y. F. Chen, X. G. Peng, *Chemistry of Materials* **2004**, *16*, 3931-3935.

[365] C. Graf, D. L. J. Vossen, A. Imhof, A. van Blaaderen, *Langmuir* **2003**, *19*, 6693-6700.

[366] J. Ge, Q. Zhang, T. Zhang, Y. Yin, *Angewandte Chemie-International Edition* **2008**, *47*, 8924-8928.

[367] K. Nozawa, H. Gailhanou, L. Raison, P. Panizza, H. Ushiki, E. Sellier, J. P. Delville, M. H. Delville, *Langmuir* **2005**, *21*, 1516-1523.

[368] S. Berger, A. Synytska, L. Ionov, K.-J. Eichhorn, M. Stamm, *Macromolecules* **2008**, *41*, 9669-9676.

[369] S. Braconnot, M. M. Eissa, A. Elaissari, *Colloid and Polymer Science* **2013**, *291*, 193-203.

[370] H. Böshagen, *Chemische Berichte* **1967**, *100*, 954-960.

10 Acknowledgements

11 Curriculum Vitae

12 List of Publications Related to the PhD Thesis

- M. B. Bannwarth*, S. W. Kazer, S. Ulrich, G. Glasser, D. Crespy, K. Landfester*, *Angew. Chem. Int. Ed.* **2013**, 52, 10107-10111, *Well-defined Nanofibers with Tunable Morphology from Spherical Colloidal Building Blocks, Angew. Chem.* **2013**, 125, 10294-10298, *Definierte Nanofasern mit einstellbarer Morphologie aus sphärischen Kolloidbausteinen.*

- M. B. Bannwarth*, T. Weidner, E. Eidmann, K. Landfester, D. Crespy*, *Chem. Mater*. **2014**, accepted, *Redox-Responsive Nanoparticles and their Reversible Assembly/Disassembly to Mimick Bacteria Cooperative Behavior.*

- V. Fischer, M. B. Bannwarth, G. Jakob, K. Landfester, R. Munoz-Espi*, *J. Phys. Chem. C*, **2013**, 117, 5999, *Luminescent and Magnetoresponsive Multifunctional Chalcogenide/Polymer Hybrid Nanoparticles.*

- C. Herrmann, M. B. Bannwarth, K. Landfester, D. Crespy*, *Macromol. Chem. Phys.* **2012**, 213, 829, *Re-dispersible Anisotropic and Structured Nanoparticles: Formation and Their Subsequent Shape Change*.

- I. Vernikouskaya*, N. Fekete, A. Erle, M. B. Bannwarth, K. Landfester, M. Rojewski, G. Schmidtke-Schrezenmeier, H. Schrezenmeier, V. Rasche, *Contrast Media Mol. Imaging*. **2013**, accepted, *Iron-Loaded PLLA (iPLLA) Nanoparticles as Highly Efficient Intracellular Markers for Visualization of Mesenchymal Stromal Cells by MRI*.

- D. Hofmann, C. Messerschmidt, M. B. Bannwarth, K. Landfester, V. Mailänder*, *Chem. Commun.* **2014**, 50, 1369-1371, *Drug Delivery without Nanoparticle Uptake: Delivery by a Kiss-and-Run Mechanism at the Cell Membrane*.

- M. B. Bannwarth, S. Ebert, M. Lauck, S. Tomcin, U. Ziener, G. Jakob, K. Münnemann, V. Mailänder, A. Musyanovych, K. Landfester*, submitted, *Magnetic Tracing and Releasing from Nanocapsules for Combined Imaging and Therapy*.

- D. Hofmann, S. Tenzer, M. B. Bannwarth, C. Messerschmidt, S.-F. Glaser, H. Schild, K. Landfester, V. Mailänder, to be submitted, *Guiding Cellular*

Nanoparticle Transport: Proteomic Analysis Reveals Routes of Uptake and Intracellular Storage.

- M. B. Bannwarth, S. Utech, S. Ebert, D. Weitz, D. Crespy, K. Landfester, to be submitted, *Defined Polymer-like Architectures from Colloidal Building Blocks.*

- S. Ebert, M. B. Bannwarth, A. Musyanovych, K. Münnemann, K. Landfester, to be submitted, *How Morphology Influences Relaxivity – Comparative Study of Superparamagnetic Iron Oxide/Polymer Hybrid Nanostructures*.

- M. B. Bannwarth, K. Landfester, D. Crespy, to be submitted, *Highly Superparamagnetic Nanocapsules for Self-Healing Coatings*.